QUANTUM MECHANICAL STUDIES OF NONADIABATIC MOLECULAR PROCESSES

A Thesis

Submitted for the Degree of

DOCTOR OF PHILOSOPHY

By

SUSANTA GHANTA

SCHOOL OF CHEMISTRY

UNIVERSITY OF HYDERABAD

HYDERABAD 500 046

INDIA

June 2011

List of Abbreviations

BO	Born-Oppenheimer
cc-pVDZ	Correlation consistent polarized valence double - ζ
aug-cc-pVTZ	Augmented correlation consistent polarized valence triple - ζ
CIs	Conical intersections
CRDS	Cavity ringdown spectroscopy
DIBs	Diffuse interstellar bands
FC	Franck-Condon
FWHM	Full-width at half-maximum
MATI	Mass analysed threshold ionization
MCTDH	Multiconfiguration time-dependent Hartree
MIS	Matrix isolation spectroscopy
MP2	Second order Møller-Plesset perturbation theory
An	Anthracene
An^+	Anthracene radical cation
OVGF	Outer valence Green's function
MC	Phenylacetylene
MC^+	Phenylacetylene radical cation
PAHs	Polycyclic aromatic hydrocarbons
PES(s)	Potential energy surface(s)
SPFs	Single particle functions
UIR	Unidentified infrared emission
WP	Wave packet
Pym	pyrimidine
Pym^+	pyrimidine radical cation
Bl	barrelene
Bl^+	barrelene radical cation
CASSCF	complete active space self consistent field
MRCI	multi reference configuration interaction
EOM -CCSD	Equation of motion coupled cluster singles and perturbative doubles

Contents

Chapter 1

Introduction

1.1 Vibronic coupling and Jahn-Teller effect

The Born-Oppenheimer approximation [1, 2] is a very successful tool to understand the chemical process that occur on the electronic ground state of the system. Within this approximation the electronic state is described at a set of rigid molecular configuration. The resulting electronic surface is then utilized to investigate the nuclear motion in a molecular system. This is successfully applied in many areas in molecular physics and chemistry like (a) local versus normal modes description of molecular vibration [3], (b) the chaotic behavior of multi-mode dynamics [4], (c) the decay of excited vibrational levels in polyatomic molecules [5], (d) the calculation of reaction cross section in atom-molecule collisions [6]. The basic idea behind this BO approximation is that the spacing of electronic eigenvalues is generally large compared to typical spacings associated with nuclear motion. Any violation of this condition leads to a transition between the adiabatic electronic PESs by the residual kinetic energy operator. In this situation the nuclear motion is no longer confined to a single "adiabatic " electronic PES, rather the electronic transition takes place during nuclear vibration. In fact, different electronic states can be coupled through suitable nuclear vibration - a

phenomena is known as "Vibronic Coupling " (VC) in the literature. The VC is ubiquitous in polyatomic molecular systems where there are large number of energetically close-lying electronic states and many nuclear degrees of freedom. One of the major consequences of VC is the occurrence of Conical Intersection (CIs) of electronic PESs.

The existence of CIs is inherent in molecules that exhibit Jahn-Teller (JT) [7–14] effect as *"that a nonlinear molecule in an orbitally degenerate state spontaneously distorts to a configuration of reduced symmetry "*. This has been one of the most fascinating phenomena in the physics and chemistry of symmetric nonlinear molecular systems. Since the classical work of Longuet-Higgins *et al.* [15–17] on the JT effect in a doubly degenerate (E) electronic state caused by the degenerate (e) vibrational modes (the so-called $E\times e$-JT effect), much effort has been devoted to elucidate its nature and importance in a wide variety of systems including, transition metal complexes [18], solid-state physics and chemistry [19–21], organic hydrocarbons, radicals and ions [8,12,22–26], and fullerenes [27]. Typically, the $(E \times e)$-JT problem with linear terms of vibronic interactions, the adiabatic potentials $V_{\pm}$ exhibit the threefold symmetry of the point group. The lower sheet, in particular, exhibits three equivalent local minima which are separated by three equivalent *saddle points*. Thus the topography of the lower adiabatic sheet resembles a "Mexican hat" . In case of multi-mode molecular systems this often leads to a highly diffuse spectral envelope - the vibrational levels of the upper surface are completely mixed with the quasi-continuum of vibrational levels of the lower surface [23]. In a time-dependent picture this generally yields a ultrafast non-radiative deactivation of excited electronic states [23, 29–32].

In 1957, Öpik and Pryce first noted that effects similar to the JT effect may be inherent in systems with near (quasi-degenerate or pseudo-degenerate) electronic states [16]. This is known as pseudo-Jahn-Teller (PJT) effect in the literature [13, 23, 33–36]. In the following year in 1958, Longuet-Higgins along with Öpik, Pryce and Sack worked on the dynamic aspects of the JT effect, that is

to say, the interaction between the motions of the nuclei and the electrons [15]. In general, the dynamical coupling between the electronic and nuclear motions presents a complex problem to which the solution can only be obtained by lengthy numerical methods. However, there is one relatively simple case which can be studied algebraically, namely that of a doubly degenerate electronic state (E) whose degeneracy is removed in the first order by a doubly degenerate vibration (e). This situation occurs rather widely in physics and chemistry [8,12,15]. Other interesting cases in which non-degenerate vibrational modes involved in the JT activity are also found in the literature [8, 12, 19, 23, 30, 37, 38]. This can only be encountered in molecules possessing two- or four- fold axes of symmetry, for example, C_4, C_{4v}, C_{4h}, D_4, D_{2d}, D_{4h}, S_4, and D_{4d} point groups. This is known as $(E \times b)$-JT effect since the degeneracy is lifted by vibrational modes of b symmetry. Usually the vibrational modes of e symmetry participate in PJT activity in this case.

Although linear molecules look like exceptions from the JT theorem, they too experience similar instabilities in their degenerate or pseudo-degenerate states when quadratic terms of VC are considered. This is known in the literature as the Renner-Teller (RT) effect, following the original paper of Renner in 1934 [39] that describes the vibronic interactions in degenerate Π electronic states of linear triatomic molecules. The JT effect as well as the PJT effect have been studied extensively over the past few decades. This JT effect has played a pivotal role in one of most important discoveries of modern physics - high temperature superconductivity (Nobel Prize in 1987) [40].

1.2 Occurrence of CIs and their implications in quantum dynamics

The electronic states of same symmetry of a diatomic molecule where the vibrational degree of freedom is one, avoid crossing. This is known as "non-crossing rule"formulated by Wigner and von Neumann [41]. For polyatomic molecules where the vibrational DOF is more than two, electronic states of same symmetry may cross in principle. The crossing of electronic states leads to the formation of CIs, which is a (3N-6-2)-dimensional seam (or a hyper-line) of the electronic energy for an N-atom molecule. CIs were reported in early 1930s [7, 39, 42]. Later on, the identification and characterization of different kinds of CIs were extensively studied by Teller [42] and by Herzberg and Longuet-Higgins [43]. They provide deep insights into the subject predicting a variety of physical phenomena that emerge from PES crossings. The field has undergone a monumental growth thereafter following the outstanding contributions of several research groups [8–10, 12, 19, 23, 44–47].

Intersections are *Symmetry-required* when the two electronic states form the components of a degenerate irreducible representation (IREP). The JT interaction of the electronic states in H_3 which corresponds to the components of an E IREP of D_{3h} symmetry point group. Conical intersections which are not required by symmetry are accidental intersections. *Accidental symmetry-allowed (different symmetry)* interactions correspond to the intersection of two states of distinct spatial symmetry. The two lowest excited singlet electronic states (A'') of H-S-H, provides an example of this type of CI. For C_{2v} geometries these states are of $^1A_2$ and $^1B_1$ symmetry, so that symmetry allowed accidental CI occurs [48–51]. Likewise when PESs of two states of same symmetry cross, the intersection is termed as *accidental same symmetry* CI. An intersection of electronically excited 2^1A and 3^1A states of CH_3-S-H provides an example of this type of CI [48, 51, 52].

Based on the shape and orientation of the PESs, CIs are further classified

as *peaked* and *sloped* CI [53–55]. *Peaked* CIs appear when both the PESs are elliptical cones pointing towards each other with a common tip. In this case, the crossing point is the minimum of the upper PES and the topology at this point looks like a double cone. At *slopped* CIs, both the PESs have downhill slope and touch each other at the crossing point in branching space. Here, the crossing point is always at higher energies compare to the minimum of the upper PES and the crossing appears as a seam of intersections. While a large variety of photochemical reactions via excited-state reaction pathways are controlled by *peaked* CIs, the *sloped* CIs are key factor for the unsuccessful chemical reactions and arrange decay channels for the ultrafast non-radiative deactivation of excited states [54, 55].

Seams of the CI can also be categorized based on the dimension of the branching space, η, for intersection of two PESs with $\eta = 2$, 3 or 5 [56]. Among them $\eta = 2$ is the most common case of a two state CI for even electronic molecular system at non-relativistic situation.

A typical dynamical outcome that bears the signature of CIs of PESs is the subpicosecond decay of excited molecular electronic states [23, 33, 57]. The corresponding electronic transition yieldls seemingly diffuse and overlapping bands that exhibits highly complex and dense line structure under high resolution. On the lower electronic state (adiabatic) the phenomena of the geometric phase [58–60], bifurcation of the wave packet [61] and dissipative vibrational motions [62] are observed. It is now fairly accepted that CIs serve as the "bottleneck" in photo-physical and photochemical transitions [63–65] and also referred to as *photochemical funnels* in the literature [66]. The book edited by Domcke, Yarkony and Köppel represents an excellent collection of articles in this emerging area of chemical dynamics [33].

1.3 Brief overview of the physics, chemistry and biology of interstellar medium

In 1919, Mary Lea Heger [67] discovered the first of what would come to be known as the "Diffuse Interstellar Bands "(DIBs). The DIBs are a series of absorption lines that are observed toward just about every star in the galaxy that has interstellar material in front of it. These lines are generally quite broad and unresolved (although a few show substructure that looks tantalizingly like a rotational band contour), and they appear "diffuse ", or fuzzy, on early photographic plates. They are known to be interstellar, because they do not suffer the periodic Doppler shifts associated with stellar lines in binary star systems. Hence the term diffuse interstellar bands [68].

The constancy of the absorption wavelengths implies that the carriers are in the gas phase, and the fact that they are broad implies that their carriers are molecular rather than atomic. Despite observations, their assignment to specific molecular carrier remains an enigmatic problem till date. Currently, this task is considered a priority in the area of interstellar physics and chemistry. So far, major attempts towards this endeavor have been made by the stellar and laboratory spectroscopists. The spectra observed by the astronomers are compared with those recorded in the laboratory under the typical conditions of interstellar medium (ISM) [69, 70]. The latter warrant a collision free environment. It was not possible to create such an environment in a laboratory until the recent past. Therefore, most of the studies relied on the laboratory experiment (matrix isolation spectroscopy (MIS), resonance-enhanced multiphoton dissociation spectroscopy (REMPD), photo dissociation of van der Walls complexes) in matrix environments [69–71]. Understandably, collision with the host matrix causes an energy shift and broadening of the spectral lines and no unambiguous identification of DIBs could be made with the aid of these experimental results obtained in matrices. In recent years, breakthrough developments in the gas phase measure-

ments such as cavity ring down spectroscopy (CRDS), made it possible to provide complementary evidence of interstellar observations [72–75]. In recent years, very high resolution spectrograph's on the world's most powerful telescopes have been used to observe and analyze DIBs. Iglesias-Groth *et al.* have discovered three new DIBs for naphthalene cation [76] and one new broad interstellar band for anthracene cation [77]. These experimental findings however awaits unambiguous confirmation from precise theoretical studies.

Identifying the carriers of DIBs has become one of the classic astrophysical spectroscopic problems. Recent work suggests they are caused by polycyclic aromatic hydrocarbons (PAHs), or, most likely, their cations, since PAH ions of all sizes, long carbon-chain molecules, and fullerenes, absorb in the visible and near infrared, and such molecules are expected to be ionized by the intense ultraviolet field present in much of the interstellar medium. PAH molecules appears to have profound implications in the physics, chemistry and biology of ISM. Recently nitrogenated PAH molecule (PANH) also found in astrophysical environment. The observed broad and diffuse vibronic band, ultrafast internal conversion rate of low-lying excited electronic state and lack of fluorescence are in favour of PAH hypothesis. The PAH cation is highly photostable than their neutral counterpart. Their formation, fragmentation and reactions with the small molecules are being studied both theoretically and experimentally [78–84] in recent years.

Methyl cyanide exists in astrophysical environment. So, the study of electronic transition in their low-lying electronic states is a choice of theoretical interest.

From the absorption spectroscopy [71, 74, 75, 85] of anthracene cation (An^+) and photoelectron spectroscopy [86–89] of anthracene molecule reveals broad vibronic band for the D_2 electronic state of An^+ . These experiments revealed diffuse vibronic bands and subpicosecond dynamics of their low-lying electronic states. Very recently, spectroscopic measurements of moderately reddened star Cernis 52 located in the Perseus molecular cloud lead to the discovery of new broad DIBs [77]. Aided by the laboratory measurements these are assigned to

the electronic transitions in the anthracene radical cation.

DNA molecule is stable under strong UV radiation. The nucleo bases are mainly responsible for this stability. There are two kind of nucleo bases, pyrimidine and purine. Pyrimidine is a prebiological molecule which is predicted to exist in the astrophysical environments. Thus a study of the photophysics of pyrimidine and its cation is also attempted.

1.4 Sequential architecture of the thesis

Chapter 2: An overview of the theoretical and computational methodologies is presented in this chapter to describe the nonadiabatic molecular processes studied in the thesis. The basic concept of BO approximation is discussed. The importance of diabatic electronic basis to investigate the static and dynamics aspect of both the JT and PJT effect and VC effect in multimode molecular processes is discussed. The normal mode description of vibrational motion and the application of symmetry selection rules are in relation to their importance in multi-mode VC theory is discussed. In this regard a simple heuristic models, the so called linear vibronic coupling (LVC) scheme is discussed. The VC Hamiltonian involving degenerate electronic state and degenerate vibrational modes are illustrated. Inclusions of totally and nontotally symmetric vibrational modes to the VC Hamiltonians are also discussed. The adequate level of *ab initio* electronic-structure theory to compute the parameters of the electronic part of the VC Hamiltonian is discussed. Both the time-independent matrix diagonalization approach and time-dependent WP propagation approach within the multi-configuration time-dependent Hartree (MCTDH) scheme to compute the vibronic spectrum are illustrated.

Chapter 3: Static and dynamic aspects of the JT and PJT interactions between the ground and first excited electronic states of the methyl cyanide radical cation are theoretically investigated in chapter 3. The latter involves

construction of a theoretical model by *ab initio* computation of electronic potential energy surfaces and their coupling surfaces and simulation of the nuclear dynamics employing time-independent and time-dependent quantum mechanical methods. The present system represents yet another example belonging to the $(E + A) \otimes e$ JT-PJT family, with common JT and PJT active degenerate (e) vibrational modes. The theoretical results are found to be in very good accord with the recent experimental data revealing that the JT interactions are particularly weak in the ground $\widetilde{X}^2E$ electronic manifold of methyl cyanide radical cation. On the other hand, the PJT interactions of this ground electronic manifold with the first excited $\widetilde{A}^2A_1$ electronic state of the radical cation are stronger which cause an increase of the spectral line density.

Chapter 4: It represents the quantum dynamics of non-adiabatic electronic transitions in the radical cation of anthracene. Both time-independent and time-dependent quantum mechanical approach combined with vibronic coupling theory is utilized to simulate the nuclear dynamics along the relevant vibrational degrees of freedom on the coupled manifold of the first few electronic states of radical cation. The results are reported in terms of vibronic spectra and non-radiative decay of electronic populations. The findings are in very good agreement with the recent experimental results, establishing for the first time the intricate coupling between electronic and nuclear motion in such systems, an understanding of which is of primary importance in astrophysical applications.

Chapter 5: This chapter deals with the static and dynamic aspect of JT and PJT interactions between ground ($\widetilde{X}^2A_2'$) and first three excited electronic states ($\widetilde{A}^2E'$, $\widetilde{B}^2E''$ and $\widetilde{C}^2A_1'$) of bicyclo-[2,2,2]-octatriene (barrelene) radical cation(BL^+). The complex vibronic spectra of the coupled electronic state of cation is simulated by both time-independent and time-dependent wave packet propagation method using multi reference time-dependent Hartree scheme. Each of the degenerate electronic states undergoes JT-split when the cation is distorted along degenerate vibrational modes of e' symmetry. The later can also undergoes

PJT type of crossing between $\widetilde{X}$ -$\widetilde{A}$ and $\widetilde{A}$ -$\widetilde{C}$ electronic state of the cation. The degenerate vibrational modes of symmetry e'' are the PJT coupling mode between $\widetilde{B}$ -$\widetilde{C}$ and $\widetilde{A}$ -$\widetilde{B}$ electronic states. These generate the multiple multidimensional curve crossing between the electronic states and complex vibronic spectra. The energy spacing between the most intense peak of the bimodal photoelectron band of BL is reported 0.30 eV from the experimental photo-electron spectroscopy experiment which is nicely corroborated with our theoretically calculated value of 0.25 eV for the same. The final theoretical results are compared with the experimental results enlightening the very strong JT and PJT interactions in the ground and excited electronic states of the cation.

Chapter 6: In this chapter multi-mode quantum dynamics of the coupled $\widetilde{X}$ -$\widetilde{A}$ -$\widetilde{B}$ -$\widetilde{C}$ electronic states of pyrimidine radical cation (Pym^+) and S_1-S_2-S_3 electronic states of neutral pyrimidine (Pym) molecule is investigated. The complex vibronic spectra and the non-radiative decay dynamics of both the neutral and radical cation of pyrimidine are simulated theoretically by both time-independent and time-dependent wave packet propagation approach using the multi-configuration time-dependent Hartree scheme. The theoretical results are compared with the experimental photoelectron spectrum and resolved (< 10 meV) vibrational energy level spectrum of pyrimidine which has good impact on astrobiology.

Chapter 7: Concluding remarks and some future directions in research in this field are given in this chapter.

Chapter 2

Theoretical Methodology

2.1 Theory of Vibronic-Coupling

2.1.1 Adiabatic approximation and diabatic basis

A proton is ~ 1840 times heavier than an electron. Therefore, the typical motion associated with nuclei is very very slow when compared to the motion of electrons in a molecule. Thus it is possible to separate the faster moving electrons from the slow moving nuclei and the molecular Hamiltonian can be written as

$$H \;=\; T_e + T_N + U(\mathbf{r}, \mathbf{R}) \tag{2.1}$$

where T_e and T_N are the operators for the kinetic energy of the electrons and nuclei, respectively, and $U(\mathbf{r}, \mathbf{R})$ is the total potential energy of the electrons and nuclei. The vectors $\mathbf{r}$ and $\mathbf{R}$ collectively denote the set of electronic and nuclear coordinates, respectively. For fixed nuclei, i.e., $T_N = 0$, the orthonormal electronic wavefunctions $\Phi_n(\mathbf{r;}\ \mathbf{R})$ and energies $V_n(\mathbf{R})$ defined by

$$\left[\underbrace{T_e + U(\mathbf{r}, \mathbf{R})}_{H_e} - V_n(\mathbf{R})\right] \Phi_n(\mathbf{r}, \mathbf{R}) \;=\; 0. \tag{2.2}$$

They are known as the BO electronic states and PESs [90], respectively. The exact eigenstates of the system can be expanded in terms of the BO electronic states as

$$\Psi(\mathbf{r},\mathbf{R}) \;=\; \sum_n \chi_n(\mathbf{R})\Phi_n(\mathbf{r},\mathbf{R}). \tag{2.3}$$

Inserting this ansatz into the Schrödinger equation

$$(H-E)\Psi(\mathbf{r},\mathbf{R}) \;=\; 0 \tag{2.4}$$

one readily obtains [90] the following set of coupled equations for the expansion coefficients in Eq. 2.1

$$\left[T_N + V_n(\mathbf{R}) - E\right]\chi_n(\mathbf{R}) \;=\; \sum_m \hat{\Lambda}_{nm}\chi_m(\mathbf{R}). \tag{2.5}$$

The operators Λ_{nm} are known as the non-adiabatic operators, given by [91]

$$\hat{\Lambda}_{nm} \;=\; -\int d\mathbf{r}\Phi_n^\star(\mathbf{r},\mathbf{R})[T_N,\Phi_m(\mathbf{r},\mathbf{R})]. \tag{2.6}$$

If we rewrite the fundamental set of equations given in Eq. (2.5) as a matrix Schrödinger equation, we have

$$\left(\underbrace{T_N\mathbf{1}+\mathbf{V}(\mathbf{R})-\hat{\mathbf{\Lambda}}}_{\mathcal{H}} - E\mathbf{1}\right)\chi = 0. \tag{2.7}$$

The matrix Hamiltonian $\mathcal{H}$ describes the nuclear motion in the manifold of electronic states. χ is the column vector with elements χ_n; $\mathbf{1}$ is the unit matrix, and $\mathbf{V}(\mathbf{R}) = V_n(\mathbf{R})\delta_{nm}$ is the diagonal matrix of electronic energies.

If we neglect the non-adiabatic operator $\hat{\mathbf{\Lambda}}$ in Eq. (2.7) then we will end up with the adiabatic approximation which is based on the assumption that the kineticenergy operator of the nuclei can be considered as a small perturbation of

the electronic Hamiltonian. In the adiabatic approximation the matrix Hamiltonian $\mathcal{H}$ is diagonal and the total wavefunction (Eqn. 2.3) becomes the product of the nuclear and electronic wavefunctions

$$\Psi(\mathbf{r},\mathbf{R}) \;=\; \chi_n(\mathbf{R})\Phi_n(\mathbf{r},\mathbf{R}). \tag{2.8}$$

The nuclear motion can be thought of as proceeding on the PES $V_n(\mathbf{R})$ of a given electronic state characterized by the index n.

When the electronic states are energetically very close (within a quantum of energy of nuclear vibration) then we can not neglect the non-adiabatic operators $\hat{\mathbf{\Lambda}}$ in the Hamiltonian $\mathcal{H}$ for those electronic indices n and m which belong to the manifold of closely lying electronic states. These electronic states are now vibronically coupled via $\hat{\Lambda}_{nm}$. In terms of the first- and second-order derivative couplings, $\hat{\Lambda}_{nm}$ in Cartesian coordinates can be written as [23, 92, 93]

$$\hat{\Lambda}_{nm} \;=\; -\sum_k \frac{\hbar^2}{M_k} F_{nm}\frac{\partial}{\partial R_k} - \sum_k \frac{\hbar^2}{2M_k} G_{nm}, \tag{2.9}$$

where M_k are nuclear masses and

$$F_{nm} \;=\; \langle \Phi_n(\mathbf{r})|\Delta_k|\Phi_m(\mathbf{r})\rangle, \tag{2.10}$$

$$G_{nm} \;=\; \langle \Phi_n(\mathbf{r})|\Delta_k^2|\Phi_m(\mathbf{r})\rangle, \tag{2.11}$$

in which $\Delta_k \equiv \partial/\partial R_k$. The matrix elements F_{nm} can be written according to the Hellmann-Feynmann type of relation as [23, 94]

$$F_{nm} \;=\; \frac{\langle \Phi_n(\mathbf{r})|\Delta_k \mathcal{H}_{el}(\mathbf{r},\mathbf{R})|\Phi_m(\mathbf{r})\rangle}{V_n(\mathbf{R}) - V_m(\mathbf{R})}, \tag{2.12}$$

where $\mathcal{H}_{el}$ defines the electronic Hamiltonian for fixed nuclear coordinates. When

the two surfaces are degenerate, $V_n(\mathbf{R}) = V_m(\mathbf{R})$, then F_{nm} exhibit singular behavior [23]. As a result, both the electronic wave function and energy become discontinuous at the seam of CIs which makes the adiabatic electronic representation unsuitable for dynamical studies. To circumvent this problem an alternative electronic representation called diabatic representation has been proposed in the literature [95–108].

2.1.2 Diabatic electronic representation

Divergent coupling terms of the adiabatic electronic representation (cf., Eq. 2.12 above) are a nuisance for the computational treatment of the nuclear dynamics, on the exact or near degeneracy of electronic PESs. An alternative electronic representation , the so called diabatic (or quasi-diabatic) representation, which avoids singular coupling elements has therefore been introduced in the literature. The diabatic electronic states are defined by a unitary transformation of the adiabatic electronic states within an affordable subspace. This transformation is chosen to render the electronic states in the relevant subspace smoothly varying as a function of the nuclear coordinates, such that the derivative coupling term are sufficiently small to be neglected. In contrast to adiabatic representation, the electronic Hamiltonian becomes non diagonal in this new representation. Neglecting residual derivative couplings in the diabatic representation, the coupled equations of motion (cf, Eq. 2.5) takes the form [47, 57]

$$\{T_N(\mathbf{R}) + \mathbf{U_{nn}}(\mathbf{R}) - E\}\chi_{\mathbf{n}}(\mathbf{R}) \;=\; \sum_{n\neq m} \mathbf{U_{nm}}(\mathbf{R})\chi_{\mathbf{m}}(\mathbf{R}), \tag{2.13}$$

where $\mathbf{U_{nn}}(\mathbf{R})$ are the diabatic PESs and $\mathbf{U_{nm}}(\mathbf{R})$ are their coupling elements. The latter are given by

$$\mathbf{U_{nm}}(\mathbf{R}) \;=\; \int d\mathbf{r}\phi_n^\star(\mathbf{r},\mathbf{R})[T_e + \mathbf{V}(\mathbf{r},\mathbf{R})]\phi_m(\mathbf{r},\mathbf{R}), \tag{2.14}$$

where ϕ represents the diabatic electronic wave function. The equation (2.13) is equivalent to the following representation of the molecular Hamiltonian in a basis of diabatic electronic states

$$H = \sum_n |\phi_n\rangle[T_N(\mathbf{R}) + V_n(\mathbf{R})]\langle\phi_n| + \sum_{n\neq m} |\phi_n\rangle V_{nm}(\mathbf{R})\langle\phi_m|, \tag{2.15}$$

The diabatic electronic states $\phi(\mathbf{r}, \mathbf{R})$ are defined via a unitary transformation of the adiabatic electronic states $\mathbf{\Phi}(\mathbf{r}, \mathbf{R})$ through

$$\phi(\mathbf{r}, \mathbf{R}) \;=\; \mathbf{S}\mathbf{\Phi}(\mathbf{r}, \mathbf{R}), \tag{2.16}$$

where $\mathbf{S}$ is a orthogonal and unitary transformation matrix. For a two-states problem it is given by

$$\mathbf{S}(\mathbf{Q}) \;=\; \begin{pmatrix} \cos\theta(\mathbf{Q}) & \sin\theta(\mathbf{Q}) \\ -\sin\theta(\mathbf{Q}) & \cos\theta(\mathbf{Q}) \end{pmatrix}. \tag{2.17}$$

The matrix $\mathbf{S(Q)}$ is called the adiabatic-to-diabatic transformation (ADT) matrix and $\theta(\mathbf{Q})$ defines the transformation angle. The required condition for such transformation is the first-order derivative coupling of Eq. (2.12) vanishes in this diabatic representation for all nuclear coordinates [95, 96]

$$\int d\mathbf{r}\phi^*_{\mathbf{n}}(\mathbf{r}, \mathbf{R})\frac{\partial}{\partial \mathbf{R_k}}\phi_{\mathbf{m}}(\mathbf{r}, \mathbf{R}) \;=\; 0. \tag{2.18}$$

This requirement yields the following differential equations for the transformation matrix [97–99]

$$\frac{\partial \mathbf{S}}{\partial \mathbf{R_k}} + \mathbf{F^{(k)}}\mathbf{S} \;=\; 0, \tag{2.19}$$

where the elements of the first-order derivative coupling matrix $F^{(k)}$ are given by

Eq. (2.12). A unique solution of the above equation exists only when [97–99]

$$\frac{\partial \mathbf{A}^{(\mathbf{k})}_{\mathbf{nm}}}{\partial \mathbf{R}_{\mathbf{l}}} - \frac{\partial \mathbf{A}^{(\mathbf{l})}_{\mathbf{nm}}}{\partial \mathbf{R}_{\mathbf{k}}} = [\mathbf{A}^{(\mathbf{k})}_{\mathbf{nm}}, \mathbf{A}^{(\mathbf{l})}_{\mathbf{nm}}]. \tag{2.20}$$

The concept of diabatic electronic basis was introduced quite early in the literature in the context of describing the electron-nuclear coupling in atomic collision processes [100] as well as in molecular spectroscopy [17, 101]. However, construction of the latter for polyatomic molecular systems is a tedious and difficult since it is a problem depending on multi-coordinates rather than a single nuclear coordinate. Therefore, various approximate mathematical schemes have been proposed in the literature [95–97, 102–108] to accomplish this task.

2.1.3 Normal Coordinates

Following the traditional approach [10–12, 17], we introduce normal coordinates [109] to describe small vibrations around the equilibrium geometry of the electronic ground state (we assume here that we are dealing with a closed-shell molecule with a well-define structure). The normal coordinates are defined by

$$\mathbf{q} = \mathbf{L}^{-1}\delta\mathbf{R} \tag{2.21}$$

where $\delta\mathbf{R}$ is the $3N-6$ ($3N-5$ for linear molecules) dimensional vector of internal displacement coordinates (changes of bond lengths and bond angles) for an N atomic molecule, and $\mathbf{L}$ is the L-matrix of the well-known Wilson FG-matrix method [109]. It is convenient to introduce dimensionless normal coordinates via

$$Q_i = (\omega_i/\hbar)^{1/2} q_i \tag{2.22}$$

where ω_i is the harmonic vibrational frequency of the i^{th} normal mode. In the *harmonic approximation*, which implies the expansion of the electronic ground

state potential energy up to second order in the displacements as well as the approximation of the metric tensor by its value at the equilibrium geometry, the kinetic-energy and potential-energy operators of the electronic ground state take the simple form

$$T_N = -\frac{1}{2}\sum_i \hbar\omega_i \frac{\partial^2}{\partial Q_i^2} \tag{2.23}$$

$$V_0 = \frac{1}{2}\sum_i \hbar\omega_i Q_i^2 \tag{2.24}$$

We proceed by expanding the diabatic excited-state potential-energy functions and coupling elements in terms of normal mode displacement coordinate Q_i.

2.1.4 Linear Vibronic Coupling Scheme

Let us assume that a diabatic basis has been obtained for a given set of vibronically interacting electronic states n and m. In this basis the matrix Hamiltonian is given by [23]

$$\mathcal{H} = T_N\mathbf{1} + \mathbf{W}(\mathbf{Q}). \tag{2.25}$$

The matrix elements of the potential matrix $\mathbf{W}(\mathbf{Q})$ read

$$W_{nm}(\mathbf{Q}) = \int d\mathbf{r}\phi_n^\star(\mathbf{r},\mathbf{Q})H_e\phi_m(\mathbf{r},\mathbf{Q}). \tag{2.26}$$

The $\phi_n(\mathbf{r},\mathbf{Q})$ are the diabatic wave functions for an electronic state of index n. For a polyatomic molecule, the accurate solution of the matrix Hamiltonian (Eq. 2.25) is very tedious and often impossible. Therefore, an approximate form of the matrix Hamiltonian is commonly considered for which the Schrödinger equation can be accurately solved. The simplest, yet elegant approximation is to expand the potential-energy matrix $\mathbf{W}(\mathbf{Q})$ about a reference nuclear configuration $\mathbf{Q}_0$ and retaining the terms linear in $\mathbf{Q}$ for the off-diagonal terms. This method is known

as the linear vibronic coupling (LVC) scheme [23,92]. The linear approximation is often sufficient since the elements of the $\mathbf{W}(\mathbf{Q})$ matrix are, by definition, slowly varying functions of $\mathbf{Q}$. Without any loss of generality it is assumed that the diabatic and adiabatic states are identical at the reference geometry $\mathbf{Q}_0$.

For the interacting electronic states n and m, the elements of the matrix Hamiltonian in the linear approximation are

$$\mathcal{H}_{nn} = T_N + V_0(\mathbf{Q}) + E_n + \sum_s \kappa_s^{(n)} Q_s \tag{2.27}$$

$$\mathcal{H}_{nm} = \mathcal{H}_{nm}(0) + \sum_c \lambda_c^{(n,m)} Q_c. \tag{2.28}$$

The energies E_n which appear in the diagonal of $\mathcal{H}$ are constants given by $W_{nn}(\mathbf{Q_0})$. The $\kappa_s^{(n)}$ represent the gradients of the excited-state potential functions at the equilibrium geometry of the ground state and are referred to as first-order *intra-state* electronic-vibrational coupling constants. The $\mathcal{H}_{nm}(0)$ is zero if the two interacting electronic states n and m, are transformed according to different irreducible representations. The $\lambda_c^{(n,m)}$ are correspondingly called first-order *interstate* coupling constants.

$$\kappa_s^{(n)} = \left(\frac{\partial V_n(\mathbf{Q})}{\partial Q_s}\right)_{\mathbf{Q_0}}, \tag{2.29}$$

$$\lambda_c^{(n,m)} = \left(\frac{\partial V_{nm}(\mathbf{Q})}{\partial Q_c}\right)_{\mathbf{Q_0}}. \tag{2.30}$$

The non-vanishing interstate coupling constants $\lambda_c^{(n,m)}$ are those for which the product of the irreducible representations of electronic states ϕ_n and ϕ_m, and of the nuclear coordinate Q_c contains the totally symmetric representation Γ_A, i.e. [23],

$$\Gamma_n \times \Gamma_{Q_c} \times \Gamma_m \supset \Gamma_A. \tag{2.31}$$

The analogous condition for the intrastate coupling constants $\kappa_s^{(n)}$ is

$$\Gamma_n \times \Gamma_{Q_s} \times \Gamma_n \supset \Gamma_A. \tag{2.32}$$

Certainly all totally symmetric modes can couple to the electronic motion which emphasize the important role of these modes in the VC problem. From the above symmetry selection rules (Eqs. 2.31 and 2.32), we can say that, only the totally symmetric modes give rise to nonzero intrastate coupling constants and only non totally symmetric modes to nonzero interstate coupling constants.

2.2 Electron-Nuclear coupling parameters

In this thesis mostly the closed-shell electronic ground state systems are treated to define the reference state for the photoinduced process. The equilibrium geometry and the harmonic force field in Cartesian displacement coordinates can routinely be obtained for electronic structure models for which analytic derivatives of the energy are available, e.g., restricted *Hatree-Fock (RHF)* [110] augmented by second-order **Møller-Plesset Perturbation Theory** [111]. Geometry *optimization* and normal-mode analysis at the MP2 level with at least Dunning's polarized valence double-zeta basis set [112] (cc-pVDZ) for large polyatomic system.

The first-order and second-order coupling parameters of the model vibronic Hamiltonian are basically the first and second derivatives of the ionization or excitation energy with respect to ground state normal coordinates. Thus we need a reliable electronic structure model which can accurately describe the ionized (excited) electronic state. We have used the *outer valence Green's function method (OVGF)* [113] for the direct calculations of vertical ionization energies (VIE). For complicated systems we generally used *Complete Active Space Self-consistent Field (CASSCF) [114]/Multi-reference configuration-interaction (MRCI)* [115]

method for the same. We have employed *Equation-of-motion Couple-Cluster-Single and Double (EOM-CCSD)* [116] method also for the generation of excited electronic state.

2.2.1 Vibronic coupling involving degenerate vibrational modes and degenerate electronic states

The presumably most widely known example of vibronic coupling is the JT effect of a doubly degenerate electronic state, that is, the coupling of the two components of the degenerate state by degenerate vibrational mode. In the case of linear molecules the VC problem is known as the RT effect [39]; otherwise, it is known as the JT effect [7].

2.2.1.1 The Jahn-Teller Effect

The JT effect is nowadays forms a whole trend in the theory of structure and properties of molecules. Let us consider a twofold degenerate (E) electronic state of a nonlinear molecule. In this there should present a non totally symmetric vibrational mode which can lift the orbital degeneracy in first order [7] when the molecule is distorted along those non totally symmetric vibrational modes. The symmetry of the desired vibrational mode for VC should be such that it is contained in the decomposition of the symmetrized product $(E)^2$. It is then found that in all but seven molecular-point groups (with two-fold and four-fold principal rotational axes of symmetry, e.g., D_{2d}, D_{4h}, C_{4v}, etc., where non- degenerate vibrational modes participate in the JT activity, the so-called $(E \times b)$-JT effect) degenerate vibrations can be JT active, leading to the $(E \times e)$-JT effect [8, 11, 12, 19, 23].

2.2.1.2 The single-mode $E \otimes e$ Jahn-Teller effect

Now we will focus on a simple case by considering a degenerate electronic state with the two component of the degenerate vibrational mode (Q_x and Q_y). The molecules possesses three-fold principal axis of rotation, will exhibit this kind of JT effect. In this system there are always doubly degenerate vibrational modes that are (linearly) JT-active, that is, the derivatives $\partial V_{\alpha\alpha'}/\partial Q_i$ do not vanish for their (Cartesian) displacement components Q_x and Q_y. Now considering the elementary symmetry selection rule mentioned above, the corresponding 2×2 JT matrix Hamiltonian takes the form [8, 14, 15]

$$\mathbf{H}^{E\otimes e} = H_0\mathbf{1}+\lambda\begin{pmatrix} Q_x & Q_y \\ Q_y & -Q_x \end{pmatrix}+\frac{\gamma}{2}\begin{pmatrix} Q_x^2+Q_y^2 & 0 \\ 0 & Q_x^2+Q_y^2 \end{pmatrix}+\frac{\eta}{2}\begin{pmatrix} Q_x^2-Q_y^2 & 2Q_xQ_y \\ 2Q_xQ_y & Q_y^2-Q_x^2 \end{pmatrix}. \tag{2.33}$$

$$H_0 = \frac{\omega}{2}\left(-\frac{\partial^2}{\partial Q_x^2}-\frac{\partial^2}{\partial Q_y^2}+Q_x^2+Q_y^2\right). \tag{2.34}$$

H_0 is seen to represent the Hamiltonian of the isotropic two-dimensional harmonic oscillator (with frequency ω), and the electronic energy at the origin $Q_x = Q_y = 0$ has been chosen to be zero. $\mathbf{1}$ denotes the 2×2 unit matrix. The parameters λ, and γ and η are called the first-order (or linear) and second-order (or quadratic) coupling constants, respectively.

To start with, let us first consider the second-order coupling constants (γ and η) to zero. This then reduces the Eq. (2.33) to the well-known Hamiltonian of the linear $E\otimes e$ JT effect which has been studied in the literature (see, for example, Refs. [8, 12, 23] and references therein). Diagonalization of the potential energy part leads to the famous "Mexican hat" potential energy surfaces

$$V_\pm = \frac{\omega}{2}\rho^2 \pm \lambda\rho, \tag{2.35}$$

$$\rho^2 = Q_x^2+Q_y^2. \tag{2.36}$$

These rotationally symmetric surfaces are characterized by the JT stabilization

energy

$$E_{JT} = \frac{\lambda^2}{2\omega}, \tag{2.37}$$

occurring at the optimum distortion

$$\rho_0 = \lambda/\omega. \tag{2.38}$$

The so-called pseudo rotational angle ϕ is defined as

$$\phi = \arctan\left(Q_y/Q_x\right). \tag{2.39}$$

The corresponding eigenvector matrix reads

$$\mathbf{S} = \begin{pmatrix} \cos\left(\phi/2\right) & -\sin\left(\phi/2\right) \\ \sin\left(\phi/2\right) & \cos\left(\phi/2\right) \end{pmatrix}, \tag{2.40}$$

where the two columns represent the expansion coefficients of the adiabatic wave functions in the diabatic electronic basis. Transforming the complete Hamiltonian (2.33) to the adiabatic basis leads to

$$\mathbf{H}_{ad}^{E\otimes e} = \mathbf{S}^{\dagger}\mathbf{H}^{E\otimes e}\mathbf{S} = H_0\mathbf{1} + \begin{pmatrix} V_+ & 0 \\ 0 & V_- \end{pmatrix} + \mathbf{\Lambda}, \tag{2.41}$$

with the non adiabatic coupling operator

$$\mathbf{\Lambda} = \frac{\omega}{2\rho^2}\begin{pmatrix} \frac{1}{4} & i\frac{\partial}{\partial\phi} \\ i\frac{\partial}{\partial\phi} & \frac{1}{4} \end{pmatrix}, \tag{2.42}$$

which is seen to diverge at the origin $\rho = 0$, where the two adiabatic potential energy surfaces exhibit the JT intersection.

2.2.2 Influence of additional modes

Most systems exhibiting the JT effect possess more than one degenerate vibrational mode (except for the triatomic systems, such as H_3, Li_3, etc.). The above presentation of the single-mode $E \otimes e$ JT serves as the basis for the discussion of related and more general systems. These will be discussed more briefly, focusing on their similarities and differences with respect to the prototype case. We start with the inclusion of additional vibrational modes.

2.2.2.1 Additional e vibrational modes

In this case the Hamiltonian (2.33) is given by

$$H = \sum_i H_i \tag{2.43}$$

Thus the additional e modes are included in the Hamiltonian (2.33) by replacing the corresponding single-mode terms by summations over all relevant vibrations, *e.g.*

$$\lambda Q_x \rightarrow \sum_i \lambda_i Q_x^i, \quad \lambda Q_y \rightarrow \sum_i \lambda_i Q_y^i, \tag{2.44}$$

in a self-explanatory notation (and an analogous extension in the zero-order Hamiltonian H_0). Since virtually all molecules exhibiting the $E \otimes e$ JT effect possess several e modes this generalization is of immediate relevance. Although the total JT stabilization energy E_{JT} is additive, *i.e.*

$$E_{JT} = \sum_i \frac{\lambda_i^2}{2\omega_i} \equiv \sum_i E_{JT}^{(i)}, \tag{2.45}$$

the Hamiltonians $\mathbf{H}_i^{E\otimes e}$ for the various modes do not commute ($i \neq j$):

$$\left[\mathbf{H}_i^{E\otimes e}, \mathbf{H}_j^{E\otimes e}\right] \neq 0. \tag{2.46}$$

Thus, the eigenvalue problem of the individual Hamiltonians cannot be solved

separately. Rather, the multi-mode vibronic secular matrix has to be diagonalized as a whole [23].

The non separability of the JT active modes makes it necessary to sum over all contributions $\mathcal{H}_j$ of the individual modes and treat the total matrix Hamiltonian $\mathcal{H}$ as a whole rather than the individual terms separately. As a consequence, the vibronic symmetries are reduced considerably. The individual vibronic angular momenta

$$\mathbf{J}_j = \frac{1}{i}\frac{\partial}{\partial\phi_j}\mathbf{1_2} + \frac{1}{2}\begin{pmatrix} 1 & 0 \\ 0 & -1 \end{pmatrix} \tag{2.47}$$

are no longer constants of the motion. It is only the total vibronic angular momentum

$$\mathbf{J} = \sum_j^M \frac{1}{i}\frac{\partial}{\partial\phi_j}\mathbf{1_2} + \frac{1}{2}\begin{pmatrix} 1 & 0 \\ 0 & -1 \end{pmatrix} \tag{2.48}$$

that commutes with $\mathcal{H}$ [23]. In the adiabatic PESs this manifests itself in a dependence of $\mathcal{V}_\pm$ on the azimuthal angles ϕ_j of the individual modes. The potentials are invariant only under a common change of the angles of all vibrational modes otherwise of a very complicated shape. In addition, the locus of intersection is no longer a single point in coordinate space, but rather a subspace of dimension $2M$ - 2. It must be evident from these remarks that the multimode JT problem leads to much more complicated nuclear dynamics than the single-mode problem. We note that it is important to take these multimode effects into consideration in order to arrive at a realistic treatment of actual molecules [23].

2.2.2.2 Inclusion of totally symmetric vibrational modes

From Eq. (2.27) it is clear that displacements along totally symmetric vibrations can *tune* the energy gap ($|E_2 - E_1|$) between two electronic states and generally

lead to intersections of the potential-energy functions, which are allowed by symmetry. These vibrational modes have therefore been termed *tuning modes* [23]. On the other hand, the non totally symmetric modes satisfying Eq. (2.31) describe the coupling between two electronic states. Therefore, they are termed as *coupling modes* [23]. Within the LVC approach, the tuning modes contribute only to the diagonal elements of the electronic Hamiltonian matrix, see Eq. (2.27). Therefore, the inclusion of these modes to the VC models described earlier becomes straightforward.

In the $(E \times e)$-JT case the N_t tuning modes are represented by

$$H_{JT}^{t} = \sum_{i=1}^{N_t} \left[\left(\frac{\partial^2}{\partial Q_i^2} + Q_i^2 \right) \mathbf{1_2} + \begin{pmatrix} \kappa_i^E & 0 \\ 0 & \kappa_i^E \end{pmatrix} Q_i \right], \tag{2.49}$$

where the normal coordinates Q_i, $i = 1 \cdots N_t$, are the totally symmetric modes and the κ_i^E are the gradients of the adiabatic potential-energy functions of the E state with respect to the i^{th} tuning mode.

From Eqs. (2.33) and (2.49), we have

$$\left[\mathbf{H}^{E\otimes e}, H_{JT}^{t} \right] = 0. \tag{2.50}$$

For this reason a_1 modes are usually omitted from JT treatments and included in the computation of vibronic spectra.

2.2.3 The pseudo-Jahn-Teller effect involving degenerate electronic states

Now we will discuss what happened when two degenerate electronic states interact with each other through suitable vibrational modes or one degenerate electronic state interacts with a non-degenerate electronic state via proper nuclear displacement coordinates. This kind of VC interaction is termed as pseudo-Jahn-Teller

(PJT) effect in literature. Let us consider a simple case where the interaction of degenerate E electronic state with a non degenerate state, characterized by the symmetry label A.

2.2.3.1 The single-mode $(E + A) \otimes e$ pseudo-Jahn-Teller effect

Considering the same general principles and symmetry selection rule for the construction of the vibronic Hamiltonian as indicated above and discussed in section (2.1.4), the Hamiltonian for the linear $(E + A) \otimes e$ pseudo-Jahn-Teller effect is found to be [23, 34]

$$\mathcal{H} = H_0\mathbf{1} + \begin{pmatrix} E_E & 0 & \lambda Q_x \\ 0 & E_E & \lambda Q_y \\ \lambda Q_x & \lambda Q_y & E_A \end{pmatrix}. \tag{2.51}$$

Here E_E and E_A denote the E and A state energies for the undistorted nuclear configuration ($Q_x = Q_y = 0$) and $\mathbf{1}$ represents the 3×3 unit matrix.

We note that the Hamiltonian (2.51) shares many features with the general vibronic coupling problem for two non degenerate electronic states, discussed amply in the literature. We also note that the notion "pseudo-Jahn-Teller" (PJT) interaction has been used for systems where one of the interacting states as well as the coupling mode are degenerate and unlike general vibronic coupling systems, the totally symmetric modes are non separable from the PJT problem and play an important role already in first order. Although they are neglected in Eq. (2.51) for simplicity but are included in the examples discussed in this thesis whenever applicable.

The adiabatic eigenvectors corresponding to Eq. (2.51) involve either the asymmetric (potential surface V_0) or symmetric (potential surfaces V_+ and V_-) linear combinations of the E component basis states. The eigenvalues are

$$\begin{aligned} V_0 &= \frac{\omega}{2}\left(Q_x^2+Q_y^2\right)+E_E \\ V_\pm &= \frac{\omega}{2}\left(Q_x^2+Q_y^2\right)+\frac{E_E+E_A}{2} \\ &\pm \sqrt{\left(\frac{E_E-E_A}{2}\right)^2+(\lambda')^2\left(Q_x^2+Q_y^2\right)}. \end{aligned} \tag{2.52}$$

It depends on the sign of $E_E - E_A$ whether V_+ or V_- correlates with the E state for $Q_x = Q_y = 0$ and becomes degenerate there with the "unperturbed" surface V_0.

2.2.3.2 The single-mode $(E \otimes e + A) \otimes e$ pseudo-Jahn-Teller effect

Let us now address the more general case of systems with simultaneous JT and PJT vibronic interactions. Depending on the particular symmetries prevailing, the same vibrational mode may be JT and PJT active in first order. This is, quite likely the case, for example, in trigonal point groups with a single doubly degenerate irreducible representation (it follows necessarily, if there exists a single mode of this symmetry only). Then the relevant Hamiltonian is obtained by adding Eqs. (2.33, 2.34, 2.51) for the same mode [23, 34, 117]:

$$\begin{aligned} \mathcal{H}^{PJT} &= H_0\mathbf{1}+\lambda\begin{pmatrix} Q_x & Q_y & 0 \\ Q_y & -Q_x & 0 \\ 0 & 0 & 0 \end{pmatrix}+\frac{\gamma}{2}\begin{pmatrix} Q_x^2+Q_y^2 & 0 & 0 \\ 0 & Q_y^2+Q_x^2 & 0 \\ 0 & 0 & 0 \end{pmatrix} \\ &+\frac{\eta}{2}\begin{pmatrix} Q_x^2-Q_y^2 & 2Q_xQ_y & 0 \\ 2Q_xQ_y & Q_y^2-Q_x^2 & 0 \\ 0 & 0 & 0 \end{pmatrix}+\begin{pmatrix} E_E & 0 & \lambda' Q_x \\ 0 & E_E & \lambda' Q_y \\ \lambda' Q_x & \lambda' Q_y & E_A \end{pmatrix} \end{aligned} \tag{2.53}$$

As in the preceding subsection, the second-order PJT couplings have been suppressed. (While their form is straightforward to work out, they may often

be less important, if the E-A energy gap is not too small). The meaning of the zero-order Hamiltonian H_0 and of the coupling constants is also the same as above. Although the totally symmetric modes has an important influence on the system dynamics, they are not included in the Hamiltonian (2.53) for simplicity. However, they may be not only Condon-active through finite first-order coupling constants, but also modulate the $E - A$ energy gap through *different* first-order constants in the two electronic states. This is the same behavior as in vibronic coupling systems with non-degenerate states [23] and as in the $(E + A) \otimes e$ PJT coupling systems discussed above. It may lead to additional conical intersections with two or three (for PJT systems) intersecting potential energy surfaces.

2.3 Discussion of the static aspect of the problem under investigation, Symmetry Breaking and Conical Intersection

The adiabatic electronic PES has numerous implications for the explanation of several phenomena in molecular physics and chemistry. Thus, it is worthwhile to investigate on the adiabatic PESs associated with different kind of problem under consideration.

Case 1: Let us consider two no-degenerate electronic states $\widetilde{X}$ and $\widetilde{A}$ with their VIE E_X^0 and E_A^0. For simplicity, we consider one tuning mode (Q_g) with the linear intra state coupling parameter κ and κ' for the $\widetilde{X}$ and $\widetilde{A}$ electronic state, respectively and these two state is coupled by the one coupling mode (Q_c) with the interstate coupling parameter λ. With this description the form of the model vibronic Hamiltonian takes the following form

$$\mathcal{H} = (T_N + V_0)\,\mathbf{1} + \begin{bmatrix} E_X^0 + \kappa Q_g & \lambda Q_c \\ \lambda Q_c & E_A^0 + \kappa' Q_g \end{bmatrix} \tag{2.54}$$

$$T_N = -\frac{1}{2}\omega_g \frac{\partial^2}{\partial Q_g^2} - \frac{1}{2}\omega_c \frac{\partial^2}{\partial Q_c^2} \tag{2.55}$$

$$V_0 = \frac{1}{2}\omega_g Q_g^2 + \frac{1}{2}\omega_c Q_c^2 \tag{2.56}$$

To get the adiabatic PESs we have to diagonalized $\mathcal{H}$ in the fixed nuclei limit, $\mathrm{T}_N \rightarrow 0$ or we have to calculate the eigenvalues of ($\mathcal{H}$ - $\mathrm{T}_N\mathbf{1}$). Thus we have

$$S^{\dagger}(\mathcal{H} - T_N\mathbf{1})S = \mathbf{V} \tag{2.57}$$

$$\tag{2.58}$$

$$\mathbf{V} = \begin{pmatrix} V_1(\mathbf{Q}) & 0 \\ 0 & V_2(\mathbf{Q}) \end{pmatrix} \tag{2.59}$$

Where $V_1(\mathbf{Q})$ and $V_2(\mathbf{Q})$ are the adiabatic PESs of the Hamiltonian (2.54). The unitary 2 $\times$ 2 matrix S transforms from the diabatic electronic basis, $\mid \phi_x \rangle$ and $\mid \phi_a \rangle$, to the adiabatic electronic basis, $\mid \Phi_x \rangle$ and $\mid \Phi_a \rangle$, via

$$\begin{pmatrix} |\Phi_x\rangle \\ |\Phi_a\rangle \end{pmatrix} = S^{\dagger} \begin{pmatrix} |\phi_x\rangle \\ |\phi_a\rangle \end{pmatrix} \tag{2.60}$$

Her **S** is the function of all nuclear coordinates **Q**. If we rewrite the Hamiltonian (2.54) in this form

$$\mathcal{H} = \mathcal{H}_0\mathbf{1} + \begin{pmatrix} -d & c \\ c & d \end{pmatrix} \tag{2.61}$$

$$\mathcal{H}_0 = T_N + V_0 + \sum + \sigma Q_g \tag{2.62}$$

$$\sum = \frac{E_X^0 + E_A^0}{2} \tag{2.63}$$

$$\Delta = \frac{E_A^0 - E_X^0}{2} \tag{2.64}$$

$$\sigma = \frac{\kappa + \kappa'}{2} \tag{2.65}$$

$$\delta = \frac{\kappa' - \kappa}{2} \tag{2.66}$$

$$d = \Delta + \delta Q_g \tag{2.67}$$

$$c = \lambda Q_c \tag{2.68}$$

The adiabatic potential then read

$$V_{1,2}(\mathbf{Q}) = V_0(\mathbf{Q}) + \sum + \sigma Q_g \pm \mathcal{W} \tag{2.69}$$

where

$$\mathcal{W} = \sqrt{(d^2 + c^2)} \tag{2.70}$$

The $V_1(\mathbf{Q})$ and $V_2(\mathbf{Q})$ are the lower and upper adiabatic PESs. The lower adiabatic PES $V_1(\mathbf{Q})$ exhibits a characteristic and important phenomenon, namely, the breaking of the molecular symmetry. Symmetry breaking suggests that minimum of the lower surface $V_1(\mathbf{Q})$ occurs at a nuclear geometry that is of lower symmetry than the equilibrium geometry of the molecule in its electronic ground state. The symmetry breaking is simply a consequence of the repulsion of the diabatic surfaces via the vibronic coupling. Therefore, the lower surface can only develop a new minima, whereas the upper surface $V_2(\mathbf{Q})$ can only become steeper.

If we set κ and κ', are zero.Thus the minimum of $V_1(\mathbf{Q})$ occurs at $Q_g^{(0)}$ and we assume one dimensionless quantity x as follows

$$x = \frac{\lambda^2}{\omega_c \Delta} \tag{2.71}$$

For $x \quad 1$ we have two equivalent minima with $Q_c^{(0)} \neq 0$ and the previous minima $Q_c = 0$ is converted to a local maximum. The barrier height E_s, that is, the energy difference between $V_1(Q_c = 0)$ and $V_1(Q_c^{(0)})$, is given by

$$\frac{E_s}{\Delta} = \begin{array}{c} 0, x \leq 1 \\ \frac{(1-x)^2}{2x}, x \geq 1 \end{array} \tag{2.72}$$

Here E_s may also be called the stabilization energy; it showing the relative lowering of the minimum of $V_1(\mathbf{Q})$ compared to the minimum in the absence of vibronic coupling ($\lambda = 0$). For $x \leq 1$ no symmetry breaking occurs. Just above the "*threshold*" x=1, the stabilization energy increases quadratically with x, approaching a linear dependence on x for large x. Including the tuning mode, we obtained the stationary point $\mathbf{Q}$ of $\mathrm{V}_1(\mathbf{Q})$

$$Q_g^{(0)} = \frac{\Delta - F}{L - D}\frac{\delta}{\omega_g} - \frac{\sigma}{\omega_g} \tag{2.73}$$

$$Q_c^{(0)} = \pm(\frac{\lambda}{\omega_c})\left[1 - (\frac{\Delta - F}{L - D})^2\right]^{\frac{1}{2}} \tag{2.74}$$

Where

$$D = \frac{\delta^2}{\omega_g} = \frac{(\kappa' - \kappa)^2}{4\omega_g} \tag{2.75}$$

$$F = \frac{\delta\sigma}{\omega_g} = \frac{(\kappa' - \kappa)(\kappa + \kappa')}{4\omega_g} \tag{2.76}$$

$$L = \frac{\lambda^2}{\omega_c} \tag{2.77}$$

So, the stabilization energy is

$$E_s = \frac{(\Delta + D - L - F)^2}{2(L - D)} \tag{2.78}$$

The criteria for the existence of a stabilized minimum with $Q_c^{(0)} \neq 0$ are

$$|\frac{\Delta - F}{L - D}| \leq 1 \tag{2.79}$$

$$L \geq D \tag{2.80}$$

The additional condition indicates that there is a certain competition between the coupling mode and tuning mode concerning the *symmetry-breaking effect*. (a) If κ and κ' have different signs, the *symmetry-breaking effect* of the coupling mode is reduced by the totally symmetric mode; that is, $Q_c^{(0)}$ and E_s are smaller than in the case $\kappa = \kappa' = 0$. This is a consequence of the fact that the tuning tends to increase the separation of the interacting electronic states near the new equilibrium geometry $Q_g^{(0)}$. (b) If κ and κ' have same sign and $| \kappa | \leq | \kappa' |$, the energy separation of the interacting states near the new minimum will decrease and the *symmetry-breaking effect* is enhanced by the tuning mode. If the additional condition (2.80) is not fulfilled, the stationary points (2.74) represent *saddle* points rather than *local* minima.

When we considered a surface in three-dimensional space, $V_1(Q_g, Q_c)$ and $V_2(Q_g, Q_c)$ form an elliptical double cone near the point of intersection which is known as CI. The adiabatic PESs $V_{1,2}(Q_g, Q_c)$ are shown in the figure. The CI is the single point where the upper surface V_2 touches the lower surface V_1. The double-minimum character of the lower surface is also noticeable. The adiabatic PESs $V_{1,2}(Q_g, Q_c)$ are strongly anharmonic, although they are generated from the diabatic harmonic potentials. Thus we seen that the lowering of the symmetry of the equilibrium position of the lower surface and the existence of a CI.

Now we have to determine the location of the seam of the CI after including additional modes. So, we have to rewrite the Eqn. 2.69 and sum over the all the specific quantity under consideration. The location of the minima of the seam of

CI is given by

$$V_{min}^{(c)} = \sum + \frac{(F-D)^2}{2D} - \frac{1}{2}\sum_{i=1}^{N} \frac{\sigma_i^2}{\omega_{gi}} \tag{2.81}$$

The position of the minimum in the space of the tuning modes is

$$(Q_{gi}^{(c)})_{min} = \frac{(\delta_i/\omega_{gi})(F-\Delta)}{D} - \frac{\sigma_i}{w_{gi}}, \quad i = 1, ..., N \tag{2.82}$$

The minimum of the seam of the CIs relative to the minimum of the upper adiabatic PESs is given by

$$V_{min}^{(c)} - (V_2)_{min} = \frac{1}{2D}(\Delta - D - F)^2 \tag{2.83}$$

Case 2. In the case of degenerate electronic state, the degeneracy of the electronic state is spited when the molecule is distorted along the degenerate vibrational modes but degeneracy of the electronic state is restored along the totally symmetric modes of vibration. The locus of this degeneracy takes place at the equilibrium symmetry configuration defines the seam of CIs of the two PESs. The minimum value of the potential energy on this seam is given by

$$\mathcal{V}_{min,JT}^{(c)} = E_E^0 - \frac{1}{2}\sum_{i=1}^{N} \frac{\kappa_i^2}{(\omega_i + \gamma_i)}, \quad i = 1, ..., N \tag{2.84}$$

occurs for, Q_i^0 = - $\frac{\kappa_i}{(\omega_i+\gamma_i)}$, i = 1, ..., N. The degeneracy of the two surfaces splits on distortion along the degenerate vibrational modes, resulting the global energy minimum on the lower adiabatic PESs, V$_-$ changes to a cusp. However the minimum of the upper adiabatic PES, V$_{sp}$ remains at the minimum of the seam of CIs and new minima appear on V$_-$ at Q_i^0 values as given above for i = 1, ..., N. Along the degenerate vibrational modes the two solution are obtained, Q_{pj}^0 (p=x/y, j=1,...M), one of them define the *minima* and the other defines the

saddle points with energies

$$\mathcal{V}_{-}^{0} = E_E^0 - \frac{1}{2}\sum_{i=1}^{N}\frac{\kappa_i^2}{(\omega_i+\gamma_i)} - \frac{1}{2}\sum_{j=1}^{M}\frac{\lambda_j^2}{(\omega_j+\gamma_j-\eta_j)} \tag{2.85}$$

and

$$\mathcal{V}_{sp}^{0} = E_E^0 - \frac{1}{2}\sum_{i=1}^{N}\frac{\kappa_i^2}{(\omega_i+\gamma_i)} - \frac{1}{2}\sum_{j=1}^{M}\frac{\lambda_j^2}{(\omega_j+\gamma_j+\eta_j)} \tag{2.86}$$

respectively. In multidimensional space this leads to a topography of three minima and three saddle points on V_{-}. Each saddle point appears in between two minima. The JT stabilization energy is the difference in energy between the $\mathcal{V}_{min,JT}^{(c)}$ and V_{-}, that is basically $\frac{1}{2}\sum_{j=1}^{M}\frac{\lambda_j^2}{(\omega_j+\gamma_j-\eta_j)}$.

Case 3. Now we will estimate the location of minimum of the seam of the CI between the two degenerate electronic state and these states are vibronically coupled by degenerate vibrational modes (Q_j). The linear JT coupling parameters for the degenerate electronic states are λ_j and λ_j'. Then the equation of minimum of the seam of the CI (Eqn. 2.81 and Eqn. 2.82) is modified and takes the form

$$\mathcal{V}_{min,PJT}^{(c)} = \Sigma + \frac{(F-\Delta)^2}{2D} - \frac{1}{2}\sum_{i=1}^{N}\frac{\sigma_i^2}{\omega_i} - \frac{1}{2}\sum_{j=1}^{M}\frac{\sigma_i'^2}{\omega_j}, \tag{2.87}$$

where

$$F = \sum_{i=1}^{N}\frac{\delta_i\sigma_i}{\omega_i} + \sum_{j=1}^{M}\frac{\delta_i'\sigma_i'}{\omega_j}, \tag{2.88}$$

$$D = \sum_{i=1}^{3}\frac{\delta_i^2}{\omega_i} + \sum_{j=1}^{N}\frac{\delta_i'^2}{\omega_j}. \tag{2.89}$$

2.4 Calculation of Spectra

The photoelectron spectrum for a transition to the coupled manifold of electronic states is described by the Fermi's Golden rule. According to this rule, the spectral intensity is given by

$$P(E) = \sum_v \left| \langle \Psi_v | \hat{T} | \Psi_0 \rangle \right|^2 \delta(E - E_v + E_0), \tag{2.90}$$

where $|\Psi_0\rangle$ is the initial electronic and vibrational ground state of the molecule with energy E_0. $|\Psi_v\rangle$ is the final vibronic state in the coupled electronic manifold and E_v is the vibronic energy. The quantity $\hat{T}$ represents the transition dipole operator for the photo-ionization process and E is the energy of the incident photon. The initial and final states are given by

$$|\Psi_0\rangle = |\Phi^0\rangle|\chi_0^0\rangle, \tag{2.91}$$

$$|\Psi_v\rangle = |\Phi^1\rangle|\chi_v^1\rangle + |\Phi^2\rangle|\chi_v^2\rangle, \tag{2.92}$$

where $|\Psi\rangle$ and $|\chi\rangle$ represent the diabatic electronic and vibrational part of the wave function, respectively. The superscripts 0, 1, and 2 refer to the ground and the two interacting diabatic electronic states, respectively. With the use of Eqs. (2.91, 2.92), the excitation function of Eq. 2.90 can be rewritten as [23]

$$P(E) = \sum_v \left| \tau^1 \langle \chi_v^1 | \chi_0^0 \rangle + \tau^2 \langle \chi_v^2 | \chi_0^0 \rangle \right|^2 \delta(E - E_v + E_0), \tag{2.93}$$

where

$$\tau^m = \langle \Phi^m | \hat{T} | \Phi^0 \rangle, \tag{2.94}$$

represent the matrix elements of the transition dipole operator of the final electronic state m. Upon rewriting Eq. (2.93), elements of the transition dipole matrix between the bound and scattering states are slowly varying functions of $\mathbf{Q}$ in a

diabatic representation [118]. Following standard practice, these are treated as constants of equal modulus utilizing the generalized Condon approximation [23]. An *ab initio* computation of these elements is highly cumbersome and techniques are lacking. The highly oscillatory wavefunction of the outgoing electron possesses very small components in the Franck-Condon region. Previous studies with this approximation of branching ratios have given results in excellent agreement with the experiment indicating its reliability [23].

2.4.1 Time-Independent Approach

In a time-independent quantum mechanical approach the photoelectron spectrum is calculated by solving the eigenvalue equation

$$\mathcal{H}|\Psi_v\rangle = E_v|\Psi_v\rangle \tag{2.95}$$

numerically, by representing the vibronic Hamiltonian $\mathcal{H}$ in a direct product basis of harmonic oscillator eigenstates of $\mathcal{H}_0$. In this basis, $|\chi_v^m\rangle$ takes the following form [23]:

$$|\chi_v^m\rangle \;=\; \sum_{n_1,n_2,\ldots,n_k} a^m_{v,n_1,n_2,\ldots,n_k}|n_1\rangle|n_2\rangle\ldots|n_k\rangle. \tag{2.96}$$

Here m is the electronic state index, n_l is the quantum number associated with the l^{th} vibrational mode, and k is the total number of such modes. The summation runs over all possible combinations of quantum numbers associated with each mode. For each vibrational mode, the oscillator basis is suitably truncated in the numerical calculations. The maximum level of excitation for each mode is approximately estimated from the corresponding Poisson parameter $[\frac{1}{2}\ (\frac{\kappa or \lambda}{\omega})^2]$. The Hamiltonian matrix written in such a direct product basis is usually highly sparse, and is tridiagonalized using the Lanczos algorithm prior to diagonalization [119]. The diagonal elements of the resulting eigenvalue matrix give the eigen

energies of the vibronic energy levels and the relative intensities of the vibronic lines are obtained from the squared first components of the Lanczos eigenvectors [57, 119].

Finally, the spectral envelope is calculated by convoluting the line spectrum with a suitable Lorentzian line-shape function of appropriate width of the following:

$$\mathcal{L}(E) \;=\; \frac{1}{\pi}\frac{\Gamma/2}{E^2+(\Gamma/2)^2}. \tag{2.97}$$

The quantity Γ represents the full width at the half maximum (fwhm) of the Lorentzian.

2.4.2 Time-Dependent Approach

In a time-dependent approach the Fourier transform representation of the Dirac delta function is used in the Golden formula (Eqs. 2.90,2.93) to calculate the spectral intensity. In this representation the delta function is expressed as

$$\delta(x) = \frac{1}{2\pi}\int_{-\infty}^{+\infty} e^{ixt/\hbar}\delta t. \tag{2.98}$$

Using this the spectral intensity (Eq. (2.90)) transforms into the following useful form, readily utilized in a time-dependent picture

$$P(E) \approx 2Re\int_0^{\infty} e^{iEt/\hbar}\langle\Psi_f(0)|\boldsymbol{\tau}^{\dagger}e^{-i\mathcal{H}t/\hbar}\boldsymbol{\tau}|\Psi_f(0)\rangle dt, \tag{2.99}$$

$$\approx 2Re\int_0^{\infty} e^{iEt/\hbar}\; C_f(t)\; dt, \tag{2.100}$$

where the elements of the transition dipole matrix $\boldsymbol{\tau}^{\dagger}$ is given by, $\boldsymbol{\tau}^f = \langle\Phi^f|\hat{T}|\Phi^i\rangle$.

The above integral represents the Fourier transform of the time-autocorrelation

function [23, 120]

$$C(t) = \langle \Psi_i(0) | e^{-i\mathcal{H}t/\hbar} | \Psi_f(0) \rangle = \langle \Psi_i(0) | \Psi_f(0) \rangle, \tag{2.101}$$

of the WP, initially prepared on the f^{th} electronic state and, $\Psi_f(t) = e^{-i\mathcal{H}t/\hbar}\, \Psi_i(0)$.

In the time-dependent calculations, the time autocorrelation function is damped with a suitable time-dependent function before Fourier transformation. The usual choice has been a function of type

$$f(t) \;\; = \;\; exp[-t/\tau_r] \;\; , \tag{2.102}$$

where τ_r being the relaxation time. This leads to a Lorentzian broadening of the spectrum with Γ (fwhm) $= 2/\tau_r$.

Huge requirement of computer hardware prevents to use this matrix diagonalization approach with an increase in the electronic and nuclear degrees of freedom. In this situations reliable and converged results can not be obtained by this method. The WP propagation approach within the multi-configuration time-dependent Hartree (MCTDH) scheme has emerged as an alternative tool for such situations [121–125]. This is a grid based method which utilizes discrete variable representation (DVR) basis combined with fast Fourier transformation and powerful integration schemes. The efficient multiset ansatz of this scheme allows for an effective combination of vibrational degrees of freedom and thereby reduces the dimensionality problem. In this ansatz the wave function for a nonadiabatic system is expressed as [122]

$$\Psi(R_1, ..., R_p, t) \;\; = \;\; \sum_{\alpha=1}^{\sigma} \sum_{j_1=1}^{n_1^{(\alpha)}} ... \sum_{j_p=1}^{n_p^{(\alpha)}} A^{(\alpha)}_{j_1,...,j_p}(t) \prod_{k=1}^{p} \varphi^{(\alpha,k)}_{jk}(R_k, t) | \alpha \rangle. \tag{2.103}$$

Where, R_1,..., R_p are the coordinates of p particles formed by combining

vibrational degrees of freedom, α is the electronic state index and $\varphi_{jk}^{(\alpha,k)}$ are the n_k single-particle functions for each degree of freedom k associated with the electronic state α. Employing a variational principle, the solution of the time-dependent Schrödinger equation is described by the time-evolution of the expansion coefficients $A_{j_1,\ldots,j_p}^{(\alpha)}$. In this scheme all multi-dimensional quantities are expressed in terms of one-dimensional ones employing the idea of mean-field or Hartree approach. This provides the efficiency of the method by keeping the size of the basis optimally small. Furthermore, multi-dimensional single-particle functions are designed by appropriately choosing the set of system coordinates so as to reduce the number of particles and hence the computational overheads. The details of the MCTDH method and algorithm are discussed in the literature [122] and we do not further reiterate them here. The Heidelberg MCTDH algorithm [121] is employed in the WP propagation.

Here we provide a brief overview on the memory requirement for the MCTDH method. The memory required by standard method is proportional to N^f, where N is the total number of grid points or primitive basis functions and f is the total number of degrees of freedom. In contrast, memory needed by the MCTDH method scales as

$$memory \quad \sim \quad fnN + n^f \tag{2.104}$$

where, n represent the SPFs. The memory requirements can however reduced if SPFs are used that describe a set of degrees of freedom, termed as *multimode* SPFs. By combining d degrees of freedom together to form a set of $p{=}f/d$ particles, the memory requirement changes to

$$memory \quad \sim \quad f\tilde{n}N^d + \tilde{n}^f \tag{2.105}$$

where $\tilde{n}$ is the number of multimode functions needed for the new particles. If

only single-mode functions are used i.e. d=1, the memory requirement, Eq. 2.105, is dominated by n^f. By combining degrees of freedom together this number can be reduced, but at the expense of longer product grids required to describe the multimode SPFs.

Chapter 3

Vibronic dynamics in the low-lying coupled electronic states of methyl cyanide radical cation

3.1 Introduction

Static and dynamic aspects of the Jahn-Teller and pseudo-Jahn-Teller interactions between the ground and first excited electronic states of the methyl cyanide radical cation [126] are theoretically investigated in this chapter. This system belongs to the $(E + A) \otimes e$ JT-PJT family, with common JT and PJT active degenerate (e) vibrational modes. Methyl cyanide (MC) belongs to the C_{3v} symmetry point group at the equilibrium geometry of its electronic ground state. The ionization of an electron from the first two highest occupied molecular orbitals of symmetry e and a_1 generates the ground ($\widetilde{X}^2E$) and first excited ($\widetilde{A}^2A_1$) electronic states of MC^+. One of the two components of the HOMO and the HOMO-1 are shown in Figure. 3.1. It can be seen that the HOMO is a π type

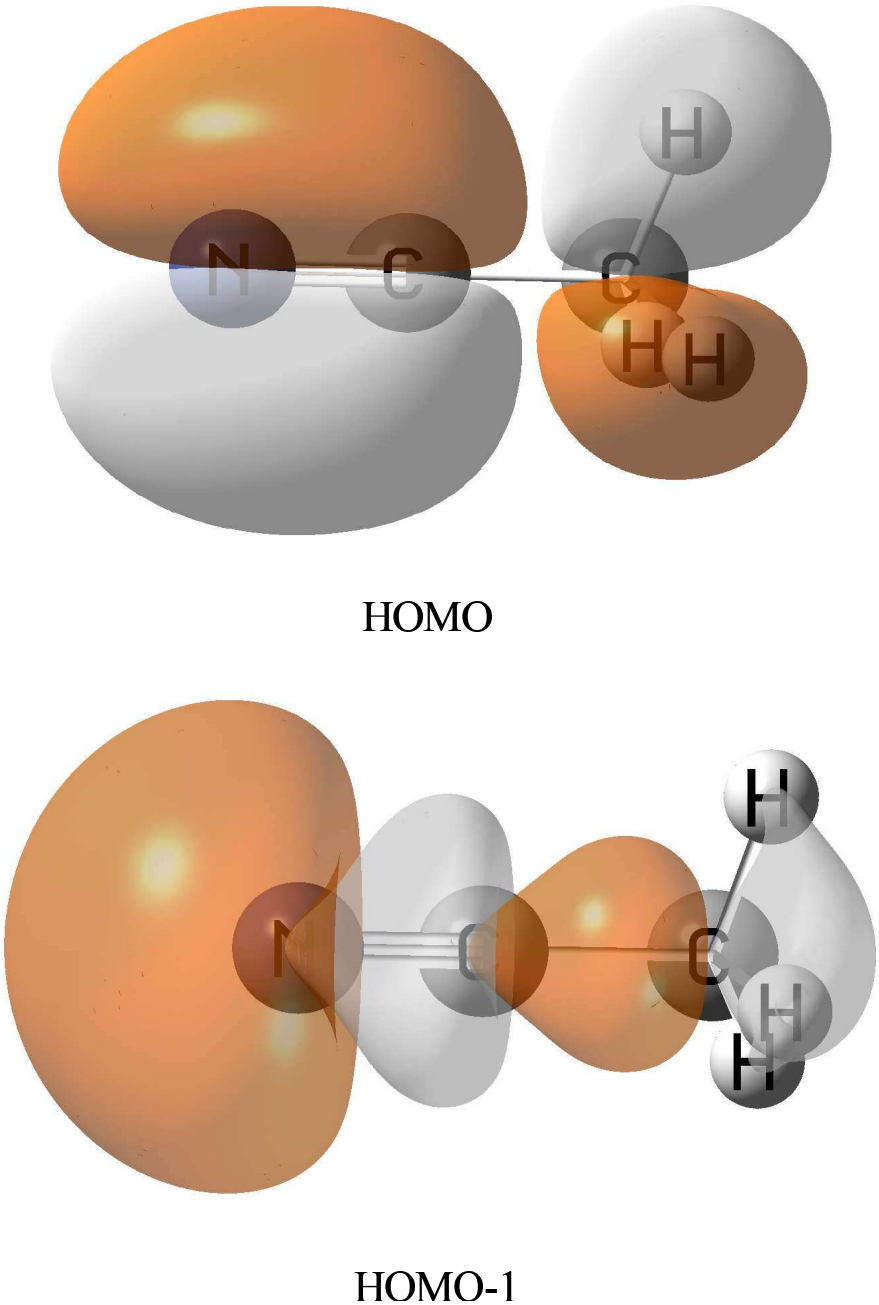

Figure 3.1: Schematic drawing of the highest occupied molecular orbital (HOMO) and the one below it (HOMO-1) of methyl cyanide.

of orbital of C-N bond where as HOMO-1 represents predominantly lone pair orbital of N atom. The twelve vibrational modes of MC decompose into $4a_1 + 4e$ irreducible representations of the C_{3v} symmetry point group. The symmetrized direct product of two E representations in the C_{3v} point group in first-order yields [109],

$$(E)^2 = a_1 + e \tag{3.1}$$

Similarly, the direct product of E and A_1 electronic states in the C_{3v} symmetry point group yields

$$E \otimes A_1 \;\; = \;\; e \tag{3.2}$$

The symmetry selection rules stated above imply that the degenerate e vibrational modes can split the degeneracy of the E electronic manifold and lead to $(E \otimes e)$-JT effects. The same vibrational modes can also cause PJT coupling between the E and A_1 electronic states. This is generally the case for molecules possessing a three-fold principal rotational axis. In contrast, the totally symmetric a_1 vibrational modes restore the degeneracy of the E electronic manifold.

Experimentally, the vibronic structures of the low-lying electronic states of MC^+ have been observed by photo-ionization of MC by various groups [127–130]. The photoelectron bands observed in the 11.5-40.0 eV electron binding energy range revealed ionization from various outer valence molecular orbitals of MC. The high-resolution HeI photoelectron spectrum [128] of acetonitrile is shown in Figure. 3.2. The first two photoelectron bands obtained in the 12-14 eV ionization energy range are considered here and the nuclear dynamics underlying their complex vibronic structure is examined. The first two bands result from ionization from the outer valence, degenerate 2e (HOMO) and non-degenerate $7a_1$ (HOMO-1) molecular orbitals of MC, respectively.

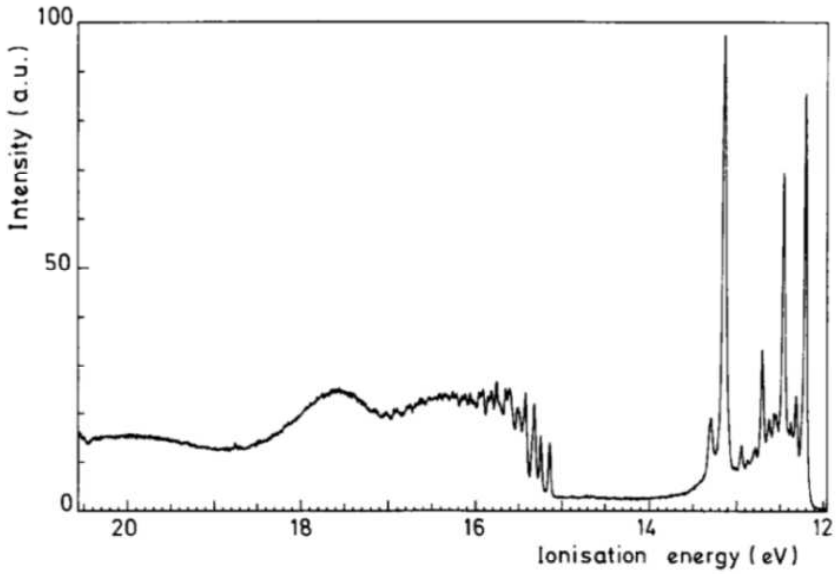

Fig. 1. HeI photoelectron spectrum of acetonitrile.

Figure 3.2: HeI photoelectron spectrum of methyl cyanide.

A quantum dynamical study to elucidate the observed vibronic structures of the photoelectron bands of MC^+ is missing in the literature. There are, however, reports available on the electronic structure and vertical ionization energies, in an effort to explain the observed structure of the photoelectron bands [131–133]. These theoretical investigations are far from quantitative and do not account for the important contributions of electronic non-adiabatic interactions relevant to understand the detailed vibronic structure of the observed photoelectron bands. We here attempt to make progress on this missing aspect of the problem and aim to uncover it by carrying out elaborate electronic structure calculations and quantum dynamical simulations of nuclear motion.

To accomplish this goal a model diabatic Hamiltonian is constructed through Taylor expansion and terms up to second-order coupling for the Condon active (a_1 symmetry) and the JT active (e symmetry) vibrational modes are considered. A first-order coupling is assumed for the PJT activity of the e vibrational modes. The various coupling parameters of the Hamiltonian are derived from electronic

Table 3.1: Equilibrium geometry of methyl cyanide in its ground electronic state ($^1A_1$) along with the experimental results [135].

	∠ H-C-H (deg)	∠ C-C-H (deg)	C-H (Å)	C-C (Å)	C-N (Å)
MP2/aug-cc-pVTZ	109.03	109.24	1.09	1.46	1.17
Expt. [135]	109.50	109.44	1.10	1.46	1.16

structure results calculated at the Möller-Plesset perturbation (MP2) level of theory using the augmented correlation consistent polarized valence triple - ζ (aug-cc-pVTZ) basis set of Dunning [112]. The photoelectron bands are computed by solving the eigenvalue equation using the Lanczos algorithm [119] as well as by a wave packet propagation approach employing the multi-configuration time-dependent Hartree algorithm [121–123, 125]. Our findings reveal that the CH_3 deformation modes of a_1 and e symmetries and C-N stretching mode of a_1 symmetry, particularly play crucial roles in the nuclear dynamics in the ^2E - $^2A_1$ coupled electronic manifold of MC^+. They form the dominant progressions in the photoelectron band at low energies and the more diffuse structure at high energies results from the PJT interactions of the ^2E and $^2A_1$ electronic states mainly through the degenerate bending and CH_3 deformation modes.

3.2 Parameters of the vibronic Hamiltonian: Electronic Structure Calculations

The optimized equilibrium geometry of the electronic ground state ($^1A_1$) of MC is calculated at the MP2 level of theory employing the aug-cc-pVTZ Gaussian basis set of Dunning [112]. The calculations were performed using the Gaussian-03 program package [134]. These optimized geometry parameters are given in Table 3.1 along with the available experimental results [135]. It can be seen from the Table 3.1 that the MP2 equilibrium geometry parameters are in good accord

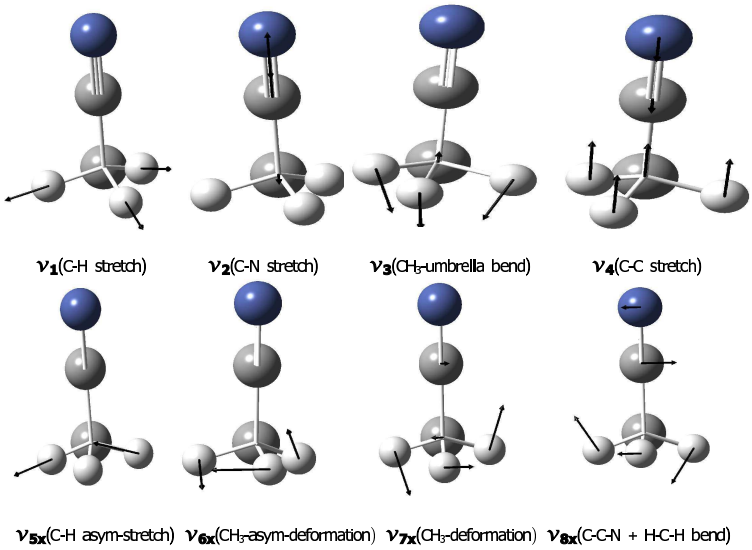

Figure 3.3: The normal vibrational modes of methyl cyanide (see, Table 3.2 and text for details).

with the available experimental data. The harmonic vibrational frequencies (ω_j) of 12 vibrational modes of the electronic ground state of MC are obtained by diagonalizing the MP2 force field calculated using the aug-cc-pVTZ basis set [112]. These normal vibrational modes of MC are schematically drawn in Figure. 3.3. The nature of these vibrational modes, their symmetry and harmonic vibrational frequencies are reported in Table 3.2, along with the available experimental results [136] for comparison. It is observed that the theoretically calculated harmonic frequencies are in good accord with their fundamental values extracted from experimental data [136]. The mass-weighted normal coordinates are calculated along with the harmonic vibrational frequencies and they are transformed to the dimensionless form (referred as Q_j, for the j^{th} vibrational mode) by multiplying with $\sqrt{\omega}_j$ (in atomic units used here) [109]. The equilibrium geometry of MC in its ground electronic state corresponds to $\mathbf{Q}$=0, and therefore, each Q_j here represents the displacement from this equilibrium configuration along the

Table 3.2: Symmetry, frequency and description of the vibrational modes of the electronic ground state of methyl cyanide. The experimental results are reproduced from Ref. [136].Note that, theoretical frequencies are harmonic, whereas, experimental ones are fundamental.

Symmetry	Mode	Vibrational Frequency (ω_j)(in eV)		Description	coordinate
		Theory	Experiment		
a_1	ν_1	0.3838	0.3663	C-H Sym-Stretching	Q_1
	ν_2	0.2738	0.2811	C-N Stretching	Q_2
	ν_3	0.1761	0.1717	CH_3umbrella bend	Q_3
	ν_4	0.1159	0.1140	C-C Stretching	Q_4
e	ν_5	0.3954	0.3731	C-H Asym Stretching	Q_{5x}, Q_{5y}
	ν_6	0.1859	0.1795	Antisym-CH_3 deformation	Q_{6x}, Q_{6y}
	ν_7	0.1323	0.1291	Sym-CH_3 deformation	Q_{7x}, Q_{7y}
	ν_8	0.0445	0.0449	C-C-N+H-C-H Bending	Q_{8x}, Q_{8y}

j^{th} vibrational mode.

To calculate the coupling parameters of the vibronic Hamiltonian of Sec. 3.3, we perform direct calculations of vertical ionization energies of MC by the outer-valence Green's function method [113] employing the aug-cc-pVTZ basis set [112]. The electronic structure calculations are carried out along the dimensionless normal displacement coordinates Q_j (j = 1-8) = $\pm$0.10, $\pm$0.25 ($\pm$0.25) $\pm$1.50, using the Gaussian-03 program package [134]. The vertical ionization energies thus obtained provide the adiabatic potential energy of the electronic states of MC^+ relative to the electronic ground state of MC. These energies are then fitted to the adiabatic form of the diabatic electronic Hamiltonian $\Delta\mathcal{H}$ of Eq. (3.3), using a least squares procedure and the coupling parameters are obtained. These coupling parameters represent derivatives of various order in the Taylor series expansion of the matrix elements of the electronic Hamiltonian $\Delta\mathcal{H}$ of Eq. (3.3). We used numerical finite difference approach also to estimate them and obtained consistent results. The numerical values of all coupling parameters of the Hamiltonian of Eq. (3.3), are given in Table 3.3 The vertical ionization energies of

the $\widetilde{X}$ and $\widetilde{A}$ electronic states of MC^+ are also included in Table 3.3 These parameters are utilized in the nuclear dynamical simulations, discussed below.

Table 3.3: *Ab initio* calculated linear and second-order coupling parameters for the $\widetilde{X}^2E$ and $\widetilde{A}^2A_1$ electronic states of methyl cyanide radical cation. The vertical ionization energies of these two electronic states and the harmonic frequencies of the vibrational modes of the electronic ground state of methyl cyanide are also given in the table. All quantities are in eV. The dimensionless Poisson parameters, $(\kappa_i/\omega_i)^2/2$, $(\lambda_i/\omega_i)^2/2$, $(\kappa'_i/\omega_i)^2/2$ and $(\lambda'_i/\omega_i)^2/2$ are given in parentheses.

Mode (symmetry)	κ_i or λ_i $\widetilde{X}^2E$	κ'_i $\widetilde{A}^2A_1$	γ_i $\widetilde{X}^2E$	γ'_i $\widetilde{A}^2A_1$	η_i $\widetilde{X}^2E$	ω_i MP2/aug-cc-pVDZ	λ'_i $\widetilde{X}^2E \otimes \widetilde{A}^2A_1$
$\nu_1(a_1)$	-0.0705(0.017)	0.0113(0.001)	-0.0065	0.0014	–	0.3838	
$\nu_2(a_1)$	0.3638(0.883)	-0.0293(0.006)	0.0169	-0.0083	–	0.2738	
$\nu_3(a_1)$	0.0315(0.016)	0.0892(0.128)	-0.0292	-0.0134	–	0.1761	
$\nu_4(a_1)$	-0.0030(0.0003)	-0.0131(0.006)	-0.0209	-0.0178	–	0.1159	
$\nu_5(e)$	0.0401(0.005)	–	-0.0022	0.0094	0.0010	0.3954	0.0534(0.009)
$\nu_6(e)$	0.0565(0.046)	–	-0.0380	-0.0083	0.0045	0.1859	0.0841(0.102)
$\nu_7(e)$	0.0476(0.065)	–	-0.030	0.0010	0.0060	0.1323	0.07(0.140)
$\nu_8(e)$	0.0101(0.026)	–	-0.009	0.010	-0.0016	0.0445	0.05(0.631)
E_E^0	12.3441						
E_A^0	13.34185						

3.3 The Vibronic coupling model

The photo-ionization of MC from its electronic ground state ($^1A_1$) to the low-lying $\widetilde{X}^2E$ and $\widetilde{A}^2A_1$ electronic states of MC^+ is examined here. Symmetry selection rules stated above allow coupling of these electronic states of MC^+ through the vibrational modes of e symmetry. In addition to the PJT type of coupling, these vibrational modes also act as JT coupling modes within the ^2E electronic manifold. The $\widetilde{X}$ and $\widetilde{A}$ electronic states are vertically ≈1.0 eV apart from each other. This implies that the PJT coupling may have profound impact on the nuclear dynamics underlying the complex vibronic structures of the $\widetilde{X}$ and $\widetilde{A}$ electronic states. It is clear from the above discussion that a $(E + A)\otimes e$ type of coupling mechanism would be more appropriate to describe the observed vibronic structure of the low-lying electronic states of MC^+. Such a vibronic Hamiltonian is used in the literature [36, 137–139] and is reconstructed here with the aid of electronic structure results obtained for MC^+. The four totally symmetric (a_1) vibrational modes, j = 1-4, are Condon active in all ionic states. The four degenerate (e) vibrational modes, j = 5-8, on the other hand, act as the JT coupling modes within the $\widetilde{X}^2E$ and the PJT coupling modes in the $\widetilde{X}^2E$ - $\widetilde{A}^2A_1$ electronic states. With these descriptions the $(E + A) \otimes e$ diabatic vibronic Hamiltonian can be written as

$$\mathcal{H} = \mathcal{H}_0\mathbf{1} + \Delta\mathcal{H}, \tag{3.3}$$

where

$$\mathcal{H}_0\mathbf{1} \;=\; \mathcal{T}_N + \mathcal{V}_0, \tag{3.4}$$

with

$$\mathcal{T}_N = -\frac{1}{2}\sum_{j=1}^{4}\omega_j\left(\frac{\partial^2}{\partial Q_j^2}\right) - \frac{1}{2}\sum_{j=5}^{8}\omega_j\left(\frac{\partial^2}{\partial Q_{jx}^2}+\frac{\partial^2}{\partial Q_{jy}^2}\right) \tag{3.5}$$

,

$$\mathcal{V}_0 = \frac{1}{2}\sum_{j=1}^{4}\omega_j Q_j^2 + \frac{1}{2}\sum_{j=5}^{8}\omega_j\left(Q_{jx}^2+Q_{jy}^2\right), \tag{3.6}$$

is the Hamiltonian for the unperturbed harmonic electronic ground state and

$$\Delta\mathcal{H} = \Delta\mathcal{H}^0 + \Delta\mathcal{H}^{ls} + \Delta\mathcal{H}^{lJT} + \Delta\mathcal{H}^{lPJT} + \Delta\mathcal{H}^{qs} + \Delta\mathcal{H}^{qJT}, \tag{3.7}$$

represents change in the electronic energy upon ionization. The elements of this Hamiltonian are expanded in a Taylor series around the equilibrium geometry of the electronic ground state as follows:

$$\Delta\mathcal{H}^0 = \begin{pmatrix} E_E^o & 0 & 0 \\ 0 & E_{A_1}^o & 0 \\ 0 & 0 & E_E^o \end{pmatrix}, \tag{3.8a}$$

$$\Delta\mathcal{H}^{ls} = \begin{pmatrix} \sum_{j=1}^{4}\kappa_j Q_j & 0 & 0 \\ 0 & \sum_{j=1}^{4}\kappa_j' Q_j & 0 \\ 0 & 0 & \sum_{j=1}^{4}\kappa_j Q_j \end{pmatrix}, \tag{3.8b}$$

$$\Delta\mathcal{H}^{lJT} = \begin{pmatrix} \sum_{j=5}^{8}\lambda_j Q_{jx} & 0 & \sum_{j=5}^{8}\lambda_j Q_{jy} \\ 0 & 0 & 0 \\ \sum_{j=5}^{8}\lambda_j Q_{jy} & 0 & -\sum_{j=5}^{8}\lambda_j Q_{jx} \end{pmatrix}, \tag{3.8c}$$

$$\Delta\mathcal{H}^{lPJT} = \begin{pmatrix} 0 & \sum_{j=5}^{8}\lambda'_j Q_{jx} & 0 \\ \sum_{j=5}^{8}\lambda'_j Q_{jx} & 0 & -\sum_{j=5}^{8}\lambda'_j Q_{jy} \\ 0 & -\sum_{j=5}^{8}\lambda'_j Q_{jy} & 0 \end{pmatrix}, \quad (3.8d)$$

$$\Delta\mathcal{H}^{qs} = \begin{pmatrix} \frac{1}{2}\sum_{j=1}^{4}\gamma_j Q_j^2 & 0 & 0 \\ 0 & \frac{1}{2}\sum_{j=1}^{4}\gamma'_j Q_j^2 & 0 \\ 0 & 0 & \frac{1}{2}\sum_{j=1}^{4}\gamma_j Q_j^2 \end{pmatrix}, \quad (3.8e)$$

$$\Delta\mathcal{H}^{qJT} = \begin{pmatrix} \frac{1}{2}\sum_{j=5}^{8}\left[\gamma_j(Q_{jx}^2+Q_{jy}^2)+\eta_j(Q_{jx}^2-Q_{jy}^2)\right] & 0 & -\sum_{j=5}^{8}\eta_j Q_{jx}Q_{jy} \\ 0 & \frac{1}{2}\sum_{j=5}^{8}\gamma'_j\left(Q_{jx}^2+Q_{jy}^2\right) & 0 \\ -\sum_{j=5}^{8}\eta_j Q_{jx}Q_{jy} & 0 & \frac{1}{2}\sum_{j=5}^{8}\left[\gamma_j(Q_{jx}^2+Q_{jy}^2)-\eta_j(Q_{jx}^2-Q_{jy}^2)\right] \end{pmatrix} \quad (3.8f)$$

The letters l, q and s in the abbreviations denote linear, quadratic and symmetric, respectively. $\Delta\mathcal{H}$ is a non-diagonal (3×3) matrix in the diabatic electronic basis, elements of this matrix represent the diabatic potential energies of the $\widetilde{X}$ and $\widetilde{A}$ electronic states of the MC^+ and the JT and PJT couplings as stated above. The quantities E_E^o and $E_{A_1}^o$ are the vertical ionization energies of the E and A_1 electronic states of MC^+, respectively. The intrastate linear coupling parameters for the totally symmetric vibrational modes are given by κ_j and κ'_j in the E and A_1 electronic states, respectively. The linear JT coupling parameters for the degenerate vibrational modes in the E electronic manifold are denoted by λ_j. The quantities λ'_j define the linear $E-A_1$ PJT coupling parameters of these degenerate vibrational modes. The second-order coupling parameters for the totally symmetric vibrational modes are denoted by γ_j and γ'_j in the E and A_1 electronic states, respectively. The diagonal second-order and quadratic JT parameters within the E electronic manifold are denoted by γ_j and η_j, respectively. All the coupling parameters of the above Hamiltonian are shown in Table 3.3 in Sec. 3.2.

3.4 Topography of the adiabatic potential energy surfaces: the JT and PJT conical intersection

In the following, we discuss the topography of the adiabatic potential energy surfaces of the $\widetilde{X}^2E$ and $\widetilde{A}^2A_1$ electronic states of the MC^+ obtained within the quadratic vibronic coupling scheme of Sec. 3.3 employing the coupling parameters of Table 3.3. These potential energy surfaces are obtained by diagonalizing the electronic Hamiltonian, $V_0 + \Delta\mathcal{H}$, given in Eqn. (3.3). In the following, we discuss one dimensional cuts of the multi-dimensional potential energy hyper surfaces for the coupled manifold of $\widetilde{X}$ -$\widetilde{A}$ electronic states along each vibrational mode. In Figure. 3.4, the adiabatic potential energy curves for the $\widetilde{X}$ -$\widetilde{A}$ coupled electronic manifold are shown. The potential energies along the four symmetric ($\nu_1 - \nu_4$) and four degenerate ($\nu_5 - \nu_8$) vibrational modes (indicated in the panel) are shown in the left and right column of the figure, respectively. The lines in the figure indicate the potential energy obtained by the present vibronic coupling model and the points superimposed on them represent the computed *ab initio* energies. The potential energies of the $\widetilde{X}$ and $\widetilde{A}$ states are shown by the solid and dashed lines, respectively. It can be seen that the computed *ab initio* energies are well reproduced by the model. The totally symmetric vibrational modes cannot lift the degeneracy of the $\widetilde{X}^2E$ electronic manifold, however, they shift the potential energy minimum considerably away from the equilibrium geometry of the neutral MC (**Q=0**) and therefore alter the energy gap between electronic states. This shift amounts to -$\kappa_j/(\omega_j + \gamma_j)$ for the symmetric vibrational mode ν_j [23]. Furthermore, the coupling constants κ and κ' for the vibrational modes ν_1 and ν_2 have opposite signs. Therefore, the minimum of the $\widetilde{X}$ and $\widetilde{A}$ states shifts in the opposite directions relative to the minimum of the electronic ground state of MC along these modes. As a result the $\widetilde{X}^2E$ and $\widetilde{A}^2A_1$ electronic states of the

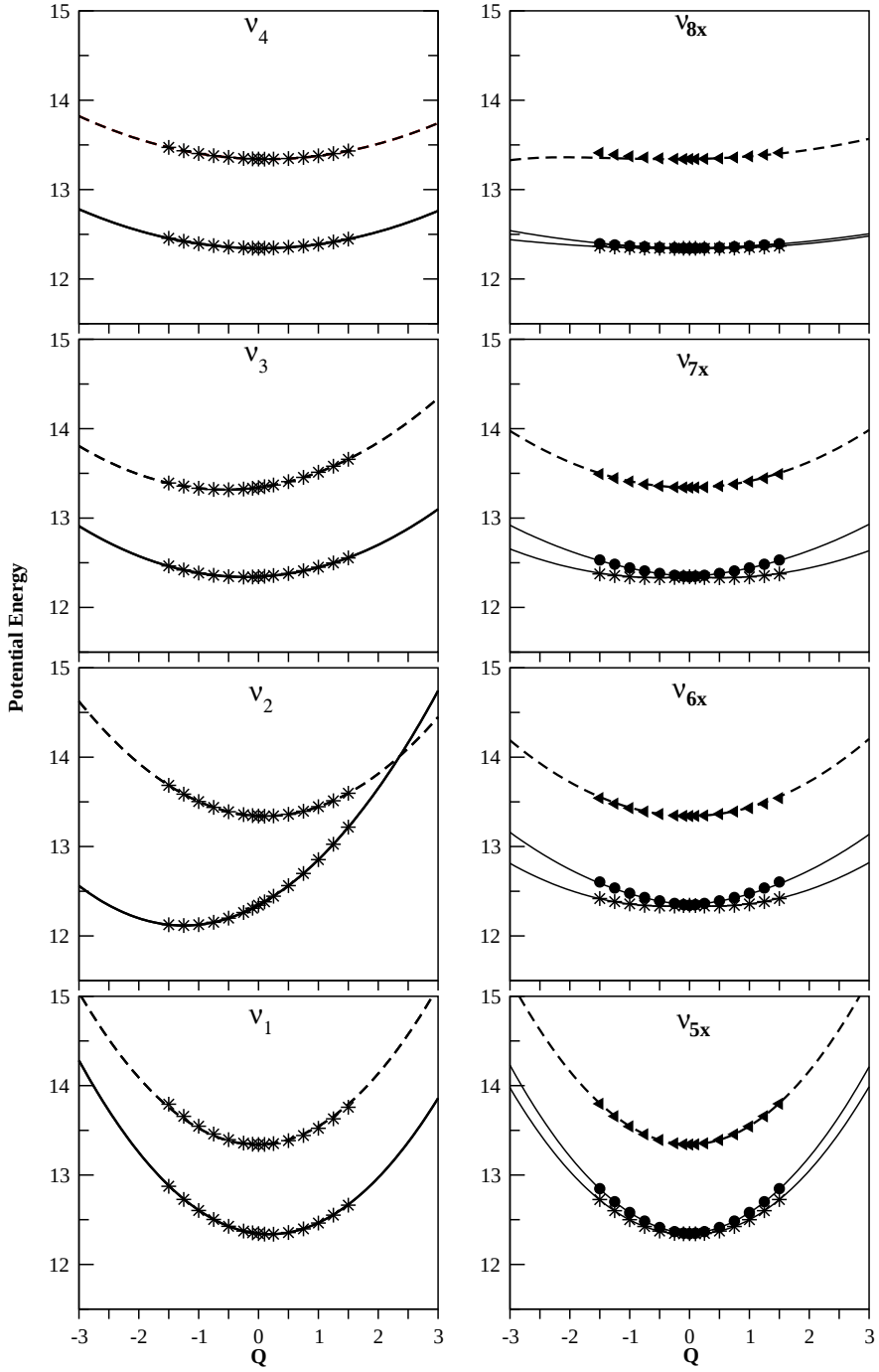

Figure 3.4: Adiabatic potential energies of the $\widetilde{X}^2E$ and $\widetilde{A}^2A_1$ electronic states of MC^+ plotted along the dimensionless normal displacement (from equilibrium configuration at Q=0) coordinates of the four symmetric vibrational modes ν_1-ν_4 (left column) and the x-component of four degenerate vibrational modes $\nu_5 - \nu_8$ (right column). The solid lines represent potential energies of the $\widetilde{X}^2E$ electronic manifold and the dashed lines represent the same of the $\widetilde{A}^2A_1$ electronic state obtained from the vibronic model of Sec. 3.3. The computed adiabatic potential energies superimposed on the respective curves and shown as points in the figure.

radical cation exhibit degeneracies along ν_2 (cf., Figure. 3.4) and would result into conical intersections when PJT coupling modes are included. The shift of these minima along ν_1 is negligibly small and therefore no such curve crossings are seen along this mode in the given energy range. The vibrational modes of e symmetry are both JT and PJT active. The adiabatic potential energy curves of the $\widetilde{X}$ and $\widetilde{A}$ electronic states of MC^+ are plotted as a function of the dimensionless normal coordinate of the x-component of these degenerate vibrational modes in the right column of Figure. 3.4. Along this component the adiabatic potential energies of the three electronic states are given by

$$V_{1,2}(Q_{jx}) = \mathcal{V}_o(Q_{jx}) + \frac{E^o_{E_g} + E^o_{A_{1g}}}{2} + \frac{\lambda_j}{2}Q_{jx} + \frac{(\gamma_{jx} + \gamma'_{jx} + \eta_{jx})Q^2_{jx}}{4} \mp \sqrt{\left((E^o_{E_g} + \lambda_j Q_{jx} + \frac{1}{2}\gamma_{jx}Q^2_{jx} + \frac{1}{2}\eta_{jx}Q^2_{jx} - E^o_{A_{1g}} - \frac{1}{2}\gamma'_{jx}Q^2_{jx})/2\right)^2 + (\lambda'_j Q_{jx})^2} \tag{3.9a}$$

$$\mathcal{V}_3(Q_{jx}) = \mathcal{V}_o(Q_{jx}) + E^o_{E_g} - \lambda_j Q_{jx} + \frac{(\gamma_{jx} - \eta_{jx})\, Q^2_{jx}}{2} \tag{3.9b}$$

Where $V_{1,2}$ refer to one component of the JT split $\widetilde{X}^2E$ and $\widetilde{A}^2A_1$ electronic states, respectively, and V_3 represents the second component of the former electronic manifold. It can be seen from Figure. 3.4 that the JT splitting is small along all degenerate vibrational modes, which is also revealed by their coupling parameters given in Table 3.3. With the parameters set of Table 3.3, the relevant stationary points of the multi-dimensional potential energy surfaces are determined [23, 137–139]. First, we estimate these stationary points in absence of $\widetilde{X}$ - $\widetilde{A}$ PJT coupling. The two sheets of the $\widetilde{X}^2E$ electronic manifold remain degenerate along the coordinate of the symmetric vibrational modes (cf., Figure. 3.4). The locus of this degeneracy defines the seam of conical intersections between the two sheets of the $\widetilde{X}^2E$ electronic manifold, occurring at the C_{3v} symmetry configuration of MC^+. The minimum of this seam is found at an energy of $\approx$ 12.11 eV for

Q_1= -0.102, Q_2= -0.371, Q_3= -0.440 and Q_4= -0.291. The degeneracy of these two sheets is split (cf., Figure. 3.4) when distorted along the coordinates of the degenerate vibrational modes. In this situation, the lower adiabatic sheet exhibits a "Mexican hat" type of topography within a linear vibronic coupling scheme. The lower adiabatic sheet is described by three equivalent minima separated by three equivalent saddle points. This "Mexican hat" acquires a distorted shape when the higher order coupling parameters are included in the Hamiltonian. For the second-order vibronic Hamiltonian of Eqn. (3.3), the minima and the saddle points occur at $\approx$ 12.080 eV and $\approx$ 12.082 eV, respectively. This correspond to a JT stabilization energy of $\approx$ 0.03 eV.

An approximate estimate of the energetic minimum of the seam of the PJT conical intersections is obtained by considering the $(E + A) \otimes e$ coupling matrix along the x-component of the degenerate electronic state and the vibrational modes [137–139]. Within a linear coupling scheme and using the parameters of Table 3.3 we find the energetic minimum of this seam between the $\widetilde{X}$ and $\widetilde{A}$ states occur at $\approx$ 12.79 eV, for Q_1=0.351, Q_2= -2.453, Q_3=0.078 and Q_4=-0.042. This minimum occurs well within the range of the second photoelectron band and only $\approx$ 0.68 eV above the minimum of the JT conical intersections.

3.5 Dynamical observables: Vibronic spectra and time-dependent dynamics

In this section we discuss on the vibronic structure of the first two photoelectron bands of MC pertaining to the $\widetilde{X}^2E$ and $\widetilde{A}^2A_1$ electronic states of MC^+. The theoretical results discussed below are obtained with the matrix Hamiltonian of Eqn. (3.3) at various levels of approximation in order to unambiguously identify the vibrational progressions and elucidate role of JT and PJT interactions in the observed complex spectral pattern [127–129]. We begin with the simplest linear

vibronic coupling approach and then consider the higher order coupling terms to accomplish this goal. In absence of any bilinear coupling terms (which are found not important in the present case) in the Hamiltonian and the PJT coupling with the $\widetilde{A}^2A_1$ electronic state, the Condon activity of the totally symmetric a_1 vibrational modes is separable from the JT activity of the degenerate e vibrational modes within the $\widetilde{X}^2E$ electronic manifold of MC^+. We, therefore, calculate the two partial spectra for the a_1 and e vibrational modes first and then convolute them to generate the complete spectrum for the $\widetilde{X}^2E$ electronic manifold. This reduces the computational effort by effectively reducing the dimensionality of the secular matrix in each calculations and the matrix diagonalization approach discussed above is readily applicable for the purpose. The vibronic energy level spectrum of $\widetilde{X}^2E$ electronic manifold is shown in Figure. 3.5. The two partial spectra of the a_1 and e vibrational modes are shown in panels a and b, respectively. The results of convolution of the two partial spectra are shown in the panel c. A careful analysis of the two partial spectra (shown in panel a and b) obtained within the linear coupling approach revealed dominant excitation of the symmetric vibrational mode ν_2 up to its third overtone level. The peaks are $\approx$ 0.274 eV spaced in energy corresponding to the frequency of this vibrational mode (cf. Table 3.2). Much weaker excitation of the ν_1, ν_3 and ν_4 vibrational modes are also seen. The excitation probability of the ν_1 and ν_3 vibrational modes is about two and that of the ν_4 vibrational mode is about three orders of magnitude less than that of the ν_2 vibrational mode. As revealed by the parameters of Table 3.3, the JT interactions due to the degenerate vibrational modes are not strong in the $\widetilde{X}^2E$ electronic manifold. Fundamental transitions due to ν_6 and ν_7 vibrational modes are observed in the partial spectrum for the degenerate vibrational modes. Very weak excitations of the ν_8 vibrational mode is also observed. Lines are $\approx$ 0.111 eV, 0.148 eV and 0.035 eV spaced in energy which nearly correspond to the frequency of the ν_7, ν_6 and ν_8 vibrational modes, respectively. These peak spacings are again modified when the second-order coupling parameters are in-

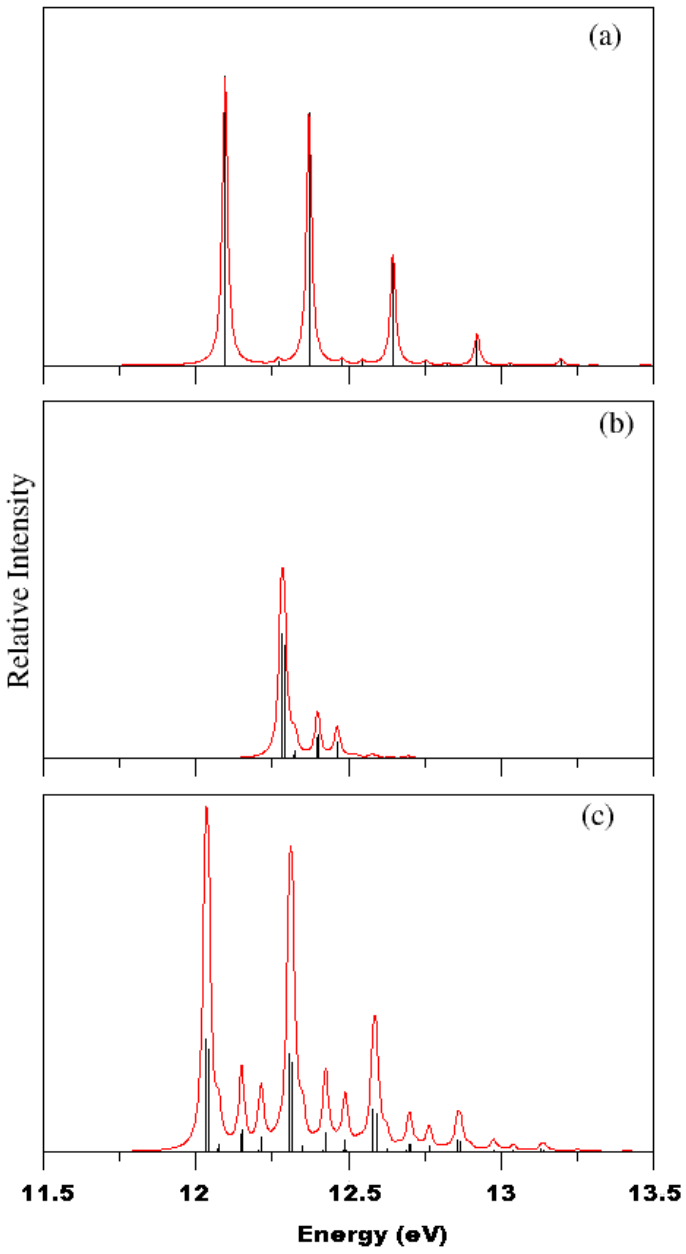

Figure 3.5: The vibronic spectra of the $\widetilde{X}^2E$ electronic states of MC^+ obtained with a linear coupling model. The relative intensity in arbitrary units is plotted as a function of the energy of the final vibronic levels. Energy is measured relative to the minimum of the ground electronic state of MC: (a) partial calculated with the four totally symmetric a_1 vibrational modes ν_1-ν_4, (b) partial spectrum for the degenerate e vibrational modes ν_5-ν_8, and (c) the composite theoretical spectrum obtained by convoluting the above two partial spectrum.

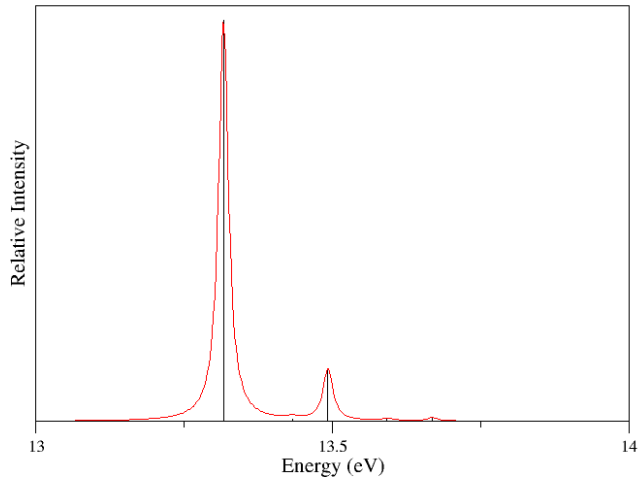

Figure 3.6: The uncoupled state vibronic spectrum of $\widetilde{A}^2A_1$ electronic state of MC^+ with LVC scheme.

cluded in the simulation. In this case the partial spectrum for the symmetric vibrational modes does reveal an increase in the intensity of the individual peaks. Peak spacings of $\approx$ 0.29 eV, 0.147 eV, 0.095 eV and 0.301 eV, respectively, are observed for ν_2, ν_3, ν_4 and ν_1 vibrational modes. The spectrum for the JT modes does not undergo major changes, the peaks become slightly broader and diffuse. Similar to the linear coupling spectrum dominant excitations of the ν_6 and ν_7 vibrational modes are observed. The spectrum for the uncoupled $\widetilde{A}^2A_1$ electronic state reveal dominant excitation of the ν_3 vibrational mode. The ν_2 and ν_4 vibrational modes are only weakly excited in this case. The uncoupled state vibronic spectrum of $\widetilde{A}^2A_1$ electronic state is shown in Figure 3.6. Furthermore, the spectra obtained within the linear and second-order coupling schemes show essentially identical structures. In each case the stick vibronic spectrum is convoluted with a Lorentzian function of 20 meV full width at the half maximum (FWHM) to generate the spectral envelope. The relative intensity in arbitrary units is plotted as a function of the energy of the final vibronic levels in Figure. 3.5. It is observed

that when the second-order coupling (particularly for the e vibrational modes) causes a slight increase of the density of spectral lines which is not shown here.

The effect of $\widetilde{X}$ -$\widetilde{A}$ PJT coupling on the above spectra is examined next. In this case the complete Hamiltonian of Eq. (3.3) is employed in the spectral simulations. Simulations are carried out by both time-independent and time-dependent methods. The latter is used particularly to check the convergence of the spectral envelope and also to examine the non-radiative decay of excited electronic states. We note that the vertical energy gap between the $\widetilde{X}$ and $\widetilde{A}$ electronic states had to be reduced by ≈ 0.3 eV in order to reproduce the adiabatic ionization positions at their experimental values in the composite theoretical bands. The time-independent matrix diagonalization approach becomes computationally impracticable with increase in the size of the basis set and an unambiguous verification of the numerical convergence of the spectrum becomes impossible. In Figures. 3.7(a-c) we show the vibronic spectrum of the $\widetilde{X}$ -$\widetilde{A}$ coupled electronic manifold. The experimental spectrum (reproduced from Ref. [128]) is shown in panel a and the theoretical results obtained by Hamiltonian matrix diagonalization and wave packet propagation approaches are shown in panel b and c, respectively. In the matrix diagonalization approach 2, 6, 15, 6, 2, 5, 4 and 2 harmonic oscillator basis functions are used along the ν_1, ν_2, ν_3, ν_4, ν_5, ν_6, ν_7 and ν_8 vibrational modes, respectively. This leads to a secular matrix of dimension $\approx 2.66 \times 10^7$, which is diagonalized with 10000 Lanczos iterations to obtain the stick spectrum. The stick spectrum is convoluted with a Lorentzian function of 20 meV FWHM to generate the spectral envelope shown in panel b. It can be seen that the overall shape of the spectral envelope in the panel b is very similar to the uncoupled $\widetilde{X}$ -$\widetilde{A}$ states results shown in the bottom panel of Figure. 3.7. Significant differences however can be seen in the density of the lines underneath the two spectra. Mixing of the lines of E and A_1 vibronic symmetries through the PJT coupling causes a large increase of the spectral line density and broadening of the spectral envelope. As discussed above that the minimum of the seam of

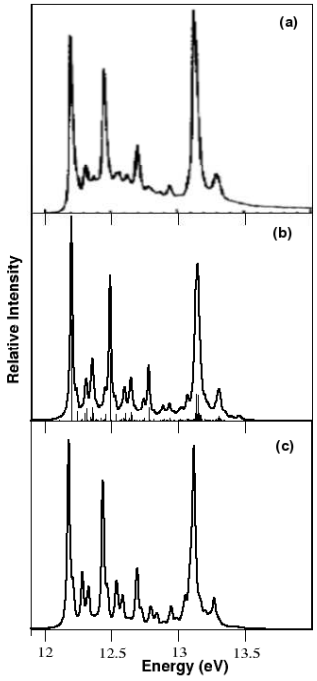

Figure 3.7: The $\widetilde{X}^2E$ -$\widetilde{A}^2A_1$, photoelectron bands of MC^+. The experimental results reproduced from Ref. [128] are shown in panel a. The results from the full dimensional theoretical simulations (see text for details) by the time-independent and time-dependent methods are shown in panel b and c, respectively.

PJT conical intersections occurs at $\approx$ 12.79 eV, therefore the low-lying vibrational levels of the $\widetilde{A}$ state mix with the higher vibrational levels of the $\widetilde{X}$ state and this mixing causes the observed increase in the density of spectral lines.

The spectral envelope shown in panel b of Figure. 3.7 is regenerated by a wave packet propagation approach employing the MCTDH algorithm [121–123, 125]. This allows a proper check of the convergence of the numerical results and also to understand the non-radiative decay of the excited molecular electronic states (see the discussion below). The details of the mode combinations, sizes of the primitive and SPF bases used in the MCTDH simulations are given in Table 3.4. The spectral envelope shown in Figure. 3.7(c) represents a sum of contributions from all three component electronic states of the $\widetilde{X}$ - $\widetilde{A}$ coupled electronic manifold. These contributions refer to the Fourier transform of the time autocorrelation functions, computed by locating the initial wave packet on three component electronic states separately and propagating them in the coupled manifold of three electronic states. The resulting autocorrelation function functions were damped with a relaxation time of 66 fs, before Fourier transformation. This approximately corresponds to a Lorentzian line shape function of 20 meV FWHM. In each case the wave packet is propagated for 150 fs which effectively yields the autocorrelation function up to 300 fs, using the prescription, $C(t) = \langle \Psi^*(\frac{t}{2}) | \Psi(\frac{t}{2}) \rangle$, applicable to a real initial wave packet. It can be seen from Figure. 3.7, that the spectral envelopes of panel b and c are in good accord with each other although there remains slight variations in the intensity of individual peaks. This comparison confirms that the stick spectrum in panel b is nearly converged. The two theoretical envelopes shown in panel b and c are in very good accord with the experimental envelope of panel a. We note that the convergence of the envelope of panel c is checked by varying the parameters given in Table 3.4. Considering the slight variations in the spectral intensities it is can be concluded that the stick spectrum in panel b is not fully, but nearly converged, and provides a reliable description of the vibronic energy levels in the $\widetilde{X}$ -$\widetilde{A}$ coupled electronic

manifold. As discussed above the main progressions in the theoretical spectrum are formed by the totally symmetric vibrational modes ν_3 and ν_2 and the degenerate vibrational modes ν_6 and ν_7. The JT effect is weak in the $\widetilde{X}^2E$ electronic manifold, however, the PJT coupling of the latter with the $\widetilde{A}^2A_1$ electronic state is relatively stronger. This causes the observed increase of the density of spectral lines and a broadening of the corresponding envelope.

3.6 Non-adiabatic transitions: Internal Conversion Rate

The time-dependence of the diabatic electronic populations in the coupled $\widetilde{X}$ - $\widetilde{A}$ states dynamics discussed above are shown in Figures. 3.8(a-b). For the dynamical simulations the wave packet is initially located on one of the JT split component of the $\widetilde{X}$ state (panel a) and on the $\widetilde{A}$ state (panel b). The decay and growth of the population of all three electronic states in each case are shown by the distinct line types (indicated in panel a). In each case the wave packet approaches all the JT and PJT conical intersections during its evolution in time. It can be seen from panel a that a very small fraction of the wave packet reaches the $\widetilde{A}$ electronic state when it is the initially launched on one of the two components of the $\widetilde{X}$ state. This is because the minimum of the seam of PJT conical intersections occurs ≈ 0.68 eV above the minimum of the JT crossing seam. In this situation, the wave packet mostly undergoes nonadiabatic transitions back and forth in between the two JT split components of the $\widetilde{X}$ state. The population of these two component states fluctuate around 0.7 and 0.3, respectively at longer times. The initial decay of the electronic population relates to a non-adiabatic decay rate of ≈ 50 fs of the JT split components of the $\widetilde{X}^2E$ electronic manifold. The above population dynamics changes dramatically when the wave packet is initially prepared on the $\widetilde{A}$ electronic state, as shown in panel b of Figure. 3.7.

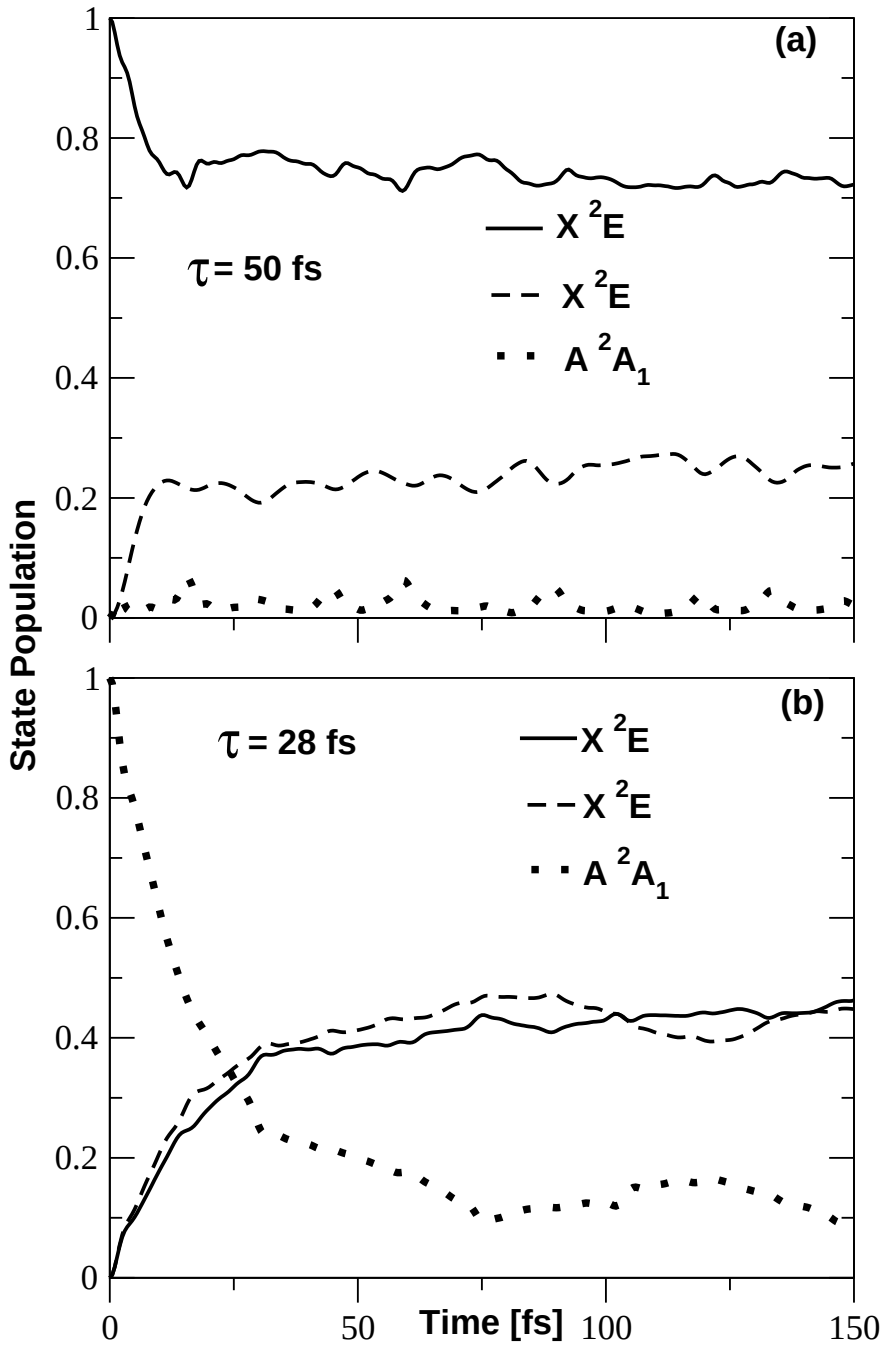

Figure 3.8: Time dependence of diabatic electronic populations in the $\widetilde{X}^2E$ - $\widetilde{A}^2A_1$, coupled states nuclear dynamics of MC^+. The results obtained by initially locating wave packet on one of the two components of the $\widetilde{X}$ electronic manifold and the $\widetilde{A}$ electronic state are shown in panel a and b, respectively.

Table 3.4: The number of harmonic oscillator (HO) basis functions along each vibrational mode and the dimension of the secular matrix used to calculate the converged theoretical stick spectrum shown in various figures noted below.

No. of HO basis functions								Dimension of the secular matrix	Figure(s)
ν_1	ν_2	ν_3	ν_4	ν_5	ν_6	ν_7	ν_8		
2	6	15	2		-	-	-	2160	Figure. 3.5 (a)
-	-	-	-	4	10	7	2	627200	Figure. 3.5 (b)
4	20	4	9	-	-	-	-	2280	Figure. 3.6

In this case the populations of the $\widetilde{A}$ electronic state decay very fast (decay rate 28 fs) to the $\widetilde{X}$ electronic manifold through the PJT conical intersections. Both the components of the JT split $\widetilde{X}^2E$ electronic manifold are almost equally populated in time.

3.7 Summary and outlook

A theoretical account of the multi-mode static and dynamic Jahn-Teller and pseudo-Jahn-Teller coupling effects in the photoelectron spectroscopy of methyl cyanide is presented in this article. The ground ($\widetilde{X}^2E$) and first excited ($\widetilde{A}^2A_1$) electronic states of methyl cyanide radical cation are calculated *ab initio* along the dimensionless normal coordinates of the electronic ground state of methyl cyanide. A second-order $(E + A) \otimes e$ vibronic Hamiltonian is constructed in a diabatic electronic basis. The nuclear dynamics on the coupled electronic states is simulated by time-independent and time-dependent quantum mechanical methods to calculate the vibronic spectra and examine the non-radiative decay of the excited electronic states. The details of the vibronic structure of the photoelectron bands are systematically analyzed. The role and importance of all 12 vibrational modes in the nuclear dynamics is examined. It is found that the JT effects due to the degenerate vibrational modes in the $\widetilde{X}^2E$ electronic manifold of MC^+ is weak, however, the PJT coupling of these vibrational modes with the

$\widetilde{A}^2A_1$ electronic state is somewhat stronger. The latter leads to a mixing of the spectral lines of two different vibronic symmetries and an increase in the density of vibronic levels. The minimum of the seam of the JT conical interactions within the $\widetilde{X}^2E$ electronic manifold occurs at $\approx$ 12.11 eV and the same of the PJT conical intersections is located $\approx$ 0.68 eV above it. The JT stabilization energy is found to be only $\approx$ 0.03 eV. The symmetric vibrational mode ν_2 (C-N stretching), ν_3 (CH_3 umbrella bend) and the degenerate vibrational modes ν_6 (antisymmetric CH_3-deformation and ν_7 (symmetric CH_3-deformation) form the dominant progressions in the photoelectron bands. Particularly, ν_3 is the crucial vibrational mode for the nuclear dynamics in the $\widetilde{A}^2A_1$ state. Excitations of the remaining vibrational modes are found to be weak in the photoelectron bands.

The final theoretical results are obtained by including all 12 vibrational modes in the coupled $\widetilde{X}$ -$\widetilde{A}$ electronic states of MC^+ employing both time-independent and time-dependent quantum dynamical methods. While the time-independent results are not fully converged because of the lack of appropriate computer hardwares, the convergence of the time-dependent results are explicitly verified. The final theoretical results are in very good accord with the experimental findings. We note that this is the first work of its kind attempting to provide a detail understanding of the observed vibronic structures of the low-lying photoelectron bands of MC.

Chapter 4

Static and dynamic aspects of electronically excited anthracene radical cation as archetypical models for astrophysical observations

4.1 Introduction

Identification of molecular carriers of diffused interstellar bands (DIBs) is a current concern to unravel the long-standing debate in astronomical observations. Recent telescopic measurements in the line of sight of star Cernis 52 in and HD281159 the Perseus Constellation led to the discovery of new interstellar bands. Aided by the laboratory measurements under the exotic condition of interstellar medium, these interstellar features have been "tentatively" assigned to electronic transitions in anthracene radical cation [140–142]. We perform a benchmark theoretical study from first principles and unambiguously validate these assign-

ments. This study establishes that polycyclic aromatic hydrocarbons can be the molecular carrier of DIBs and ultrafast non-radiative deactivation of their excited electronic states makes them photostable against strong UV irradiation in the interstellar medium.

Discovery of carbon containing molecular species seems to have important implication in the origin of life in the chemistry of early universe. Meaningful efforts have been made in recent years to unearth the polycyclic aromatic hydrocarbon (PAH) hypothesis in relation to the observed (over 300) diffused interstellar bands (DIBs) in the spectrum of the interstellar dust clouds [68, 143–146]. Aided by the laboratory measurements they are assigned to the electronic transitions in the anthracene radical cation (An^+). The detailed complementary theoretical study is missing to date.

The experimental photoelectron measurements were carried out by several groups for An [86–89, 147–149]. The high resolution gas phase spectrum recorded by Sánchez-Carrera *et al.* [86], shown in Figure. 4.1 reveals well resolved vibronic structures of the $\widetilde{X}$ and $\widetilde{A}$ electronic states and a broad band for the $\widetilde{B}$ state. The highly overlapping bands for the $\widetilde{C}$ and $\widetilde{D}$ electronic states show complex structure in the 10.75-11.75 eV ionization energy range. The broadening of the $\widetilde{B}$ band in the spectrum is attributed to the vibronic coupling of $\widetilde{A}$ with the $\widetilde{B}$ state.

The gas phase electronic absorption spectrum [71, 75, 85] of An^+ has been the subject of major interest. The DIBs, the absorption features observed over the interstellar media in the range of ultraviolet and infrared region of electromagnetic spectrum, are linked to the electronic transitions of An^+ . The novel experimental spectroscopic techniques such as matrix isolation spectroscopy (MIS) (shown in Figure 4.2), cavity ring down spectroscopy and resonance enhanced multi-photon dissociation spectra (shown in Figure 4.2 on top of MIS) are developed and utilized to explore the intrinsic band profiles of the low-lying electronic states of An^+ . The vibrational peak positions and widths are measured in the laboratory

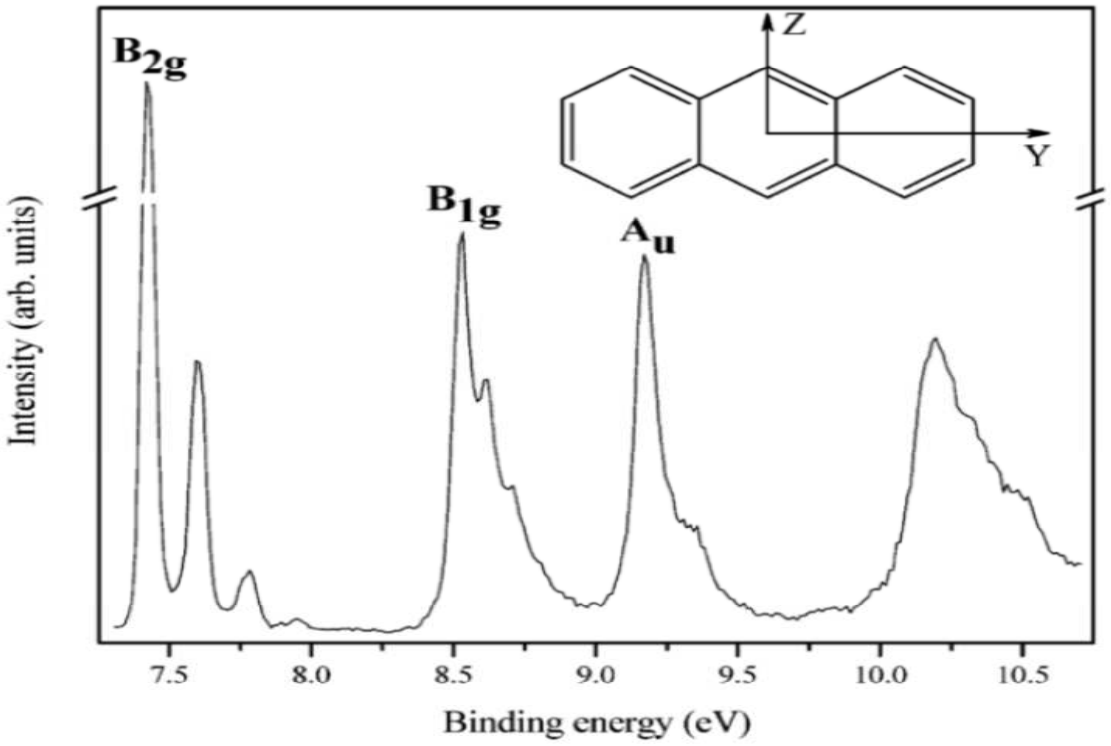

Figure 4.1: The experimental gas phase photoelectron spectrum of anthracene reproduced from Ref. [86].

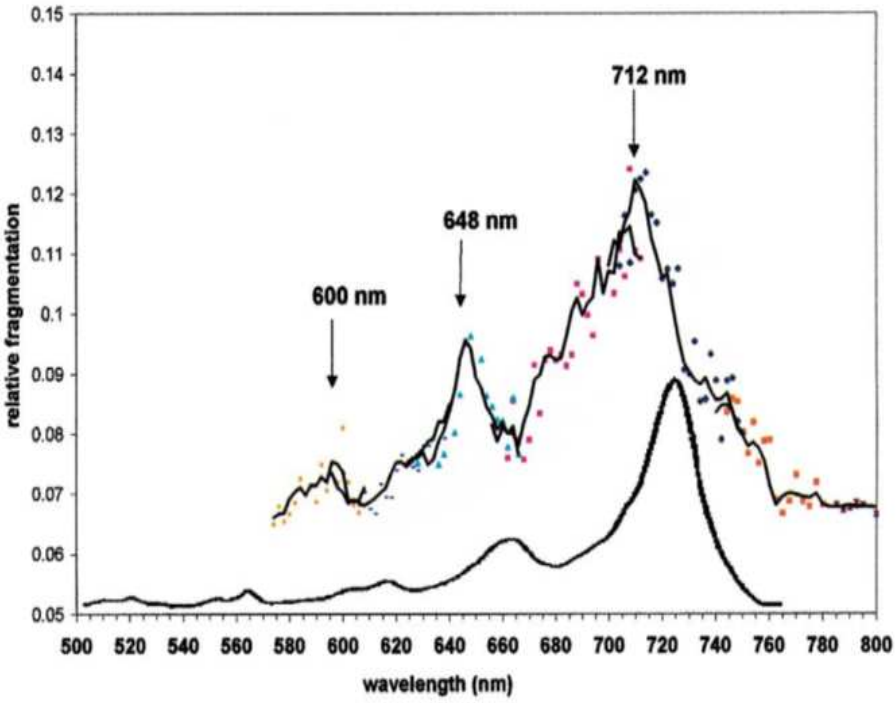

Figure 4.2: The vibrational progression of the D_2 ($\widetilde{B}$) $\leftarrow$ D_0 ($\widetilde{X}$) electronic transition of An^+ reproduced from Ref. [85].

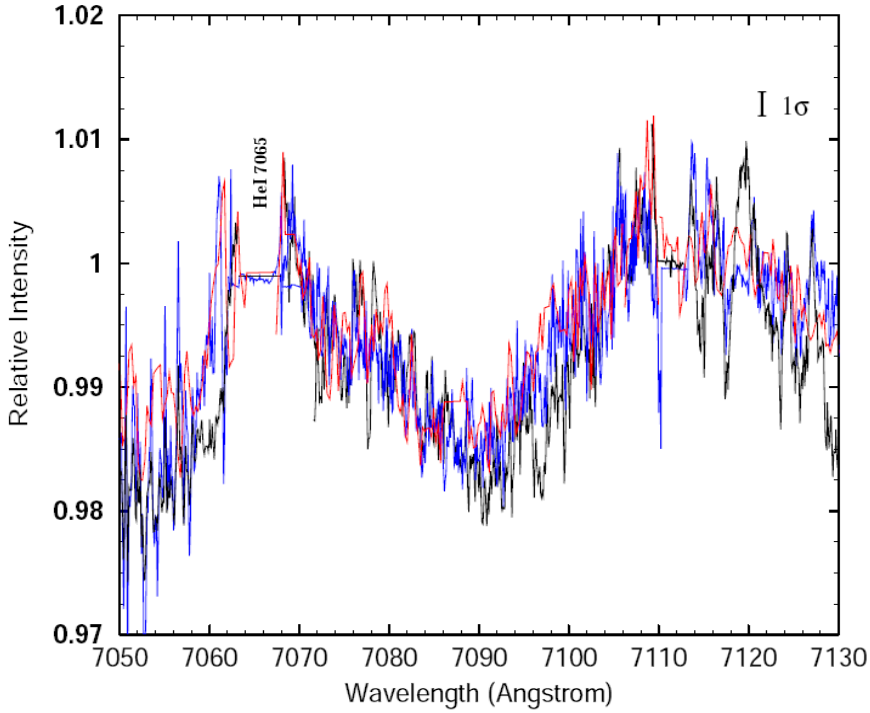

Figure 4.3: The HET and WHT spectra of Cernis 52 corrected for the photospheric and DIB contributions of An^+ reproduced from Ref. [77].

experiments and are directly compared with the observed DIBs. A broad band assigned to the D_2 ($\widetilde{B}$) $\leftarrow$ D_0 ($\widetilde{X}$) electronic transition in An^+ has been recorded in the spectrum of star Cernis 52 [77] and HD281159 [150]. This spectral profile is shown in Figure 4.3. The laboratory experimental data [71, 75, 85] have been used recently to assign this broad interstellar feature discovered by the astronomers [77]. So far no theoretical data is available to validate this assignment.

The relaxation dynamics of electronically excited An^+ is studied in glass matrix environments using (femto) picoseconds transient grating spectroscopic techniques [74]. A bi-exponential recovery kinetics of the photo-bleached D_0 ($\widetilde{X}$) state containing a fast ($\approx$ 200 fs) and a slow ($\approx$ 3-20 ps) component is observed [74]. The faster relaxation is attributed to the D_2 ($\widetilde{B}$) $\leftarrow$ D_0 ($\widetilde{X}$) transition and the latter is to the vibrational relaxation of the D_0 ($\widetilde{X}$) state in the matrix. The D_2 state relaxation time was estimated below $\approx$ 50 fs from

this experiment. A non-radiative decay rate of $\sim$ 56 fs (FWHM $\sim$ 94 cm^{-1} is estimated for D_2 ($\widetilde{B}$) electronic state from the cavity ring down absorption spectroscopy measurements [75]. These results reveal that the excited state intra molecular dynamics of An^+ is quite involved and is dominated by ultrafast internal conversion mechanism. This issue is also unraveled below.

We address some of these unresolved issues here and develop a theoretical model through *ab initio* electronic structure calculations and simulate the nuclear dynamics quantum mechanically.

4.2 Details of Electronic structure calculations

The equilibrium geometry of the reference electronic ground state of An is optimized at the second-order Möller-Plesset perturbation level of theory employing Dunning's polarized valence double-zeta basis set (cc-pVDZ) [112] using the Gaussian 03 suite of program [134]. The equilibrium geometry converged to the D_{2h} symmetry point group. The optimized equilibrium geometry data agree very well with those available in the literature [151]. These theoretical results along with the literature data are given in Table 4.1. The atom numbering in the Table 4.1 is shown in Figure 4.5.

Table 4.1: *Ab initio* calculated equilibrium geometry parameters of the electronic ground state of neutral naphthalene along with the experimental data.

An (MP2/cc-pVDZ)	our data	Expt data[b]
Bond length ($\mathring{A}$)		
C_1 - C_2	1.3844	1.397
C_1 - C_6	1.4299	1.422
C_2 - C_3	1.4337	1.437
C_3 - C_4	1.4511	1.437
C_3- C_7	1.4103	1.392
C_1 - H_{17}	1.0954	–
C_2 - H_{18}	1.0966	–
C_7 - H_{16}	1.0979	–
Bond Angle (deg)		
C_1 - C_2 - C_3	120.815	–
C_2 - C_3 - C_4	118.775	–
C_2 - C_3 - C_7	121.990	122.3
C_2 - C_1 - C_6	120.416	120.4
C_5 - C_6 - C_1	120.410	–
C_3 - C_7 - C_{10}	121.529	121.0
C_7 - C_{10} - C_9	119.236	–
C_7 - C_3 - C_4	119.236	118.4
H_{17} - C_1 - C_2	119.938	–
H_{17} - C_1 - C_6	119.652	–
H_{18} - C_2 - C_3	118.697	–
H_{18} - C_2 - C_1	120.488	–
H_{16} - C_7 - C_3	119.236	–

By diagonalizing the *ab initio* force constant matrix of the optimized equilibrium configuration of the electronic ground state, the harmonic vibrational frequencies ω_i are obtained. These vibrational frequencies along with their symmetry and description are given in Table 4.2. The theoretically calculated harmonic frequencies are also compared with the experimentally [152] determined fundamental frequencies in the Table 4.2.

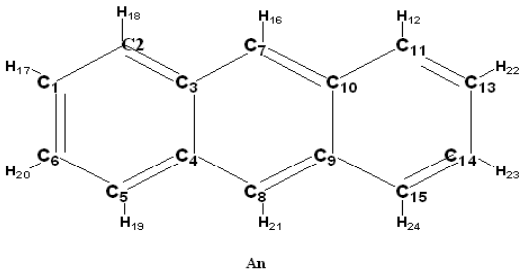

Figure 4.4: The schematic structures of An and atom numbering.

Table 4.2: *Ab initio* calculated harmonic vibrational frequencies and their description of An. The experimentally determined [152] fundamental frequencies are given in the parentheses.

Mode	Freq in eV (Exp[a]) MP2/cc-pVDZ	Description of mode	Mode	Freq in eV (Exp[a]) MP2/cc-pVDZ	Description of mode
a_g		**In Plane**	b_{2u}		**In Plane**
ν_1	0.0491(0.0492)	ring(r) breathing	ν_{39}	0.0752(0.0745)	outer ring bending
ν_2	0.0772(0.0775)	ring deformation	ν_{40}	0.1023(0.1003)	C-H and ring CCC bend
ν_3	0.0945(0.0935)	ring squeezing	ν_{41}	0.1286(0.1237)	C_b-C_b str, C-$H_{(a,b)}$ bend
ν_4	0.1289(0.1249)	C_b-C_b str, C-H bend	ν_{42}	0.1448(0.1394)	C-H bend, r CCC bend
ν_5	0.1455(0.1443)	C-$H_{(a,b)}$ bending	ν_{43}	0.1484(0.1441)	C-$H_{(9,10)}$ bend + CC str
ν_6	0.1615(0.1567)	ring CCC str, C-H bend	ν_{44}	0.1787(0.1669)	C-$C_{(b,b)}$ and C-C str
ν_7	0.1823(0.1751)	C_b-C_b and C-C str	ν_{45}	0.1837(0.1732)	C_b-C str
ν_8	0.1890(0.1835)	C_a-C str + C-$H_{(a,b)}$ bend	ν_{46}	0.1905(0.1854)	C-$C_{(a,b)(b,b)}$ and C-C str
ν_9	0.1986(0.1929)	C-C and C_b-C_b str	ν_{47}	0.1977(0.1902)	C_b-C_b str, C-$H_{(9,10)}$ bend
ν_{10}	0.3958(0.3746)	C-$H_{(9,10)}$ sym str	ν_{48}	0.3976(0.3746)	sym C_a-H str
ν_{11}	0.3977(0.3779)	sym C-H_a + asym C-H_b str	ν_{49}	0.4013(0.3779)	C-$H_{(a,b)}$ str
ν_{12}	0.4014(0.3796)	sym C-$H_{(a,b)}$ str	b_{1g}		**Out of Plane**
b_{3g}		**In Plane**	ν_{18}	0.0281(0.0300)	wave shape r CCCC bend
ν_{50}	0.0476(0.0492)	ring deformation	ν_{19}	0.0565(0.0591)	CCC and C-H bending
ν_{51}	0.0644(0.0646)	CCCC bending	ν_{20}	0.0936(0.0926)	side r CCC and C-H bend
ν_{52}	0.1131(0.1120)	outer ring CCC bending	ν_{21}	0.1150(0.1185)	C-$H_{(a,b)}$ bending
ν_{53}	0.1389(0.1366)	CCC bend + C-H bend	b_{2g}		**Out of Plane**
ν_{54}	0.1487(0.1472)	C-$H_{(9,10)}$ bending	ν_{33}	0.0320(0.0352)	ring twisting
ν_{55}	0.1583(0.1578)	C-$H_{(9,10)}$ and C_a-H bending	ν_{34}	0.0485(0.0715)	center r chair bending
ν_{56}	0.1738(0.1777)	CC str + C-$H_{(a,b)}$ bend	ν_{35}	0.0655(0.0956)	side r CCC bending
ν_{57}	0.2001(0.1951)	C_a-C_b str	ν_{36}	0.1023(0.1111)	C-$H_{(9,10)(a,b)}$ bending
ν_{58}	0.2093(0.2017)	C-$C_{(9,10),(a,b)}$, C-C_a str	ν_{37}	0.1038(0.1136)	C-$H_{(9,10)}$ and CC bending
ν_{59}	0.3971(0.3726)	asym C_a-H str	ν_{38}	0.1162(0.1209)	side r C-H and CCC bend
ν_{60}	0.3997(0.3787)	asym C_b-H str	a_u		**Out of Plane**
b_{1u}		**In Plane**	ν_{13}	0.0146(0.0169)	diagonal r twist bending
ν_{22}	0.0287(0.02900	outer ring CCCC bend	ν_{14}	0.0580(0.0684)	C-C and C-H bending
ν_{23}	0.0814(0.0810)	ring deformation	ν_{15}	0.0674(0.0921)	side r chair shape bend
ν_{24}	0.1117(0.1123)	ring CCC bending	ν_{16}	0.1036(0.1064)	C-$H_{(a,b)}$ and side r bend
ν_{25}	0.1437(0.1422)	C-$H_{(a,b)}$ bending	ν_{17}	0.1165(0.1188)	C-$H_{(a,b)}$ bending
ν_{26}	0.1582(0.1577)	C_a-H and outer ring bend	b_{3u}		**Out of Plane**
ν_{27}	0.1647(0.1633)	C-H bend + ring CCC str	ν_{61}	0.0109(0.0119)	butterfly ring bending
ν_{28}	0.1839(0.1795)	C-C_a str + C-$H_{(a,b)}$ bend	ν_{62}	0.0451(0.0475)	wave shape r bending
ν_{29}	0.2074(0.2009)	C_a-C_b str + ring CCC bend	ν_{63}	0.0554(0.0625)	C-H and CCC bending
ν_{30}	0.3956(0.3728)	$C_{(9,10)}$-H asym str	ν_{64}	0.0904(0.0908)	C-H bending
ν_{31}	0.3971(0.3785)	asym C-$H_{(a,b)}$ str	ν_{65}	0.1041(0.1106)	r CCC and C-$H_{(9,10)}$ bend
ν_{32}	0.3997(0.3824)	C-H str	ν_{66}	0.1153(0.1180)	C-$H_{(a,b)(9,10)}$ bending

The mass-weighted normal coordinates of these vibrational modes are calculated using the eigenvectors of the force constant matrix. The dimensionless normal displacement coordinates (Q_i) are obtained by multiplying the mass-weighted normal coordinates with $\sqrt{\omega}_i$ (in atomic units) [109].

Energies of the low-lying six doublet electronic states of An^+ are calculated *ab initio* along the normal coordinates of all the vibrational modes mentioned above. The outer valence Green's function method [113] and the cc-pVDZ basis set are used for this purpose. The vertical ionization energies (VIEs) of the first six highest occupied MOs of An are calculated along each $Q_i = \pm 0.10$ and ± 0.25 (± 0.25) $\pm$ 1.50. These VIEs plus the harmonic potentials of the reference electronic ground state are equated with the adiabatic potentials of the first six low-lying electronic states of An^+ , to derive the parameters appeared in Eqs.

4.5. All these coupling parameters are shown in Tables 4.3 to 4.7.

A care full analysis of the coupling parameters of the Hamiltonian is as follows. For the totally symmetric vibrational modes, it can be seen from Table 4.4 that the ν_9 vibrational modes is the most crucial in all the electronic states. The vibrational modes ν_1 and ν_3 in the $\widetilde{A}$, ν_1 and ν_2 in the $\widetilde{B}$, ν_1 and ν_7 in the $\widetilde{C}$, ν_3, ν_4 and ν_8 in the $\widetilde{D}$ and ν_1, ν_3 and ν_7 in the $\widetilde{E}$ state are expected to be strongly excited. The vibrational modes ν_7 and ν_8 in the $\widetilde{X}$, ν_3 and ν_5 in the $\widetilde{A}$, ν_2 and ν_7 in the $\widetilde{B}$, ν_2 in the $\widetilde{C}$ state, have moderate excitation strength. The excitation of the remaining a_{1g} vibrational modes are very weak. The coupling between $\widetilde{X}$ -$\widetilde{A}$ states are very strong along the vibrational modes ν_{50}, ν_{51} and ν_{58}, of b_{3g} symmetry (cf., Table 4.6). The same symmetry vibrational modes can also coupled the $\widetilde{A}$ - $\widetilde{C}$ and $\widetilde{B}$ - $\widetilde{D}$ electronic states. The vibrational mode ν_{57} is crucial for these couplings. The vibrational modes of b_{1u} symmetry are important in the $\widetilde{A}$ - $\widetilde{B}$, $\widetilde{C}$ - $\widetilde{D}$ and $\widetilde{X}$ - $\widetilde{D}$ interstate coupling. The vibrational modes cause strongest coupling of $\widetilde{A}$ and $\widetilde{B}$ electronic states are ν_{23}, ν_{27} and ν_{29}. The coupling strengths of ν_{27} is largest in the $\widetilde{C}$ - $\widetilde{D}$ electronic states. The $\widetilde{X}$ - $\widetilde{B}$, $\widetilde{A}$ - $\widetilde{D}$ and $\widetilde{B}$ - $\widetilde{C}$ electronic states are coupled by the vibrational modes of b_{2u} symmetry. The coupling strength of ν_{44}, ν_{45} and ν_{47} vibrational modes in the $\widetilde{X}$ - $\widetilde{B}$ states can be seen to be important. The vibrational modes ν_{39}, ν_{40} and ν_{46} on the other hand are strongly active in the $\widetilde{B}$ - $\widetilde{C}$ electronic states. The ν_{47} vibrational mode is the strongest coupling mode in the $\widetilde{A}$ - $\widetilde{D}$ states. The ν_{19} vibrational mode of symmetry b_{1g} is responsible for the $\widetilde{A}$ - $\widetilde{E}$ interstate coupling. The $\widetilde{X}$ - $\widetilde{E}$ and $\widetilde{C}$ - $\widetilde{E}$ electronic states are coupled by the vibrational modes of symmetry b_{2g}. The coupling strengths of these vibrational modes are quite large in the $\widetilde{C}$ - $\widetilde{E}$ states. The vibrational modes ν_{35} is the strongest in the $\widetilde{X}$ - $\widetilde{E}$ states. The vibrational mode ν_{16} of symmetry a_u reveals moderate coupling between $\widetilde{B}$ - $\widetilde{E}$ states. The $\widetilde{D}$ and $\widetilde{E}$ states are strongly coupled by the vibrational modes of symmetry b_{3u}.

Table 4.3: *ab initio* calculated linear coupling constants for the $\widetilde{X}^2B_{2g}$, $\widetilde{A}^2B_{1g}$, $\widetilde{B}^2A_u$, $\widetilde{C}^2B_{2g}$, $\widetilde{D}^2B_{3u}$ and $\widetilde{E}^2A_g$ electronic states of An^+. The vertical ionization energies of these three electronic states and the harmonic vibrational frequencies of the electronic ground state of anthracene are also given in the table. All quantities are in eV.

Mode (symmetry)	κ_i^X $\widetilde{X}$	κ_i^A $\widetilde{A}$	κ_i^B $\widetilde{B}$	κ_i^C $\widetilde{C}$	κ_i^D $\widetilde{D}$	κ_i^E $\widetilde{E}$	ω_i MP2/cc-pVDZ
ν_1	0.0004	0.0296	-0.0316	-0.0726	0.0023	-0.0848	0.04906
	(0.0001)	(0.1823)	(0.2072)	(1.094)	(0.001)	(1.49)	
ν_2	0.0007	0.0185	-0.0387	0.0172	0.0120	0.0275	0.07716
	(0.0001)	(0.0287)	(0.1256)	(0.025)	(0.034)	(0.064)	
ν_3	0.0032	-0.0939	-0.0112	-0.0124	-0.0572	0.0398	0.09453
	(0.0006)	(0.493)	(0.007)	(0.009)	(0.183)	(0.089)	
ν_4	0.0101	-0.0444	-0.0129	0.0030	-0.0855	0.0327	0.12893
	(0.0031)	(0.0594)	(0.005)	(0.0003)	(0.220)	(0.032)	
ν_5	0.0338	-0.0342	0.0348	0.0173	-0.0026	-0.0076	0.14547
	(0.0271)	(0.0277)	(0.0286)	(0.007)	(0.0002)	(0.001)	
ν_6	-0.0539	-0.0058	0.0692	-0.0205	-0.0455	-0.0170	0.16145
	(0.0557)	(0.0007)	(0.0919)	(0.008)	(0.039)	(0.006)	
ν_7	0.1060	0.0406	0.0382	-0.0775	0.0678	0.1410	0.18232
	(0.169)	(0.025)	(0.022)	(0.09)	(0.069)	(0.299)	
ν_8	0.0564	0.0178	-0.0490	0.0075	0.1269	-0.0461	0.18903
	(0.045)	(0.004)	(0.034)	(0.001)	(0.226)	(0.030)	
ν_9	0.1383	-0.1067	0.1203	0.1080	0.0298	-0.2337	0.19859
	(0.243)	(0.144)	(0.183)	(0.148)	(0.011)	(0.692)	
ν_{10}	0.0051	-0.0125	0.0044	0.0063	0.0146	-0.0581	0.39580
	(0.0001)	(0.0005)	(0.0001)	(0.001)	(0.001)	(0.011)	
ν_{11}	0.0044	-0.1330	0.0035	0.0045	0.0092	-0.0458	0.39766
	(0.0001)	(0.056)	(0.0001)	(0.001)	(0.001)	(0.007)	
ν_{12}	0.0125	-0.0170	0.0159	0.0158	0.0238	-0.0115	0.40138
	(0.001)	(0.001)	(0.001)	(0.001)	(0.0001)	(0.001)	
E_X^0	7.00462						
E_A^0	8.22561						
E_B^0	8.84452						
E_C^0	10.04423						
E_D^0	10.11909						
E_E^0	11.15221						

Table 4. 4: *Ab initio* Quadratic coupling parameters for the $\widetilde{X}$, $\widetilde{A}$, $\widetilde{B}$, $\widetilde{C}$, $\widetilde{D}$ and $\widetilde{E}$ electronic states of An^+ . All quantities are in eV.

Mode	γ_i^X	γ_i^A	γ_i^B	γ_i^C	γ_i^D	γ_i^E	Freq (eV)
A_g							
ν_1	-0.0009	0.0004	0.0002	0.0012	-0.0007	0.0029	0.04906
ν_2	-0.0048	-0.0010	-0.0034	0.0030	-0.0011	-0.0034	0.07716
ν_3	-0.0018	0.0036	-0.0014	-0.0024	-0.0002	-0.0020	0.09453
ν_4	0.0001	0.0019	-0.0004	0.0008	0.0005	-0.0013	0.12893
ν_5	0.0048	0.0063	0.0049	0.0049	0.0052	-0.0042	0.14547
ν_6	-0.0008	0.0043	0.0035	0.0136	-0.0066	-0.0085	0.16145
ν_7	-0.0049	0.0204	0.0141	0.0080	0.0023	-0.0285	0.18232
ν_8	-0.0010	-0.0045	0.0015	0.0045	0.0002	-0.0344	0.18903
ν_9	0.0042	0.0073	0.0026	0.0002	0.0037	-0.0074	0.19859
ν_{10}	0.0039	0.0039	0.0019	0.0025	0.0027	-0.0110	0.39580
ν_{11}	0.0034	0.0038	0.0033	0.0028	0.0029	-0.0006	0.39766
ν_{12}	0.0028	0.0044	0.0024	0.0025	0.0026	0.0009	0.40138
B_{3g}							
ν_{13}	-0.0039	0.0015	-0.0014	-0.00184	-0.0014	-0.0050	0.0476
ν_{14}	-0.00402	0.00172	-0.0016	-0.00068	-0.0002	-0.0320	0.06439
ν_{15}	-0.00049	0.0030	-0.00056	0.00044	-0.00124	-0.0162	0.11312
ν_{16}	0.00112	0.00154	-0.0022	-0.0037	0.0046	-0.0260	0.1389
ν_{17}	-0.0009	0.00604	0.00326	0.00448	0.003134	-0.0229	0.14871
ν_{18}	0.00286	0.00144	0.00202	0.00626	0.0044	-0.0252	0.1583
ν_{19}	-0.0018	-0.0010	0.00067	0.0015	0.00169	-0.0262	0.17381
ν_{20}	-0.00076	-0.00986	-0.0178	0.0144	0.0234	-0.0264	0.20013
ν_{21}	-0.0381	0.03864	-0.0014	0.00129	0.20929	0.3860	0.20929
ν_{22}	0.0038	0.00372	0.0370	0.0034	0.00352	-0.0071	0.39706
ν_{23}	0.0038	0.0034	0.0370	0.00336	0.0032	-0.0112	0.39973
B_{1u}							
ν_{24}	-0.00025	—	-0.00405	-0.00244	-0.00092	0.0008	0.02866
ν_{25}	0.00112	-0.0107	0.00814	-0.01637	0.0136	-0.0151	0.08139
ν_{26}	-0.00139	-0.000104	-0.00173	-0.00766	0.0043	-0.0304	0.11172
ν_{27}	0.0022	0.00244	0.00214	-0.0080	0.0155	-0.0124	0.14369
ν_{28}	0.00206	-0.00398	0.00738	-0.00056	0.00367	-0.0175	0.15824
ν_{29}	-0.0002	-0.00324	0.00498	-0.1016	0.0988	-0.0156	0.16474
ν_{30}	-0.00073	-0.00182	0.0036	-0.0781	0.0844	-0.020	0.18387
ν_{31}	-0.00724	-0.0371	0.0392	-0.0090	0.0231	-0.0525	0.20741
ν_{32}	0.00376	0.00289	0.00192	0.00176	0.00386	-0.0144	0.39556
ν_{33}	0.0037	0.0037	0.0036	0.0033	0.0036	-0.0016	0.39712
ν_{34}	0.00374	0.00331	0.0035	0.00328	0.0034	-0.0015	0.39974

Table 4. 5: *Ab initio* Quadratic coupling parameters for the $\widetilde{X}$, $\widetilde{A}$, $\widetilde{B}$, $\widetilde{C}$, $\widetilde{D}$ and $\widetilde{E}$ electronic states of An^+ . All quantities are in eV.

Mode	γ_i^X	γ_i^A	γ_i^B	γ_i^C	γ_i^D	γ_i^E	Freq (eV)
B_{2u}							
ν_{35}	-0.00273	-0.00029	-0.01023	0.0072	-0.00024	-0.0268	0.07515
ν_{36}	-0.0009	-0.00071	-0.0031	0.00466	0.001983	-0.0055	0.10233
ν_{37}	0.0004	0.0009	-0.004	0.0008	-0.0023	-0.0017	0.12859
ν_{38}	0.0058	0.0076	0.00426	0.0078	0.0072	-0.0039	0.14478
ν_{39}	0.00384	0.00690	0.00371	0.0088	0.0056	-0.0215	0.14837
ν_{40}	-0.0016	0.0150	0.0102	0.00327	0.0098	-0.0728	0.17866
ν_{41}	-0.0066	-0.00040	0.0128	0.0090	-0.0072	-0.0250	0.18366
ν_{42}	0.03382	0.03778	-0.0054	0.0367	0.0302	-0.0996	0.19054
ν_{43}	-0.0102	-0.0064	0.0142	0.0092	0.0132	-0.0709	0.19768
ν_{44}	0.00346	0.0032	0.00348	0.0028	0.00306	-0.0106	0.3976
ν_{45}	0.0029	–	0.0026	0.0026	–	-0.0011	0.40133
B_{1g}							
ν_{46}	-0.0122	-0.0011	-0.0102	-0.0079	-0.0105	-0.0014	0.0281
ν_{47}	-0.0042	-0.0013	-0.0136	-0.0167	-0.0091	0.0086	0.05652
ν_{48}	0.0039	0.0049	–	0.0002	-0.0024	-0.0064	0.0936
ν_{49}	0.0092	0.0077	0.0028	0.00092	-0.0145	-0.0244	0.11502
B_{2g}							
ν_{50}	0.0056	-0.0158	-0.0066	-0.0086	-0.0082	-0.0019	0.03202
ν_{51}	0.0052	0.0008	-0.0006	-0.0325	0.0055	-0.0080	0.04852
ν_{52}	-0.0012	-0.0186	-0.0094	-0.0075	-0.0169	0.0011	0.06545
ν_{53}	0.0047	0.0034	0.0022	-0.0187	-0.0047	-0.0051	0.10233
ν_{54}	0.0144	0.0048	-0.00052	-0.0403	-0.0068	0.0324	0.10383
ν_{55}	0.0080	0.0034	-0.0033	-0.0072	-0.0109	0.0136	0.11615
A_u							
ν_{56}	0.00608	-0.0146	-0.00015	-0.0061	-0.0102	-0.0017	0.01464
ν_{57}	-0.0048	-0.0152	-0.0052	-0.0062	-0.0157	-0.0112	0.0580
ν_{58}	0.0031	0.00124	-0.0062	-0.0118	-0.0138	-0.0066	0.06739
ν_{59}	0.0116	0.0042	-0.0017	-0.0075	-0.0093	0.0009	0.10362
ν_{60}	0.0073	0.0038	-0.0031	-0.0031	-0.0204	0.0078	0.11646
B_{3u}							
ν_{61}	-0.0058	0.0023	-0.0143	-0.0073	-0.0049	-0.0021	0.01088
ν_{62}	-0.0035	-0.0096	-0.0139	-0.0213	-0.0126	0.0091	0.04507
ν_{63}	-0.0091	—	-0.0095	-0.0175	-0.0037	0.0140	0.0554
ν_{64}	0.01004	0.00366	0.00058	-0.0056	–	-0.0080	0.09036
ν_{65}	0.0134	0.008	0.00172	-0.0056	-0.0172	-0.0230	0.10405
ν_{66}	0.0091	0.00767	0.0026	0.0026	-0.0129	-0.0087	0.11527

Table 4. 6: *Ab initio* The interstate linear coupling parameters of An^+ . All quantities are in eV. The dimensionless Poisson parameters $(\lambda_i/\omega_i)^2/2$ are given in parentheses.

Mode	λ_{i-j}	λ_{i-j}	λ_{i-j}
B_{3g}	i - $j \in \widetilde{X}$ - $\widetilde{A}$	i - $j \in \widetilde{A}$ - $\widetilde{C}$	i - $j \in \widetilde{B}$ - $\widetilde{D}$
ν_{13}	0.0416 (0.382)	–	–
ν_{14}	0.0421 (0.214)	–	0.0221 (0.059)
ν_{15}	–	0.0376 (0.055)	–
ν_{16}	–	–	–
ν_{17}	0.0456 (0.047)	–	–
ν_{18}	–	0.0458 (0.042)	0.0272 (0.015)
ν_{19}	–	0.0276 (0.013)	0.0192 (0.006)
ν_{20}	–	0.1052 (0.138)	0.1154 (0.166)
ν_{21}	0.1535 (0.269)	–	0.0220 (0.006)
ν_{22}	–	–	–
ν_{23}	–	0.0027 (0.00002)	–
B_{1u}	i - $j \in \widetilde{X}$ - $\widetilde{D}$	i - $j \in \widetilde{A}$ - $\widetilde{B}$	i - $j \in \widetilde{C}$ - $\widetilde{D}$
ν_{24}	–	–	–
ν_{25}	0.1015 (0.777)	0.0539 (0.219)	0.0250 (0.047)
ν_{26}	0.0651 (0.170)	–	0.0153 (0.009)
ν_{27}	0.1035 (0.259)	–	0.0219 (0.012)
ν_{28}	0.0361 (0.026)	0.0392 (0.031)	0.0093 (0.002)
ν_{29}	0.3264 (1.964)	0.0347 (0.022)	0.0840 (0.130)
ν_{30}	0.2930 (1.26)	–	0.0719 (0.076)
ν_{31}	0.1553 (0.280)	0.1107 (0.142)	0.0260 (0.008)
ν_{32}	0.0094 (0.0003)	–	–
ν_{33}	–	–	0.002 (0.00001)
ν_{34}	–	–	–
B_{2u}	i - $j \in \widetilde{X}$ - $\widetilde{B}$	i - $j \in \widetilde{A}$ - $\widetilde{D}$	i - $j \in \widetilde{B}$ - $\widetilde{C}$
ν_{35}	–	0.0043 (0.002)	0.0718 (0.456)
ν_{36}	–	0.0346 (0.057)	0.0483 (0.112)
ν_{37}	–	–	0.0191 (0.011)
ν_{38}	–	–	–
ν_{39}	–	–	0.0395 (0.035)
ν_{40}	0.0739 (0.086)	–	–
ν_{41}	0.0941 (0.131)	–	–
ν_{42}	–	–	0.1133 (0.177)
ν_{43}	0.1056 (0.143)	0.0962 (0.118)	–
ν_{44}	–	–	–
ν_{45}	–	–	–

Table 4. 7: Interstate linear coupling parameters of An^+ . All quantities are in eV. The dimensionless Poisson parameters $(\lambda_i/\omega_i)^2/2$ are given in parentheses.

Mode	λ_{i-j}	λ_{i-j}
B_{1g}	i - $j \in \widetilde{A}$ - $\widetilde{E}$	
ν_{46}	–	
ν_{47}	0.0736 (0.849)	
ν_{48}		
ν_{49}		
B_{2g}	i - $j \in \widetilde{X}$ - $\widetilde{E}$	i - j $\in \widetilde{C}$ - $\widetilde{E}$
ν_{50}	–	0.0444 (0.963)
ν_{51}	–	0.0834 (1.479)
ν_{52}	0.0487 (0.276)	0.0505 (0.297)
ν_{53}	–	0.0636 (0.193)
ν_{54}	0.1395 (0.903)	0.1433 (0.953)
ν_{55}	0.0775 (0.222)	0.0769 (0.219)
A_u	i - $j \in \widetilde{B}$ - $\widetilde{E}$	
ν_{56}	–	
ν_{57}	–	
ν_{58}	–	
ν_{59}	0.0418 (0.081)	
ν_{60}	–	
B_{3u}	i - $j \in \widetilde{D}$ - $\widetilde{E}$	
ν_{61}	0.0256 (2.758)	
ν_{62}	0.0754 (1.398)	
ν_{63}	0.0680 (0.753)	
ν_{64}	–	
ν_{65}	–	
ν_{66}	0.0327 (0.040)	

4.3 Vibronic Hamiltonian

In order to treat the nuclear dynamics quantum mechanically in the low-lying electronic states of An^+ , we develop a suitable vibronic Hamiltonian in this section. For this purpose we resort to a diabatic electronic basis to avoid the singular derivative coupling terms of the complementary adiabatic electronic basis. We employ dimensionless normal displacement coordinates (Q) for the nuclear vibrations to express the Hamiltonian matrix. We focus on the electronic structure of anthracene (An) and the quantum dynamics on the coupled $\widetilde{X}^2B_{2g}$ -$\widetilde{A}^2B_{1g}$ -$\widetilde{B}^2A_u$ -$\widetilde{C}^2B_{2g}$ -$\widetilde{D}^2B_{3u}$ -$\widetilde{E}^2A_g$ electronic states of An^+ . The equilibrium geometry of the An molecule converges to the D_{2h} symmetry point group in its electronic ^1A_g ground state. The ionization of an electron from the valance molecular orbitals of symmetry b_{2g}, b_{1g}, a_u, b_{2g}, b_{3u} and a_g of anthracene produces the $D_0(\widetilde{X}^2B_{2g}$), $D_1(\widetilde{A}^2B_{1g}$), $D_2(\widetilde{B}^2A_u$), D_3 ($\widetilde{C}^2B_{2g}$), D_4 ($\widetilde{D}^2B_{3u}$) and D_5 ($\widetilde{E}^2A_g$) electronic states of An^+ . The molecular orbital (MO) diagrams are shown in Figures. 4. 5. The nature of the first five MOs(HOMO, HOMO-1, HOMO-2, HOMO-3, HOMO-4) are of π type and the next MO HOMO-5 is of σ type for AN. Anthracene radical cation possesses 66 vibrational degrees of freedom and they belong to the following irreducible representations of the D_{2h} symmetry point group,

$$\Gamma_{vib} = 12a_g + 5a_u + 4b_{1g} + 11b_{1u} + 6b_{2g} + 11b_{2u} + 11b_{3g} + 6b_{3u}$$

The coupling of various electronic states is described by the standard symmetry selection rules

$$\Gamma_n \otimes Q_{vib} \otimes \Gamma_m \supset A_g \tag{4.1}$$

In the above the indices n and m refer to the electronic states. According to the

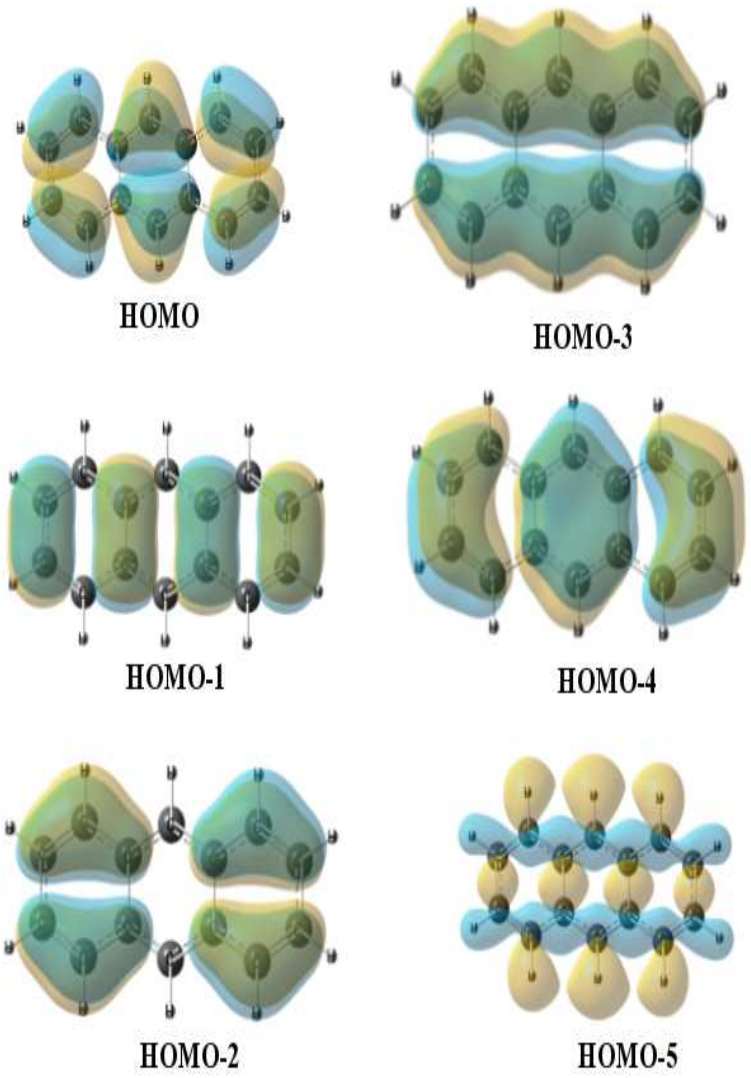

Figure 4.5: The first six highest occupied molecular orbital pictures of An

above rule the totally symmetric vibrational modes (a_g) are always Condon active within a given electronic state [23]. The possible interstate coupling vibrational modes between different electronic states of An^+ is also derived from the above rule.

With this description the general form of the vibronic Hamiltonian pertinent to the $\widetilde{X}$ - $\widetilde{A}$ - $\widetilde{B}$ - $\widetilde{C}$ - $\widetilde{D}$ - $\widetilde{E}$ electronic states of An^+ can be given by

$$\mathcal{H} = (\mathcal{T}_N + \mathcal{V}_0)\mathbf{1_6} + \Delta\mathcal{H} \tag{4.2}$$

$$\begin{aligned} \mathcal{T}_N &= -\frac{1}{2}\sum_i^f \omega_i \left(\frac{\partial^2}{\partial Q_i^2}\right) \\ \mathcal{V}_0 &= \frac{1}{2}\sum_i^f \omega_i Q_i^2 \end{aligned} \tag{4.3}$$

where $\mathbf{1_6}$ is a 6×6 unit matrix and $(\mathcal{T}_N + \mathcal{V}_0)$ is the Hamiltonian for the reference state (the vibrational and electronic ground state of neutral An). This reference state is assumed to be harmonic and vibronically decoupled from the other states. The quantity $\Delta\mathcal{H}$ in Eqn. 4. 2 represents the change in ionization and defines the electronic Hamiltonian of the An^+ .

$$\Delta\mathcal{H} = \begin{pmatrix} W_{\widetilde{X}} & W_{\widetilde{X}-\widetilde{A}} & W_{\widetilde{X}-\widetilde{B}} & W_{\widetilde{X}-\widetilde{C}} & W_{\widetilde{X}-\widetilde{D}} & W_{\widetilde{X}-\widetilde{E}} \\ & W_{\widetilde{A}} & W_{\widetilde{A}-\widetilde{B}} & W_{\widetilde{A}-\widetilde{C}} & W_{\widetilde{A}-\widetilde{D}} & W_{\widetilde{A}-\widetilde{E}} \\ & & W_{\widetilde{B}} & W_{\widetilde{B}-\widetilde{C}} & W_{\widetilde{B}-\widetilde{D}} & W_{\widetilde{B}-\widetilde{E}} \\ H.C & & & W_{\widetilde{C}} & W_{\widetilde{C}-\widetilde{D}} & W_{\widetilde{C}-\widetilde{E}} \\ & & & & W_{\widetilde{D}} & W_{\widetilde{D}-\widetilde{E}} \\ & & & & & W_{\widetilde{E}} \end{pmatrix} \tag{4.4}$$

The elements of this Hamiltonian matrix are written in terms of the dimensionless normal coordinates (Q) of the electronic ground state of PAH which is to

a good approximation treated as harmonic [23]. The non-diagonal matrix Hamiltonian in Eqn. 4. 2 represent the change in the electronic energy upon ionization and describe the diabatic electronic potentials (diagonal elements) of the $\widetilde{X}$, $\widetilde{A}$, $\widetilde{B}$, $\widetilde{C}$, $\widetilde{D}$, $\widetilde{E}$ electronic states of An^+ and their coupling potentials (off-diagonal elements). These are expanded in a Taylor series around the reference equilibrium geometry (**Q**=0) of the electronic ground state of An as

$$W_j \;=\; E_0^{(j)} + \sum_i^{a_g} \kappa_i^{(j)} Q_i + \frac{1}{2}\sum_i^{N} \gamma_i^{(j)} Q_i^2;\; j \;\in \widetilde{X},\; \widetilde{A},\; \widetilde{B},\; \widetilde{C},\; \widetilde{D},\; \widetilde{E} \quad (4.5)$$

$$W_{j-k} = \sum_i \lambda_i^{j-k} Q_i \quad (4.6)$$

where j - $k \in \widetilde{X}$ -$\widetilde{A}$, $\widetilde{X}$ -$\widetilde{B}$, $\widetilde{X}$ -$\widetilde{C}$, $\widetilde{X}$ -$\widetilde{D}$, $\widetilde{X}$ -$\widetilde{E}$, $\widetilde{A}$ -$\widetilde{B}$, $\widetilde{A}$ -$\widetilde{C}$, $\widetilde{A}$ -$\widetilde{D}$, $\widetilde{A}$ -$\widetilde{E}$, $\widetilde{B}$ -$\widetilde{C}$, $\widetilde{B}$ -$\widetilde{D}$, $\widetilde{B}$ -$\widetilde{E}$, $\widetilde{C}$ -$\widetilde{D}$, $\widetilde{C}$ -$\widetilde{E}$, $\widetilde{D}$ -$\widetilde{E}$ with i $\in$ b_{3g}; b_{2u}; - ; b_{1u}; b_{2g}; b_{1u}; b_{3g}; b_{2u}; b_{1g}; b_{2u}; b_{3g}; a_u; b_{1u}; b_{2g}; b_{3u} for An^+ .

In the above equations the quantity $E_0^{(j)}$ represents the vertical ionization energy of the j^{th} electronic states. κ_i^j and γ_i^j are the linear and second-order vibronic coupling parameters of the i^{th} vibrational mode in the j^{th} electronic state, respectively. The quantity $\lambda_i^{(j-k)}$ describes the first-order coupling parameter between the j and k electronic states through the vibrational mode i.

4.4 Results and Discussion

4.4.1 Adiabatic potential energy surfaces: Topography and stationary points

In this section we begin with a discussion on the topography of the adiabatic potential energy surfaces and the stationary points found on them employing the vibronic coupling model introduced above. The results of this analysis are related

to the findings of the nuclear dynamical studies presented later in this section. The adiabatic potential energies are obtained by diagonalizing the 6×6 diabatic electronic Hamiltonian defined in Eq. 4.2. We show the cuts of the potential energy surfaces along all the totally symmetric vibrational modes in Figure 4. 6. The cuts of the potential energy surfaces along ν_9 totally symmetric vibrational modes in Figure 4. 7 for better quality of representation. We note that this representative figures display the most important features of the underlying potential energy hyper-surfaces. The adiabatic potential energies in the above figures are plotted against the dimensionless normal coordinate of the given vibrational mode ν_9 keeping all others at their equilibrium value (at Q=0). The solid curves represent the potential energies obtained from the model and the points superimposed on them represent the computed *ab initio* data. It can be seen that the vibronic coupling model developed in Sec. 4.3 reproduces the *ab initio* data very well. This comparison is most valuable in the vicinity of various curve crossings in the above figures. These curve crossings develop into conical intersections in multi-dimensions and these intersections are the mechanistic bottleneck for the nuclear motion in a given electronic state. The location of the energetic minimum of these intersections relative to the equilibrium minimum of a given state play the key role in the subsequent dynamical event. It is important to add that the two groups comprising of $\widetilde{X}$ -$\widetilde{A}$ -$\widetilde{B}$ and $\widetilde{C}$ -$\widetilde{D}$ -$\widetilde{E}$ electronic states of An^+ are energetically well separated from each other, however, the states within a group are vertically close in energy. The energetic minimum of various conical intersections in the six lowest electronic states as well as their equilibrium minimum of An^+ have been estimated within a linear coupling approach [23]. We note that when a second-order coupling model is considered the relevant equations for the energetic minimum become nonlinear [153] and their solutions become nontrivial with an increase in the nuclear degrees of freedom. Despite this, we have attempted to estimate the stationary points including the second-order terms also. However, no significant difference from the linear coupling results is found when-

ever a converged solution is obtained in the second-order model. The energetic minimum of the seam of $\widetilde{X}$ -$\widetilde{A}$, $\widetilde{A}$ -$\widetilde{B}$ and $\widetilde{X}$ -$\widetilde{B}$ CIs are found to occur at $\sim$ 8.82 eV, $\sim$ 8.86 and $\sim$ 15.44 eV, respectively. The $\widetilde{X}$, $\widetilde{A}$ and $\widetilde{A}$, $\widetilde{B}$ electronic states are vertically $\sim$ 1.22 and 0.62 eV spaced, respectively. The energetic minimum of $\widetilde{A}$ -$\widetilde{B}$ CIs in An^+ occurs only $\sim$ 0.76 and $\sim$ 0.10 eV above the equilibrium minimum of its $\widetilde{A}$ and $\widetilde{B}$ state, respectively. The consequence of this energy lowering in the spectral and dynamical properties is discussed later in the text. As the $\widetilde{X}$ -$\widetilde{B}$ CIs of An^+ occur at much higher energies, they do not play any role in the present investigations. The $\widetilde{B}$ -$\widetilde{C}$ and $\widetilde{B}$ -$\widetilde{D}$ CIs occur at much higher energies and expected to have no impact on the dynamics of $\widetilde{C}$ and $\widetilde{D}$ electronic states. Interestingly, $\widetilde{B}$ -$\widetilde{E}$ CIs occur at $\sim$ 0.9 eV above the $\widetilde{E}$ state minimum. The $\widetilde{C}$ and $\widetilde{D}$ states of An^+ are quasi-degenerate at the vertical configuration. The minimum of the $\widetilde{C}$ -$\widetilde{D}$ CIs is located nearly at the equilibrium minimum of the $\widetilde{D}$ state and $\sim$ 0.1 eV above the minimum of the $\widetilde{C}$ state. Similarly, the minimum of the $\widetilde{C}$ -$\widetilde{E}$ and $\widetilde{D}$ -$\widetilde{E}$ CIs occurs at $\sim$ 10.97 and 10.93 eV, respectively. These are very close to the equilibrium minimum of the $\widetilde{E}$ state estimated at $\sim$ 10.86 eV. The effect of the low-energy CIs on the vibronic bands and excited state relaxation dynamics of An^+ are discussed in relation to the astrophysical observations in the next section. All these energetic minima are given in Table 4.8.

Table 4. 8. Equilibrium minimum (diagonal entries) and minimum of the seam of various CIs (off-diagonal entries) of the potential energy surfaces of An^+ . All quantities are given in eV.

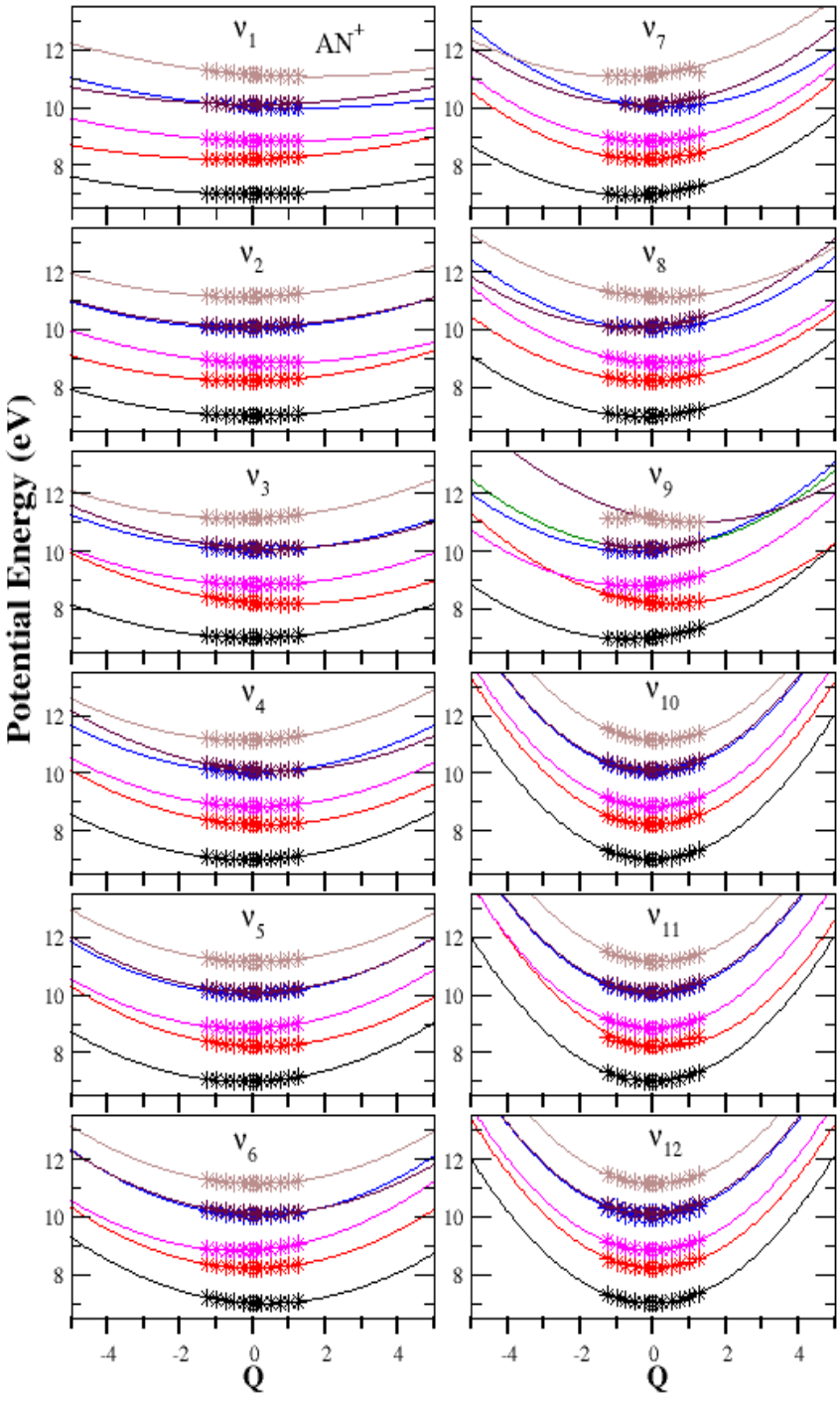

Figure 4.6: Adiabatic potential energies of the $\widetilde{X}$, $\widetilde{A}$, $\widetilde{B}$, $\widetilde{C}$, $\widetilde{D}$ and $\widetilde{E}$ electronic states of An^+ as a function of the dimensionless normal coordinates of the totally symmetric (a_g) vibrational modes, ν_1-ν_9 are shown by different colour line

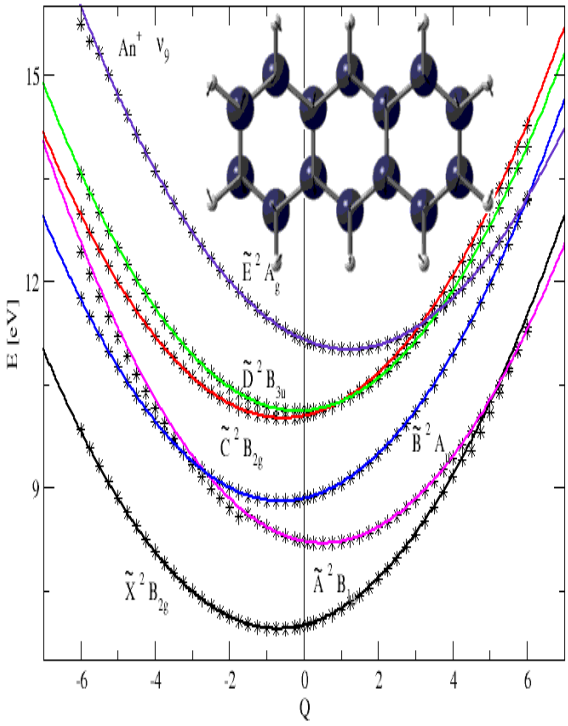

Figure 4.7: Adiabatic potential energy surfaces of the six low-lying electronic states of An^+ along the vibrational modes ν_9. A sketch of the vibrational mode is also shown. The potential energy surfaces are obtained with the quadratic vibronic coupling scheme. The computed *ab initio* potential energies of these states are superimposed and shown by the points on each curve. The equilibrium geometry of An in its electronic ground state (^1A_g) corresponds to $\mathbf{Q} = 0$.

	$\widetilde{X}$	$\widetilde{A}$	$\widetilde{B}$	$\widetilde{C}$	$\widetilde{D}$	$\widetilde{E}$
$\widetilde{X}$	–	8.82	15.44	22.60	30.90	17.03
$\widetilde{A}$		8.10	8.86	11.59	15.65	15.06
$\widetilde{B}$			8.76	12.55	11.29	12.31
$\widetilde{C}$				9.94	10.03	10.97
$\widetilde{D}$					10.01	10.93
$\widetilde{E}$						10.86

The mentioned various CIs among these electronic states open up complex pathways for the nuclear motion on them. The effect of the low-energy CIs in the vibronic bands and excited state relaxation dynamics of An^+ are discussed in relevance to the astrophysical observations in the next section.

4.4.2 Vibronic band structures of $\widetilde{X}$, $\widetilde{A}$, $\widetilde{B}$, $\widetilde{C}$, $\widetilde{D}$ and $\widetilde{E}$ electronic states of An^+

4.4.2.1 $\widetilde{X}$, $\widetilde{A}$, $\widetilde{B}$, $\widetilde{C}$, $\widetilde{D}$ and $\widetilde{E}$ uncoupled state spectrum

The uncoupled state spectrum for the $\widetilde{X}$, $\widetilde{A}$, $\widetilde{B}$, $\widetilde{C}$, $\widetilde{D}$ and $\widetilde{E}$ electronic states of An^+ is calculated by a matrix diagonalization approach using the Lanczos algorithm [23]. The theoretical stick spectra are calculated using 9 totally symmetric vibrational modes (ν_1-ν_9) using the vibronic Hamiltonian of Eqn. 4. 2 and the parameters of Tables 4.3 - 4.4. The results are numerically converged with respect to the number of vibrational basis functions and the number of Lanczos iteration. In the spectrum of the $\widetilde{X}$ state which is shown in Figure 4.8, the series of peaks are $\sim$ 0.162, $\sim$ 0.182, $\sim$ 0.190 and $\sim$ 0.199 eV spaced in energy corresponding to the progression along ν_6 (C-H bending), ν_7 (outer ring C=C

stretching), ν_8 (inner ring C=C stretching) and ν_9 (inter-ring C=C stretching) vibrational modes, respectively. The ring deformation mode ν_2 is also weakly excited in this state. In the $\widetilde{A}$ state spectrum of An^+ vibrational modes ν_1(ring deformation) and ν_3(C-C-C bending) form the major progressions. The peaks are ~ 0.049 and ~ 0.095 eV spaced, respectively, corresponding to the frequencies of these vibrational modes. The inter-ring C=C stretching mode ν_9 is also moderately excited in this state. The uncoupled state spectra of $\widetilde{A}$ and $\widetilde{B}$ states are shown in Figure 4. 9 and Figure 4. 10, respectively. The vibrational modes ν_1 and ν_2 form dominant progressions in the $\widetilde{B}$ state of An^+ . Peak spacings of ~ 0.049 and ~ 0.077 eV due to these modes, respectively, are extracted from the spectrum of this electronic state. The inter-ring C=C stretching mode ν_9 is also weakly excited in this band. The vibrational spectrum of the uncoupled $\widetilde{B}$ state reveals resolved vibrational structures whereas, a broad and structureless band of this state is observed in the experiment [86]. The coupling of the $\widetilde{B}$ state particularly, with the $\widetilde{A}$ state appears to be extremely important in this case. We note that the $\widetilde{B}$ band of An^+ has received special attentions recently. A signature of this band has been discovered in the spectrum of the star Cernis 52 in the Perseus molecular cloud by the astronomers [77]. This issue is taken up separately and discussed at length later in Sec. 4. 4. 4. The uncoupled state vibronic structure of $\widetilde{C}$, $\widetilde{D}$ and $\widetilde{E}$ states are shown in Figures 4. 11 to 4. 13, respectively. The vibrational mode ν_1 is highly excited up to its fourth overtone level in the $\widetilde{C}$ band of An^+ . Peak spacings of ~ 0.049 eV due to this mode, is extracted from the spectrum. The vibrational modes ν_3, ν_4, ν_7 and ν_8 form the major progressions in the $\widetilde{D}$ band of An^+ . It is found that the vibrational modes ν_1 and ν_9 form the detectable progressions in the $\widetilde{E}$ state of An^+ . The number of harmonic oscillator basis functions along each vibrational mode, the dimension of the secular matrix and the number of Lanczos iterations are used to generate the uncoupled states vibronic spectra of $\widetilde{X}$, $\widetilde{A}$, $\widetilde{B}$, $\widetilde{C}$, $\widetilde{D}$ and $\widetilde{E}$ electronic states of An^+ is shown in Table 4. 9. In summary, the inter-ring C=C stretching and the

C-C-C bending vibrational modes (ν_1, ν_2, ν_3, ν_7, ν_8 and ν_9) play crucial role in the vibronic dynamics of An^+ .

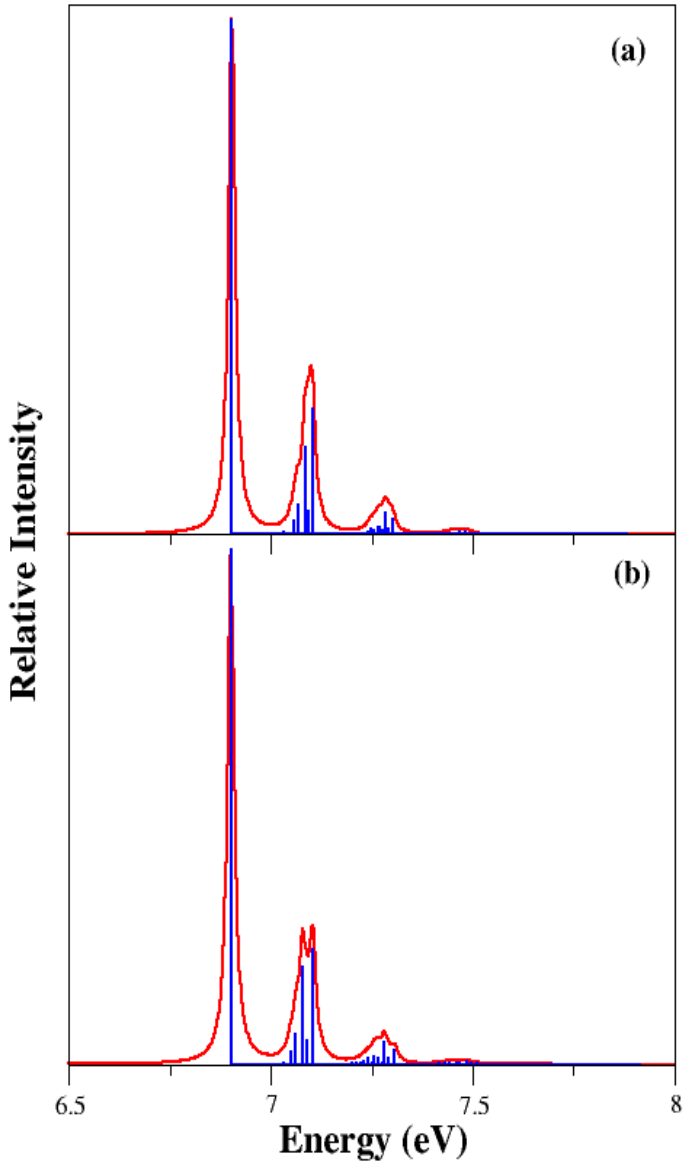

Figure 4.8: The uncoupled vibronic band of the $\widetilde{X}$ electronic state of An^+ computed with relevant seven a_g (ν_1-ν_7) vibrational modes within the linear (panel a) and quadratic (panel b) vibronic coupling scheme. The theoretical stick spectrum in each panel is convoluted with a Lorentzian function of 20 meV FWHM to calculate the spectral envelope.

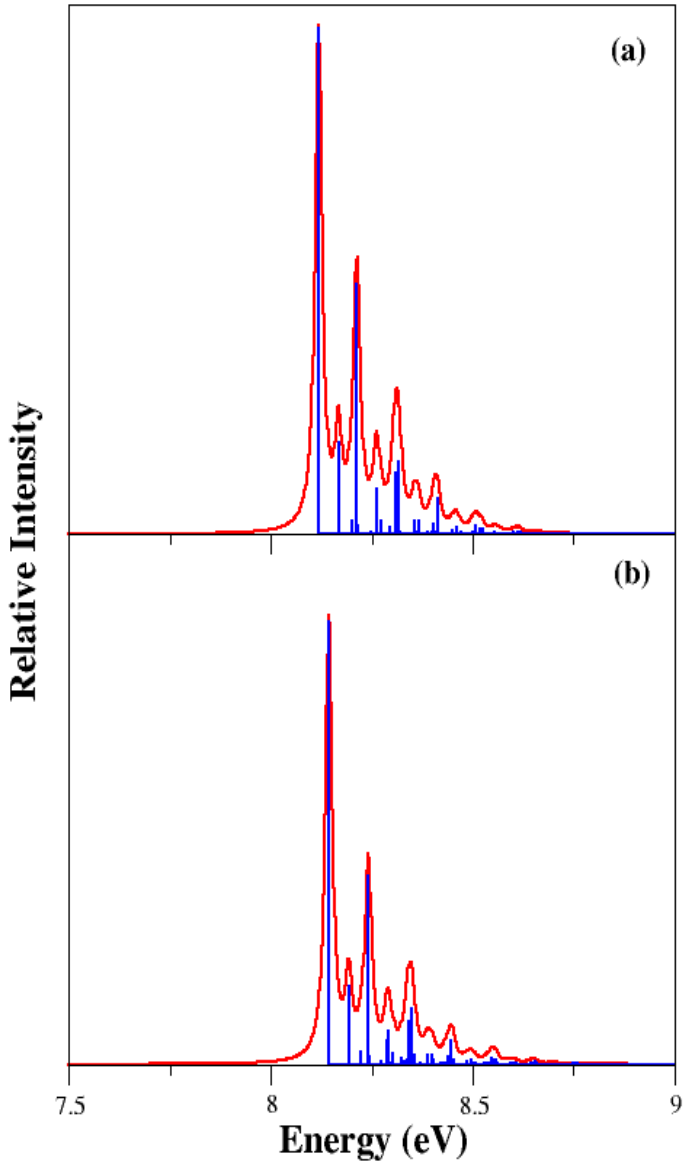

Figure 4.9: Same as in Figure. 4.8 shown for the uncoupled vibronic band of $\widetilde{A}$ state of An^+ .

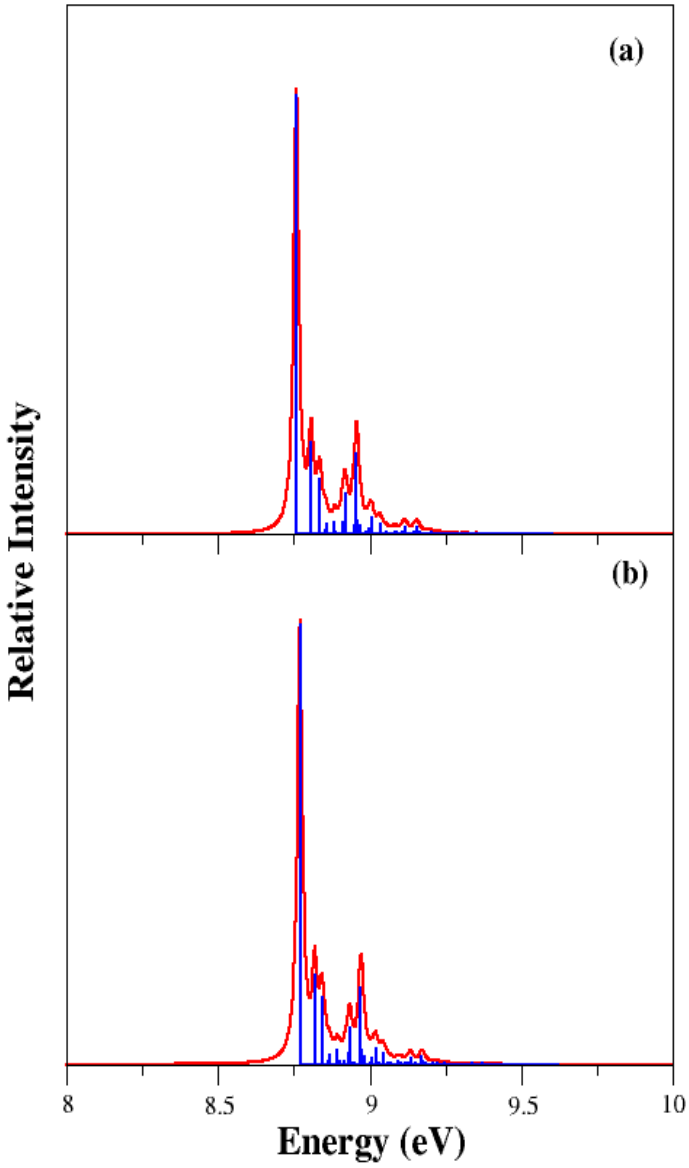

Figure 4.10: Same as in Figure. 4.8 shown for the uncoupled vibronic band of $\widetilde{B}$ state of An^+ .

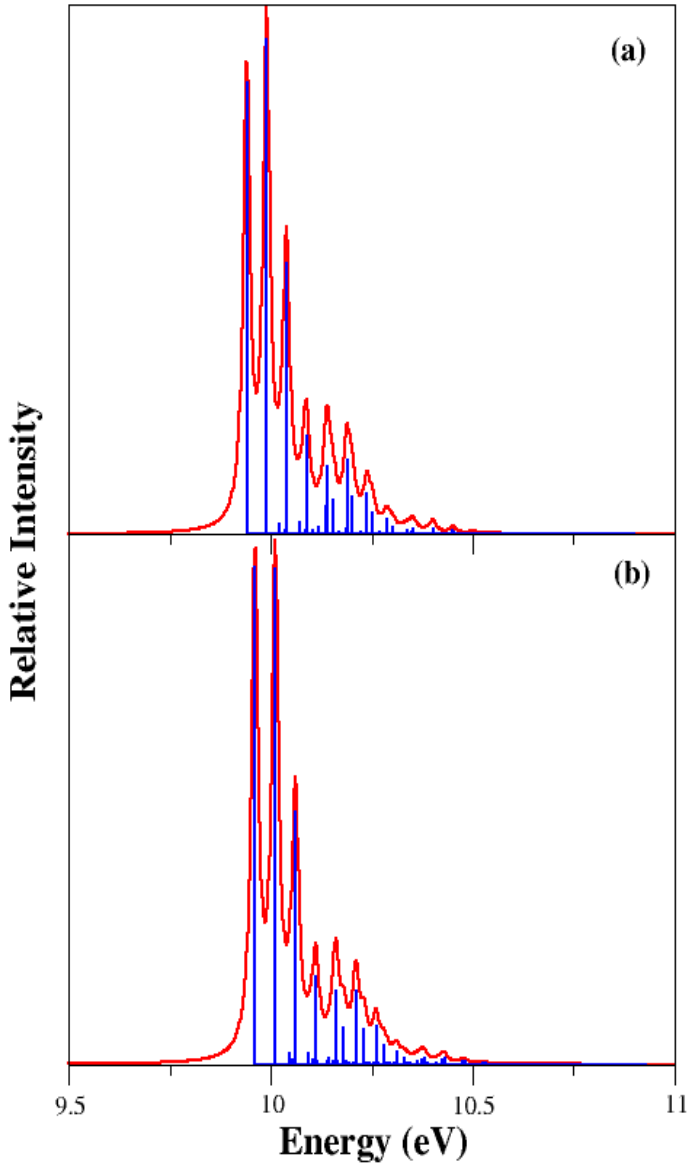

Figure 4.11: Same as in Figure. 4.8 shown for the uncoupled vibronic band of $\widetilde{C}$ state of An^+ .

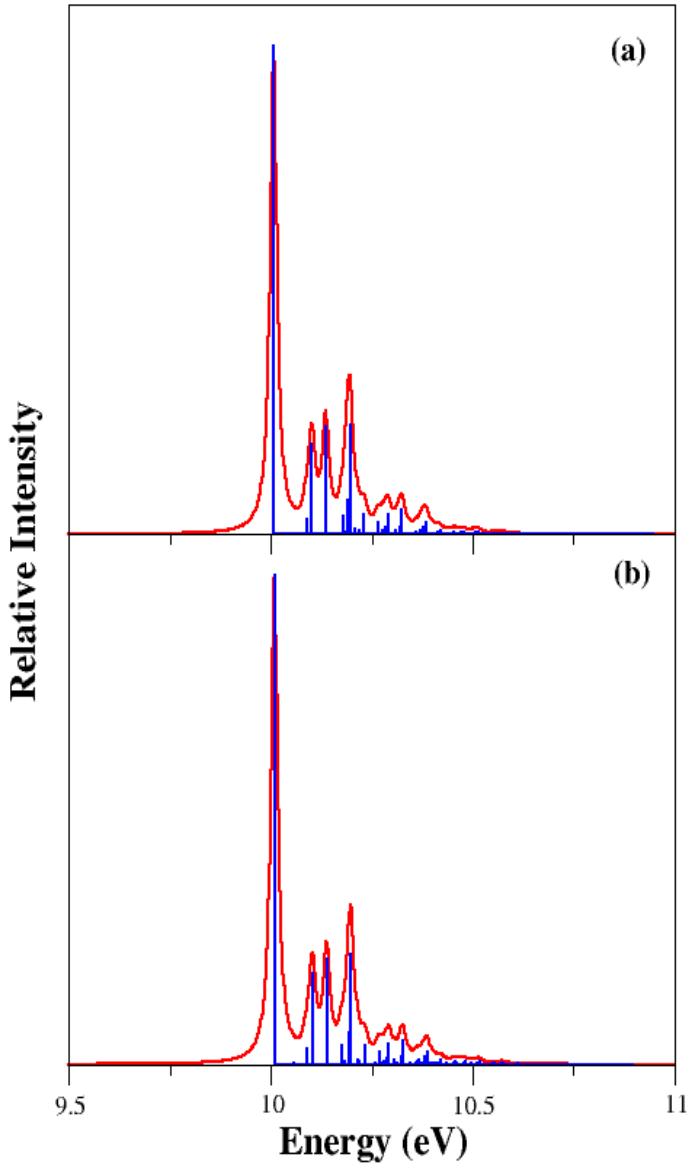

Figure 4.12: Same as in Figure. 4.8 shown for the uncoupled vibronic band of $\widetilde{D}$ state of An^+ .

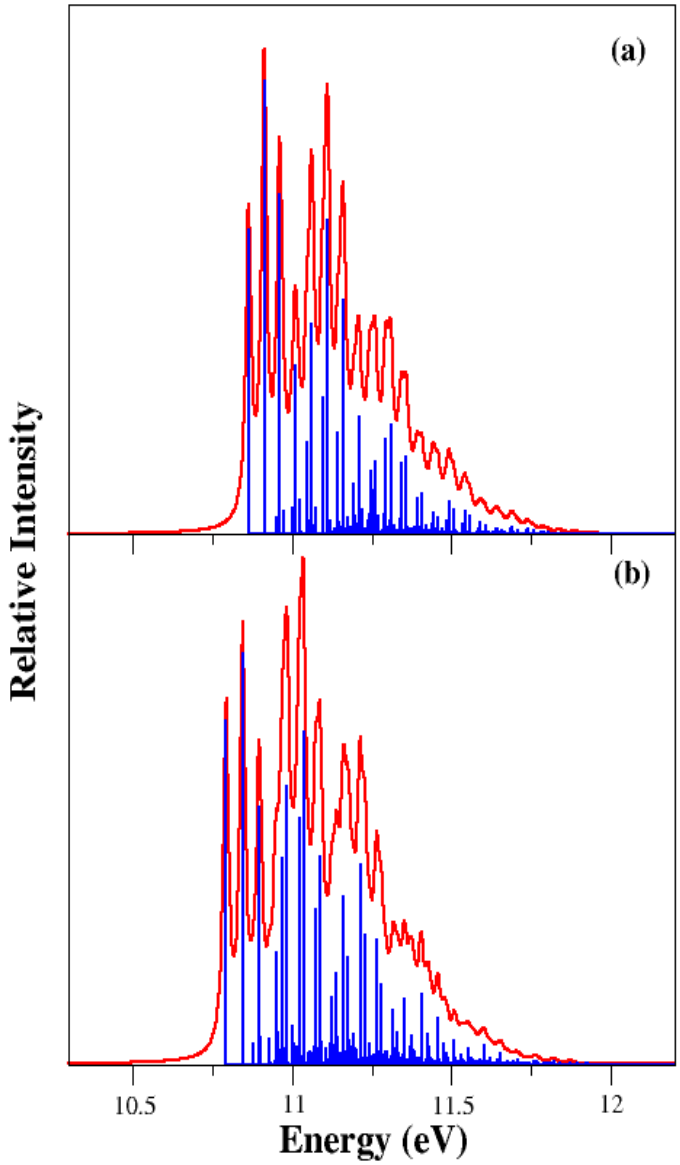

Figure 4.13: Same as in Figure. 4.8 shown for the uncoupled vibronic band of $\widetilde{E}$ state of An^+ .

Table 4. 9

The number of harmonic oscillator (HO) basis functions along each vibrational mode, the dimension of the secular matrix and the number of Lanczos iterations used to calculate the converged theoretical stick spectrum shown in Figures. 4.8 - 4.13.

No. of HO basis functions									Dimension of the secular matrix	No. of Lanczos iterations	Figure(s)
ν_1	ν_2	ν_3	ν_4	ν_5	ν_6	ν_7	ν_8	ν_9			
2	2	2	2	2	3	10	3	15	43200	5000	4.8 (a)
6	2	15	2	2	2	2	5	2	28800	5000	4.9 (a)
20	12	2	2	3	9	2	3	18	2799360	5000	4.10 (a)
20	2	2	2	2	2	2	2	4	10240	5000	4.11 (a)
2	2	10	12	2	2	4	12	2	184320	5000	4.12 (a)
25	2	2	2	2	2	5	2	12	96000	5000	4.13 (a)

4.4.2.2 Vibronic spectrum of coupled $\widetilde{X}$ -$\widetilde{A}$ -$\widetilde{B}$ -$\widetilde{C}$ -$\widetilde{D}$ -$\widetilde{E}$ electronic states

Despite the fact that the uncoupled state spectra discussed above are helpful in understanding the important roles played by different vibrational modes in each electronic state, they deviate significantly from the observed bands in practice. Coupling between states is necessarily be considered to capture most of the features of the experimental observations [86]. A careful analyze is of the coupling strength of 66 vibrational modes of An^+ indicates that 31 ($9a_g + 1a_u + 1b_{1g} + 5b_{1u} + 3b_{2g} + 5b_{2u} + 5b_{3g} + 2b_{3u}$) of them are relevant in the nuclear dynamics on the coupled manifold of six electronic states. Therefore, in the final calculations we considered all these 31 vibrational modes and carried out WP propagations on the coupled manifold of six electronic states using the MCTDH algorithm. Six WP calculations are carried out by launching the initial WP on each of the six electronic states separately. The details of the mode combinations and the sizes of the basis sets are given in Table 4. 10. In each calculation the WP

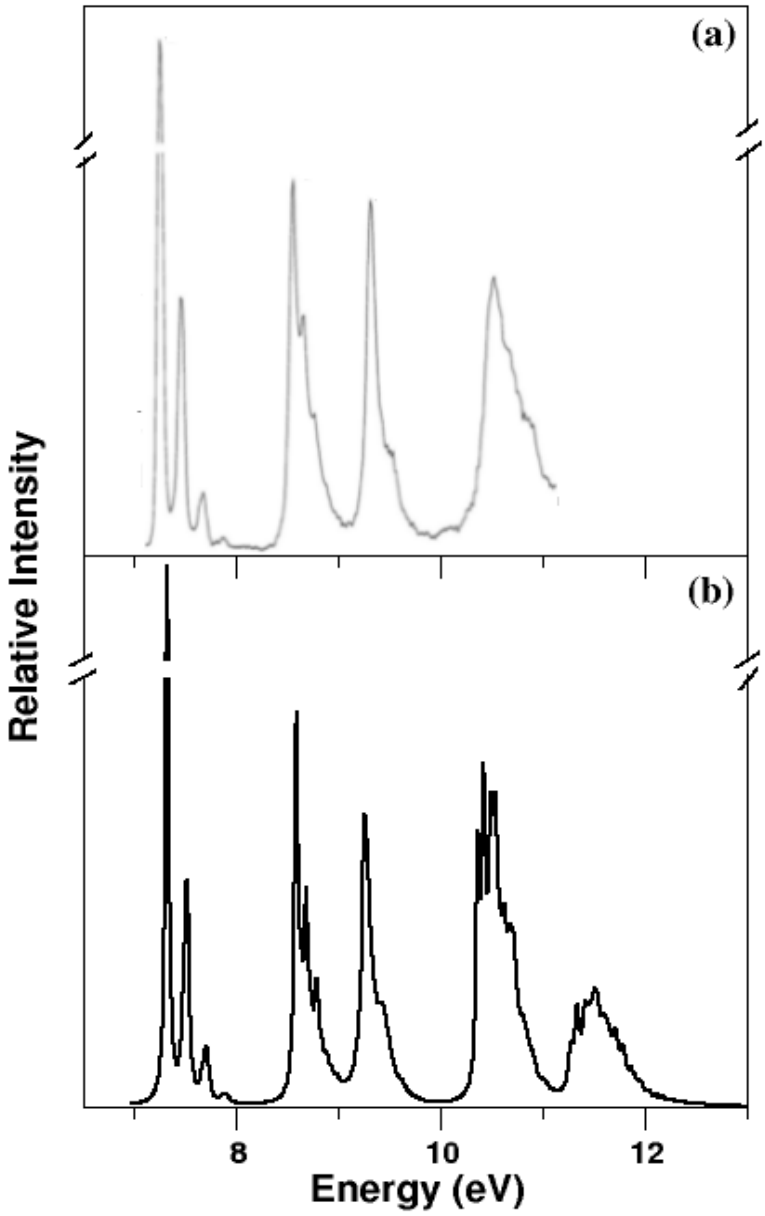

Figure 4.14: The vibronic band structure of the coupled $\widetilde{X}$ -$\widetilde{A}$ -$\widetilde{B}$ -$\widetilde{C}$ -$\widetilde{D}$ electronic states of An^+ . The experimental (reproduced from Ref [86]) and the present theoretical results are shown in the top and bottom panels, respectively. The intensity (in arbitrary units) is plotted along the energy (measured relative to electronic ground state (^1A_g) of An) of the final vibronic states.

is propagated for 400 fs. The time autocorrelation function is damped with an exponential function of relaxation time 33 fs, and then Fourier transformed to generate the spectrum. The results from six different calculations are combined with equal weighteage to generate the composite theoretical band shown in Fig. 4.14 (bottom panel) along with the experimental results (top panel) reproduced from Reference [86]. It can be seen from the figure that except for the first band, the distinct vibronic structures of the uncoupled state spectrum are completely blurred in the coupled state spectrum. The non-adiabatic coupling effects are particularly severe for the third and fourth bands. While the third band could be related to the vibronic structure of the $\widetilde{B}$ state, the fourth one is formed by highly overlapping $\widetilde{C}$ and $\widetilde{D}$ electronic states of An^+ . It can be seen from Figure. 4. 14 that the present theoretical results are in very good agreement with the laboratory experiment [86]. We note that experimental band structure of the $\widetilde{E}$ state is not available. We find that the $\widetilde{E}$ state is coupled with further higher excited electronic states of An^+ . As revealed by Figure 4. 14 that, the $\widetilde{A}$ band is structured, $\widetilde{B}$ band is broad and structureless and the $\widetilde{C}$ and $\widetilde{D}$ bands are overlapping. The results in both the cases are in very good accord with the experiment [86]. These results can be clearly interpreted and understood from the findings of section 4.3. We reiterate that, the minimum of the $\widetilde{A}$ -$\widetilde{B}$ CIs is closer to the $\widetilde{B}$ state whereas, the minimum of the $\widetilde{X}$ -$\widetilde{A}$ CIs is far from the $\widetilde{A}$ state minimum. The minimum of the $\widetilde{X}$ -$\widetilde{B}$ CIs occurs at higher energies. Therefore, it is clear that the blurring of the vibronic structure of the $\widetilde{B}$ state is mainly caused by the $\widetilde{A}$ -$\widetilde{B}$ CIs. From the theoretical perspective these are quite novel findings that contribute significantly to understand the details of experimental observations.

Table 4. 10: The normal mode combinations, sizes of the primitive and the single particle bases used in the wave packet propagation (using the MCTDH algorithm) on the $\widetilde{X}$ -$\widetilde{A}$ -$\widetilde{B}$ -$\widetilde{C}$ -$\widetilde{D}$ -$\widetilde{E}$ and $\widetilde{A}$ -$\widetilde{B}$ coupled electronic manifold of An^+ .

Electronic States	Normal modes[a]	Primitive basis[b]	Single particle basis[c]	Figure
$\widetilde{X}$ -$\widetilde{A}$ -$\widetilde{B}$ -$\widetilde{C}$ -$\widetilde{D}$ -$\widetilde{E}$ (31-Vibrational modes)	(ν_1,ν_{26},ν_{58},ν_{34},ν_{62})	(5,5,4,5,5)	[7,5,6,7,6,5]	4.14 (b)
	(ν_2,ν_{23},ν_{27},ν_{35},ν_{51})	(5,5,5,4,5)	[5,6,7,6,7,6]	
	(ν_3,ν_{29},ν_{33},ν_{61})	(5,5,4,4)	[5,6,6,5,6,5]	
	(ν_5,ν_{47},ν_{45},ν_{55})	(4,5,5,4)	[5,6,6,7,6,5]	
	(ν_7,ν_4,ν_{40},ν_{57})	(4,4,5,5)	[6,5,6,7,6,5]	
	(ν_8,ν_{39},ν_6,ν_{46})	(5,6,4,5)	[6,5,6,7,6,6]	
	(ν_9,ν_{50},ν_{25},ν_{16},ν_{19})	(5,5,5,5,4)	[6,5,5,6,7,6]	
$\widetilde{A}$ -$\widetilde{B}$ (10-vibrational modes)	(ν_1,ν_6,ν_{23})	(7, 4, 6)	[5, 6]	4.17 (a)
	(ν_2,ν_7,ν_{26},ν_{27})	(6, 5, 4, 4)	[6, 7]	
	(ν_3,ν_9,ν_{29})	(5, 6)	[5, 6]	

4.4.3 Non-radiative decay dynamics

The time-dependent populations of the six diabatic electronic states of An^+ in the coupled state dynamics of section 4.4.1 are shown in Figures 4.15 (a-e). The results obtained by initially populating the $\widetilde{A}$, $\widetilde{B}$, $\widetilde{C}$, $\widetilde{D}$ and $\widetilde{E}$ electronic states are shown in panels a-e, respectively. The six electronic populations are indicated by six different line types in panel *a*. It is observed that insignificant population flows to all the five excited states when the WP is initially prepared on the $\widetilde{X}$ state and the corresponding figure is therefore not included here. This is due to the fact that the CIs of the $\widetilde{X}$ state with all other states are located at higher energies and are not accessible to the WP during its evolution on this state. This results into the observed sharp vibrational level structure of the $\widetilde{X}$ band (cf., Figure 4.8). Time-dependence of diabatic electronic populations in the coupled $\widetilde{X}$ -$\widetilde{A}$ -$\widetilde{B}$ -$\widetilde{C}$ -$\widetilde{D}$ -$\widetilde{E}$ states dynamics of An^+ by initially locating the WP on $\widetilde{A}$, $\widetilde{B}$, $\widetilde{C}$ and $\widetilde{D}$ states are shown in the panel a-d, respectively, of Figure 4. 15. As mentioned before that the $\widetilde{E}$ state is coupled with further higher excited states, detailed examination of which is beyond the scope of the present investigation.

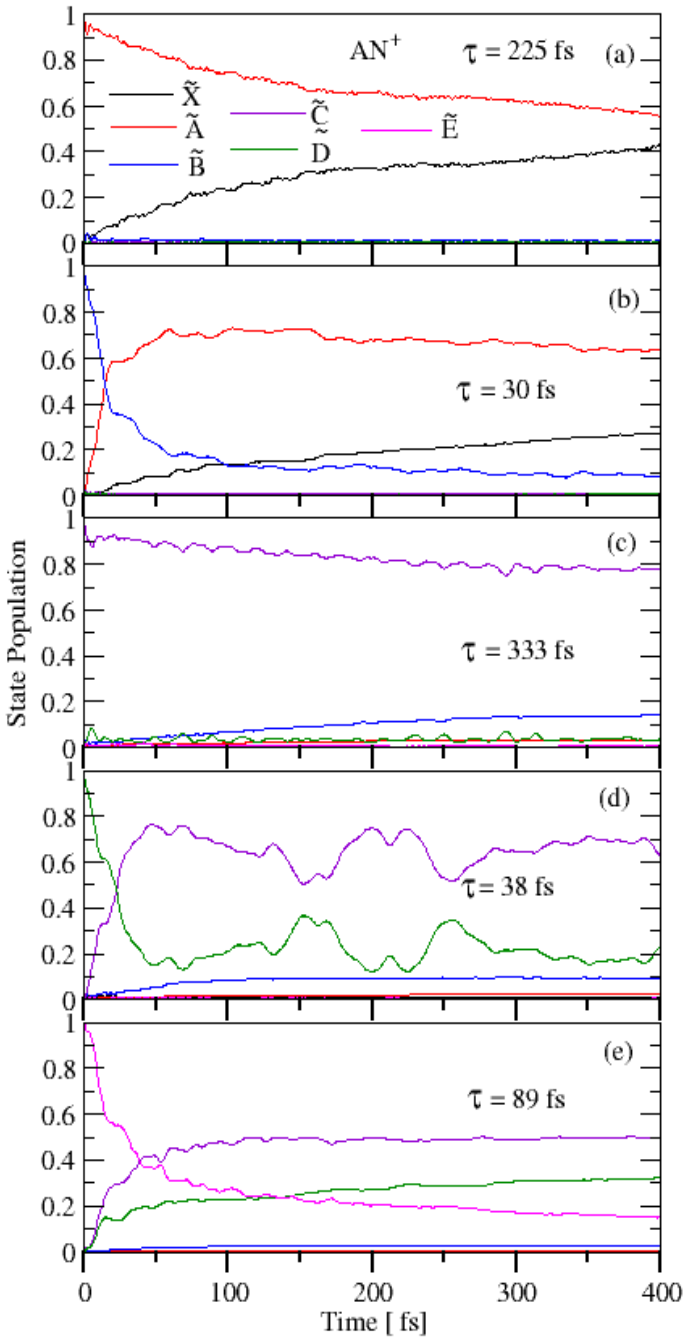

Figure 4.15: The populations (diabatic) in time of the $\widetilde{X}$ (black lines), $\widetilde{A}$ (red lines), $\widetilde{B}$ (blue lines), $\widetilde{C}$ (violet line), $\widetilde{D}$ (green lines) and $\widetilde{E}$ (pink lines) states for an initial transition of the WP to the $\widetilde{A}$ (panel a), $\widetilde{B}$ (panel b), $\widetilde{C}$ (pane c), $\widetilde{D}$ (panel d) and $\widetilde{E}$ (panel e) in the coupled $\widetilde{X}$ -$\widetilde{A}$ -$\widetilde{B}$ -$\widetilde{C}$ -$\widetilde{D}$ -$\widetilde{E}$ states dynamics of An^+ .

Therefore, the electronic populations for an initial preparation of the WP on the $\widetilde{E}$ state is not included in the figure. The line types of the population curves shown in Figure 4.15 are indicated in panel a.

The electronic populations for an initial location of the WP on the $\widetilde{A}$ state shown in panel a of Figure 4.15 reveal population transfer to the $\widetilde{X}$ state. The minimum of the $\widetilde{X}$ -$\widetilde{A}$ CIs located $\sim$ 0.72 eV above the minimum of the $\widetilde{A}$ state. Thus the decay of the $\widetilde{A}$ state population is much slower. The slow decay of $\widetilde{A}$ state population relates to a decay rate of $\sim$ 225 fs, and accounts for the relatively structured band of this state (cf., Figure 4.14).

The decay of the population of the $\widetilde{B}$ state is much faster. A decay rate of $\sim$ 30 fs can be estimated from the initial fast decay of the $\widetilde{B}$ state. The occurrence of the minimum of the $\widetilde{A}$ -$\widetilde{B}$ CIs $\sim$ 0.1 eV above the minimum of the $\widetilde{B}$ state causes this rapid decay. A decay rate of $<$ 50 fs is predicted in the experiment [75]. We note that the minimum of the $\widetilde{X}$ -$\widetilde{B}$ CIs occur $\sim$ 6.68 eV above the minimum of the $\widetilde{B}$ state. Therefore, it is highly unlikely for the WP to access the $\widetilde{X}$ -$\widetilde{B}$ CIs during its evolution on the $\widetilde{B}$ state. This implies that the WP evolving on the $\widetilde{B}$ states undergoes internal conversion to the $\widetilde{A}$ state via the low-energy $\widetilde{A}$ -$\widetilde{B}$ CIs and subsequently moves to the $\widetilde{X}$ state via the $\widetilde{X}$ -$\widetilde{A}$ CIs.

Time-dependence of electronic populations for an initial location of the WP on the $\widetilde{C}$ state is shown in panel c. In this case the internal conversion takes place first to the $\widetilde{D}$ state via the low-lying $\widetilde{C}$ -$\widetilde{D}$ CIs. The energetic minimum of the latter occurs only $\sim$ 0.1 eV above the minimum of the $\widetilde{C}$ state. The WP from the $\widetilde{D}$ state moves to the $\widetilde{B}$ state via $\widetilde{B}$ -$\widetilde{D}$ CIs, minimum of which occurs $\sim$ 1.28 eV above the minimum of the $\widetilde{D}$ state. The very slow decay of the $\widetilde{C}$ state relates to a decay rate of $\sim$ 333 fs.

Finally the time evolution of the WP on the $\widetilde{D}$ state is shown in panel d. In this case most of the population flows to the $\widetilde{C}$ state via the $\widetilde{C}$ -$\widetilde{D}$ CIs located nearly at the minimum of the $\widetilde{D}$ state. Some population also flows (as also seen from panel c) to the $\widetilde{B}$ state via the $\widetilde{B}$ -$\widetilde{D}$ CIs. The initial fast decay of the

population relates to a life-time of $\sim$ 38 fs of the $\widetilde{D}$ state.

In the panel (e), we show the electronic populations of the six electronic states when the initial WP launched on the $\widetilde{E}$ state. Within $\sim$ 25 fs the $\widetilde{E}$ state population sharply decays and the $\widetilde{D}$ state population rises simultaneously. As already mentioned above that the energetic minimum of the $\widetilde{D}$ state occurs at $\sim$ 0.06 above the minimum of the $\widetilde{D}$ -$\widetilde{E}$ CIs, and the $\widetilde{E}$ state population flows to the $\widetilde{D}$ state via these CIs. Similarly the minimum of the $\widetilde{C}$ -$\widetilde{E}$ CIs occurs at $\sim$ 0.32 eV above the $\widetilde{E}$ state minimum. Due to this the population of $\widetilde{C}$ state increases to $\sim$ 0.3 in $\sim$ 25 fs and remains unchanged for the rest of the propagation time. Non-radiative decay rates of $\sim$ 29 fs is estimated for the $\widetilde{E}$ state.

4.4.4 Vibronic dynamics of $\widetilde{B}$ state: Astrophysical relevance

The $\widetilde{B}$ band of An^+ is found to be the strongest in experiments [74, 75]. In view of the coupling of the $\widetilde{B}$ state with the neighboring states of An^+ (*vide supra*), we critically examined how the vibronic structure of the $\widetilde{B}$ state is modified by them. Several reduced dimensional calculations are therefore performed by a matrix diagonalization (MatD) approach in a direct product harmonic oscillator basis utilizing the Lanczos algorithm [23]. In all dynamical treatment six (most relevant) totally symmetric and the strong coupling vibrational modes are considered. The numerical details of all the reduced dimensional calculations are presented in Table 4. 11.

Within the BO picture only 480 vibrational levels of the uncoupled $\widetilde{B}$ state are found. Number of vibronic levels increases to 819 when $\widetilde{X}$ - $\widetilde{B}$ coupling via three b_{2u} modes are considered. The maximum coupling strength of $\sim$ 0.14 is found in this case and is caused by the ν_{47} mode (ring CC stretch). Number of vibronic levels dramatically increases to $\sim$ 3766 when $\widetilde{A}$ and $\widetilde{B}$ coupling is considered. The coupling in this case is caused by four b_{1u} modes with a maximum coupling

Table 4. 11: The number of harmonic oscillator basis functions along each vibrational mode, the dimension of the secular matrix and the number of Lanczos iterations used to calculate the converged theoretical stick spectrum of the $\widetilde{B}$ state of An^+ in the uncoupled and various coupled state situations (see text for discussion).

State	Vibrational Modes	No. of HO basis functions	Dimension of the secular matrix	No. of Lanczos iterations
$\widetilde{B}$	ν_1, ν_2, ν_3, ν_6, ν_7, ν_9	10,6,2,4,2,9	8640	5000
$\widetilde{X}$ - $\widetilde{B}$	ν_1, ν_2, ν_3, ν_6, ν_7, ν_9, ν_{44}, ν_{45}, ν_{47}	9,6,2,4,8,8 4,6,6	7962624	5000
$\widetilde{A}$ - $\widetilde{B}$	ν_1, ν_2, ν_3, ν_6, ν_7, ν_9, ν_{23}, ν_{26}, ν_{27}, ν_{29}	10,6,4,5,3,9 10,3,3,7	40824000	5000
$\widetilde{B}$ - $\widetilde{C}$	ν_1, ν_2, ν_3, ν_6, ν_7, ν_9, ν_{39}, ν_{40}, ν_{46}	9,6,2,4,2,5 20,5,8	6912000	5000
$\widetilde{B}$ - $\widetilde{D}$	ν_1, ν_2, ν_3, ν_6, ν_7, ν_9, ν_{51}, ν_{55}, ν_{57}	12,8,4,5,2,11 4,2,10	6758400	5000
$\widetilde{B}$ - $\widetilde{E}$	ν_1, ν_2, ν_3, ν_6, ν_7, ν_9, ν_{35}	15,9,3,7,7,12 6	2857680	5000

strength of ~ 0.22 along ν_{23} (in-plane ring bending) vibrational mode. The $\widetilde{B}$ - $\widetilde{C}$, $\widetilde{B}$ - $\widetilde{D}$ and $\widetilde{B}$ - $\widetilde{E}$ coupling is caused by the $3b_{2u}$, $3b_{3g}$ and $1a_u$ vibrational modes, respectively. It is found that these couplings increase the number of levels to 1083, 774 and 660, respectively, in that order. In the 707.0 - 711.0 nm range of the recorded DIB [77], the $\widetilde{A}$ - $\widetilde{B}$ coupling causes a fifteen-fold increase of the line density of the $\widetilde{B}$ state and contributes most to the intensity maximum of the origin (0-0) peak. It therefore emerges that it is necessary to include all relevant couplings in order to precisely describe the location and shape of the $\widetilde{B}$ band of An^+ . Understandably, a $\widetilde{X}$ - $\widetilde{A}$ - $\widetilde{B}$ - $\widetilde{C}$ - $\widetilde{D}$ - $\widetilde{E}$ coupled states dynamical simulation including 31 relevant nuclear DOF is out of the scope of the matrix diagonalization approach. This task is therefore accomplished by a WP propagation approach using the multi-configuration time-dependent Hartree (MCTDH) algorithm [122]. In this case the dynamical calculation is performed by launching the WP on the $\widetilde{B}$ state. The time autocorrelation function is damped

by an exponential function, $e^{-\frac{t}{\tau}}$, (with τ = 127 fs) and Fourier transformed to calculate the spectrum.

Important theoretical results of the present investigation are plotted in Figure. 4. 16(a-b) along with the experimental resonance enhanced multi-photon dissociation (REMPD) [85] and Ar-matrix [71] spectroscopy results. In panel a, the (converged) stick lines shown are obtained by diagonalizing the most important $\widetilde{A}$ - $\widetilde{B}$ coupled states Hamiltonian including the ten relevant vibrational modes. About $\sim$ 1272 vibronic levels are obtained in the 707.0 - 711.0 nm wavelength range of the recorded DIB.

The entire $\widetilde{B}$ band of An^+ spans over a wavelength range of $\sim$ 200 nm. Both the stellar ([77]) and laboratory spectroscopy ([75]) experiments probed the most intense 0-0 peak at a narrow wavelength range of $\sim$ 4.0 and 23.0 nm, respectively. The entire $\widetilde{B}$ band from two-states ($\widetilde{A}$ - $\widetilde{B}$) plus 10 modes (solid line) and six-states plus 31 modes (dashed line) dynamical calculations is shown in panel b of Figure 4.16. The calculations are converged with respect to all relevant numerical parameters. It can be seen that both results agree extremely well with each other. Expectedly, the six-states results are more diffuse and confirms an increase of vibronic line density arising from the nonadiabatic coupling to the higher excited electronic states of An^+ . It is gratifying to note that the third peak at $\sim$ 582.4 nm is absent in the two-states results, whereas it appears in the six-states results. Further confirmation of this peak emerges from the REMPD ([85]) and Ar-matrix spectra ([71]) shown in the inset of panel b. These two spectra additionally confirm the energy range of the entire $\widetilde{B}$ band of An^+ .

The entire $\widetilde{B}$ band of An^+ spans over a wavelength range of $\sim$ 200 nm. Both the stellar [77] and laboratory cavity ring down (CRD) [75] spectroscopy experiments probed the most intense 0-0 peak at a narrow wavelength range of $\sim$ 4.0 and 23.0 nm, respectively. The entire $\widetilde{B}$ band from two-states ($\widetilde{A}$ - $\widetilde{B}$) plus 10 modes (solid line) and six-states plus 31 modes (dashed line) dynamical calculations (cf., Table 4. 10) is shown in panel b of Figure 4. 16. It can be seen

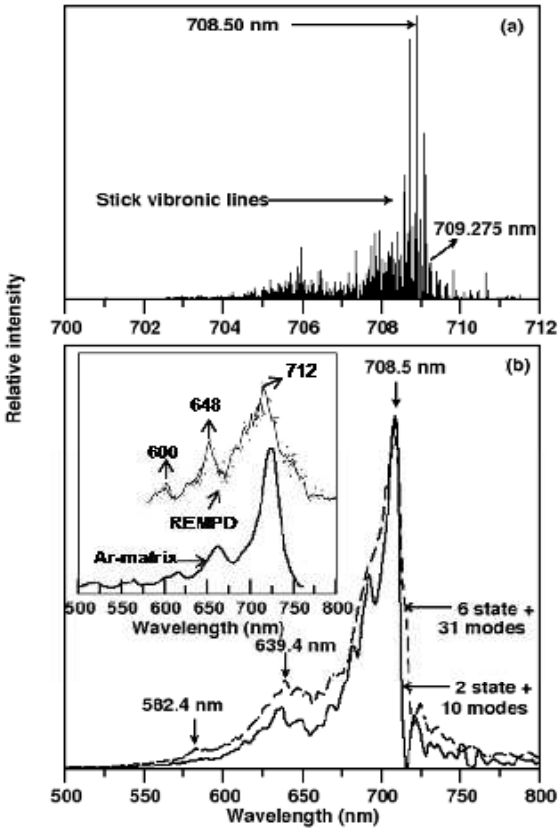

Figure 4.16: The $\widetilde{B}$ band of An^+ . Intensity in arbitrary units is plotted as a function of wavelength in nanometer. Panel (a): The theoretical stick spectrum is obtained by considering the coupling between the $\widetilde{A}$ and $\widetilde{B}$ states (see text for details). Panel (b): The complete $\widetilde{B}$ band obtained from the two-states plus 10 modes (solid line) and six-states plus 31 modes (dashed line) studies is shown. The REMPD ([85]) and Ar-matrix ([71]) spectroscopy results are presented in the inset. The numerical details of the theoretical spectra are given in Table 4. 10.

that both results agree extremely well with each other. Expectedly, the six-states results are more diffuse and confirms an increase of vibronic line density arising from the non-adiabatic coupling to the higher excited states of An^+ . It is intriguing to note that the third peak at $\sim$ 582.4 nm is absent in the two-states results, whereas it appears in the six-states results. Further confirmation of this peak emerges from the REMPD [85] and Ar-matrix [71] spectra shown in the inset of panel b. These two spectra additionally confirm the energy range of the entire $\widetilde{B}$ band. The shift of the spectral lines to higher wavelength in these experimental spectra perhaps originates from collisions among the fragment ions or with the host matrix.

The change in the equilibrium geometry of the electronic ground state of An and An^+ is negligible (less than $\sim$ 1.0 %). This is also evidenced by the most intense 0-0 peak obtained for the $\widetilde{X}$ state of An^+ in the photoelectron spectroscopy experiments [86]. We note that the $\widetilde{X}$ and $\widetilde{B}$ state of An^+ are vertically $\sim$ 1.84 and $\sim$ 1.75 eV spaced at the ground state equilibrium geometry of the neutral and cation [74, 75], respectively. Therefore, it adds further to the fact that the equilibrium geometry of the neutral and the cation ground state remains almost unchanged and preserves the Franck-Condon Zone center from a transition either from the neutral or from the cation. After a trivial energy correction, the 0-0 peak of the $\widetilde{B}$ band can be located $\sim$ 708.5 nm relative to the An^+ $\widetilde{X}$ state. This is the most intriguing result and closely corresponds to the band location found in the spectrum of Cernis 52 [77] (at $\sim$ 708.88 nm) and HD281159 [150] (at $\sim$ 708.494 nm). With this theoretical energetic location of the 0-0 peak, the second and third one appears at $\sim$ 639.4 nm and 582.4 nm, respectively. We further note that the band at $\sim$ 708.5 nm is very asymmetric as observed in the spectrum of HD281159 [150]. The twin peak as found in the latter is masked in the convolution procedure of the theoretical spectrum of Figure. 4. 16(b). A stick line however can be found at $\sim$ 709.275 nm in the theoretical data of Figure 4. 16(a).

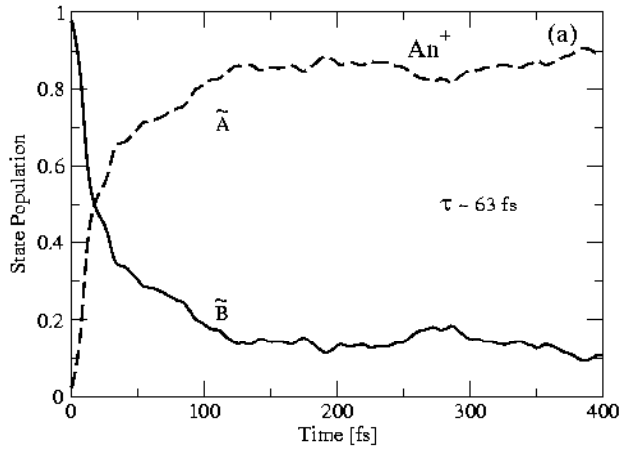

Figure 4.17: Adiabatic electronic populations during the evolution of the $\widetilde{B}$ state of An^+ in the $\widetilde{A}$ - $\widetilde{B}$ coupled state dynamics. Population curves of both the $\widetilde{A}$ (dashed line) and $\widetilde{B}$ (solid line) state are given in each panel. The numerical details of the calculations are given in Tables 4. 10.

It is certainly not worthwhile to discuss on the differences in the full width at half maximum (FWHM) of the recorded DIB [77] vis-a-vis the CRD [75] results, as they span a narrow energy range of the entire 0-0 peak. Rather, we attempted to estimate the decay of the (adiabatic) $\widetilde{B}$ state of An^+ within the viable two-states and ten modes model. Understandably, starting from a diabatic electronic Hamiltonian it requires further computationally intensive matrix diagonalization to calculate the eigenvector matrix to arrive at the adiabatic representation. As admitted before that such an exercise with the six-states model is out of the scope of the computer hardware. Rather, given the agreement shown above, we considered the most important $\widetilde{A}$ - $\widetilde{B}$ CIs to estimate this quantity (cf., Table 4.8). Most importantly, they are the ones immediately drive the WP prepared on the $\widetilde{B}$ state to undergo internal conversion. The results are shown in panel a of Figure 4.17. The initial fast depletion of population through $\widetilde{A}$ - $\widetilde{B}$ CIs relates to a decay rate of $\sim$ 63 fs of the $\widetilde{B}$ state. This decay rate corresponds to a spectral

envelope of $\sim$ 4.27 nm of FWHM Lorentzian function. We note that this is the second most important and natural result that provides an estimate of the width of the anthracene DIB.

4.5 Summary and Outlook

A detailed theoretical study of the nuclear dynamics of An^+ in their lowest six coupled electronic states is presented in this chapter. Topography of energetically lowest six electronic states of An^+ is investigated by performing detailed *ab initio* quantum chemistry calculations. The adiabatic electronic structure data are critically analyzed and numerous conical intersections among the electronic states are established. Diabatic model Hamiltonians are developed with the aid of the calculated adiabatic electronic energies and symmetry selection rules in order to treat the nuclear dynamics in the coupled manifold of six electronic states of An^+ . The results obtained from both reduced dimensional and full dimensional studies are presented and discussed in relation to the recent observations by the stellar and laboratory spectroscopists. In the full dimensional study 31 vibrational degrees of freedom are found to be relevant in the nuclear dynamics of An^+ .

In summary, excellent synergism of the spectral features of the An^+ obtained from the present first principles theoretical studies with those recently recorded by the astronomers and also by laboratory spectroscopists eloquently demonstrates that the An^+ can be the potential DIB carriers and the electron-nuclear coupling plays a decisive role in the dynamics of their low-lying excited electronic states. The detail analysis of the results also provides the mechanism of photostability of these cations against strong UV absorption from young stars. This study is the first of its kind and makes an affirmative contribution to the PAH hypothesis in interstellar physics and chemistry and opens the doorway to further research on more complex systems recently detected in a planetary Nebula by the astronomers

[154]. Finally, it is gratifying to state that detection of specific PAHs would help in identifying biogenic compounds like amino acids and would possibly provide a clue towards the origin of life in the early universe.

Chapter 5

Quantum dynamics through conical intersections: The Jahn-Teller and pseudo-Jahn-Teller effects in barrelene radical cation

5.1 Introduction

The static and dynamic aspects of JT and PJT interactions of the ground ($\widetilde{X}^2A_2'$) and first three excited electronic states ($\widetilde{A}^2E'$, $\widetilde{B}^2E''$ and $\widetilde{C}^2A_1'$) of bicyclo-[2,2,2]-octatriene (barrelene) radical cation(Bl^+) is theoretically investigated in this chapter. This belongs to the well-known $(E + A) \otimes e$ JT-PJT class of compounds as described by the symmetry of the electronic states and the molecular point group (D_{3h}). The JT effects in the $\widetilde{A}$ and $\widetilde{B}$ electronic state and the PJT coupling between the $\widetilde{B}$ and $\widetilde{C}$ electronic states of Bl^+ are found very strong. These complex interactions lead to a complex and diffuse structure of the ob-

served vibronic bands of this cation. The equilibrium geometry of the electronic ground state of neutral barrelene (Bl), its chemical bonding and the photophysics and photochemistry have drawn considerable attention of organic chemists as well as theoretical chemists. Bl is a highly strained and possesses a rigid molecular structure. Its structure defines a unique model system to study and understand the "through space" interaction [155] and "through bond" interaction. The interactions between its π-molecular orbitals are connected "through space" interaction [155] and the interactions of its pseudo-σ-molecular orbitals are designated as the "through bond" interaction in this molecule. Therefore, the consequences of these interactions in the photophysics and photochemistry of Bl^+ is examined here in details. We find that the vibronic interactions among lowest four electronic states play pivotal role in shaping up the overall band structures of Bl^+ . Understandably, a full quantum mechanical treatment of the problem is highly cumbersome and can not be carried out within the capability of modern computational resources. We therefore, critically examined various reduced dimensional theoretical models and considered the most relevant electronic and nuclear degrees of freedom to arrive at the final results given in this chapter.

The equilibrium geometry of both Bl and Bl^+ possesses D_{3h} point group symmetry. The ionization of an electron from the first four occupied molecular orbitals (MOs) of symmetry a_2', e', e'' and a_1' generates the ground ($\widetilde{X}^2A_2'$) and first three excited ($\widetilde{A}^2E'$, $\widetilde{B}^2E''$ and $\widetilde{C}^2A_1'$) electronic states of Bl^+. These MOs are shown in Figure 5.1. The highest occupied molecular orbital and one of the component of HOMO-1 are of π-type. The nature of the one of the component of HOMO-2 and HOMO-3 are of σ type.

The forty two vibrational modes of Bl decompose into $6a_1' + a_2' + 7e' + 2a_1'' + 5a_2'' + 7e''$ irreducible representations of the D_{3h} symmetry point group. The symmetrized direct product of two E' or E'' representations in the D_{3h} point

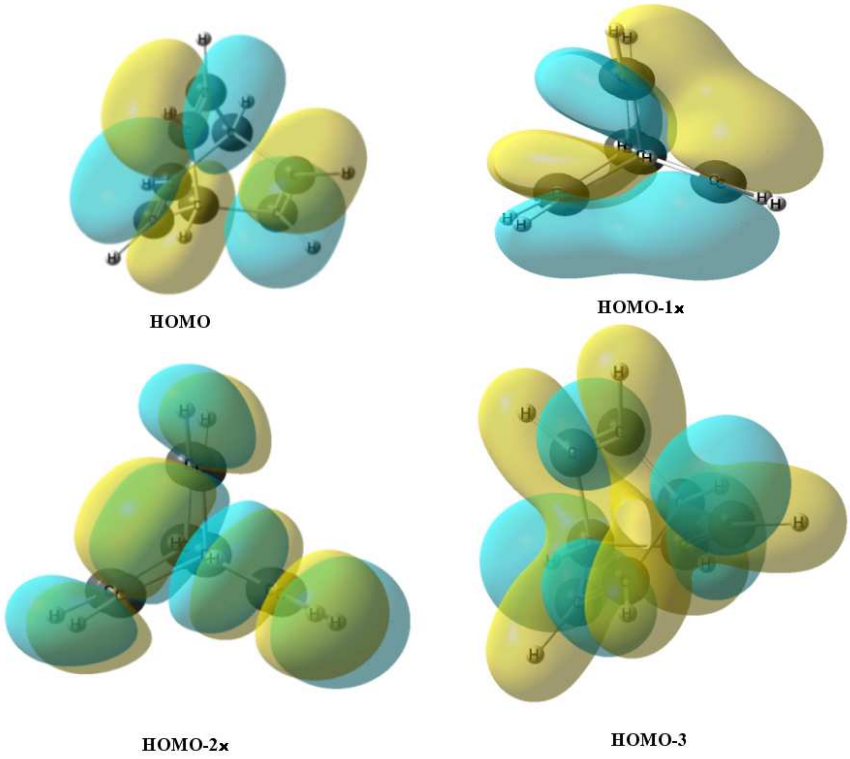

Figure 5.1: The schematic diagram of the canonical molecular orbitals of barrelene molecule.

group in first-order yields [109],

$$(E')^2 = (E'')^2 = a_1' + e'. \tag{5.1}$$

Similarly, the direct product of E' or E'' and A_1' or A_2' electronic states in the D_{3h} symmetry point group yields

$$\begin{aligned} A_2' \otimes A_1' &= A_2' \\ E' \otimes A_1' &= e' \\ E' \otimes A_2' &= e' \\ E' \otimes E'' &= a_1'' + a_2'' + e'' \end{aligned} \tag{5.2}$$

The symmetry selection rules stated above implies that the degenerate e' vibrational modes can split the degeneracy of the E' and E'' electronic manifold and can lead to $(E \otimes e)$-JT effects. The same vibrational modes can also cause PJT coupling between the $\widetilde{X}$ - $\widetilde{A}$ and $\widetilde{A}$ - $\widetilde{C}$ electronic states. The e'' vibrational modes are the PJT active modes between $\widetilde{X}$ - $\widetilde{B}$, $\widetilde{A}$ - $\widetilde{B}$ and $\widetilde{B}$ - $\widetilde{C}$ electronic states. In contrast, the totally symmetric a_1' vibrational modes restore the degeneracy of the degenerate electronic state. The vibrational mode of symmetry a_2' can coupled the $\widetilde{X}$ and $\widetilde{C}$ electronic states.

The photoelectron spectrum [156] of Bl recorded by Haselbach *et al.* within binding energy range of 7 eV to 20 eV is reproduced in Figure 5.2. It can be seen from Figure 5.2 that the first vibronic band is well resolved and the spacing between the successive peaks is ~ 570 cm^{-1}. The second vibronic band exhibits a bimodal shape and the energy spacing between the two maxima of this profile is ~ 0.30 eV. Strong excitation of vibrational mode of frequency ~ 420 cm^{-1} is observed in this band. This bears the signature of strong JT interactions in this state. The first two vibronic bands (discussed above) originate from the ionization of π-type MOs (cf., HOMO and HOMO-1 of Figure 5.1) of Bl. The

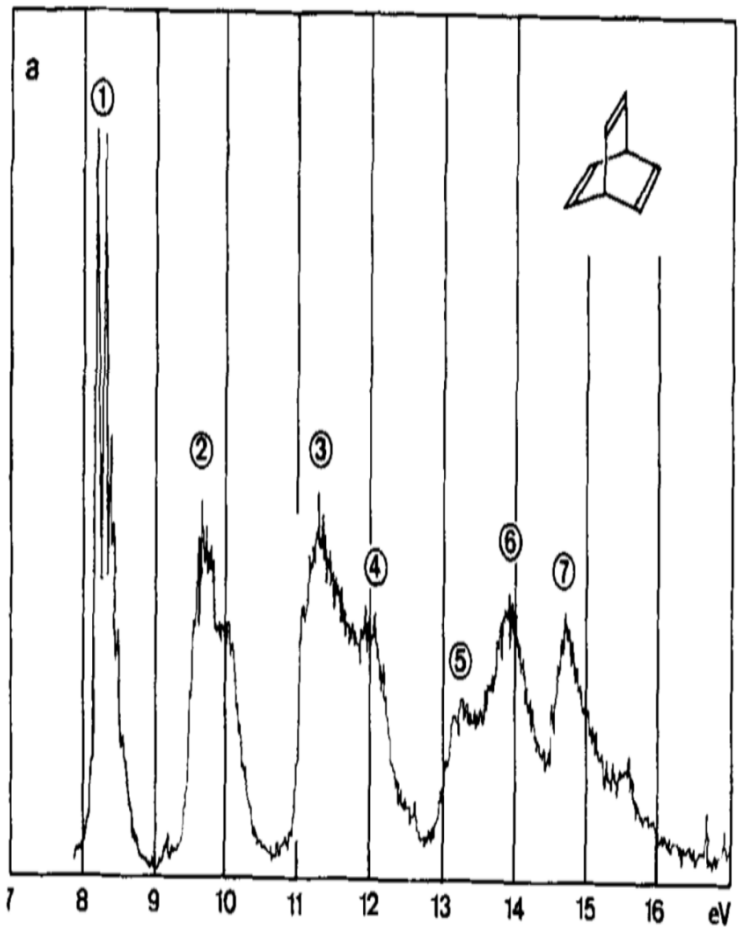

Figure 5.2: The photoelectron spectrum of barrelene

third photoelectron band is broad and highly diffuse and the fourth vibronic band is also quite broad. The third and fourth vibronic bands are produced from the ionization of σ types of MOs (cf., HOMO-2 and HOMO-3 of Figure 5.1) of Bl. The third and fourth bands are also highly overlapping. This suggests that strong PJT interactions between the $\widetilde{B}$ and $\widetilde{C}$ electronic states of Bl^+ .

In the following a model diabatic vibronic Hamiltonian is constructed to study the nuclear dynamics within the coupled manifold of $\widetilde{X}$ -$\widetilde{A}$ -$\widetilde{B}$ -$\widetilde{C}$ electronic states of Bl^+ . Extensive *ab initio* calculations have been performed to obtained the parameters of this Hamiltonian. The quantum dynamical observables are calculated by solving the time-independent as well as time-dependent Schrödinger equation. In the time-independent case, Lanczos algorithm [119] is used to diagonalize the Hamiltonian matrix expressed in the basis of harmonic oscillator functions. The diagonal elements of the resulting eigenvalue matrix yield the location of the vibronic energy levels and the relative intensities are obtained from the squared first component of the Lanczos eigenvectors. This matrix diagonalization approach becomes computationally very expensive and often intractable for systems with large number of electronic and vibrational degrees of freedom. The wave packet propagation approach within the multi-configuration time-dependent Hartree [121] scheme has emerged as an alternative tool for such situations. The JT stabilization energy for $\widetilde{A}$ electronic state is found $\sim$ 0.30 eV from the photoelectron spectroscopy experiment [156] which is in quite good accord with the theoretically calculated value of $\sim$ 0.25 eV for the same. The final theoretical results are compared with the experimental results and very strong JT and PJT interactions in the ground and excited electronic states of Bl^+ is established.

Table 5.1: Optimized (MP2/cc-pVDZ) geometry parameters of the equilibrium minimum configuration of the electronic ground state of Bl.

parameters	Present results	Experimental [157] data
$C = C$ Å	1.349	1.335
$C - C$ Å	1.537	1.538
$C - H$ Å	1.093	1.087
$C - C = C$ (deg)	112.99	112.9
$C = C - H$ (deg)	125.4	125.4
$C - C - C$ (deg)	105.7	105.9

5.2 Equilibrium structure and normal modes of vibration of Bl and adiabatic electronic energies of Bl^+

The equilibrium geometry of the ground electronic state of Bl is optimized at the second-order Möller-Plesset perturbation level of theory using Dunning's polarized valence double-zeta basis set [112] utilizing the Gaussian 03 program package [134]. The optimized geometry parameters of the equilibrium ground electronic state of Bl are compared with the gas electron diffraction experimental [157] data available in Table 5.1. It can be seen from the latter that the present theoretical results are in good accord with the experimental data [157]. By diagonalizing the *ab initio* force constant matrix of this optimized equilibrium geometry, the harmonic vibrational frequencies ω_i are obtained. These vibrational frequencies of Bl are compared with their fundamental values extracted from the gas phase experimental data [158] in Table 5.2. The symmetry and description of these vibrational modes are also given in this table.

Table 5. 2: Symmetry, frequency and description of the vibrational modes of electronic ground state of Bl

Symmetry	Mode	Vibrational Frequency (in cm^{-1})		Description	Normal displacement coordinate
		Theory	Experiment		
a_1'	ν_1	3270	3072	C-H stretching	Q_1
	ν_2	3171	2985	C-H stretching	Q_2
	ν_3	1669	1624	C=C stretching	Q_3
	ν_4	1138	1128	Olefin C-H bending	Q_4
	ν_5	898	870	C-C-C angle bending	Q_5
	ν_6	646	640	Ring deformation	Q_6
a_1''	ν_7	885		out of plane C-H bending	Q_7
	ν_8	450		ring deformation	Q_8
a_2'	ν_9	601		out of plane olefin C-H bending	Q_9
a_2''	ν_{10}	3243	3086	C-H stretching	Q_{10}
	ν_{11}	3168	2998	bridgehead C-H stretching	Q_{11}
	ν_{12}	1351	1338	butterfly C-H bending	Q_{12}
	ν_{13}	1014	1020	bridgehead C-C-C angle bending	Q_{13}
	ν_{14}	838	812	in plane olefin C-H bending	Q_{14}
e'	ν_{15}	3266	3086	C-H stretching	Q_{15x}, Q_{15y}
	ν_{16}	1612	1583	C=C stretching	Q_{16x}, Q_{16y}
	ν_{17}	1246	1218	bridgehead C-H bending	Q_{17x}, Q_{17y}
	ν_{18}	1088	1084	in plane C-H bending	Q_{18x}, Q_{18y}
	ν_{19}	936	900	C-C-C angle bending	Q_{19x}, Q_{19y}
	ν_{20}	702	697	out of plane C-H bending	Q_{20x}, Q_{20y}
	ν_{21}	422	411	framework deformation	Q_{21x}, Q_{21y}
e''	ν_{22}	3241	3072	C-H stretching	Q_{22x}, Q_{22y}
	ν_{23}	1302	1258	bridgehead C-H bending	Q_{23x}, Q_{23y}
	ν_{24}	1280	1228	bridgehead C-H bending	Q_{24x}, Q_{24y}
	ν_{25}	998	1128	olefin C-H in plane bending	Q_{25x}, Q_{25y}
	ν_{26}	899	910	olefin C-H out of plane bending	Q_{26x}, Q_{26y}
	ν_{27}	678	684	olefin C-H out of plane bending	Q_{27x}, Q_{27y}
	ν_{28}	487	485	ring deformation	Q_{28x}, Q_{28y}

The normal coordinates (Q_i) of these vibrational modes are calculated by using the eigenvectors of the force constant matrix.

In order to obtain the coupling parameter of the model diabatic vibronic Hamiltonian we have performed direct calculations of vertical ionization energies (VIE) of Bl by the outer valence Green's function method [113] employing the cc-pVDZ basis set. The VIEs are calculated along the normal displacement coordinates Q_i ($i = 1$ - 42) = $\pm$ 0.10, $\pm$ 0.25 ($\pm$0.25) $\pm$ 1.50 of the vibrational modes of Bl. These VIEs are then equated with the adiabatic potential energies (relative to the energy of the electronic ground state of neutral Bl) of the electronic states of Bl^+ .

5.3 The Vibronic coupling model

The $\widetilde{X}$ -$\widetilde{A}$, $\widetilde{A}$ -$\widetilde{B}$ and $\widetilde{B}$ -$\widetilde{C}$ electronic states of Bl^+ are vertically $\sim$ 1.53, $\sim$ 1.90 and $\sim$ 0.26 eV apart respectively, at the equilibrium geometry of the reference state ($\mathbf{Q}$ =0). Because of their close proximity a total of six electronic states and most relevant vibrational modes are considered for the nuclear dynamics simulations. Five Condon active modes ($\nu_1 - \nu_5$), six JT active as well as PJT active vibrational modes ($\nu_{15} - \nu_{20}$), interstate coupling mode of symmetry a_1'' (ν_{12}) and PJT active vibrational modes ($\nu_{22} - \nu_{27}$) of symmetry e'' are found to be relevant in dynamical simulations. The model diabatic Hamiltonian is written in terms of dimensionless normal coordinates (as introduced above) of the reference electronic ground state of neutral Bl. With this description the diabatic vibronic Hamiltonian of the $\widetilde{X}$ -$\widetilde{A}$ -$\widetilde{B}$ -$\widetilde{C}$ coupled electronic states of Bl^+ can be written

as

$$\mathcal{H} = \mathcal{H}_0\mathbf{1_6} + \begin{pmatrix} \mathcal{W}^X & \mathcal{W}_1^{X-A} & \mathcal{W}_2^{X-A} & \mathcal{W}_1^{X-B} & \mathcal{W}_2^{X-B} & 0 \\ & \mathcal{W}_1^A & \mathcal{W}_{12}^A & 0 & 0 & \mathcal{W}_1^{A-C} \\ & & \mathcal{W}_2^A & 0 & 0 & \mathcal{W}_2^{A-C} \\ & & & \mathcal{W}_1^B & \mathcal{W}_{12}^B & \mathcal{W}_1^{B-C} \\ & & h.c. & & \mathcal{W}_2^B & \mathcal{W}_2^{B-C} \\ & & & & & \mathcal{W}^C \end{pmatrix}. \quad (5.3)$$

In Eq. (5.3) the quantity, $\mathcal{H}_0 = \mathcal{T}_N + \mathcal{V}_0$, is the unperturbed Hamiltonian (which is uncoupled from the other electronic states and assumed to be harmonic) of the reference electronic ground state of Bl with

$$\mathcal{T}_N = -\frac{1}{2}\sum_{i\ \in\ a_1',\ a_1'',\ a_2',\ a_2''} \omega_i \frac{\partial^2}{\partial Q_i^2} - \frac{1}{2}\sum_{i\ \in\ e',\ e''} \omega_i \left(\frac{\partial^2}{\partial Q_{ix}^2} + \frac{\partial^2}{\partial Q_{iy}^2}\right), \quad (5.4)$$

and

$$\mathcal{V}_0 = \frac{1}{2}\sum_{i\ \in\ a_1',\ a_1'',\ a_2',\ a_2''} \omega_i Q_i^2 + \frac{1}{2}\sum_{i\ \in\ e',\ e''} \omega_i \left(Q_{ix}^2 + Q_{iy}^2\right). \quad (5.5)$$

The nuclear kinetic and potential energy operator of this reference state is denoted as $\mathcal{T}_N$ and $\mathcal{V}_0$, respectively. The change of electronic energy upon ionization from this reference state is described by the electronic Hamiltonian matrix with elements $\mathcal{W}$ in Eq. (5.3). The diagonal elements of this matrix represent the diabatic potential energies of the electronic states and the off-diagonal elements describe the coupling between them. These elements are expanded in a Taylor series around the reference equilibrium configuration (at $\mathbf{Q}$=0) as follows

$$\mathcal{W}^{X(C)} = E_0^{X(C)} + \sum_{i\ \in\ a_1'} \kappa_i^{X(C)} Q_i + \frac{1}{2}\sum_{i\ \in\ a_1',\ a_1'',\ a_2',\ a_2''} \gamma_i^{X(C)} Q_i^2 + \frac{1}{2}\sum_{i\ \in\ e',\ e''} [\gamma_i^{X(C)}(Q_{ix}^2 + Q_{iy}^2) \quad (5.6)$$

$$\mathcal{W}_{1,2}^{A(B)} = E_0^{A(B)} + \sum_{i \in a_1'} \kappa_i^{A(B)} Q_i \pm \sum_{i \in e'} \lambda_i^{A(B)} Q_{ix} + \frac{1}{2} \sum_{i \in a_1',\, a_1'',\, a_2',\, a_2''} \gamma_i^{A(B)} Q_i^2 + \frac{1}{2} \sum_{i \in e'} [\gamma_i^{A(B)} (Q_{ix}^2 + Q_{iy}^2) \pm \eta_i^{A(B)} (Q_{ix}^2 - Q_{iy}^2)] + \frac{1}{2} \sum_{i \in e''} [\gamma_i^{A(B)} (Q_{ix}^2 + Q_{iy}^2)], \quad (5.7a)$$

$$\mathcal{W}_{12}^{A(B)} = \sum_{i \in e'} \lambda_i^{A(B)} Q_{iy} - \sum_{i \in e'} \eta_i^{A(B)} Q_{ix} Q_{iy}, \quad (5.7b)$$

$$\mathcal{W}_1^{j-k} = \sum_i \lambda_i^{j-k} Q_{ix}, \quad (5.7c)$$

$$\mathcal{W}_2^{j-k} = -\sum_i \lambda_i^{j-k} Q_{iy}, \quad (5.7d)$$

where, $(j\text{-}k) \in$ $(\widetilde{X}\text{-}\widetilde{A})$, $(\widetilde{X}\text{-}\widetilde{B})$, $(\widetilde{X}\text{-}\widetilde{C})$, $(\widetilde{A}\text{-}\widetilde{B})$, $(\widetilde{A}\text{-}\widetilde{C})$, $(\widetilde{B}\text{-}\widetilde{C})$ with, $i \in e'$, e'', a_2', e'', e', e'' respectively. The quantity E_0^j is the VIE of the j^{th} electronic state and κ_i^j is the first-order intrastate coupling parameter of the symmetric (a_1') vibrational modes in this state. The second-order intrastate coupling parameter of the vibrational modes in the j^{th} electronic state is denoted by γ_i^j. The first-order and second-order coupling parameters of JT active vibrational modes are given by the λ_i^j and η_i^j for the degenerate electronic states. The first-order PJT coupling parameter of vibrational modes Q_i between the electronic states j and k is denoted by λ_i^{j-k}.

All the coupling parameters defined above are estimated from a least squares fit of the calculated adiabatic energies (cf., Sec. 5.2) to the adiabatic form of the diabatic electronic Hamiltonian described above. These parameters are given in Tables 5.3 to 5.6.

Table 5. 3: *Ab initio* calculated linear and quadratic coupling parameters of the symmetric vibrational modes in the $\widetilde{X}^2A_2'$, $\widetilde{A}^2E'$, $\widetilde{B}^2E''$ and $\widetilde{C}^2A_1'$ electronic states of Bl^+. The vertical ionization energies (E_0^j) of these electronic states at the reference equilibrium geometry are also given in the table. All quantities are in eV. The dimensionless Poisson parameters $(\kappa_i/\omega_i)^2/2$ are given in the parentheses.

Mode	κ_i^X	γ_i^X	κ_i^A	γ_i^A	κ_i^B	γ_i^B	κ_i^C	γ_i^C
(symmetry)	$\widetilde{X}^2A_2'$		$\widetilde{A}^2E'$		$\widetilde{B}^2E''$		$\widetilde{C}^2A_1'$	
$\nu_1(a_1')$	0.0096	0.0047	0.0132	0.0034	-0.0846	-0.0016	-0.0334	-0.00001
	(0.00001)		(0.001)		(0.022)		(0.003)	
$\nu_2(a_1')$	-0.0167	0.0047	-0.0178	0.0042	0.0508	0.0253	0.1694	0.0228
	(0.001)		(0.001)		(0.008)		(0.092)	
$\nu_3(a_1')$	0.1461	-0.0260	0.1115	0.0041	-0.2295	-0.0096	0.1227	0.2018
	(0.249)		(0.146)		(0.615)		(0.177)	
$\nu_4(a_1')$	0.0534	0.0050	0.0816	0.0024	0.1266	-0.0160	-0.1165	0.0466
	(0.072)		(0.169)		(0.405)		(0.345)	
$\nu_5(a_1')$	0.0173	-0.0012	-0.0401	-0.0008	-0.0881	-0.0009	0.0417	-0.0080
	(0.012)		(0.065)		(0.313)		(0.071)	
$\nu_6(a_1')$	-0.1044	-0.0036	-0.0357	-0.0036	0.0287	-0.0134	0.0662	0.0142
	(0.851)		(0.099)		(0.064)		(0.342)	
E_0^X	7.93558							
E_0^A	9.46779							
E_0^B	11.40068							
E_0^C	11.66064							

Table 5. 4: *Ab initio* calculated linear and quadratic coupling parameters of the degenerate e' vibrational mode in $\widetilde{X}^2A_2'$, $\widetilde{A}^2E'$, $\widetilde{B}^2E''$ and $\widetilde{C}^2A_1'$ electronic states of Bl^+. All quantities are in eV. The dimensionless Poisson parameters $(\lambda_i/\omega_i)^2/2$ are given in the parentheses.

Mode (symmetry)	γ_i^X $\widetilde{X}^2A_2'$	λ_i^A	γ_i^A $\widetilde{A}^2E'$	η_i^A	λ_i^B $\widetilde{B}^2E''$	γ_i^B	η_i^B	γ_i^C $\widetilde{C}^2A_1'$
$\nu_{15}(e')$	0.0055	0.0019	0.0036	-0.0001	0.0754	-0.0052	0.0008	-0.0016
		(0.00001)			(0.017)			
$\nu_{16}(e')$	-0.03222	0.1175	0.0276	-0.0270	0.0993	-0.0108	-0.0063	-0.0740
		(0.174)		0.0020	(0.123)		0.00086	
$\nu_{17}(e')$	0.0044	0.0712	-0.00001	0.00036	0.0602	-0.0310	0.0292	-0.0844
		(0.110)			(0.076)		0.002	
$\nu_{18}(e')$	0.0064	0.0127	0.0058	-0.00098	0.0779	-0.0215	0.0137	-0.0252
		(0.005)			(0.176)		0.0018	
$\nu_{19}(e')$	0.0003	0.0850	-0.0108	-0.00024	0.09014	-0.0102	-0.0073	-0.0180
		(0.269)			(0.301)			
$\nu_{20}(e')$	0.0167	0.0192	0.0001	0.0036	0.0943	-0.0240	0.0101	0.0175
		(0.024)		0.0004	(0.584)			
$\nu_{21}(e')$	-0.0229	0.1389	0.0087	-0.0019	0.0331	-0.0060	-0.0004	-0.00196
		(3.570)			(0.201)			

A careful examination of the coupling strength of the totally symmetric vibrational modes of Bl^+ given in Table 5.3 suggests excitations of the ν_6 mode in the $\widetilde{X}$ and $\widetilde{C}$ and ν_3 and ν_4 modes in $\widetilde{A}$ and $\widetilde{B}$ electronic states. The mode ν_3 in the $\widetilde{X}$ and $\widetilde{B}$ and ν_4 in $\widetilde{B}$ and the $\widetilde{C}$ states are also expected to be excited. The coupling strength of the ν_3 mode is moderate in all other electronic states. The vibrational mode ν_5 can be expected to be excited in the $\widetilde{B}$ band of Bl^+ . The degenerate ν_{21} is a strong JT coupling mode in the $\widetilde{A}$ state. The coupling strength of the remaining e' modes (cf., Table 5.4) is moderate or weak in this state. The JT coupling strength of all e' vibrational modes is moderate or weak in the $\widetilde{B}$ state. It is therefore expected that the JT coupling effects will be far more stronger on the vibronic structure of the $\widetilde{A}$ state compared to that of the $\widetilde{B}$ state. The second-order coupling parameters of the a_1'', a_2', a_2'' and e'' vibrational modes of the Hamiltonian (cf., Eq. (5.3)) are given in Table 5.5.

Among the interstate coupling modes of Bl^+ listed in Table 5.6, the strongest coupling is caused by mode ν_{21} in $\widetilde{X}$ -$\widetilde{A}$, ν_{27} in $\widetilde{X}$ -$\widetilde{B}$, ν_{20} in $\widetilde{A}$ -$\widetilde{C}$ and ν_{23} in $\widetilde{B}$ -$\widetilde{C}$ electronic state. The $\widetilde{A}$ state is strongly coupled by the vibrational modes ν_7 and ν_8 of symmetry a_1'' and the modes ν_{25} and ν_{28} of symmetry e'' with the $\widetilde{B}$ electronic state.

5.4 Results and Discussion

5.4.1 The topography of the adiabatic potential energy surfaces

The topography of the adiabatic potential energy surfaces of the $\widetilde{X}$, $\widetilde{A}$, $\widetilde{B}$ and $\widetilde{C}$ electronic states of Bl^+ and the stationary points located on them employing the vibronic coupling model introduced above are discussed here. The adiabatic potential energies are obtained by diagonalizing the electronic matrix Hamiltonian, $V_0 + \Delta\mathcal{H}$, given in Eqn. 5.3. One dimensional cuts of the multi-dimensional po-

Table 5. 5: *Ab initio* calculated second-order coupling parameters of the a_1'', a_2',a_2'' and e'' vibrational modes in the $\widetilde{X}^2A_2'$, $\widetilde{A}^2E'$, $\widetilde{B}^2E''$ and $\widetilde{C}^2A_1'$ electronic states of Bl^+ .

Mode (symmetry)	γ_i^X $\widetilde{X}^2A_2'$	γ_i^A $\widetilde{A}^2E'$	γ_i^B $\widetilde{B}^2E''$	γ_i^C $\widetilde{C}^2A_1'$
a_1''				
ν_7	0.0172	-0.0197	0.00528	-0.0122
ν_8	-0.02125	-0.0163	0.002486	-0.010
a_2'				
ν_9	0.0270	0.0072	-0.0208	0.0106
a_2''				
ν_{10}	0.00496	0.00406	-0.00724	-0.00736
ν_{11}	0.00492	0.00222	0.00514	-0.0562
ν_{12}	0.00128	-0.00892	-0.070	-0.0350
ν_{13}	-0.00188	-0.00454	-0.02962	-0.1002
ν_{14}	-0.00498	-0.00444	-0.00546	-0.01230
e''				
ν_{22}	0.00536	0.0044	-0.0324	0.0624
ν_{23}	0.00144	-0.0226	-0.1462	0.2506
ν_{24}	0.00452	0.0028	-0.0597	0.0383
ν_{25}	0.00066	-0.0165	0.00488	-0.00186
ν_{26}	0.0058	0.0032	-0.0159	-0.0098
ν_{27}	-0.0092	-0.0256	-0.0263	0.0740
ν_{28}	-0.0276	-0.0111	-0.0014	0.0084

Table 5. 6: Linear interstate coupling parameters of the e', a_1'', a_2'' and e'' vibrational modes of the Hamiltonian (cf., Eq. (5.3)). All quantities are in eV. The coupling strength of the vibrational modes is given in the parentheses.

Mode	λ_i^{X-A}	λ_i^{X-B}	λ_i^{A-B}	λ_i^{A-C}	λ_i^{B-C}
e'					
ν_{15}	—	—	—	—	—
ν_{16}	0.1529 (0.293)	—	—	—	—
ν_{17}	—	—	—	—	—
ν_{18}	—	—	—	—	—
ν_{19}	—	—	—	—	—
ν_{20}	—	—	—	0.0982 (0.637)	—
ν_{21}	0.1098 (2.20)	—	—	—	—
a_1''					
ν_7	—	—	0.1106 (0.508)	—	—
ν_8	—	—	0.0960 (1.477)	—	—
a_2''					
ν_{10}	—	—	—	—	—
ν_{11}	—	—	0.0201 (0.001)	—	—
ν_{12}	—	—	—	—	—
ν_{13}	—	—	—	—	—
ν_{14}	—	—	—	—	—
e''					
ν_{22}	—	—	—	—-	0.0867 (0.023)
ν_{23}	—	—	—	—-	0.2293 (1.010)
ν_{24}	—	—	—	—-	0.0908 (0.164)
ν_{25}	—	0.0606 (0.120)	0.1023 (0.342)	—-	—
ν_{26}	—	—	—	—-	0.0201 (0.016)
ν_{27}	—	—	—	—-	0.0907 (0.585)
ν_{28}	—	0.1496 (3.077)	0.0678 (0.632)	—-	0.0258 (0.092)

tential energy hyper-surfaces of the $\widetilde{X}$, $\widetilde{A}$, $\widetilde{B}$ and $\widetilde{C}$ electronic states of Bl^+ along the totally symmetric a_1' vibrational modes and the JT active e' vibrational modes are shown in Figures 5.3 and 5.4, respectively. The adiabatic potential energies in the above figures are plotted along the dimensionless normal displacement coordinates of the vibrational modes. The solid curves in the figures represent the potential energies obtained from the constructed vibronic coupling model in Sec. 5.3 and the points superimposed on them represent the computed *ab initio* data discussed in Sec. 5.2. It can be seen that the model reproduces the *ab initio* data extremely well. This comparison is most valuable in the vicinity of various curve crossings in the above figures. These curve crossings develop into conical intersections in multi-dimensions and these intersections are the mechanistic bottleneck for the nuclear motion in a given electronic state. The tuning modes (a_1') do not split the electronic degeneracy when the molecule is distorted along them. They can only modulate the energy gap between the electronic states. It is seen that there is no curve crossing between the $\widetilde{X}$ and $\widetilde{A}$ electronic states within the FC region (around $Q = 0$) but the crossing between the $\widetilde{B}$ and $\widetilde{C}$ electronic states are immediately seen along ν_2, ν_3, ν_4 and ν_5 vibrational modes. Thus, one can expect that there may be strong PJT coupling between these electronic states and these modes can play crucial role in the nuclear dynamics in the $\widetilde{B}$ and $\widetilde{C}$ electronic states of Bl^+ . When the molecule is distorted along any of the components of degenerate e' vibrational modes, the electronic degeneracy is lifted. This is obvious from the Figure 5.4 the JT splitting can be seen to be larger along ν_{16}, ν_{17}, ν_{19} and ν_{21} vibrational modes in the $\widetilde{A}$ electronic state and is quite smaller along ν_{15}, ν_{18} and ν_{20} vibrational modes. The JT splitting is quite large along all the e' vibrational modes (except ν_{15}) in the $\widetilde{B}$ electronic state of Bl^+ . Multiple curve crossing between $\widetilde{B}$ and $\widetilde{C}$ electronic states along ν_{16}, ν_{17}, ν_{18} and ν_{19} vibrational modes can also be seen from the figure. The PJT coupling among these states is expected to be very strong. Within a linear vibronic coupling scheme the location of the energetic minimum of the seam of PJT CIs between $\widetilde{X}$ -$\widetilde{A}$, $\widetilde{X}$ -$\widetilde{B}$ and

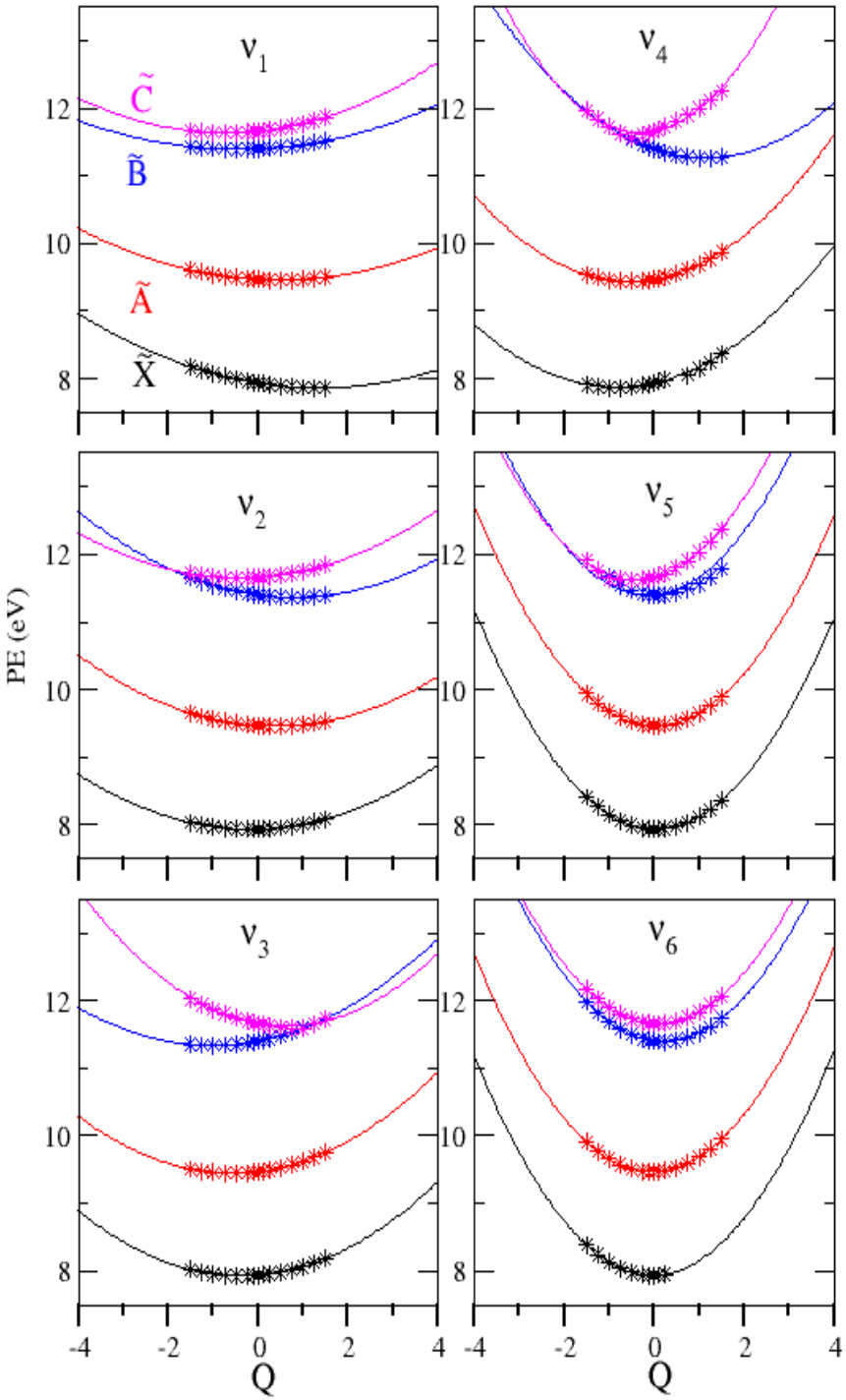

Figure 5.3: Adiabatic potential energies of the $\widetilde{X}$, $\widetilde{A}$, $\widetilde{B}$ and $\widetilde{C}$ electronic states of Bl^+ along the totally symmetric vibrational modes. The energy values obtained from the present theoretical model and *ab initio* quantum chemistry calculations are shown by the lines and points, respectively.

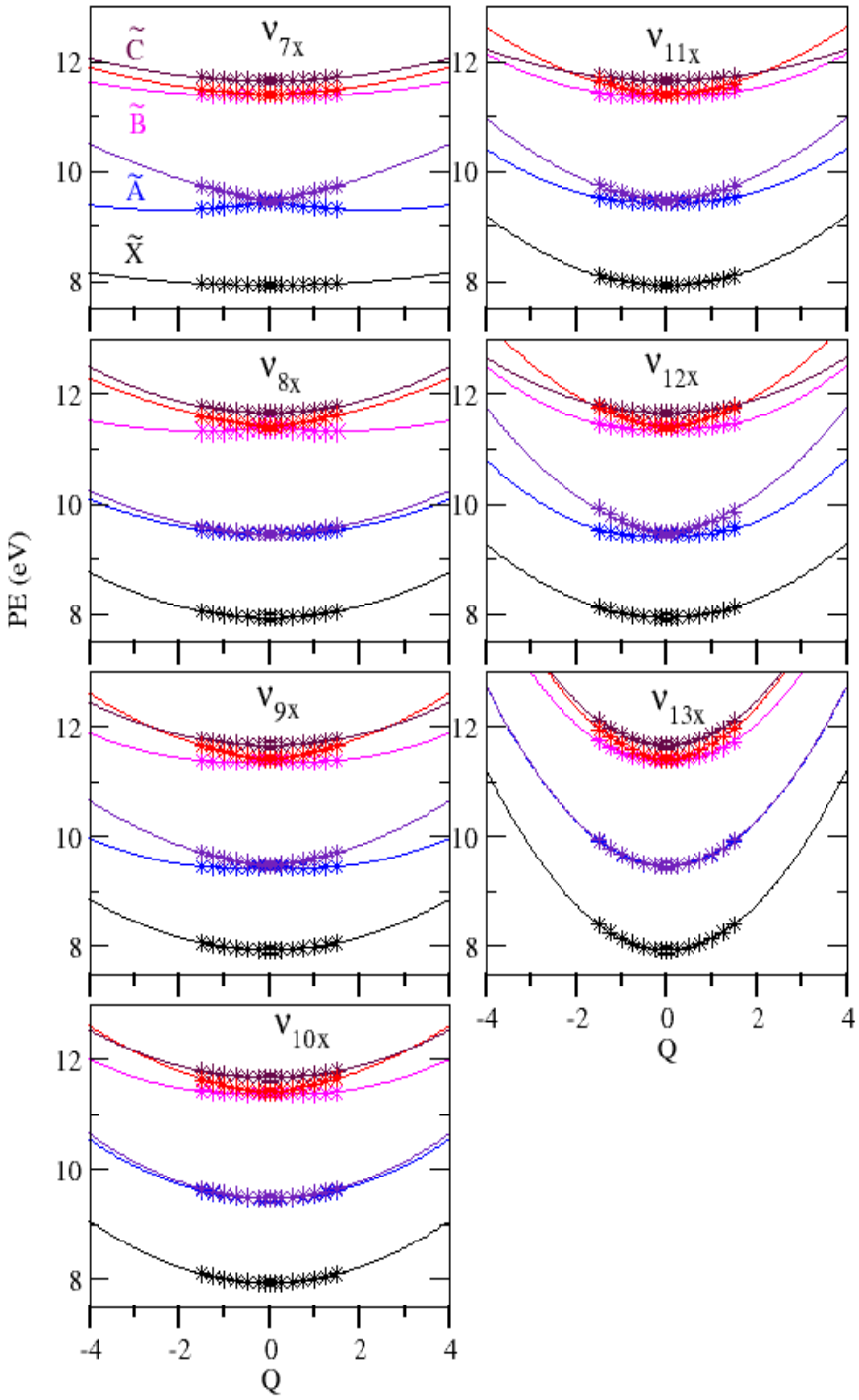

Figure 5.4: Adiabatic potential energies of the $\widetilde{X}$, $\widetilde{A}$, $\widetilde{B}$ and $\widetilde{C}$ electronic states of Bl^+ along the JT active e' vibrational modes. The energy values obtained from the present theoretical model and *ab initio* quantum chemistry calculations are shown by the lines and points, respectively.

$\widetilde{X}$ -$\widetilde{C}$ electronic states of Bl^+ are found at $\sim$ 21.33 eV, 24.66 eV and 19.97 eV, respectively. These CIs occurs at very high energies and are not expected to play any role in the nuclear dynamics in the energy range considered here. The locus of the electronic degeneracy of the $\widetilde{A}$ and $\widetilde{B}$ electronic states along the totally symmetric a_1' vibrational modes defines the seam of CIs within these electronic states, occurring at the D_{3h} symmetry configuration of Bl^+ . The energetic minimum on this seam in the $\widetilde{A}$ ($\widetilde{B}$) electronic state is found at $\sim$ 9.40 eV (11.15 eV), for Q_1= -0.03(0.21), Q_2= 0.05(-0.12), Q_3= -0.53 (1.16), Q_4= -0.57 (-1.01), Q_5= 0.36 (0.80) and Q_6= 0.47 (-0.43). It is shown above that the electronic degeneracy is lifted when Bl^+ is distorted along any of the JT active vibrational mode of e$'$ symmetry. Within a linear coupling scheme the lower adiabatic sheet of the JT split surfaces develops three equivalent minima separated by three equivalent saddle points and exhibits a "Maxican hat" type of topography. When the second-order coupling parameters are considered this "Maxican hat" acquires a distorted shape. The estimated energies of the minimum and saddle point are $\sim$ 9.15 eV and $\sim$ 9.16 eV, respectively, in $\widetilde{A}$ electronic state and $\sim$ 10.94 eV and $\sim$ 10.96 eV, respectively, in the $\widetilde{B}$ electronic state. These minima (saddle points) are located at Q_{15} = 0.01(-0.005), Q_{16} = 0.52(-0.51), Q_{17} = 0.46(-0.46), Q_{18} = 0.09(-0.09), Q_{19} = 0.81(-0.81), Q_{20} = 0.22(-0.22) and Q_{21} = 2.21(2.35) in the $\widetilde{A}$ electronic state. The same are located at Q_{15} = 0.19(-0.19), Q_{16} = 0.53(-0.52), Q_{17} = 0.50(-0.48), Q_{18} = 0.70(-0.68), Q_{19} = 0.80(-0.92), Q_{20} = 1.78(-1.29) and Q_{21} = 0.71(-0.72) in the $\widetilde{B}$ electronic state. The JT stabilization energy amounts to $\sim$ 0.25 eV and $\sim$ 0.21 eV, respectively, for the $\widetilde{A}$ and $\widetilde{B}$ electronic states of Bl^+ . A twin vibronic band is observed for the $\widetilde{A}$ electronic state in the photoelectron spectroscopy experiment [156]. The separation between the two maxima of the bimodal spectral profile of $\sim$ 0.30 eV is in good accord with our theoretically calculated value of the JT stabilization of the $\widetilde{A}$ electronic state. Furthermore, the minimum of the seam of PJT CIs between the $\widetilde{A}$ - $\widetilde{B}$ and $\widetilde{A}$ - $\widetilde{C}$ occurs at $\sim$ 11.87 eV and $\sim$ 14.52 eV, respectively. The energetic minimum of the seam

of PJT CIs between $\widetilde{A}$ -$\widetilde{B}$ is located $\sim$ 0.79 eV below to the minimum of the $\widetilde{B}$ electronic manifold. Within the linear vibronic coupling scheme the location of the minimum of the seam of $\widetilde{B}$ - $\widetilde{C}$ CIs is found at $\sim$ 11.54 eV. The minimum of the $\widetilde{C}$ electronic state almost coincides with the minimum of the seam of $\widetilde{B}$ - $\widetilde{C}$ CIs (separated by 0.004 eV of energy only). The multiple CIs among these electronic states are expected to have profound effect on the nuclear dynamics of these electronic states of Bl^+ which is discussed next.

5.4.2 Dynamical Observables

The complex vibronic band structures of the first few low-lying electronic states of Bl^+ are theoretically calculated and discussed here. The precise location of the vibrational energy levels of the uncoupled electronic states are calculated by the time-independent matrix diagonalization approach using the Lanczos algorithm [23]. The vibrational energy level spectrum of the $\widetilde{X}$ state is shown in Figure 5.5. The theoretical stick spectrum is calculated using six totally symmetric vibrational modes (ν_1-ν_6) and the vibronic Hamiltonian of Eqn.5.3 excluding all interstate coupling elements. The vibrational mode ν_6 (ring deformation) form the dominant progression up to its seventh overtone level in this band. Eight distinct peaks observed in this band are $\sim$ 646 cm^{-1} spaced in energy within a linear vibronic coupling (LVC) approach. Inclusion of quadratic coupling terms reduces this spacing to 616 cm^{-1}. A value of $\sim$ 570 cm^{-1} was estimated for this spacing from the photoelectron spectroscopy experiment [156]. The second vibronic band pertinent to the degenerate $\widetilde{A}$ electronic state of Bl^+ is shown in Figures 5.6(a-c). The Hamiltonian for the uncoupled degenerate electronic state commutes along the a_1' and e' vibrational modes in absence of any bilinear coupling parameter. In this situation, two partial spectra corresponding to the a_1' and e' vibrational modes can be calculated separately and the two can be convoluted to generate the final composite energy level structure of the degenerate

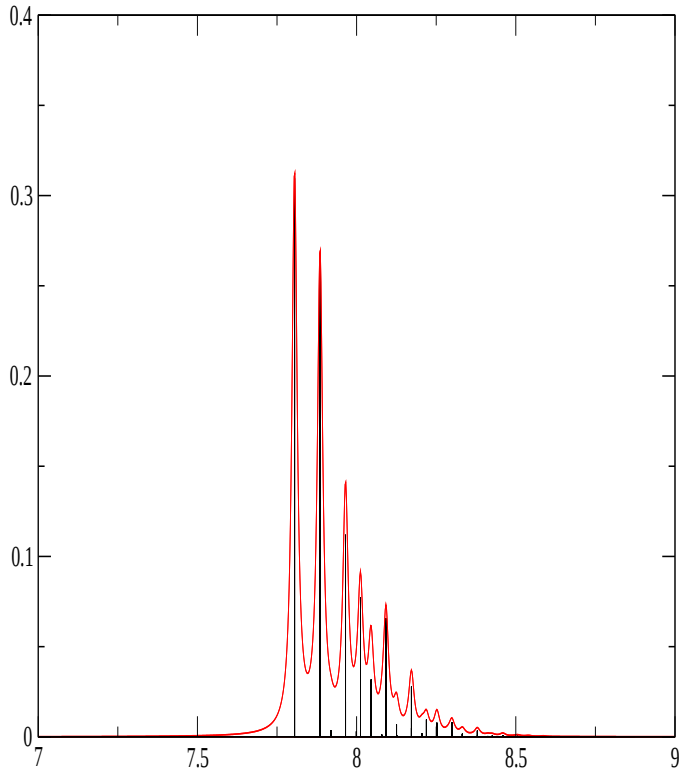

Figure 5.5: The vibrational energy level spectrum of the uncoupled $\widetilde{X}$ electronic state of Bl^{+} .

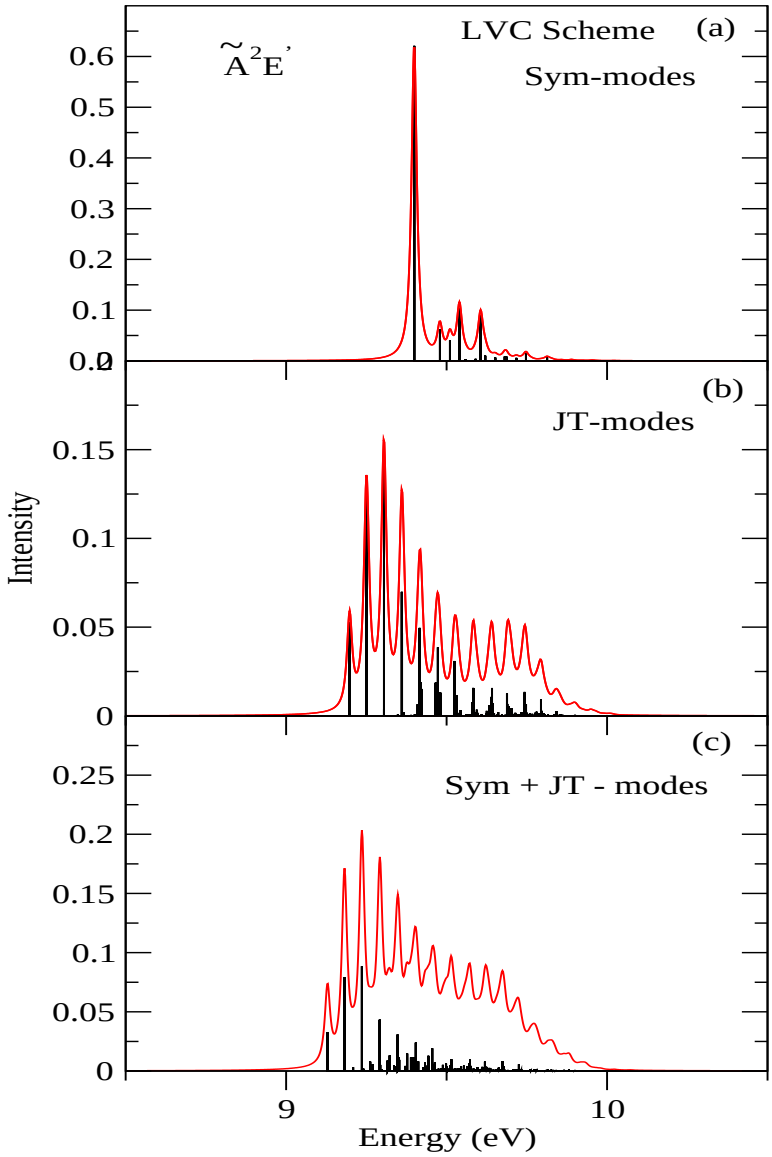

Figure 5.6: The vibronic energy level spectra of the $\widetilde{A}$ electronic states of Bl^+ obtained within a linear coupling model. The relative intensity in arbitrary units is plotted as a function of the energy of the final vibronic levels. Energy is measured relative to the equilibrium minimum of the reference state: (a) partial spectrum calculated including the six totally symmetric a_1' vibrational modes ν_1-ν_6, (b) partial spectrum for the degenerate e' vibrational modes ν_{18}-ν_{21}, and (c) the composite theoretical spectrum obtained by convoluting the above two partial spectrum.

$\widetilde{A}$ electronic state. The two partial spectra corresponding to the a_1' and e' vibrational modes thus obtained are shown in panels *a* and *b* and the final convoluted spectrum is shown in panel it c of Figure 5.6. These spectra are obtained considering a linear coupling Hamiltonian only. The symmetric mode spectrum in panel a reveals dominant progressions of ν_3, ν_4, ν_5 and ν_6 vibrational modes. The corresponding peak spacings of $\sim$ 1670 cm^{-1}, $\sim$ 1138, $\sim$ 898 and $\sim$ 645, respectively, can be estimated from this spectrum. As stated above the JT effect is strong in the $\widetilde{A}$ electronic state. In the spectrum of e$'$ vibrational mode shown in panel b the mode ν_{21} is strongly excited. The peak spacing with respect to the origin 0-0 peak of $\sim$ 427 cm^{-1} is found and it corresponds to the frequency of ν_{21} vibrational modes. A peak spacing of $\sim$ 420 cm^{-1} was estimated from the photoelectron spectroscopy experiment [156]. Similar calculation are carried out for the $\widetilde{B}$ electronic state. The resulting spectra are shown in Figures 5.7(a-c). Peak spacings of $\sim$ 1668 cm^{-1} $\sim$ 1138 and $\sim$ 897 corresponding to the excitation of ν_3, ν_4 and ν_5 vibrational modes, respectively, have been observed in the spectrum of panel *a*. Dominant progressions of ν_{17}, ν_{18}, ν_{19}, ν_{20} and ν_{21} vibrational modes are found from the partial spectrum of the e' vibrational modes (panel b). Peak spacings of $\sim$ 1269 cm^{-1}, $\sim$ 1054, $\sim$ 920, $\sim$ 686 and $\sim$ 439, respectively, corresponding to these vibrational modes (in that order) can be estimated from this spectrum. The vibrational level spectrum of the uncoupled $\widetilde{C}$ state is shown in Figure 5.8. Vibrational modes ν_3, ν_4 and ν_6 form the dominant progression in this band. Corresponding peak spacing of $\sim$ 1669 cm^{-1}, $\sim$ 1138 and $\sim$ 646 can be estimated from this spectrum. In contrast to the $\widetilde{A}$ state, both the a_1' and e$'$ vibrational modes are strongly active in the $\widetilde{B}$ state of Bl^+ . As a result, the vibronic band structure of this state is more complex and diffuse. The same can be correlated with the observed feature of the underlying potential energy surfaces and the large value of the JT stabilization energy discussed in the Sec 5.4.1. It is observed from the uncoupled state results that the first vibronic band correlates nicely with the photoelectron spectroscopy experiment but the other

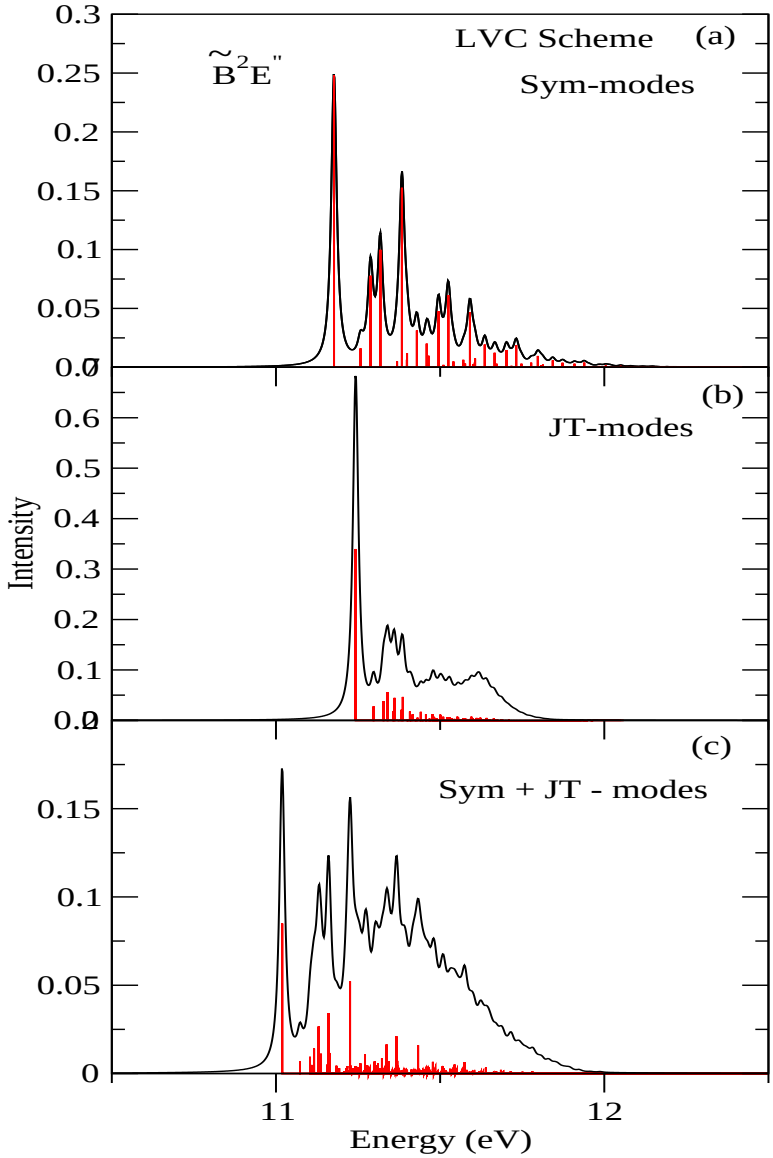

Figure 5.7: The partial spectrum and the composite spectrum of uncoupled $\widetilde{B}$ electronic state of Bl^+ . The designation of the panel are same as in Figure 5.6.

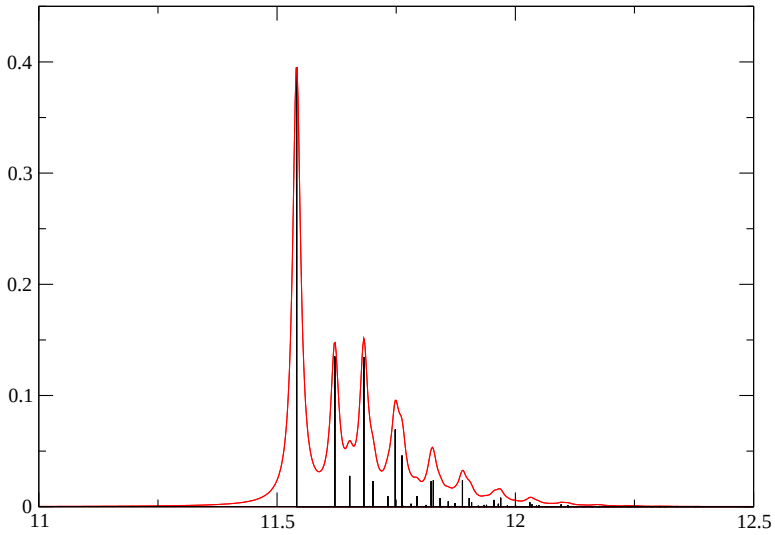

Figure 5.8: The uncoupled state vibronic spectrum of $\widetilde{C}$ electronic state of Bl^+ with LVC scheme.

three vibronic bands are far from the experimental results.

In order to describe the observed structure of these vibronic bands, it appears to be necessary to consider the interstate couplings terms of the vibronic Hamiltonian of Eq. 5.3 in the dynamical simulations. Such an exercise includes six electronic states and thirty vibrational modes in the nuclear dynamics simulations to arrive at the final results. Understandably, this exercise is beyond the capability of the matrix diagonalisation method employed above. This task is therefore attempted by the WP propagation method employing the MCTDH method [121] as used in other chapters of this thesis.

The vibronic spectrum of the $\widetilde{X}$ -$\widetilde{A}$ -$\widetilde{B}$ -$\widetilde{C}$ coupled electronic state of Bl^+ is finally calculated by including thirty relevant vibrational modes and six electronic states. Six separate calculations are carried out by launching the initial WP on each of these six electronic states. In each calculation, the WP is propagated up to 150 fs and the resulting time autocorrelation function is damped with an exponential function [exp (-t/τ_r); with τ_r = 66 fs] before Fourier transformation. This damping corresponds to convolution of spectral lines with a Lorentzian line

Table 5. 6: Number of basis functions for the primitive as well as the single particle basis used in the MCTDH calculations.

Normal modes	Primitive basis[a]	SPF basis[b] [$\widetilde{X}$, $\widetilde{A}_x$, $\widetilde{A}_y$, $\widetilde{B}_x$, $\widetilde{B}_y$, $\widetilde{C}$]
(ν_1,ν_{15x},ν_{15y},ν_{22x},ν_{22y})	(9, 9, 9, 6, 6)	[8, 9, 9, 7, 7, 6]
(ν_2,ν_{16x},ν_{16y},ν_{23x},ν_{23y})	(8, 7, 7, 6, 6)	[7, 8, 8, 9, 9, 5]
(ν_3,ν_{17x},ν_{17y},ν_{24x},ν_{24y})	(10, 8, 8, 6, 6)	[6, 6, 6, 7, 7, 7]
(ν_4,ν_{18x},ν_{18y},ν_{25x},ν_{25y})	(8, 7, 7, 6, 6)	[8, 8, 8, 6, 6, 8]
(ν_5,ν_{19x},ν_{19y},ν_{26x},ν_{26y})	(8, 6, 6, 6, 6)	[8, 7, 7, 8, 8, 7]
(ν_8,ν_{20x},ν_{20y},ν_{27x},ν_{27y})	(6, 7, 7, 6, 6)	[4, 6, 6, 6, 6, 6]

[a]The primitive basis is the number of Harmonic oscillator DVR functions, in the dimensionless coordinate system required to represent the system dynamics along the relevant mode. The primitive basis for each particle is the product of the one-dimensional bases; e.g for particle 1 in the primitive basis contains $9 \times 9 \times 9 \times 6 \times 6 = 26244$ functions and the full primitive basis consists of a total of 1.3×10^{25} functions. [b] The SPF basis is the number of single-particle functions used.

shape function of 20 meV FWHM. The results of six different calculations are combined with a statistical ratio of 1:1 to get the composite theoretical band structure shown in Figure 5.9 (bottom panel) along with the experimental results (top panel) reproduced from Reference [156]. The details of the mode combinations and numbers of SPF and PBF used in the MCTDH calculations, are given in Table 5.6. Six five dimensional particles are formed by combining the vibrational modes in the MCTDH calculations [121–123]. It can be seen from Figure 5.9 that the vibronic structure of the $\widetilde{X}$ electronic state remains similar to the uncoupled state results however the vibronic structures of the $\widetilde{A}$, $\widetilde{B}$ and $\widetilde{C}$ electronic state is heavily modified by the non-adiabatic coupling. We reiterate that the minimum of the seam of CIs between $\widetilde{X}$ state with other states ($\widetilde{A}$, $\widetilde{B}$ and $\widetilde{C}$) occur at high energy (cf., Sec 5.4.1) and therefore do not influence the nuclear dynamics studied here. Accordingly the results emerged are: (i) the vibronic structure of the $\widetilde{X}$ state will not affected by the nonadiabatic coupling effects; (ii) the bimodal spectral profile of the $\widetilde{A}$ band is heavily modified by the strong JT interactions in this state; (iii) the complex vibronic structure of the overlapping $\widetilde{B}$ and $\widetilde{C}$ electronic states is caused by the strong JT and PJT interactions of these states. The

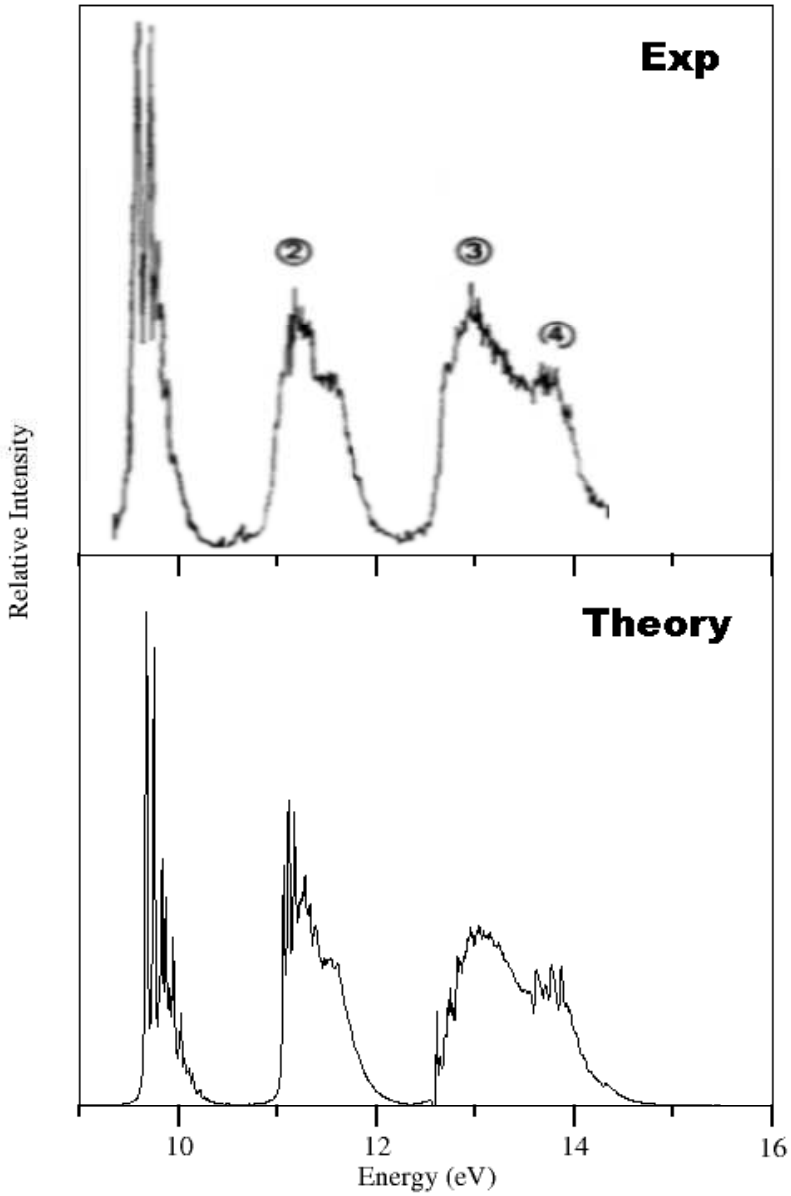

Figure 5.9: The final theoretical spectra of coupled $\widetilde{X}$ -$\widetilde{A}$ -$\widetilde{B}$ -$\widetilde{C}$ electronic of Bl^{+} with the experimental photo-ionization spectrum. The numerical details of the theoretical spectra are given in Tables 5.6.

close proximity of the latter electronic states (separated by $\sim$ 0.24 eV vertically) and very strong $\widetilde{B}$ -$\widetilde{C}$ PJT coupling leads to the observed complex, diffuse and overlapping $\widetilde{B}$ -$\widetilde{C}$ vibronic band. The minimum of the seam of the $\widetilde{B}$ -$\widetilde{C}$ CIs is located $\sim$ 0.60 eV above the minimum of the JT crossing seam of the $\widetilde{B}$ state and $\sim$ 0.004 eV below the minimum of the $\widetilde{C}$ state. This leads to a strong mixing of low-lying vibronic levels of $\widetilde{C}$ state with the high-lying vibronic levels of upper adiabatic component of $\widetilde{B}$ state. It is worth mentioning that the theoretical results presented in Figure5.9 are in very good accord with the experiment [156].

5.4.3 Ultrafast relaxation dynamics

The nonradiative internal conversion dynamics in the coupled $\widetilde{X}$ -$\widetilde{A}$ -$\widetilde{B}$ -$\widetilde{C}$ electronic states of Bl^+ is examined here. The time-dependence of the diabatic electronic populations in the $\widetilde{X}$ -$\widetilde{A}$ -$\widetilde{B}$ -$\widetilde{C}$ electronic manifold of Bl^+ are shown in Figures 5.10(a-c). The electronic populations are obtained by initially launching the WP on one of the component of $\widetilde{A}$ (panel a), one of the component of $\widetilde{B}$ (panel b) and the $\widetilde{C}$ state (panel c) of Bl^+ . In each case the WP moves to the JT and PJT CIs during its evolution in time. Six diabatic electronic populations are indicated by six different line types in panel *b*. It is observed that the WP does not move to the other five excited states when it is initially prepared on the $\widetilde{X}$ state and the corresponding figure is therefore not included here. This is due to the fact that the CIs of the $\widetilde{X}$ state with the other states are located at higher energies and these CIs are not accessible to the WP during its evolution on this state. This yields the observed sharp vibrational level structure of the $\widetilde{X}$ band (cf., Figure. 5.9).

It is observed from panel a of Figure. 5.10 that very minor population is transferred to the $\widetilde{X}$ state through $\widetilde{X}$ -$\widetilde{A}$ CIs when the WP is initially prepared on the $\widetilde{A}$ state. Similarly, population transfer to the remaining excited states ($\widetilde{B}$ and $\widetilde{C}$) is also very minor in this situation. This suggests that the vibronic

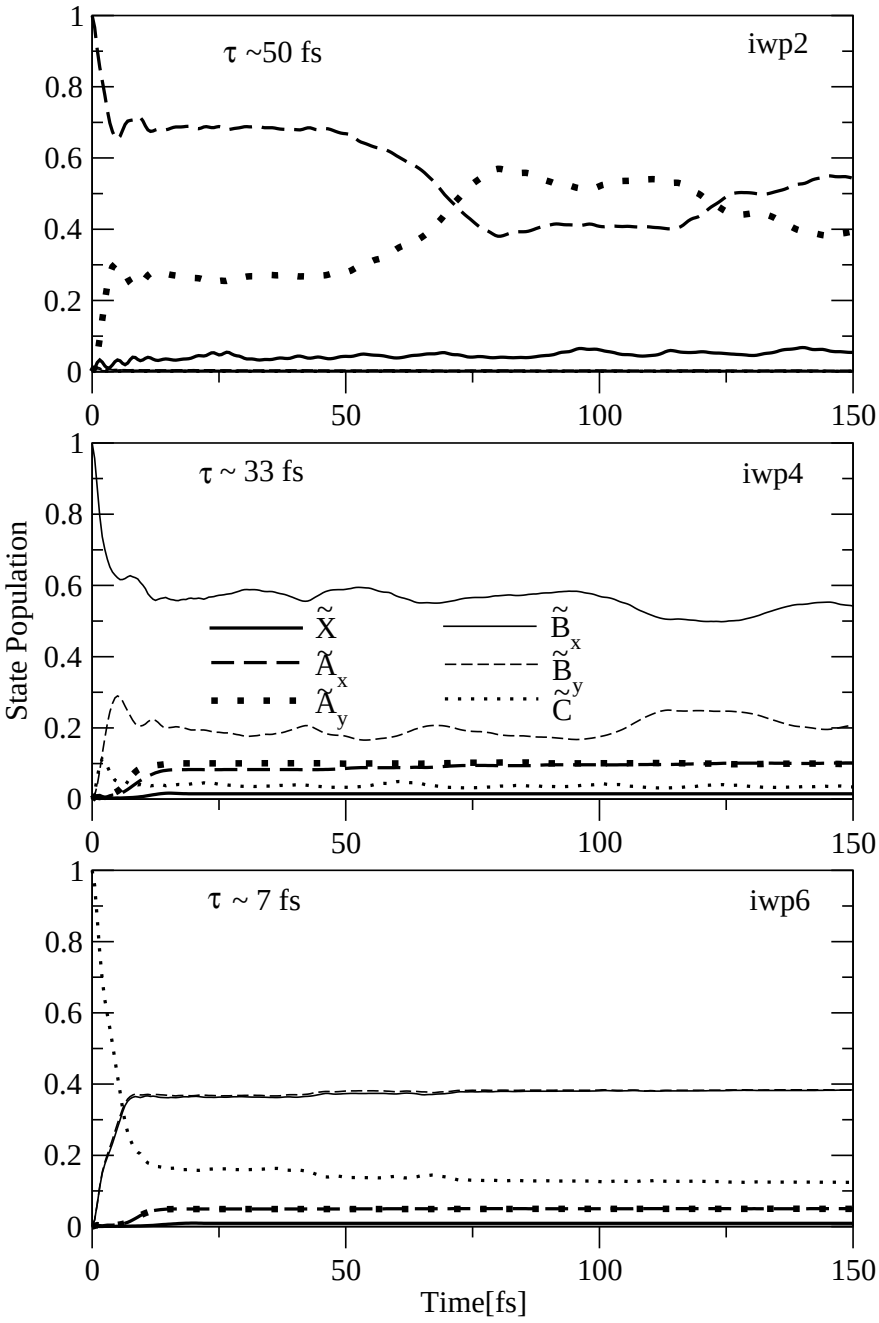

Figure 5.10: Diabatic electronic populations during the evolution of the $\widetilde{A}$, $\widetilde{B}$ and $\widetilde{C}$ state of Bl^+ in the coupled $\widetilde{X}$ -$\widetilde{A}$ -$\widetilde{B}$ -$\widetilde{C}$ states dynamics. Population curves of these state are shown by the different lines indicated in panel b.

band of $\widetilde{A}$ state is not significantly affected by its coupling to the $\widetilde{C}$ state. It can be seen from this figure that the WP mostly moves back and forth between the two JT split component of the $\widetilde{A}$ state. The initial decay of the population relates to a nonradiative internal conversion rate of $\sim$ 50 fs of the $\widetilde{A}$ state. We conclude that complex bimodal profile of the vibronic band of $\widetilde{A}$ state arises due to the strong JT interactions in this state and the estimated value of JT stabilization energy of this state is $\sim$ 0.25 eV.

The diabatic populations of the six electronic states shown in panel (b) for an initial location of the WP on one of the component of degenerate $\widetilde{B}$ state. The decay and growth of population of the two components of the JT split $\widetilde{B}$ state can be observed from the diagram. The population of these two components fluctuates around 0.6 and 0.2, during the entire course of evolution. A slow rise in the population of $\widetilde{C}$ and $\widetilde{A}$ state as time increases indicates that the population transfer occurs through $\widetilde{B}$ -$\widetilde{C}$ PJT CIs. A very minor population is transfered to the $\widetilde{X}$ electronic states. A decay rate of $\sim$ 33 fs is estimated from the initial decay of population of the $\widetilde{B}$ state. The fast relaxation of this state is in par with the observed broadening of this band in Figure. 5.9.

In the panel (c), we show the electronic populations of the six electronic states when the initial WP is prepared on the $\widetilde{C}$ state. Within $\sim$ 15 fs the $\widetilde{C}$ state population sharply decays and the $\widetilde{B}$ state population rises simultaneously. After 15 fs, the population of $\widetilde{C}$ state fluctuates around 0.15 and the population of both the components of $\widetilde{B}$ state remains almost constant around 0.38. As already mentioned above that the energetic minimum of the seam of the $\widetilde{B}$ -$\widetilde{C}$ CIs located only $\sim$ 0.31 eV above the minimum of the JT crossing seam of $\widetilde{B}$ state and the $\widetilde{C}$ state population flows to the $\widetilde{B}$ state via these PJT CIs. All other states remain almost unpopulated. Nonradiative decay rate of $\sim$ 7 fs is estimated for the $\widetilde{C}$ states. Such an ultrafast internal conversion leads to the observed broad and diffuse structure of the $\widetilde{C}$ band of Bl^+ .

5.5 Summary and outlook

The static and dynamic aspect of JT and PJT effects in the ground ($\widetilde{X}^2A_2'$) and first three ($\widetilde{A}^2E'$, $\widetilde{B}^2E''$ and $\widetilde{C}^2A_1'$) excited electronic states of Bl^+ are examined with the aid of quantum mechanical methods. A model diabatic vibronic Hamiltonian is constructed. The coupling parameters of diabatic Hamiltonian are determined by performing *ab initio* quantum chemistry calculations. One dimensional cuts of the multi-dimensional potential energy hyper-surfaces along dimensionless normal displacement coordinates of symmetric a_1' and degenerate e' modes of vibrations are examined. Curve crossing between $\widetilde{B}$ and $\widetilde{C}$ electronic states along ν_2, ν_3, ν_4 and ν_5 vibrational modes are found. Within LVC scheme the estimated JT stabilization energy are ~ 0.25 eV and ~ 0.21 eV for the $\widetilde{A}$ and $\widetilde{B}$ electronic state of Bl^+ , respectively. The PJT coupling is very strong between the $\widetilde{B}$ and $\widetilde{C}$ electronic states of Bl^+ . The detailed of the vibronic energy level structure of these electronic states are critically examined. The ν_6 vibrational mode is excited strongly in the first vibronic band. The dominant progressions are formed by the ν_6 and ν_{21} vibrational modes in the second vibronic band. In the third vibronic band, the ν_3, ν_4, ν_5, ν_{17},ν_{18}, ν_{19}, ν_{20} and ν_{21} vibrational modes are strongly excited. Excitation of ν_3, ν_4 and ν_6 vibrational modes is observed in the fourth vibronic band. The uncoupled state results for the $\widetilde{X}$ band is in good agreement with the experiment. This is not true for the remaining electronic states. The nuclear dynamics is therefore finally studied by considering all possible coupling in the $\widetilde{X}$ -$\widetilde{A}$ -$\widetilde{B}$ -$\widetilde{C}$ electronic states including thirty relevant vibrational modes. The dynamical simulations are carried out by propagating wave packets using the MCTDH method. The final theoretical results so obtained are in good accord with the experiment. The bimodal spectral profile of $\widetilde{A}$ vibronic band is observed due to the strong JT interaction in this state. The strong PJT coupling and close proximity of the $\widetilde{B}$ and $\widetilde{C}$ electronic state leads to broad, diffuse and overlapping vibronic bands for the $\widetilde{B}$ and $\widetilde{C}$ electronic states of Bl^+ .

The internal conversion rate for the $\widetilde{A}$ electronic state is $\sim$ 50 fs originates from strong JT intersections in this state. The estimated nonradiative decay rates of the $\widetilde{B}$ and $\widetilde{C}$ states are found to be $\sim$ 33 fs and 7 fs, respectively. Strong $\widetilde{B}$ -$\widetilde{C}$ PJT coupling leads to a very fast decay of the $\widetilde{C}$ state and also makes the corresponding vibronic bands broad and diffuse.

Chapter 6

Theoretical investigations of the photostability of pyrimidine and its radical cation

6.1 introduction

Pyrimidine (Pym) molecule is of great importance in biochemistry because it forms the fundamental structure for the bases in the nucleic acids DNA and RNA. Pym bases are Thymine, Cytosine and Uracil. The photoinduced dynamics of both pyrimidine cation (Pym^+) and Pym are valuable to assess their photophysical (chemical) properties in relation to their existence in the building blocks of life. Photoelectron spectroscopy study has been useful to understand the nature of molecular orbitals and complex inter electronic interactions underlying vibronic band structures. Therefore, in conjunction with experimental results, a theoretical study of multimode vibronic dynamics of $\widetilde{X}$, $\widetilde{A}$, $\widetilde{B}$ and $\widetilde{C}$ electronic states of Pym^+ is attempted here. The experimental band structures of these ionic states have been recorded by several groups [159–161]. The complex experimental vibronic band structure of the low-lying electronic states of Pym^+ is

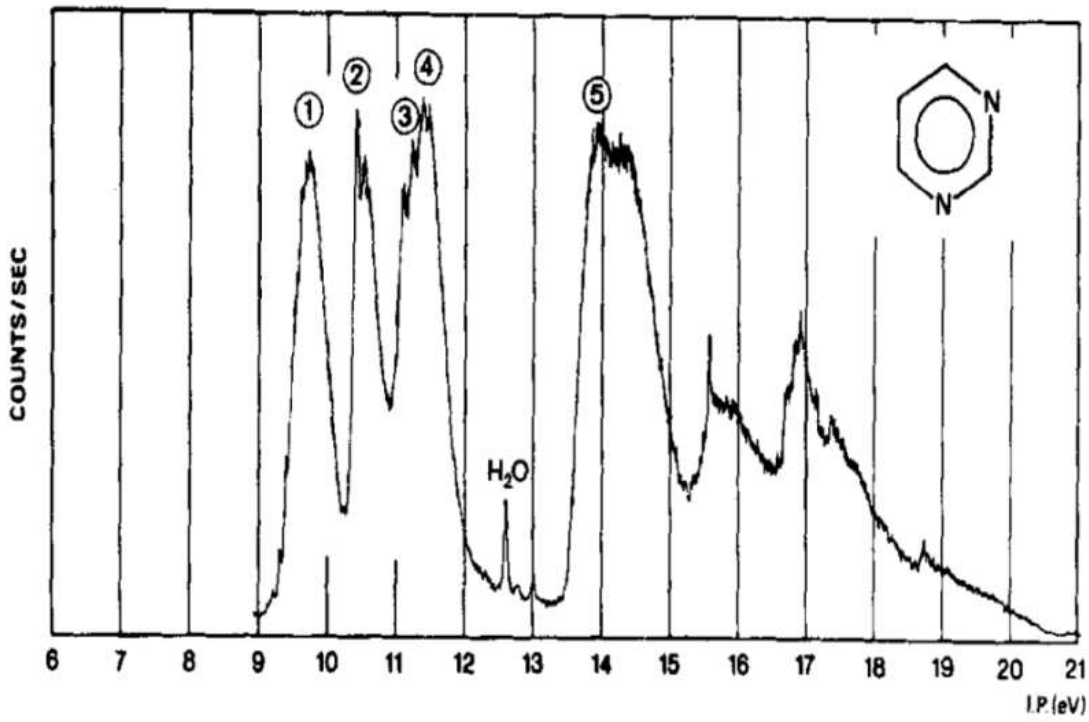

Figure 6.1: The experimental gas phase photoelectron spectrum of pyrimidine reproduced from Ref. [159].

shown in Figure 6.1.

Investigation of the vibrational energy level spectrum of the electronic ground and excited states of Pym molecule is valuable for understanding its photophysical properties [162]. Pym molecule is also reported to exist in astrophysical environment (with less population) specially in the molecular cloud region [163, 164]. When Pym molecule is irradiated with UV light in ice-water mixture it forms uracil molecule [165]. Thus a study of vacuum UV absorption spectrum [166–168] of Pym has attracted much attention. The experimental vacuum UV absorption spectrum of Pym is shown in Figure 6.2. This spectrum is recorded with moderate energy resolution in the region 3.5 - 9.5 eV. The first two bands are assigned to n to π^* transitions. Previous theoretical calculations reported that the second transition observed in the region $\sim$ 4.3 eV to 4.9 eV, is symmetry forbidden. But this band can be allowed via vibronic coupling of this state with the lowest $\pi\pi^*$

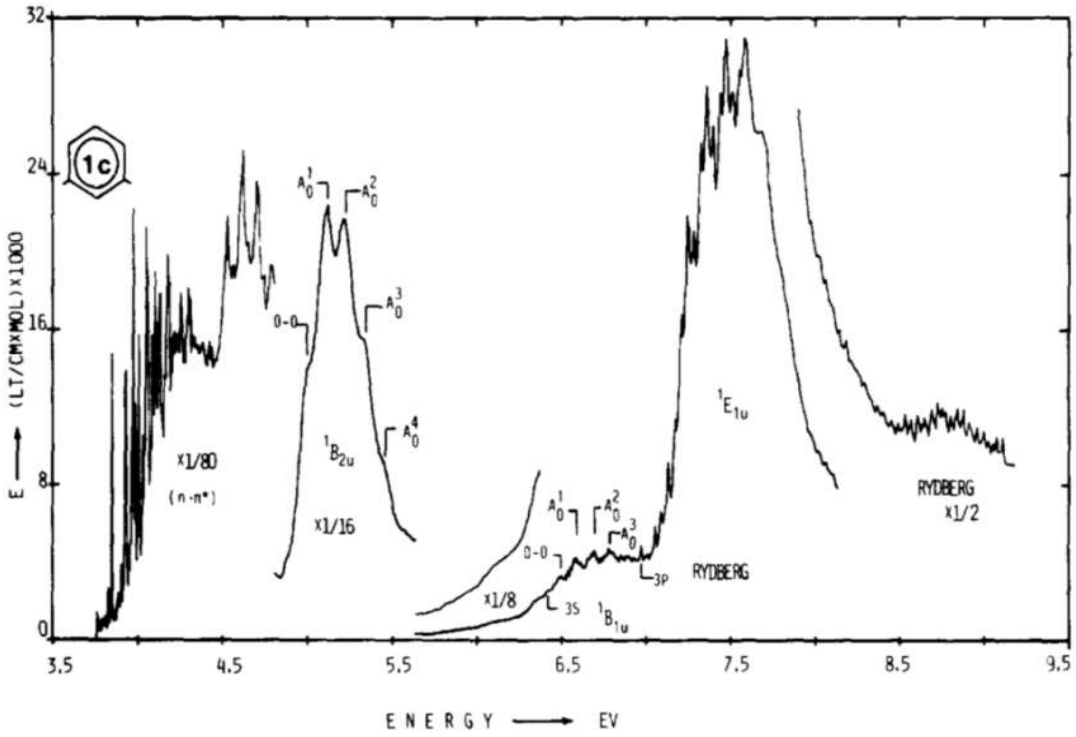

Figure 6.2: The experimental vapor phase UV absorption spectrum of pyrimidine reproduced from Ref. [166].

(S_3) which forms the third band in the absorption spectrum of Pym.

The present chapter is aimed towards accurate quantum dynamical studies of the nonadiabatic effects in the photo-physics and photochemistry of the excited electronic states of Pym and its radical cation. This is an example where some of the electronic states exhibit near degeneracies. Theoretical studies on the nuclear dynamics on the low-lying electronic states of Pym and Pym^+ have not been attempted so far. Using recently developed techniques it can now be possible to carry out such studies including all the vibrational degrees of freedom on coupled multi-sheeted PESs. Efforts towards this goal have been made in this chapter.

6.2 Electronic structure calculation

Electronic structure calculation for the reference electronic ground state of Pym molecule is carried out at the second-order Möller-Plesset perturbation level of theory employing the aug-cc-pVTZ basis set [112] using the Gaussian 03 program package [134]. In Table 6.1 the parameters of the reference equilibrium geometry of Pym molecule are shown along with the experimental results [169, 170]. By diagonalizing the *ab initio* force constant matrix of the optimized equilibrium geometry of the electronic ground state, the harmonic vibrational frequencies ω_i are obtained. The transformation matrix from the symmetry coordinates to the mass-weighted normal coordinates is obtained along with the harmonic vibrational frequencies. The dimensionless normal displacement coordinates are obtained by multiplying the latter with $\sqrt{\omega_i}$ (in atomic units) [109]. The description of normal modes of vibrations and the theoretically computed harmonic frequencies along with the experimentally observed fundamental frequencies are presented in Table 6.2.

Table 6. 1: Equilibrium geometry of Pyrimidine in its ground electronic state ($^1A_1$) along with the experimental results [169, 170].

Geometry	Theory MP2/aug-cc-pVTZ	Exp-1(ED)	Exp-2 (LCNMR)
C_1-N_2	1.338	1.340	1.328
C_3-N_2	1.339	1.340	1.350
C_3-C_4	1.389	1.393	1.393
C_1-H_8	1.083	1.099	1.082
C_3-H_7	1.083	1.099	1.079
C_4-H_6	1.081	1.099	1.087
N_2-C_1-N_6	127.2	127.6	–
C_1-N_2-C_3	115.1	115.5	–
C_4-C_5-N_6	122.1	122.3	121.2
C_3-C_4-C_5	116.9	116.8	117.8
H_8-C_1-N_2	116.4	–	–
H_7-C_3-N_2	116.5	115.3	–
H_6-C_5-C_6	121.5	121.6	–

Table 6. 2: Symmetry, frequency and description of the vibrational modes of the electronic ground state of Pym. The experimental results are reproduced from Ref. [?].Note that, theoretical frequencies are harmonic, where as, experimental ones are fundamental.

Symmetry	Mode	Vibrational Frequency(ω_j)(in cm^{-1})		Description	coordinate	Wilkinson notation
		Theory	Experiment			
A_1	ν_1	683	681	C-C and C-N in plane bending	Q_1	6a
	ν_2	1007	990	Ring deformation	Q_2	1
	ν_3	1076	1060	C-N-H in plane bending	Q_3	12
	ν_4	1156	1138	C-H bending	Q_4	9a
	ν_5	1432	1402	N-C-H bending	Q_5	19a
	ν_6	1606	1570	C-N stretching + C-H bending	Q_6	8a
	ν_7	3197	3002	Sym C-H stretching	Q_7	13
	ν_8	3213	3050	C-H stretching	Q_8	2
	ν_9	3240	3078	C-H stretching	Q_9	20a
B_2	ν_{10}	620	621	C-N in plane bending	Q_{10}	6b
	ν_{11}	1088	1075	C-H in plane bending	Q_{11}	18b
	ν_{12}	1235	1154	C-H in plane bending	Q_{12}	15
	ν_{13}	1333	1223	C-N stretching	Q_{13}	3
	ν_{14}	1391	1355	C-H bending	Q_{14}	14
	ν_{15}	1487	1466	Sym C-H bending	Q_{15}	19b
	ν_{16}	1614	1559	C-C stretching + C-H bending	Q_{16}	8b
	ν_{17}	3201	3095	Asym C-H stretching	Q_{17}	7b
A_2	ν_{18}	405	394	C-N-H out of plane bending	Q_{18}	16a
	ν_{19}	994	870	C-H out of plane bending	Q_{19}	17a
B_1	ν_{20}	351	344	C-C + C-H out of plane bending	Q_{20}	16b
	ν_{21}	746	709	C-H out of plane bending	Q_{21}	4
	ν_{22}	821	719	C-H out of plane bending	Q_{22}	10b
	ν_{23}	982	804	C-H out of plane bending	Q_{23}	11
	ν_{24}	1022	993	C-C-C out of plane bending	Q_{24}	5

The vertical ionization energies (VIEs) of Pym molecule along each of their vibrational modes are then calculated for various nuclear displacements, Q_i (i = 1-24) by MRCI method [115] employing the aug-cc-pVDZ basis set. Similarly the vertical excitation energy are calculated directly by the EOM-CCSD [116] method with aug-cc-pVDZ basis set using MOLPRO [172] quantum chemistry package. These computed energies are then fitted (using a least squares algorithm) to the adiabatic form of the diabatic electronic Hamiltonian All the coupling parameters for the cation and neutral pyrimidine are shown in Table-6.3 to Table-6.6 along with the VIE and VEE.

Table 6. 3: *Ab initio* calculated linear and quadratic coupling constants for the $\widetilde{X}^2B_2$, $\widetilde{A}^2B_1$, $\widetilde{B}^2A_2$ and $\widetilde{C}^2A_1$ electronic states of Pym^+. The vertical ionization energies of these three electronic states and the harmonic vibrational frequencies of the electronic ground state of pyrimidine are also given in the table. All quantities are in eV. The dimensionless Poisson parameters $(\kappa_i/\omega_i)^2/2$ are given in parentheses.

Mode (symmetry)	$\kappa_i^{D_0}$ $\widetilde{X}^2B_2$	$\kappa_i^{D_1}$ $\widetilde{A}^2B_1$	$\kappa_i^{D_2}$ $\widetilde{B}^2A_2$	$\kappa_i^{D_3}$ $\widetilde{C}^2A_1$	$\gamma_i^{D_0}$ $\widetilde{X}^2B_2$	$\gamma_i^{D_1}$ $\widetilde{A}^2B_1$	$\gamma_i^{D_2}$ $\widetilde{B}^2A_2$	$\gamma_i^{D_3}$ $\widetilde{C}^2A_1$	ω_i MP2/aug-cc-pVTZ
ν_1	0.1891	-0.0869	0.0853	0.0114	-0.0034	-0.0086	-0.0048	-0.0014	0.0847
	(2.492)	(0.526)	(0.507)	(0.009)					
ν_2	0.1655	-0.0410	-0.1004	0.1894	-0.0100	-0.0040	-0.0004	-0.0066	0.1248
	(0.879)	(0.054)	(0.324)	(1.152)					
ν_3	-0.1641	-0.1187	-0.0845	-0.1523	-0.0060	0.0062	-0.0046	-0.0016	0.1335
	(0.755)	(0.395)	(0.200)	(0.651)					
ν_4	0.1478	-0.0261	0.1037	0.0455	-0.0006	-0.0070	0.0034	-0.0242	0.1433
	(0.532)	(0.017)	(0.262)	(0.050)					
ν_5	-0.0388	-0.0630	0.0782	0.0761	-0.0004	-0.0036	0.0048	-0.0130	0.1776
	(0.024)	(0.063)	(0.097)	(0.092)					
ν_6	0.0789	0.2300	-0.2137	-0.0766	-0.0198	-0.0036	0.0166	-0.0218	0.1991
	(0.079)	(0.667)	(0.576)	(0.074)					
ν_7	0.0059	0.0018	0.0093	0.0312	0.0146	0.0058	0.0034	0.0124	0.3964
	(.0001)	(0.00001)	(0.0003)	(0.003)					
ν_8	-0.0601	-0.0066	-0.0171	0.0347	0.0040	0.0058	0.0032	-0.0210	0.3984
	(0.011)	(0.0001)	(0.001)	(0.004)					
ν_9	-0.0215	-0.0230	-0.0160	-0.0112	-0.0044	0.0060	0.0034	-0.0056	0.4017
	(0.001)	(0.002)	(0.0008)	(.0004)					
E_X^0	9.9885								
E_A^0	10.3227								
E_B^0	11.0595								
E_C^0	11.7252								

6.3 The Vibronic Hamiltonian

In order to investigate the photo-physics, the relevant potential energy surfaces of Pym and its radical cation need to be determined first. Extensive electronic structure calculations are carried out for this purpose. We resort to a diabatic electronic representation [23, 100] in order to explore the smooth nature of the inter electronic coupling potentials in the nuclear dynamics. Thus model vibronic Hamiltonians are constructed for these system in a diabatic electronic basis. In the following we discuss the salient features of the developed theoretical model.

6.3.1 Pyrimidine radical cation

Pym belongs to the C_{2v} symmetry point group at the equilibrium geometry of its electronic ground state $S_0(^1A_1)$. The 24 normal modes of vibrations of Pym decompose into 9 $a_1 \oplus$ 2 $a_2 \oplus$ 5 $b_1 \oplus$ 8 b_2 irreducible representations (IREPs) of the C_{2v} point group. The ground and first three excited electronic states of Pym^+ belong to the $\widetilde{X}^2B_2$, $\widetilde{A}^2B_1$, $\widetilde{B}^2A_2$ and $\widetilde{C}^2A_1$ symmetry species of the equilibrium C_{2v} point group. They result from an ionization from b_2, b_1, a_2 and a_1 MOs of Pym, respectively. These MOs are schematically shown in Figure 6. 3.

For the nuclear dynamical simulations, a vibronic Hamiltonian is constructed below in terms of the dimensionless normal coordinates of the vibrational modes. The coupling mechanisms in this Hamiltonian are governed by the following symmetry rules

$$\Gamma_m \otimes \Gamma_{Qc} \otimes \Gamma_n \supset \Gamma_{A_1}, \tag{6.1}$$

$$\Gamma_n \otimes \Gamma_{Qs} \otimes \Gamma_n \supset \Gamma_{A_1}, \tag{6.2}$$

In the above Γ represents the IREPs of the equilibrium symmetry point group of the system. The indices m, n and Q describe the electronic states and vibrational

Table 6. 4: *Ab initio* Interstate linear coupling constants for the $\widetilde{X}^2B_2$, $\widetilde{A}^2B_1$,$\widetilde{B}^2A_2$ and $\widetilde{C}^2A_1$ electronic states of Pym^+. The harmonic vibrational frequencies of the electronic ground state of pyrimidine are also given in the table. All quantities are in eV. The dimensionless Poisson parameters $(\lambda_i/\omega_i)^2/2$ are given in parentheses.

Mode	λ_i^{x-y}	λ_i^{x-y}	γ_i^X	γ_i^A	γ_i^B	γ_i^C	ω_i
b_2	A - B	X - C					
ν_{10}	0.0580(0.285)	0.1541(2.013)	-0.0314	-0.0138	0.0016	0.0272	0.07684
ν_{11}	—	0.0425(0.050)	-0.0028	0.0024	-0.0026	0.0018	0.13495
ν_{12}	0.0475(0.048)	0.0154(0.005)	-0.0050	-0.0040	0.0062	-0.0044	0.15315
ν_{13}	0.0970(0.172)	0.1017(0.189)	-0.0226	0.0462	0.0922	0.0020	0.16531
ν_{14}	0.0228(0.009)	–	0.0018	0.0018	0.0042	-0.0190	0.17255
ν_{15}	—	–	-0.0090	0.0026	-0.0156	-0.0290	0.18438
ν_{16}	0.1412(0.249)	0.0964(0.116)	-0.0324	-0.0464	0.0536	-0.0090	0.20012
ν_{17}	—	0.0356(0.004)	0.0104	0.0036	0.0018	0.0136	0.39693
a_2	X - A	B - C					
ν_{18}	–	0.1434(4.080)	0.0000	-0.0578	-0.2156	0.0872	0.05022
ν_{19}	0.0933(0.286)	0.0326(0.035)	-0.1120	0.1136	0.0076	0.0184	0.12325
b_1	X - B	A - C					
ν_{20}	—	0.1568(6.500)	-0.0013	-0.0608	-0.0208	0.0158	0.04352
ν_{21}	0.1546(1.400)	0.0546(0.174)	-0.0558	-0.0258	0.0245	-0.0188	0.09252
ν_{22}	0.0627(0.190)	0.1781(1.530)	0.0025	-0.0526	0.0152	0.0526	0.10182
ν_{23}	0.0487(0.080)	0.1146(0.443)	0.0067	-0.0228	0.0148	0.0216	0.12178
ν_{24}	0.0625(0.122)	—	-0.0036	0.0126	0.0096	-0.0024	0.12672

Table 6. 5: *Ab initio* calculated linear and quadratic coupling constants for the S_1, S_2 and S_3 electronic states of Pym. The vertical excitation energies of these three electronic states and the harmonic vibrational frequencies of the electronic ground state of pyrimidine are also given in the table. All quantities are in eV. The dimensionless Poisson parameters $(\kappa_i/\omega_i)^2/2$ are given in parentheses.

Mode (symmetry)	$\kappa_i^{S_1}$ S_1	$\kappa_i^{S_2}$ S_2	$\kappa_i^{S_3}$ S_3	$\gamma_i^{S_1}$ S_1	$\gamma_i^{S_2}$ S_2	$\gamma_i^{S_3}$ S_3	ω_i MP2/aug-cc-pVTZ
ν_1	0.1297	0.1434	-0.0604	-0.0088	-0.0258	-0.0126	0.0847
	(1.172)	(1.433)	(0.254)				
ν_2	0.0731	0.060	-0.1524	-0.0084	-0.0072	0.0012	0.1248
	(0.172)	(0.116)	(0.746)				
ν_3	-0.1970	-0.1966	-0.1452	-0.0094	-0.0060	0.0014	0.1335
	(1.089)	(1.084)	(0.592)				
ν_4	0.1446	0.1513	0.0474	-0.0010	-0.0160	-0.0076	0.1433
	(0.509)	(0.557)	(0.055)				
ν_5	0.0960	-0.1752	0.0278	-0.0066	-0.0190	-0.0016	0.1776
	(0.146)	(0.487)	(0.012)				
ν_6	-0.1132	0.3178	-0.0131	-0.0092	-0.0210	0.0156	0.1991
	(0.162)	(1.274)	(0.002)				
ν_7	0.0287	-0.0128	0.0308	-0.0032	-0.0006	-0.0012	0.3964
	(0.003)	(0.001)	(0.003)				
ν_8	-0.0304	-0.0743	-0.0142	0.0008	-0.0034	-0.0010	0.3984
	(0.003)	(0.017)	(0.001)				
ν_9	-0.0093	-0.0340	-0.0249	0.0016	-0.0014	-0.0002	0.4017
	(0.0003)	(0.004)	(0.002)				
$E^0_{S_1}$	4.756						
$E^0_{S_2}$	5.218						
$E^0_{S_3}$	5.569						

Table 6. 6: *Ab initio* Interstate linear coupling constants for the S_1, S_2 and S_3 electronic states of Pym. The harmonic vibrational frequencies of the electronic ground state of pyrimidine are also given in the table. All quantities are in eV. The dimensionless Poisson parameters $(\lambda_i/\omega_i)^2/2$ are given in parentheses.

Mode	λ_i^{S1-S2}	λ_i^{S1-s3}	λ_i^{S2-s3}	$\gamma_i^{S_1}$	$\gamma_i^{S_2}$	$\gamma_i^{S_3}$	ω_i
a_2							
ν_{10}	–	0.0822(1.341)	–	-0.0491	0.0307	-0.0715	0.05022
ν_{11}	–	0.1096(0.395)	–	-0.1045	-0.0314	-0.0481	0.12325
b_1							
ν_{12}	–	–	0.0306(0.247)	0.0226	-0.060	-0.0531	0.04352
ν_{13}	–	–	0.0818(0.391)	-0.0558	-0.0879	-0.0274	0.09252
ν_{14}	–	–	0.0722(0.252)	-0.0263	-0.040	-0.0874	0.10182
ν_{15}	–	–	0.0522(0.092)	-0.0080	-0.0894	-0.0642	0.12178
ν_{16}	–	–	0.0687(0.147)	-0.0464	-0.080	-0.0348	0.12672
b_2							
ν_{17}	0.0537(0.244)	–	–	-0.0568	-0.0248	-0.0257	0.07684
ν_{18}	0.0322(0.029)	–	–	-0.0154	-0.0067	-0.0080	0.13495
ν_{19}	0.0951(0.193)	–	–	-0.0442	0.0304	0.0064	0.15315
ν_{20}	0.0369(0.025)	–	–	0.0304	0.0416	0.1662	0.16531
ν_{21}	—	–	–	-0.0080	–	–	0.17255
ν_{22}	0.0332(0.016)	–	–	-0.0131	-0.0079	-0.0053	0.18438
ν_{23}	0.2029(0.514)	–	–	-0.2118	0.1502	0.0053	0.20012
ν_{24}	—	–	–	-0.0079	–	–	0.39693

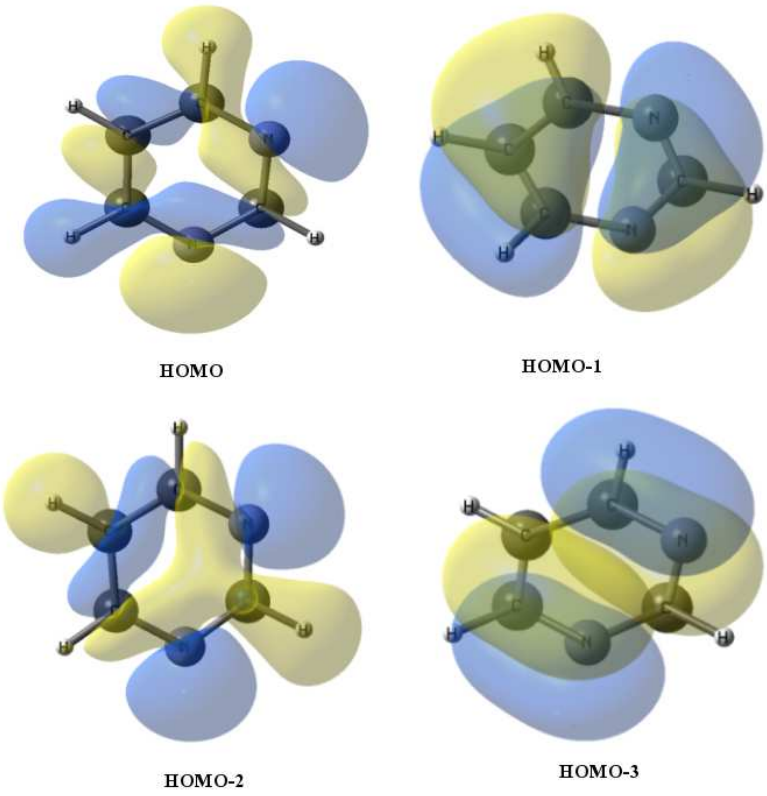

Figure 6.3: Schematic drawing of the first four highest occupied molecular orbital of Pyrimidine.

mode, respectively. The above rule imply that totally symmetric (a_1) vibrational modes are always active in a given electronic state and the first-order coupling between the $\widetilde{X}$ -$\widetilde{A}$, $\widetilde{X}$ -$\widetilde{B}$, $\widetilde{X}$ -$\widetilde{C}$, $\widetilde{A}$ -$\widetilde{B}$, $\widetilde{A}$ -$\widetilde{C}$ and $\widetilde{B}$ -$\widetilde{C}$ electronic states of Pym^+ is caused by the vibrational modes of a_2, b_1, b_2, b_2, b_1 and a_2 symmetry, respectively. These couplings would lead to multiple multidimensional conical intersections in the mentioned manifold of electronic states of Pym^+. The impact of the electronic non-adiabatic effects on the vibrational energy level structure of a state depends on the strength of the associated coupling.

With the above description Hamiltonian of the coupled manifold of $\widetilde{X}$ -$\widetilde{A}$ -$\widetilde{B}$ -$\widetilde{C}$ electronic states of Pym^+ can be written as

$$\mathcal{H} \;=\; (\mathcal{T}_N + \mathcal{V}_0)\mathbf{1_4} + \begin{pmatrix} W_{\widetilde{X}} & W_{\widetilde{X}-\widetilde{A}} & W_{\widetilde{X}-\widetilde{B}} & W_{\widetilde{X}-\widetilde{C}} \\ & W_{\widetilde{A}} & W_{\widetilde{A}-\widetilde{B}} & W_{\widetilde{A}-\widetilde{C}} \\ h.c. & & W_{\widetilde{B}} & W_{\widetilde{B}-\widetilde{C}} \\ & & & W_{\widetilde{C}} \end{pmatrix}, \tag{6.3}$$

where 1_4 is a 4×4 unit matrix and $(\mathcal{T}_N + \mathcal{V}_0)$ is the Hamiltonian for the unperturbed electronic ground state of the neutral Pym. This reference state is assumed to be harmonic and vibronically decoupled from the other states. Therefore, $\mathcal{T}_N$ and $\mathcal{V}_0$ are given by

$$\mathcal{T}_N = -\frac{1}{2}\sum_{i=1}^{24}\omega_i\frac{\partial^2}{\partial Q_i^2}, \tag{6.4}$$

$$\mathcal{V}_0 = \frac{1}{2}\sum_{i=1}^{24}\omega_i Q_i^2. \tag{6.5}$$

The non-diagonal matrix Hamiltonian in Eqn. (6.3) represents the change in the electronic energy upon ionization of Pym and describes the diabatic electronic PESs (diagonal elements) of the $\widetilde{X}$, $\widetilde{A}$, $\widetilde{B}$ and $\widetilde{C}$ electronic states of Pym^+ and

their coupling potentials (off-diagonal elements). These are expanded in a Taylor series (excluding the inter-mode bilinear coupling terms) around the equilibrium geometry of the reference state at (Q=**0**) as [23]

$$W_j = E_0^{(j)} + \sum_{i=1}^{9} \kappa_i^{(j)} Q_i + \frac{1}{2} \sum_{i=1}^{24} \gamma_i^{(j)} Q_i^2 \;\; ; \;\; j \in \widetilde{X}, \widetilde{A}, \widetilde{B}, \widetilde{C} \tag{6.6}$$

$$W_{j-k} = \sum_i \lambda_i^{(j-k)} Q_i \tag{6.7}$$

where $j-k \in \widetilde{X}$ -$\widetilde{A}$, $\widetilde{X}$ -$\widetilde{B}$, $\widetilde{X}$ -$\widetilde{C}$, $\widetilde{A}$ -$\widetilde{B}$, $\widetilde{A}$ -$\widetilde{C}$, $\widetilde{B}$ -$\widetilde{C}$ with $i \in a_2$,b_1, b_2, b_2, b_1, a_2 in that order. In the above equations the quantity $E_0^{(j)}$ represents the vertical ionization energy of the j^{th} electronic state and $\kappa_i^{(j)}$ and $\gamma_i^{(j)}$ are the linear and second-order coupling parameters of the i^{th} vibrational mode in the j^{th} electronic state. The quantity $\lambda_i^{(j-k)}$ describes the first-order coupling parameter between the j and k electronic states through the vibrational mode i. All these coupling parameters are tabulated in the Tables 6.1 and 6.2.

A thorough analysis of the coupling strength ($\kappa^2/2\omega^2$) of the totally symmetric vibrational modes of Pym^+ of Table 6.1 shows that ν_1 is strongly active in the $\widetilde{X}$, $\widetilde{A}$ and $\widetilde{B}$ electronic states. The vibrational mode ν_2 has the strongest coupling strength in the $\widetilde{C}$ electronic states. The vibrational mode ν_2, ν_3 and ν_4 are moderately active in the $\widetilde{X}$ and $\widetilde{B}$ electronic states. Likewise the coupling strength of ν_3 and ν_6 are considerable in the $\widetilde{A}$, $\widetilde{B}$ and $\widetilde{C}$ states. The vibrational modes ν_5 is weakly active in all the electronic states.

Among the interstate coupling modes of Pym^+ listed in Table 6.2, the strongest coupling is caused by ν_{19} in $\widetilde{X}$ -$\widetilde{A}$, ν_{21} in $\widetilde{X}$ -$\widetilde{B}$ and ν_{10} in $\widetilde{X}$ -$\widetilde{C}$ electronic state. The $\widetilde{A}$ state is strongly coupled by ν_{10} and ν_{13} vibrational modes with the $\widetilde{B}$ electronic state. The $\widetilde{B}$ state is also strongly coupled with the $\widetilde{C}$ electronic state through ν_{18} and ν_{19} vibrational modes. The modes ν_{20} and ν_{22} cause strong coupling between $\widetilde{A}$ and $\widetilde{C}$ electronic states. The excitation of the nontotally

symmetric modes ν_{10}, ν_{11}, ν_{18}, ν_{19}, ν_{20} and ν_{21} have been found in the MATI experiment [162]. It can be seen from Table 6.2 that the coupling strength of all these modes are considerable and are expected to be observed in the vibronic band of the $\widetilde{X}$ state in accordance with the results of Ref. [162].

6.3.2 Pyrimidine molecule

The Hamiltonian for the coupled manifold of S_1 ($n\pi^*$)-S_2 ($n\pi^*$)-S_3 ($\pi\pi^*$) electronic states of Pym is constructed in terms of the dimensionless normal displacement coordinates ($\mathbf{Q}$) of its 24 nondegenerate vibrational modes (introduced in Sec 6.2) in a diabatic electronic basis as

$$\mathcal{H} = (\mathcal{T}_N + \mathcal{V}_0)\mathbf{1_3} + \begin{pmatrix} W_{S_1} & W_{S_1-S_2} & W_{S_1-S_3} \\ h.c. & W_{S_2} & W_{S_2-S_3} \\ & & W_{S_3} \end{pmatrix}, \tag{6.8}$$

where 1_3 is a 3×3 unit matrix and ($\mathcal{T}_N$ + $\mathcal{V}_0$) is the Hamiltonian for the unperturbed electronic ground state (S_0) of the neutral Pym (same as in Eqn. 6.3 - 6.5). The non-diagonal matrix Hamiltonian in Eqn. (6. 7) represents the change in energy upon electronic excitation of Pym and describe the diabatic electronic PESs (diagonal elements) of the S_1, S_2 and S_3 electronic states and their coupling potentials (off-diagonal elements). These are expanded in a Taylor series (excluding the inter-mode bilinear coupling terms) around the equilibrium geometry of the reference state at ($\mathbf{Q}$=0) as [23]

$$W_j = E_0^{(j)} + \sum_{i=1}^{9} \kappa_i^{(j)} Q_i + \frac{1}{2} \sum_{i=1}^{24} \gamma_i^{(j)} Q_i^2 \;\; ; \;\; j \in S_1, S_2, S_3 \tag{6.9}$$

$$W_{j-k} = \sum_i \lambda_i^{(j-k)} Q_i \tag{6.10}$$

where j - $k \in S_1$-S_2, S_1-S_3, S_2-S_3 with $i \in a_2$,b_1, b_2 in that order. In the above equations the quantity $E_0^{(j)}$ represents the vertical excitation energy of the j^{th} electronic state and $\kappa_i^{(j)}$ and $\gamma_i^{(j)}$ are the linear and second-order coupling parameters of the i^{th} vibrational mode in the j^{th} electronic state. The quantity $\lambda_i^{(j-k)}$ describes the first-order coupling parameter between the j and k electronic states through the vibrational mode i. A linear interstate coupling is considered throughout this study. All these coupling parameters are given in Tables 6.3 and 6.4.

A similar analysis of the coupling parameters of the vibronic Hamiltonian of Pym reveals the following. For the totally symmetric vibrational modes, it can be seen from Table 6.3 that the modes ν_1 and ν_3 are strongly active in the S_1, S_2 and S_3 electronic states. The vibrational mode ν_2 has the highest coupling strength in the S_3 state. The ν_2, ν_4, ν_5 and ν_6 vibrational modes in the S_1 and S_2 electronic states are moderately active. The vibrational modes ν_4 and ν_5 are weakly active in the S_3 electronic state. The excitation of the remaining a_1 vibrational modes are very weak in a given electronic state. The coupling between S_1-S_2 states is very strong along the vibrational modes ν_{17}, ν_{19} and ν_{20} of b_2 symmetry (cf., Table 6.4). The S_2 and S_3 electronic states are strongly coupled by the vibrational modes ν_{12}, ν_{13}, ν_{14} and ν_{16} of b_1 symmetry. The ν_{10} and ν_{11} vibrational modes of symmetry a_2 are responsible for the S_1-S_3 interstate coupling.

6.4 Results and Discussion

6.4.1 Adiabatic potential energy surfaces and stationary points:

In this section we begin with a discussion on the topography of the adiabatic potential energy surfaces and the stationary points found on them employing the vibronic coupling model introduced above. The results of this analysis are

related to the findings of the nuclear dynamical studies presented later in this section. The adiabatic potential energies are obtained by diagonalizing the 4 × 4 diabatic electronic Hamiltonian defined in Eqn. 6.3. The cuts of the potential energy surfaces along the symmetric vibrational modes are shown in Figure 6. 4 for Pym^+ and Pym.

The adiabatic potential energies in the above figure are plotted along the dimensionless normal displacement coordinate of the given vibrational mode (ν_1 - ν_9 for the neutral and cationic electronic states of Pym) keeping all others at their equilibrium value (at $\mathbf{Q}$=0). It can be seen that there are several curve crossings among the electronic states shown in the figure. These curve crossings develop into conical intersections in multi-dimensions and these intersections are the mechanistic bottleneck for the nuclear motion in a given electronic state. The energetic minimum of various conical intersections (CIs) in the four (three) lowest electronic states and the minimum of excited electronic states of both Pym^+(Pym) have been estimated within a linear coupling approach [23]. These CIs play the key role in the dynamical events discussed latter in this thesis.

Within the linear coupling scheme the energetic minimum [23] of the seam of the $\widetilde{X}$ -$\widetilde{A}$, $\widetilde{A}$ -$\widetilde{B}$ and $\widetilde{B}$ -$\widetilde{C}$ conical intersections is estimated to occur at $\sim$ 10.26 eV, $\sim$ 10.98 eV and $\sim$ 11.22 eV respectively. The minimum of the seam of the CI between $\widetilde{X}$ -$\widetilde{A}$ states occurs $\sim$ 0.01 eV above the equilibrium minimum of the $\widetilde{A}$ electronic state. The vibrational structure of the $\widetilde{A}$ state is therefore expected to be strongly perturbed by the associated non-adiabatic interactions. The minimum of the $\widetilde{A}$ -$\widetilde{B}$ conical intersections occurs at $\sim$ 0.63 eV and $\sim$ 0.01 eV above the minimum of the $\widetilde{A}$ and $\widetilde{B}$ electronic states, respectively. The minimum of the $\widetilde{B}$ -$\widetilde{C}$ conical intersections occurs $\sim$ 0.05 eV above the global minimum of the $\widetilde{C}$ state. This leads to the complex structure of the vibronic bands of Pym. All these energetic minima are given below in Table 6.7.

Table 6.7

Equilibrium minimum (diagonal entries) and minimum of the seam of various CIs

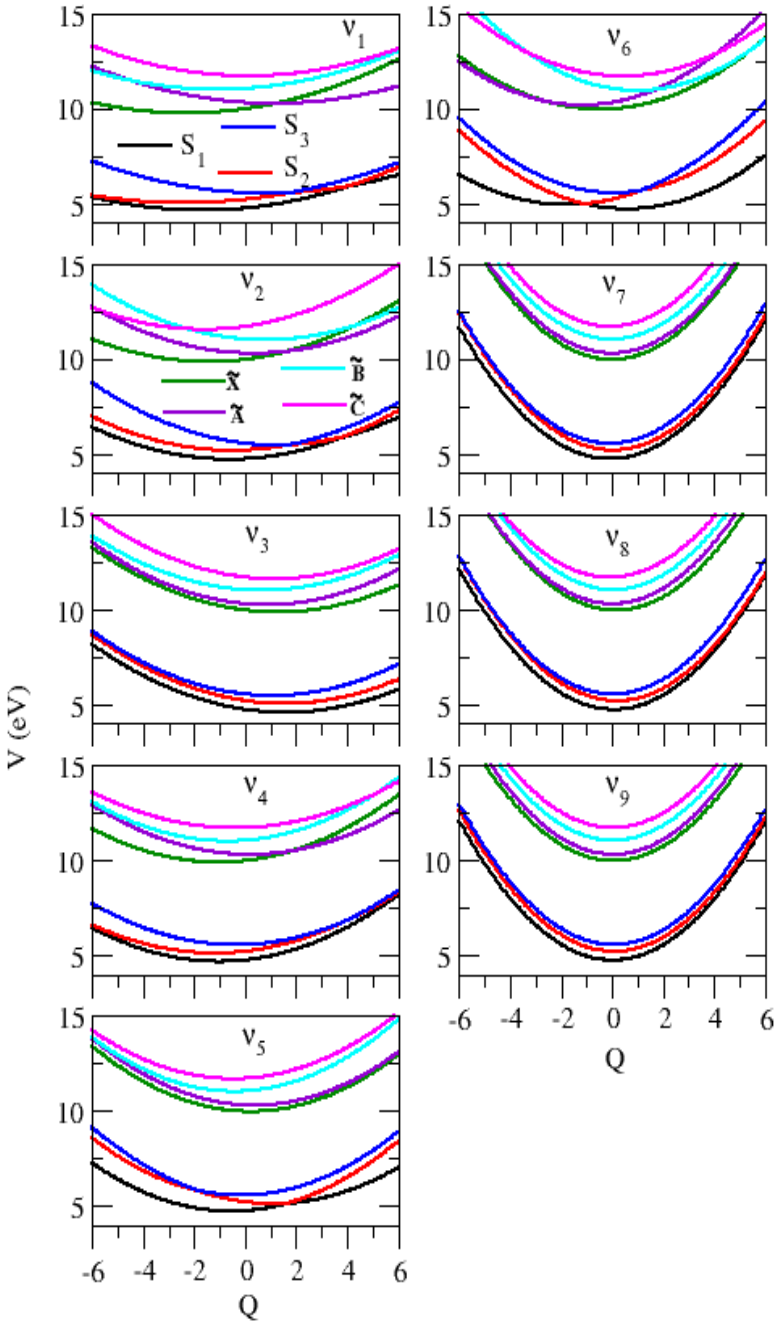

Figure 6.4: Adiabatic potential energies of the $\widetilde{X}$, $\widetilde{A}$, $\widetilde{B}$ and $\widetilde{C}$ for electronic states of Pym^+ and S_1, S_2 and S_3 electronic states of Pym as a function of the dimensionless normal coordinates of the totally symmetric (a_1) vibrational modes, ν_1-ν_9 by different color line.

(off-diagonal entries) of the PESs of Pym. All quantities are given in eV.

$$\begin{pmatrix} & \widetilde{X} & \widetilde{A} & \widetilde{B} & \widetilde{C} \\ \widetilde{X} & - & 10.083 & 10.962 & 13.482 \\ \widetilde{A} & & 10.072 & 10.782 & 11.723 \\ \widetilde{B} & & & 10.779 & 11.481 \\ \widetilde{C} & & & & 11.453 \end{pmatrix}$$

In case of Pym the energetic minimum of the seam of S_1-S_2, S_1-S_3 and S_2-S_3 CIs are found to occur at ~ 4.61 eV, ~ 5.49 eV and ~ 5.46 eV, respectively. The minimum of the S_1-S_2 CIs occurs ≈ 0.10 eV above the minimum of the S_2 state. The minimum of the S_2-S_3 CIs occurs at ≈ 0.10 eV above the minimum of the S_3 state. The S_1-S_3 CIs occur ~ 0.98 and ~ 0.13 eV above the minima of the S_2 and S_3 electronic states. All these energetic minima are given below in Table 6.8.

Table 6.8
shows the equilibrium minimum (diagonal entries) and minimum of the seam of various CIs (off-diagonal entries) of the PESs of Pym. All quantities are given in eV.

$$\begin{pmatrix} & S_1 & S_2 & S_3 \\ S_1 & - & 4.612 & 5.493 \\ S_2 & & 4.510 & 5.462 \\ S_3 & & & 5.363 \end{pmatrix}$$

6.4.2 Vibronic band structures

The vibronic band structures of the mentioned electronic states of Pym and Pym^+ are calculated, assigned and the impact of the electronic non-adiabatic interactions on them is examined below. In order to develop a systematic understanding of the details, we first examined the vibronic energy level structures of the un-

coupled electronic states, and, subsequently included the coupling between states to reveal its impact on the energy level structure. A time-independent matrix diagonalization method is used to calculate the precise location of the energy levels of a uncoupled electronic state. As stated before, because of dimensionality problem this method can no longer be used in the coupled states situation. The final spectral envelopes for the coupled states situation are therefore calculated by a time-dependent wave packet propagation method employing the MCTDH algorithm.

6.4.2.1 $\widetilde{X}$, $\widetilde{A}$, $\widetilde{B}$ and $\widetilde{C}$ electronic states of Pym^+

The uncoupled state spectrum for the $\widetilde{X}$, $\widetilde{A}$, $\widetilde{B}$ and $\widetilde{C}$ electronic states of Pym^+ are calculated by a matrix diagonalization approach using the Lanczos algorithm [23]. The theoretical stick spectra are calculated using 9 totally symmetric vibrational modes (ν_1-ν_9) using the vibronic Hamiltonian of Eqn. 6.3 and the parameters of Table 6.1. The results are numerically converged with respect to the number of vibrational basis functions and the number of Lanczos iteration.

The vibrational modes ν_1 (in plane ring deformation), ν_2 (in plane NCN bend), ν_3 (in plane CCC bend) and ν_4 (in plane C-H bend) form the dominant progressions in the $\widetilde{X}$ state of Pym^+. The peaks are $\sim$ 0.0847 eV, $\sim$ 0.1248 eV, $\sim$ 0.1335 eV and $\sim$ 0.1483 eV spaced in energy and correspond to the vibrational frequencies of these modes, respectively. The vibrational modes ν_5 (CN stretch+ C-H bend) and ν_6 (CN stretch) are weakly excited in this band. The peak spacings of $\sim$ 0.0632, $\sim$ 0.0968, $\sim$ 0.1335 eV and $\sim$ 0.2064 eV corresponding to the excitation of ν_1, ν_2, ν_3 and ν_6 vibrational modes, respectively, have been observed in the $\widetilde{A}$ state. These uncoupled state spectra panel a ($\widetilde{X}$ state) and panel b ($\widetilde{A}$ state) electronic states are shown in Figure 6.5.

The peak spacings of $\sim$ 0.0632, $\sim$ 0.0968, $\sim$ 0.1335 eV and $\sim$ 0.2064 eV corresponding to the excitation of ν_1, ν_2, ν_3 and ν_6 vibrational modes, respectively, have been observed in the $\widetilde{A}$ state.

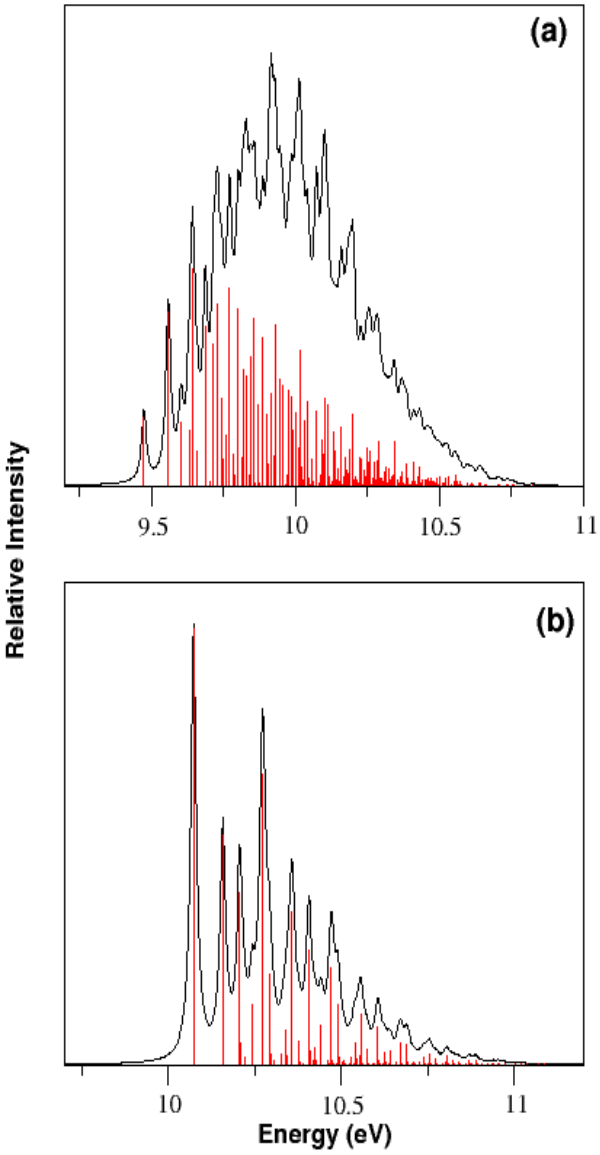

Figure 6.5: The uncoupled vibronic band of the $\widetilde{X}$ and $\widetilde{A}$ electronic state of Pym^+ computed with relevant nine a_1 (ν_1-ν_9) vibrational modes within the linear vibronic coupling scheme in panel a and b respectively. The theoretical stick spectrum in each panel is convoluted with a Lorentzian function of 20 meV FWHM to calculate the spectral envelope.

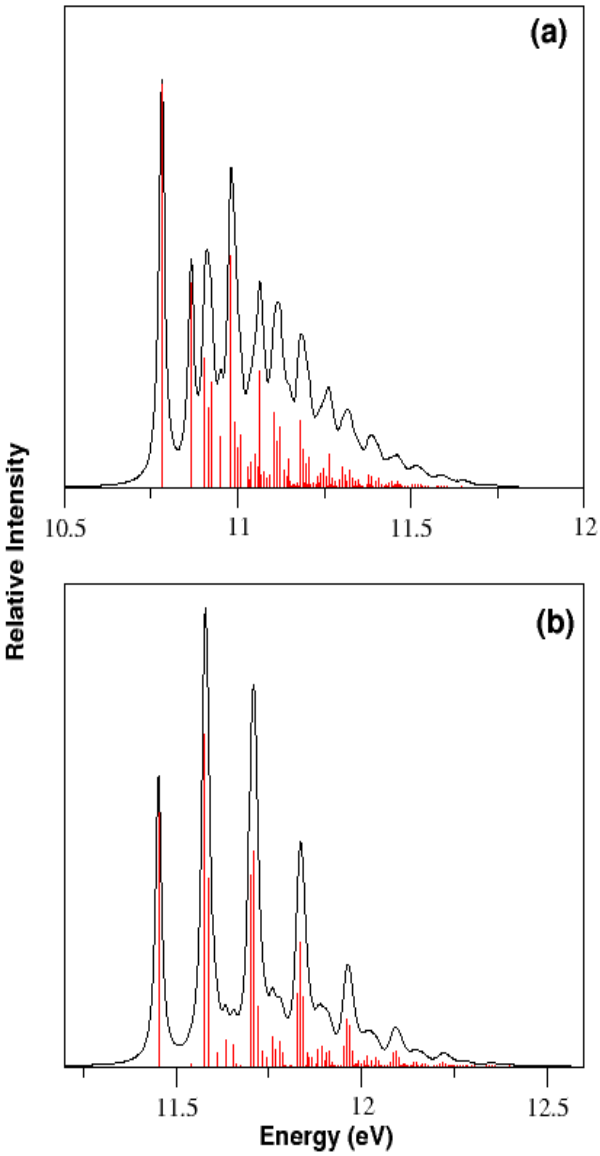

Figure 6.6: Same as in Figure 5.6 shown for the uncoupled vibronic band of $\widetilde{X}$ state of Pym^+.

Dominant progressions of vibrational modes ν_1, ν_2, ν_3 and ν_4 in the $\widetilde{B}$ state are found with the corresponding peak spacings of ~ 0.0643, ~ 0.1852, ~ 0.1874 and ~ 0.2019 eV, respectively.

It is also found that the vibrational modes ν_2 and ν_3 in the $\widetilde{C}$ state form the detectable progressions. The uncoupled state spectra of the $\widetilde{B}$ and $\widetilde{C}$ electronic states are shown in Figure 6.6.

The vibrational structures of the uncoupled $\widetilde{X}$ state reveal close resemblance with the experimental results [159]. The vibrational spectrum of the uncoupled $\widetilde{A}$ state reveals resolved vibrational structures whereas, it is found to be broad and structureless in the experiment. The coupling of $\widetilde{A}$ state particularly, with the $\widetilde{X}$ state appears to be extremely important in this case (also, see, the low-energy curve crossing in Figure 6.4). Similarly, the spectrum of uncoupled $\widetilde{B}$ and $\widetilde{C}$ electronic states are well resolved, whereas, complex and overlapping bands for these states are found in the experimental measurements [159]. This is due to the fact that these electronic states are very close in energy and various CIs occur well within their FC zone centers. These CIs are expected to have profound effect on the vibrational structure of these electronic states. Therefore, in order to understand the observed experimental vibronic structures, possible interstate couplings need to be considered in the nuclear dynamics. Such a dynamical simulation using the matrix diagonalization approach can no longer be carried out because of the huge number of electronic and nuclear degrees of freedom of these systems. A WP propagation approach within the MCTDH framework happened to be plausible and is therefore undertaken to accomplish the goal. The complete $\widetilde{X}$ -$\widetilde{A}$ -$\widetilde{B}$ -$\widetilde{C}$ electronic spectrum of Pym^+ is calculated by including the coupling among these states [cf., Hamiltonian of Eq.(6.3)] and considering 18 most relevant vibrational modes. In the WP calculations using the MCTDH approach [121] three, four dimensional and two, three dimensional particles are constructed by combining the vibrational modes. The details of the basis set and mode combinations employed in the WP propagations are given Table. 6. 9. The resulting

four states vibronic spectrum is presented in Figure 6.6 (bottom panel) along with the experimental [159] results (top panel). The former represents combined results of four separate WP propagations for four separate initial transitions to the $\widetilde{X}$, $\widetilde{A}$, $\widetilde{B}$ and $\widetilde{C}$ electronic states. In each calculation, the WP is propagated up to 150 fs and the resulting time autocorrelation function is damped with an exponential function [exp(-t/τ_r); with τ_r = 33 fs] before Fourier transformation. This damping corresponds to convolution of spectral lines with a Lorentzian line shape function of 40 meV FWHM. While the vibronic structures of the $\widetilde{X}$ state in Figure 6.7 remain almost same as the uncoupled state results, the vibronic structure of the $\widetilde{A}$, $\widetilde{B}$ and $\widetilde{C}$ states are heavily demolished by the non-adiabatic coupling. This is due to the fact that the minimum of the seam of $\widetilde{X}$ -$\widetilde{A}$ CIs is located only $\sim$ 0.01 eV above the minimum of the $\widetilde{A}$ state and therefore the low-lying vibronic levels of this state are strongly mixed with the high-lying vibronic levels of the $\widetilde{X}$ state. It can be seen that the overall broadening and the detail fine structures of the $\widetilde{A}$ band are in perfect accord with the experiment [159]. The complex vibronic structures of the overlapping $\widetilde{B}$ -$\widetilde{C}$ electronic manifold are also in very good accord with the experiment. The energetic minimum of these electronic states occurs in the vicinity of the minimum of the seam of various CIs within the $\widetilde{B}$ -$\widetilde{C}$ electronic states (cf., Section 6.3.1). The associated non-adiabatic coupling causes a strong mixing of their vibrational energy levels and as a result the vibronic bands become highly overlapping and complex.

6.4.2.2 S_1, S_2 and S_3 electronic states of Pym

Similar time-independent quantum mechanical calculations have been performed to examine the vibrational energy level structure of the uncoupled S_1, S_2 and S_3 electronic states of Pym. All the totally symmetric vibrational modes (ν_1 - ν_9) are consider in this case.

In the spectrum of the S_1 state, the series of peaks are $\sim$ 0.085, $\sim$ 0.133 and $\sim$ 0.143 eV spaced in energy corresponding to the progression along ν_1, ν_3 and

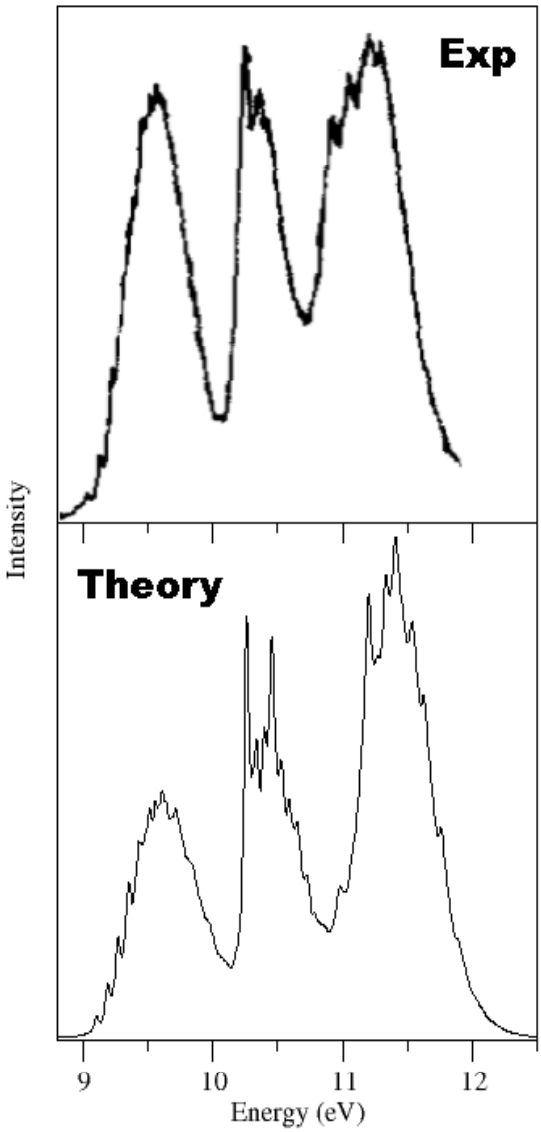

Figure 6.7: The photoelectron spectrum of the coupled $\widetilde{X}$ -$\widetilde{A}$ -$\widetilde{B}$ -$\widetilde{C}$ electronic states of Pym^+. The experimental (reproduced from Ref [159]) and the present theoretical results are shown in the top and bottom panels, respectively. The intensity (in arbitrary units) is plotted along the energy (measured relative to electronic ground state of Pym) of the final vibronic states.

Table 6. 9: Number of basis functions for the primitive as well as the single particle basis used in the MCTDH calculations.

Pym^+ Normal modes	Primitive basis[a]	SPF basis[b] [$\widetilde{X}$, $\widetilde{A}$, $\widetilde{B}$, $\widetilde{C}$]
(ν_1,ν_{10},ν_{19},ν_{21})	(8, 9, 8, 7)	[13, 8, 10, 8]
(ν_2,ν_7,ν_{13})	(9, 7, 8, 8)	[11, 12, 7]
(ν_3,ν_8,ν_{10})	(8, 9, 7, 8)	[11, 9, 11]
(ν_4,ν_5,ν_9,ν_{16})	(7, 8, 9, 8)	[10, 7, 8, 7]
(ν_6,ν_{18},ν_{14},ν_{24})	(9, 8, 7, 8)	[12, 10, 10, 9]
Pyrimidine		
(ν_1,ν_8,ν_{13},ν_{15})	(8, 9, 8)	[10, 4, 8, 10]
(ν_2,ν_4,ν_{11},ν_{19})	(9, 7, 8)	[12, 10, 10, 10]
(ν_5,ν_{12},ν_{16})	(8, 9, 7)	[11, 10, 10]
(ν_6,ν_9,ν_{14},ν_{18})	(7, 8, 9)	[12, 4, 7, 10]
(ν_3,ν_7,ν_{10},ν_{17})	(8, 7, 8)	[10, 4, 10, 10]

[a]The primitive basis is the number of Harmonic oscillator DVR functions, in the dimensionless coordinate system required to represent the system dynamics along the relevant mode. The primitive basis for each particle is the product of the one-dimensional bases; e.g for particle 1 in the set given for Figure 6.6. the primitive basis contains $13 \times 8 \times 10 \times 8 = 8320$ functions and the full primitive basis consists of a total of 3.544×10^{17} functions. [b] The SPF basis is the number of single-particle functions used.

ν_4 vibrational modes, respectively.

In the S_2 state spectrum the vibrational modes ν_1, ν_3, ν_5 and ν_6 form the major progressions. The peaks are $\sim$ 0.085, $\sim$ 0.133, $\sim$ 0.177 and $\sim$ .199 eV spaced, respectively, corresponding to the frequencies of these vibrational modes. The uncoupled state spectra of S_1, S_2 and S_3 electronic state of Pym is shown in Figure 6.8. The vibrational modes ν_1, ν_2 and ν_3 form dominant progressions in the S_3 state.

The vibrational spectrum of the uncoupled S_1, S_2 and S_3 electronic states reveal resolved vibrational structures whereas, a broad and structureless band for the S_2 and S_3 electronic states are observed in the experiment [166]. The coupling between S_1-S_2, S_1-S_3, and S_2-S_3 electronic states appears to be extremely important in this case.

Despite the fact that the uncoupled state spectra discussed above are helpful in understanding the important roles played by different vibrational modes in each electronic state, they deviate significantly from the observed bands in practice. Coupling between states is necessarily be considered to capture most of the features of the experimental observations [166]. The MCTDH algorithm is used for this dynamical simulation. Three WP calculations are carried out by launching the initial WP on each of the three electronic states separately. The details of the mode combinations and the sizes of the basis sets are given in Table 6.9. In each calculation the WP is propagated for 150 fs. The time autocorrelation function is damped with an exponential function of relaxation time 66 fs, and then Fourier transformed to generate the spectrum. The results from three different calculations are combined with equal weighteage to generate the composite theoretical band shown in Figure 6.8 (bottom panel) along with the experimental results (top panel) reproduced from Reference [166]. It can be seen from the figure that except for the first band, the distinct vibronic structures of the uncoupled state spectrum are completely blurred in the coupled state spectrum. The non-adiabatic coupling effects are particularly severe for the second

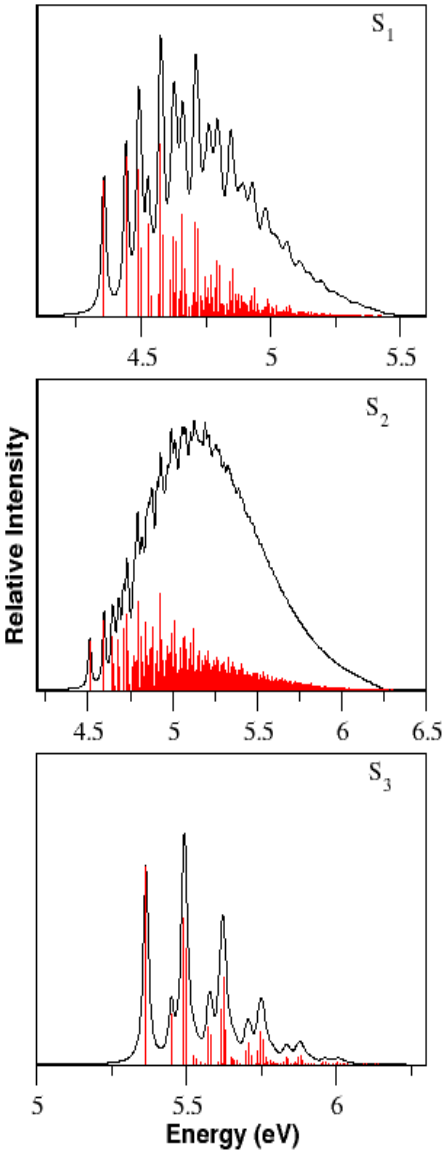

Figure 6.8: The uncoupled vibronic band of the S_1, S_2 and S_3 electronic state of Pym computed with relevant nine a_1 (ν_1-ν_9) vibrational modes within the linear vibronic coupling scheme in panel a, b and c respectively. The theoretical stick spectrum in each panel is convoluted with a Lorentzian function of 20 meV FWHM to calculate the spectral envelope.

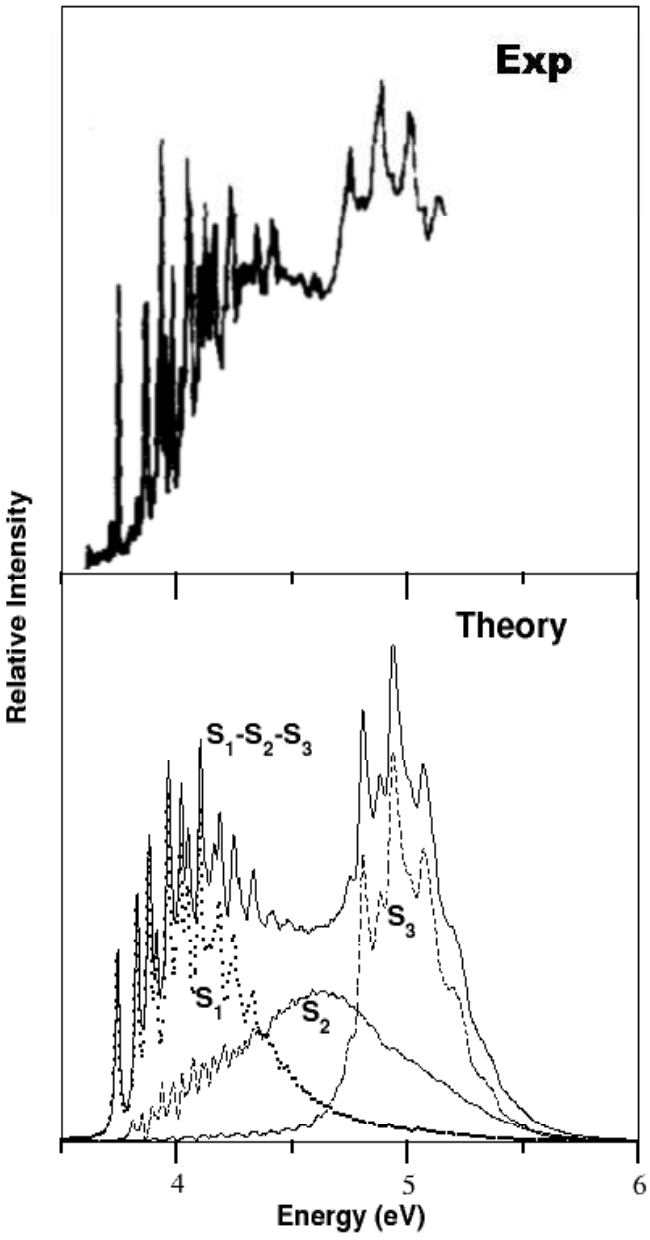

Figure 6.9: The absorption spectrum of the coupled S_1 - S_2 - S_3 electronic states of Pym and the experimental (reproduced from Ref [166]) and the present theoretical results are shown in the bottom and top panels, respectively. The intensity (in arbitrary units) is plotted along the energy (measured relative to electronic ground state of Pym) of the final vibronic states.

and third bands. It can be seen from Figure 6.8 that the present theoretical results are in very good agreement with the laboratory experiment [166].

6.4.3 Internal conversion rate

6.4.3.1 Electronic states of Pym^+

The time-dependent populations of the four diabatic electronic states of Pym^+ in the coupled state dynamics of section 6.4.2.1 are shown in Figures 6.10 (a-c). The results obtained by initially populating the $\widetilde{A}$, $\widetilde{B}$ and $\widetilde{C}$ electronic states are shown in panels a-c, respectively. The four electronic populations are indicated by four different line types in panel *b*. It is observed that insignificant population flows to all the three excited states when the WP is initially prepared on the $\widetilde{X}$ state and the corresponding figure is therefore not included here. This is due to the fact that the CIs of the $\widetilde{X}$ state with all other states are located at higher energies and are not accessible to the WP during its evolution on this state. This results into the observed sharp vibrational level structure of the $\widetilde{X}$ band (cf., Figure 6.7). A rapid transfer of $\widetilde{A}$ state population to the $\widetilde{X}$ state can be seen from panel (a) of Figure 6.9. Within $\sim$ 50 fs, 50% of the population transfers to the $\widetilde{X}$ state through the $\widetilde{X}$ -$\widetilde{A}$ CIs. This is due to the fact that the minimum of the seam of $\widetilde{X}$ -$\widetilde{A}$ CIs located only $\approx$ 0.02 eV above the equilibrium minimum of the $\widetilde{A}$ state. A decay rate of $\sim$ 50 fs is estimated from an exponential fit to the initial decay of population of the $\widetilde{A}$ state. Very minor population transfer to the remaining electronic states ($\widetilde{B}$ and $\widetilde{C}$) indicates that the dynamics of $\widetilde{A}$ state is not affected by these excited states in the present time scale.

The diabatic populations of the four electronic states are shown in panel (b) for an initial location of the WP on the $\widetilde{B}$ state. The population of $\widetilde{B}$ state decays to $\sim$ 0.25 within 50 fs and remains almost unchanged during the entire course of propagation time. A sharp rise in the population of $\widetilde{A}$ state as time increases indicates that the population transfer occurs through $\widetilde{A}$ -$\widetilde{B}$ CI. It is

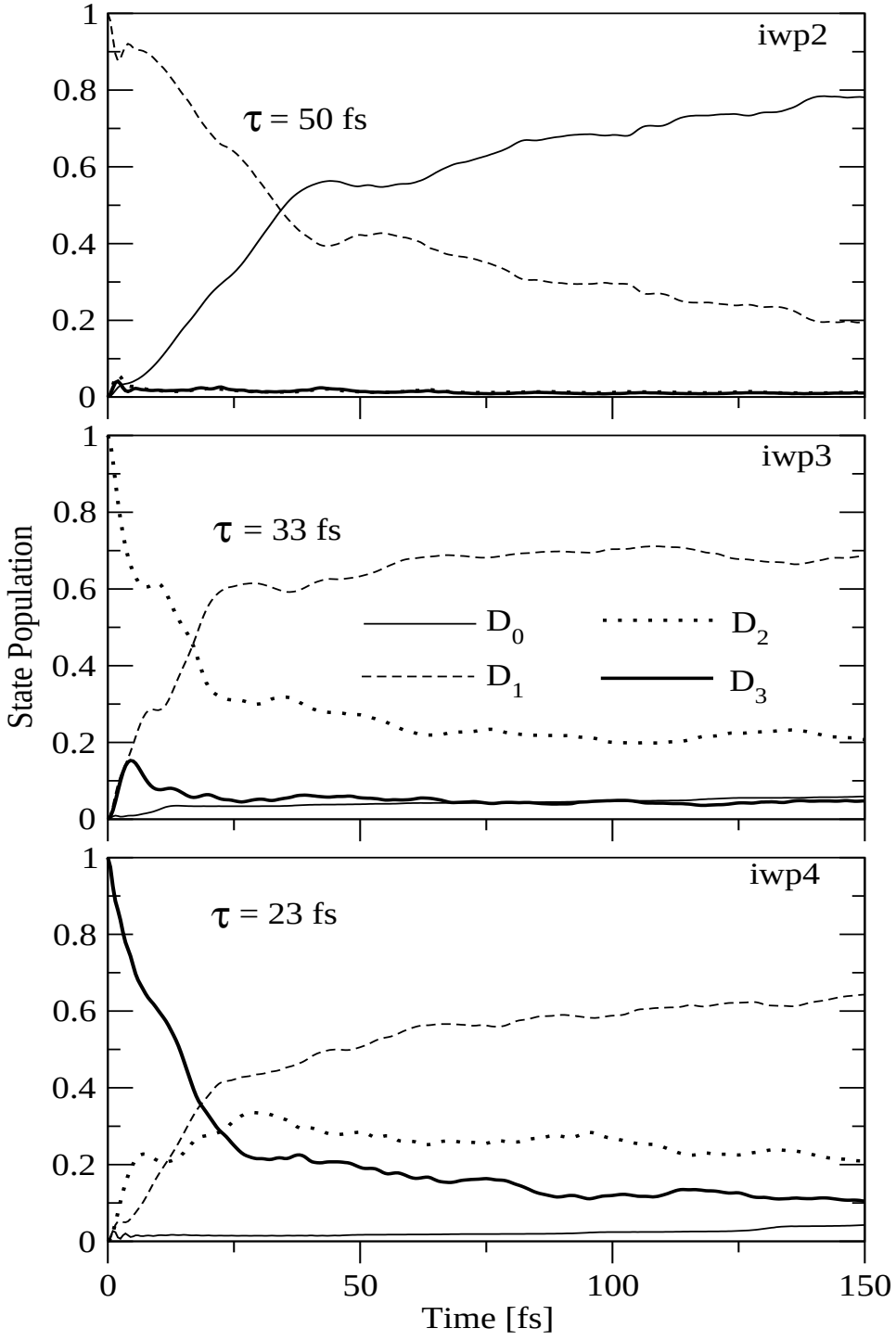

Figure 6.10: The populations (diabatic) in time of the $\widetilde{X}$ (thin lines), $\widetilde{A}$ (thin dashed lines), $\widetilde{B}$ (thin dotted lines) and $\widetilde{C}$ (thick line) states for an initial transition of the WP to the $\widetilde{A}$ (panel a), $\widetilde{B}$ (panel b) and $\widetilde{C}$ (pane c) in the coupled $\widetilde{X}$ -$\widetilde{A}$ -$\widetilde{B}$ -$\widetilde{C}$ states dynamics of Pym^+.

clear from the diagram that the remaining excited ($\widetilde{X}$ and $\widetilde{C}$) states do not have any significantly contribution to the dynamics of the $\widetilde{B}$ state. A decay rate of $\approx$ 33 fs is derived from an exponential fit to the population curve of the $\widetilde{B}$ state. This faster relaxation of the $\widetilde{B}$ state is in par with the observed broadening of this band in Figure 6.6. This supports the observed lack of fluorescence emission from this state and photostability of Pym^+.

Finally the time evolution of the WP on the $\widetilde{C}$ state is shown in panel d. In this case most of the population flows to the $\widetilde{B}$ and $\widetilde{A}$ state via the $\widetilde{A}$ -$\widetilde{C}$ and $\widetilde{B}$ -$\widetilde{C}$ CIs located nearly at the minimum of the $\widetilde{C}$ state. A very minor population also flows to the $\widetilde{X}$ state via the $\widetilde{X}$ -$\widetilde{C}$ CIs. The initial fast decay of the population relates to a life-time of $\sim$ 23 fs of the $\widetilde{C}$ state of Pym^+.

6.4.3.2 Electronic states of Pym

Time-dependence of diabatic electronic populations in the coupled S_1-S_2-S_3 states dynamics of Pym by initially locating the WP on S_1, S_2 and S_3 states are shown in the panel a-c, respectively, of Figure 6.11. The line types of the population curves are shown in panel a of Figure 6.11. The electron population flows to the S_2 state very slowly when the WP initially prepared on the S_1 state. As discussed in section 6.3.1 that the CIs of S_1-S_2 state occur at lower energies relative to the minimum of S_2 electronic state. Thus the WP can access the S_1-S_2 CI during the evolution of time. As a result the internal conversion rate of 240 fs is found from an exponential fit of diabatic electronic population.

The electronic populations for an initial location of the WP on the S_2 state shown in panel a of Figure 6.11 reveal population transfer to the S_1 state. The minimum of the S_1-S_2 CIs located $\sim$ 0.72 eV above the minimum of the S_2 state. The faster decay of S_2 state population relates to a decay rate of $\sim$ 30 fs, and accounts for the relatively structureless band of this state (cf., Figure 6.9).

The decay of the population of the S_3 state is much faster. A decay rate of $\sim$ 22 fs can be estimated from the initial fast decay of the S_3 state. The occurrence

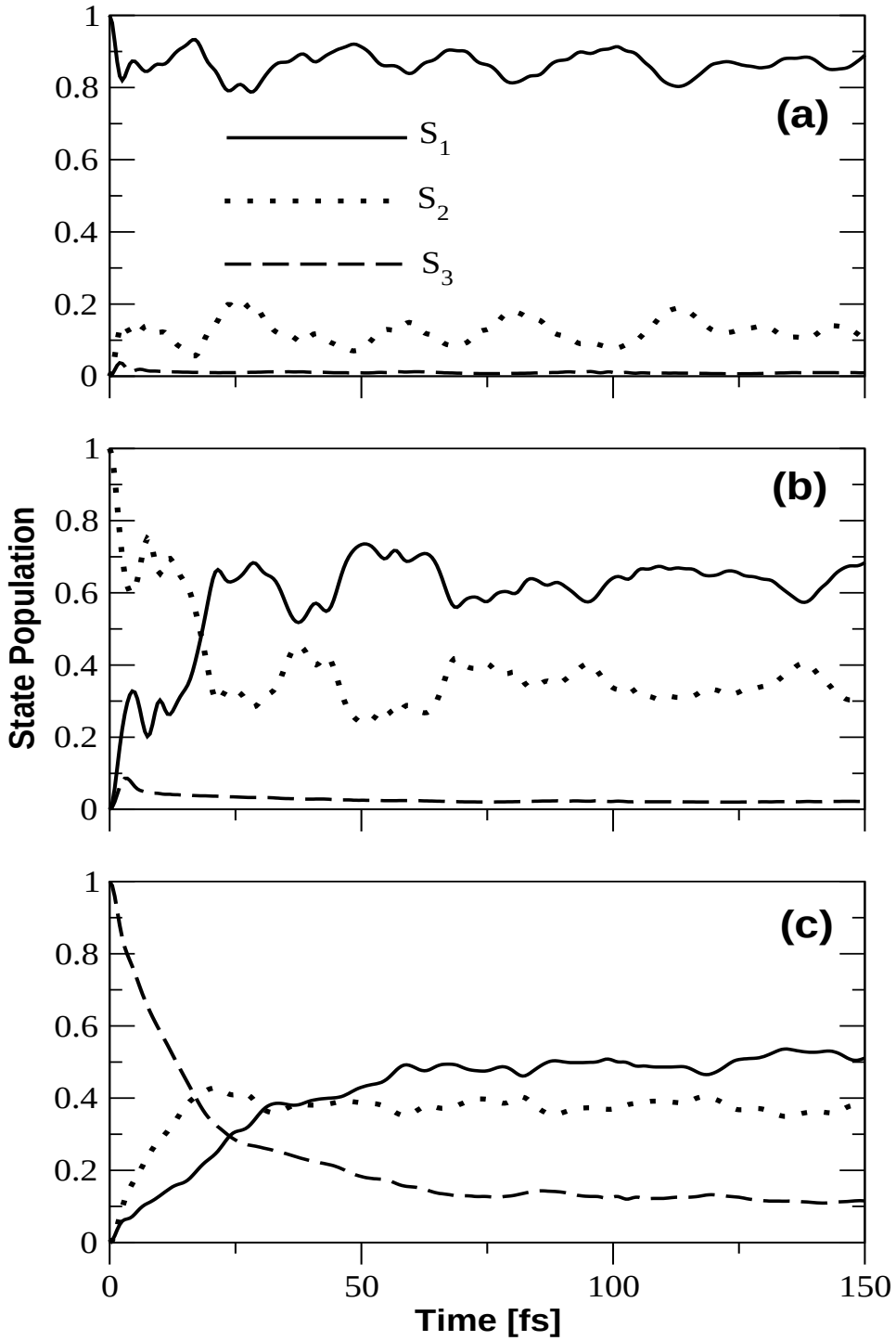

Figure 6.11: The populations (diabatic) in time of the S_1 (solid lines), S_2 (dotted lines) and $\widetilde{B}$ (dashed lines) states for an initial transition of the WP to the S_1 (panel a), S_2 (panel b) and S_3 (pane c) in the coupled S_1-S_2-S_3 states dynamics of Pym.

of the minimum of the S_2-S_3 and S_1-S_3 CIs $\sim$ 0.1 eV and $\sim$ 0.13 eV above the minimum of the S_3 state causes this rapid decay. This implies that the WP evolving on the S_3 states undergoes internal conversion to the S_2 state via the low-energy S_2-S_3 CIs and subsequently moves to the S_1 state via the S_1-S_3 and S_1-S_2 CIs. The ultrafast deactivation of S_3 state of Pym relates to the broadening of the S_3 absorption band and lack of fluorescence of this state and photostability of this state.

6.5 Summary

The vibronic energy level spectrum and dynamics of coupled first three excited electronic states of Pym and first four excited electronic states of Pym^+, are theoretically examined. A model diabatic vibronic Hamiltonian is constructed and the coupling parameters of the model Hamiltonian are obtained from the extensive *ab initio* electronic structure calculations. The nuclear dynamical simulations are carried out by time-independent and time- dependent quantum dynamical methods. The theoretical observations are in good accord with the experimental findings.

Relevant electronic ground and excited PESs and their coupling surfaces are constructed *ab initio*. Various stationary points on these PESs (minimum of the seam of CIs and minimum of the state) are estimated and their impact on the nuclear dynamics is studied in details. The existence of the several low-laying CIs of the PESs makes the dynamics on the coupled electronic manifold very complex and the resulting vibronic bands exhibit diffuse and broad structure.

The uncoupled states vibronic spectrum are obtained by matrix diagonalization method and full vibronic bands for the coupled electronic states of Pym^+ and Pym, are obtained by WP propagation method. The theoretical results are in good accord with the experimental photoelectron spectrum and UV absorption spectrum.

We have estimated the life-time of excited electronic states from the diabatic electronic state population. The calculated internal conversion rates for the $\widetilde{A}$, $\widetilde{B}$ and $\widetilde{C}$ electronic states of Pym^+ are $\sim$ 50 fs, $\sim$ 33 fs and $\sim$ 23 fs, respectively. The ultrafast deactivation of excited electronic states of Pym are $\sim$ 240 fs, $\sim$ 30 and $\sim$ 22 fs for the S_1, S_2 and S_3 electronic states, respectively.

Chapter 7

Summarizing remarks and future directions

A detailed theoretical study of the photoinduced nonadiabatic quantum dynamics on coupled electronic states of polyatomic molecules and molecular radical cations is presented in this thesis. It is established in conjunction with observed experimental data that complex VC of electronic states plays crucial role in all the studied examples. The most important result of VC is occurrence of conical intersections of electronic states. Theoretical treatment of VC in polyatomic molecules of growing size progressively becomes tedious. Thus the essential assumptions and simplifications are often exercised to in a theoretical study. Suitable VC model Hamiltonians are developed in the thesis by performing detailed *ab initio* electronic structure calculations. These Hamiltonians are used subsequently to investigate the nuclear dynamics by quantum mechanical methods. The final theoretical results are compared with the available experimental results of all the problems treated. The major findings are the following.

The quantum dynamical study of the coupled $\widetilde{X}^2E$ -$\widetilde{A}^2A_1$ electronic states of MC^+ reveals that the JT interactions are particularly weak in the ground $\widetilde{X}^2E$ electronic manifold of this cation but the PJT interactions of this ground

electronic manifold with the first excited $\widetilde{A}^2A_1$ electronic state of the radical cation are stronger which cause an increase of the spectral line density. The estimated JT stabilization energy for the $\widetilde{X}^2E$ electronic state is ~ 0.03 eV. The energetic minimum of this seam of CI between the $\widetilde{X}$ and $\widetilde{A}$ states occur at $\approx$ 12.79 eV. This minimum occurs well within the range of the second photoelectron band and only ≈ 0.68 eV above the minimum of the JT CIs. The CH_3 deformation modes of a_1 and e symmetries and C-N stretching mode of a_1 symmetry, play crucial roles in the nuclear dynamics. The nonradiative decay rates of ~ 50 fs and ~ 28 fs, are estimated for the JT split components of the $\widetilde{X}$ ^{2}E and the $\widetilde{A}$ ^{2}A$_1$ electronic states of MC^+, respectively.

Investigation of the structure and dynamics of the energetically lowest six electronic states of An^+ reveals that 31 (out of 66) vibrational modes are relevant for the dynamical simulations. One Condon active (a_g) mode ν_9 (C=C stretching) is found to contribute mostly to the nuclear dynamics in all the electronic manifold. The strong nonadiabatic coupling between $\widetilde{A}$ and $\widetilde{B}$ states is responsible for the broad and structureless vibronic band of $\widetilde{B}$ state which relates to a decay rate of ~ 30 fs. Such an ultrafast decay is the mechanism mechanism underlying low quantum yield of fluorescence from this state. A rapid noradiative transfer of this state makes it photostable. The close proximity of $\widetilde{C}$ and $\widetilde{D}$ electronic states and the strong nonadiabatic coupling between them leads to the observed overlapping broad and structureless vibronic bands of these states. Nonradiative decay of ~ 333 fs and ~ 38 fs are estimated for the $\widetilde{C}$ and $\widetilde{D}$ states, respectively. The energetic minima of CIs of the $\widetilde{X}$ state with the other electronic states are located at higher energies. Therefore, the vibronic structure of the $\widetilde{X}$ band is not perturbed by the nonadiabatic interactions. The $\widetilde{A}$ state is weakly coupled with the $\widetilde{X}$ state through the vibrational mode of symmetry b_{3g} which yields the resolved vibronic structure of the $\widetilde{A}$ band and a nonradiative decay rate of ~ 225 fs is estimated for this state.

Vibronic dynamics of coupled $\widetilde{X}$ -$\widetilde{A}$ -$\widetilde{B}$ -$\widetilde{C}$ electronic states of Bl^+ reveals

that the JT effect is very strong in the $\widetilde{A}$ and $\widetilde{B}$ states, and the PJT coupling of the $\widetilde{B}$ state with the $\widetilde{C}$ state is also found to be very strong. The estimated JT stabilization energy for the $\widetilde{A}$ and $\widetilde{B}$ states is $\sim$ 0.25 eV and $\sim$ 0.21 eV, respectively. The energetic location of the minimum of seam of CIs between the $\widetilde{B}$ and $\widetilde{C}$ states is found at $\sim$ 11.54 eV which is $\sim$ 0.004 eV below the minimum of the $\widetilde{C}$ electronic state. The ν_6 vibrational mode is excited strongly in the $\widetilde{X}$, $\widetilde{A}$ and $\widetilde{B}$ electronic states. The dominant progression is formed by the degenerate ν_{21} vibrational mode in the second vibronic band. In the third vibronic band, the ν_3, ν_4, ν_5, ν_{17}, ν_{18}, ν_{19}, ν_{20} and ν_{21} vibrational modes are strongly excited. The nuclear dynamics on the coupled $\widetilde{X}$ -$\widetilde{A}$ -$\widetilde{B}$ -$\widetilde{C}$ state with thirty vibrational modes is studied by the WP propagation method. The final theoretical results so obtained are in good accord with the experiment. The bimodal spectral profile of $\widetilde{A}$ vibronic band is observed due to the strong JT interaction in this state. The strong PJT coupling and close proximity of the $\widetilde{B}$ and $\widetilde{C}$ electronic state leads to broad, diffuse and overlapping vibronic bands for the $\widetilde{B}$ and $\widetilde{C}$ electronic states of Bl^+ . The internal conversion rate for the $\widetilde{A}$ electronic state is estimated to be $\sim$ 50 fs. The later originates from strong JT intersections in this state. The estimated nonradiative decay rates of the $\widetilde{B}$ and $\widetilde{C}$ states are found to be $\sim$ 33 fs and $\sim$ 7 fs, respectively. Strong $\widetilde{B}$ -$\widetilde{C}$ PJT coupling leads to a very fast decay of the $\widetilde{C}$ state and also makes the corresponding vibronic bands broad and diffuse.

Investigation of vibronic dynamics of first three excited electronic states of Pym and first four electronic states of Pym^+ reveals strong VC effects in their vibronic energy level structure. The theoretical findings are in good accord with the experimental observations. Relevant electronic ground and excited PESs and their coupling surfaces are constructed *ab initio*. Various stationary points on these PESs (minimum of the seam of CIs and minimum of the state) are estimated and their impact on the nuclear dynamics is studied in details. The existence of the several low-laying CIs of the PESs makes the dynamics on the coupled electronic manifold very complex and the resulting vibronic bands exhibit

diffuse and broad structure. The calculated internal conversion rates for the $\widetilde{A}$, $\widetilde{B}$ and $\widetilde{C}$ electronic states of Pym^+ are $\sim$ 50 fs, $\sim$ 33 fs and $\sim$ 23 fs, respectively. The nonradiative decay rates of excited electronic states of Pym are $\sim$ 240 fs, $\sim$ 30 and $\sim$ 22 fs for the S_1, S_2 and S_3 electronic states, respectively.

Identifying the carriers of DIBs has become one of the classic astrophysical spectroscopic problems. Recent work suggests they are caused by PAHs, or, most likely, their cations, since PAH ions of all sizes, long carbon-chain molecules, and fullerenes, absorb in the visible and near infrared, and such molecules are expected to be ionized by the intense ultraviolet field present in much of the interstellar medium. PAH molecules appears to have profound implications in the physics, chemistry and biology of ISM. The observed broad and diffuse vibronic band, ultrafast internal conversion rate of low-lying excited electronic state and lack of fluorescence are in favor of PAH hypothesis. The PAH cation is highly photostable than their neutral counterpart. Recently nitrogenated PAH molecule (PANH) also found in astrophysical environment. These N-heterocycles are found in the genetic material of all living organisms on Earth. The work underlying this thesis is a step forward in theoretical studies of PAH molecules. The developed strategies can be further extended to more complex systems in order to identify a large part of the DIBs unambiguously.

The quantum dynamics on coupled electronic manifold of PESs is examined without incorporating the spin-orbit coupling parameters in the model diabatic Hamiltonian. It will be worthwhile to include the spin-orbit coupling in the VC models developed in this thesis.

Bibliography

[1] M. Born and R. Oppenheimer, Ann. Phys. **84**, 457 (1927).

[2] M. Born and K. Haung: Dynamical Theory of Crystal Lattices. Oxford University Press, New York (1954).

[3] R. G. Bray and M. J. Berry, J. Chem. Phys. **71**, 4909 (1979); P. R. Stannard, M. L. Elert and W. M. Gelbart, ibid. **74**, 6050 (1981).

[4] J. Ford, Advan. Chem. Phys. **24**, 155 (1973); I. C. Percival, ibid. **36**, 1 (1977).

[5] D. F. Heller and S. Mukamel, J. Chem. Phys. J. Chem. Phys. **70**, 463 (1979); K. F. Freed and A. Nitzan, ibid. **73**, 4765 (1980).

[6] W. H. Miller, ed., Dynamics of Molecular Collisions

[7] H. A. Jahn and E. Teller, Proc. R. Soc. London, Ser. A **161**, 220 (1937).

[8] R. Englman, *The Jahn-Teller Effect in Molecules and Crystals* (Wiley, New York, 1972).

[9] I. B. Bersuker *The Jahn-Teller Effect and Vibronic Interactions in Modern Chemistry* (Plenum Press, New York, 1984).

[10] G. Fischer, *Vibronic Coupling* (Academic Press, London, 1984).

[11] *The Dynamical Jahn-Teller Effect in Localized Systems*, edited by Y. E. Perlin and M. Wagner (North-Holland, Amsterdam, 1984).

[12] I. B. Bersuker and V. Z. Polinger, *Vibronic Interactions in Molecules and Crystals* (Springer-Verlag, Berlin, 1989).

[13] I. B. Bersuker, Chem. Rev. **101**, 1067 (2001) and the references therein.

[14] I. B. Bersuker, *The Jahn-Teller Effect* (Cambridge University Press, 2006).

[15] H. C. Longuet-Higgins, U. Öpik, M. H. L. Pryce, and R. A. Sack, Proc. R. Soc. London, Ser. A **244**, 1 (1958).

[16] U. Öpik and M. H. L. Pryce, Proc. R. Soc. London, Ser. A **238**, 425 (1957).

[17] H. C. Longuet-Higgins, in *Advances in Spectroscopy*, H. W. Thompson (Ed.), Interscience, New York, 1961, Vol. II, p.429.

[18] J. E. Huheey, E. A. Keiter, and R. L. Keiter, *Inorganic Chemistry: Principles of structure and reactivity, 4th ed.* (Haper Collins, New York, 1993).

[19] M. D. Sturge, Solid State Phys. **20**, 91 (1967).

[20] M. D. Kaplan and B. G. Vekhter, *Cooperative phenomena in Jahn-Teller Crystals* (Plenum Press, New York, 1995).

[21] L. R. Falvello, J. Chem. Soc., Dalton Trans. **23**, 4463 (1997).

[22] *In Molecular Ions: Spectroscopy, Structure, and Chemistry*, edited by T. A. Miller and V. E. Bondybey (North-Holland, Amsterdam, 1983).

[23] H. Köppel, W. Domcke, and L. S. Cederbaum, Adv. Chem. Phys. **57**, 59 (1984).

[24] H. Köppel, Z. für Physikal. Chemie. **200**, 3 (1997).

[25] T. A. Barckholtz and T. A. Miller, Int. Rev. Phys. Chem. **17**, 435 (1998).

[26] T. A. Barckholtz and T. A. Miller, J. Phys. Chem. A **103**, 2321 (1999).

[27] C. C. Chancey and M. C. M. O'Brien, *The Jahn-Teller Effect in C_{60} and Other Icasahedral Complexes* (Princeton University Press, Princeton, New Jersey, 1997).

[28] G. Herzberg, *Molecular Spectra and Molecular Structure* (Van Nostrand, New York, 1966), Vol. **III**.

[29] S. Mahapatra and H. Köppel, J. Chem. Phys. **109**, 1721 (1998); H. Köppel, M. Döscher, and S. Mahapatra, Int. J. Quant. Chem. **80**, 942 (2000).

[30] S. Mahapatra, G. A. Worth, H. -D. Meyer, L. S. Cederbaum, and H. Köppel, J. Phys. Chem. A **105**, 5567 (2001).

[31] H. Köppel, M. Döscher, I. Bâldea, H. -D. Meyer, and P. G. Szalay, J. Chem. Phys. **117**, 2657 (2002).

[32] C. Woywod, S. Scharfe, R. Krawczyk, W. Domcke, and H. Köppel, J. Chem. Phys. **118**, 5880 (2003).

[33] *Conical Intersections: Electronic Structure, Dynamics and Spectroscopy*, edited by W. Domcke, D. R. Yarkony, and H. Köppel (WorldScientific, Singapore, 2004).

[34] M. H. Perrin and M. Gouterman, J. Chem. Phys. **46**, 1019 (1967); J. H. van der Waals, A. M. D. Berghuis, and M. S. de Groot, Mol. Phys. **13**, 301 (1967); J. H. van der Waals, A. M. D. Berghuis, and M. S. de Groot, Mol. Phys. **21**, 497 (1971); P. J. Stephens, J. Chem. Phys. **51**, 1995 (1969).

[35] M. Z. Zgierski and M. Pawlikowski, J. Chem. Phys. **70**, 3444 (1979).

[36] H. Köppel, L. S. Cederbaum, and W. Domcke, J. Chem. Phys. **89**, 2023 (1988).

[37] L. S. Cederbaum, W. Domcke, and H. Köppel, Chem. Phys. **33**, 319 (1978).

[38] S. Mahapatra, L. S. Cederbaum, and H. Köppel, J. Chem. Phys. **111**, 10452 (1999).

[39] R. Renner, Z. Phys. **92**, 172 (1934).

[40] J. G. Bednorz and K. A. Müller, Perovskite type oxides: The new approach to high-Tc superconductivity, in: Nobel Lectures, Physics 1981-1990, (World Scientific, Singapore, 1993).

[41] J. V. Neumann and E. P. Wigner, Physik. Z. **30**, 467 (1929).

[42] E. Teller, J. Phys. Chem. **41**, 109 (1937).

[43] G. Herzberg and H. C. Longuet-Higgins, Discuss. Farad. Soc. **35**, 77 (1963).

[44] T. Carrington, Discuss. Farad. Soc. **53**, 27 (1972); Acc. Chem. Res. **7**, 20 (1974).

[45] C. A. Mead and D. G. Truhlar, J. Chem. Phs. **70**, 2284 (1979).

[46] M. Desouter-Lecomte, C. Galloy, J. C. Lorquet, and M. Vaz Pires, J. Chem. Phys. **71**, 3661 (1979).

[47] W. Domcke and G. Stock, Adv. Chem. Phys. **100**, 1 (1997).

[48] B. Heumann, R. Düren and R. Schinke, Chem. Phys. Lett. **180**, 583 (1991).

[49] B. Heumann, K. Weide, R. Düren and R. Schinke, J. Chem. Phys. **98**, 5508 (1993).

[50] B. Heumann and R. Schinke, J. Chem. Phys. **101**, 7488 (1994).

[51] N. Matsunaga and D. R. Yarkony, J. Chem. Phys. **107**, 7825 (1997).

[52] D. R. Yarkony, J. Chem. Phys. **104**, 7866 (1996).

[53] G. J. Atchity, S. S. Xantheas, K. Ruedenberg, J. Chem. Phys. **95**, 1862 (1991).

[54] A. Migani and M. Olivucci, Chapter 6, In; *Conical Intersections: Electronic Structure, Dynamics and Spectroscopy*, edited by W. Domcke, D. R. Yarkony, and H. Köppel (WorldScientific, Singapore, 2004).

[55] M. J. Paterson, M. A. Robb, L. Blancafort and A. D. DeBellis, J. Phys. Chem. A **109**, 7527 (2006).

[56] D. R. Yarkony, J. Phys. Chem. A **105**, 6277 (2001).

[57] H. Köppel and W. Domcke, Encyclopedia of Computational Chemistry, Ed., P. V. R. Schleyer, Wiley: New York, 1998, P. 3166.

[58] C. A. Mead, Rev. Mod. Phys. **64**, 51 (1992).

[59] B. K. Kendrick, J. Phys. Chem. A, **107**, 6739 (2003).

[60] B. K. Kendrick in Ref. [33], p.521.

[61] H. Müller and H. Köppel, Chem. Phys. **183**, 107 (1994).

[62] R. Schneider, W. Domcke, and H. Köppel, J. Chem. Phys. **92**, 1045 (1990).

[63] M. A. Robb, F. Bernardi, and M. Olivucci, Pure and Appl. Chem. **67**, 783 (1995).

[64] F. Bernardi, M. Olivucci, and M. A. Robb, Chem. Soc. Rev. **25**, 321 (1996).

[65] *Conical intersections in photochemistry, spectroscopy and chemical dynamics*, Chem. Phys. **259**, 121-337 (2000).

[66] J. Michl and V. Bonacic-Koutecky, *Electronic Aspects of Organic Photochemistry* (Wiley, New York, 1990).

[67] M. L. Heger, Lick. Obs. Bull. **10**, 141 (1922).

[68] Tielens. AGGM, Snow. TP, eds (1995) *The Diffuse Interstellar Bands* (Kluwer Academic, Dordrecht).

[69] Shida. T, Iwata. S (1973), *Electronic spectra of ions radicals and their molecular orbital interpretation. III. Aromatic Hydrocarbons.* J Am Chem Soc 95:3473-3483 .

[70] Salama. F, eds (1999) *Solid Interstellar Matter: The ISO Revolution* (Sciences, France).

[71] Szczepanski. J, Vala. M, Talbi. D, Parisel. O, Ellinger. Y (1993) *Electronic and vibrational spectra of matrix isolated anthracene radical cations: experimental and theoretical aspects.* J Chem Phys 98:4494-4511.

[72] Bréchignac. P, Pino. T (1999) *Electronic spectra of cold gas phase PAH cations: Towards the identification of the Diffuse Interstellar Bands carriers.* Astron Astrophys 343:L49-L52.

[73] Biennier. L, Salama. F, Allamandola. LJ (2003), *Pulsed discharge nozzle cavity ring-down spectroscopy of cold polycyclic aromatic hydrocarbon ions.* J Chem Phys 118:7863-7872.

[74] Zhao. L *et al.* (2004) *Ultrafast studies on the photophysics of matrix-isolated radical cations of polycyclic aromatic hydrocarbons.* J Phys Chem A 108:25-31.

[75] Sukhorukov. O *et al.* (2004) $D_2 \leftarrow D_0$ *transition of the anthracene cation observed by cavity ring-down absorption spectroscopy in a supersonic jet.* Chem Phys Lett 386:259-264.

[76] Iglesias-Groth. S, Manchado. A, García-Hernández. DA, González Hernández. JI, Lambert. DL (2008) *Evidence for the naphthalene cation in a region of the interstellar medium with anomalous microwave emission.* Astrophys J 685:L55-L58.

[77] Iglesias-Groth. S *et al.* (2010) *A search for the interstellar anthracene towards the Perseus anomalous microwave emission region.* Mon Not R Astron Soc 407:2157-2165.

[78] T. Allain, E. Sedlmayr and S. Leach, Astrophys. Space. Sci. **224**, 417 (1995).

[79] A. Goeres, Rev. Modern Astron. **6**, 165 (1993).

[80] K. Schroeter, D. Schröder and H. Schwarz **103**, 4174 (1999).

[81] T. Allain, S. Leach and E. Sedlmayr, Astron. Astrophys. **305**, 602 (1996).

[82] W. J. van der Hart, Int. J. Mass Spectrom. **214**, 269 (2002).

[83] G. Granucci, Y. Ellinger and P. Boissel, Chem. Phys. **191**, 165 (1995).

[84] F. Jolibois, A. Klotz, F. X. Gadéa and C. Joblin, Astron. Astrophys. **444**, 629 (2005).

[85] D. Rolland *et al.* , *Chem. Phys. Lett.* **373**, 292 (2003).

[86] R. S. Sánchez-Carrera *et al.* , *J. Phys. Chem. B.* **110**, 18904 (2006).

[87] P. A. Clark *et al.*, *Helv. Chim. Acta.* **1972** 55, 1415.

[88] R. Boschi *et al.*, *Faraday Discuss. Chem. Soc.* **1972** 54, 116.

[89] W. Schmidt, J. Chem. Phys. **66** 828 (1977).

[90] M. Born, Nachirichten Akad. Wiss. Göttingen, Math.-Physik Kl. II, Berlin, (1951).

[91] M. Born and K. Huang, *The Dynamical Theory of Crystal Lattices* (Oxford University Press, London, UK, 1954).

[92] L. S. Cederbaum and W. Domcke, Adv. Chem. Phys. **36**, 205 (1977).

[93] B. H. Lengsfield and D. R. Yarkony, Adv. Chem. Phys. **82**, 1 (1992).

[94] G. A. Worth and L. S. Cederbaum, Ann. Rev. Phys. Chem. **55**, 127 (2004).

[95] M. Baer, Mol. Phys. **40**, 1011 (1980).

[96] C. A. Mead and D. G. Truhlar, J. Chem. Phys. **77**, 6090 (1982).

[97] M. Baer, Chem. Phys. Lett. **35**, 112 (1975).

[98] V. Sidis, Adv. Chem. Phys. **82**, 73 (1992).

[99] M. Baer, Adv. Chem. Phys. **82**, 187 (1992).

[100] W. Lichten, Phys. Rev. **131**, 229 (1963).

[101] H. C. Longuet-Higgins, Proc. Roy. Soc. London, Ser. A, **344**, 147 (1975).

[102] R. K. Preston and J. C. Tully, J. Chem. Phys. **54**, 4297 (1971).

[103] G. Hirsch, P. J. Bruna, R. J. Buenker, and S. D. Peyerimhoff, Chem. Phys. **45**, 335 (1980)

[104] H. J. Werner and W. Meyer, J. Chem. Phys. **74**, 5802 (1981).

[105] T. Pacher, L. S. Cederbaum, and H. Köppel, Adv. Chem. Phys. **84**, 293 (1993).

[106] A. Thiel and H. Köppel, J. Chem. Phys. **110**, 9371 (1999).

[107] H. Köppel, J. Gronki, and S. Mahapatra, J. Chem. Phys. **115**, 23771 (2001).

[108] H. Köppel in Ref. [33], p.429

[109] E. B. Wilson Jr., J. C. Decius, and P. C. Cross, *Molecular vibrations* (McGraw-Hill, New York, 1955).

[110] D. R. Hartree, The Calculation of Atomic Structures, Wiley, 1957; C. Froese Fischer, The Hartree Fock Method for Atoms, Wiley, 1977.

[111] P. Pulay and S. Saebo, Theor. Chim. Acta. **69**, 357 (1986).

[112] T. H. Dunning, Jr., J. Chem. Phys. 90 (1989) 1007.

[113] L. S. Cederbaum, J. Phys. B, 8 (1975) 290.

[114] P. J. Knowles and H.-J. Werner, Chem. Phys. Lett. **115**, 259 (1985).

[115] H.-J. Werner and P. J. Knowles, J. Chem. Phys. **89**, 5803 (1988).

[116] T. Korona and H.-J. Werner, J. Chem. Phys. **118**, 3006 (2003).

[117] R. Meiswinkel and H. Köppel, Chem. Phys. **144**, 117 (1990).

[118] W. Domcke, H. Köppel, and L. S. Cederbaum, Mol. Phys. **43**, 851 (1981).

[119] J. Cullum and R. Willoughby, *Lanczos Algorithms for Large Symmetric Eigenvalue Problems* (Birkhäuser, Boston, 1985), Vols. I and II.

[120] E. Heller, J. Chem. Phys. **68**, 2066 (1978); Acc. Chem. Res. **84**, 293 (1981).

[121] G. A. Worth, M. H. Beck, A. Jäckle, and H. -D. Meyer, The MCTDH Package, Version 8.2, (2000), University of Heidelberg, Germany. H. -D. Meyer, Version 8.3, (2002). See http://www.pci.uni-heidelberg.de/tc/usr/mctdh/

[122] H. -D. Meyer, U. Manthe, and L. S. Cederbaum, Chem. Phys. Lett. **165**, 73 (1990).

[123] U. Manthe, H. -D. Meyer, and L. S. Cederbaum, J. Chem. Phys. **97**, 3199 (1992).

[124] M. Ehara, H. -D. Meyer, and L. S. Cederbaum, J. Chem. Phys. **105**, 8865 (1996).

[125] M. H. Beck, A. Jäckle, G. A. Worth, and H. -D. Meyer, Phys. Rep. **324**, 1 (2000).

[126] S. Ghanta and S. Mahapatra, Chem. Phys. **347**, 97 (2008).

[127] D.M.P. Holland, L. Karlsson Journal of Electron Spectroscopy and Related Phenomena 150 (2006)47-55

[128] M. Gochel-Dupuis, J. Delwiche, M.-J. Hubin-Franskin and J.E. Collin,Chem. Phys. Letters **1,2,3** (1992)**193**

[129] Ralph H. Staley, James E. Kleckner, and J.L.Beauchamp J. Am. Chem. Soc. **98** 2081 (1976).

[130] By R. F. Lake and Sir Harold Thompson, For.Sec.R.S. Proc. R. Soc. London. A.**317** 187 (1970).

[131] G. Bieri, E. Heilbronner, V. Hornung, E. Kloster-Jensen, J. P. Maier, F. Thommen, W. von Niessen, Chem. Phys. 36 (1979) 1.

[132] L. Åsbrink, W. von Niessen, G. Bieri, J. Electron Spectrose. Relat. Phenom. 21 (1980) 93.

[133] L. Åsbrink, A. Svensson, W. von Niessen, G. Bieri, J. Electron Spectrose. Relat. Phenom. 24 (1981) 293.

[134] M. J. Frisch et. al. Gaussian 03, Revision B. 05, Gaussian, Inc., Pittsburgh PA, 2003.

[135] G. Herzberg, Electronic spectra and electronic structure of poltatomic molecule, Van Nostrand, New York, (1966). See http://srdata.nist.gov/cccbdb/expgeom2.asp/

[136] T. Shimanouchi, Tables of molecular vibrational frequencies, NSRDS-NBS, Circular No. 39 (US GPO, Washington, 1972).

[137] S. Mahapatra, V. Vallet, C. Woywod, H. Köppel and W. Domcke, Chem. Phys. 304 (2004) 17; S. Mahapatra, V. Vallet, C. Woywod, H. Köppel and W. Domcke, J. Chem. Phys. 123 (2005) 231103.

[138] T. S. Venkatesan and S. Mahapatra, J. Chem. Phys. 123 (2005) 114308.

[139] R. R. Kumar, T. S. Venkatesan, and S. Mahapatra, Chem. Phys. 329 (2006) 76.

[140] V. Sivaranjana Reddy, S. Ghanta and S. Mahapatra, Phys. Rev. Lett. **104**, 111102 (2010).

[141] S. Ghanta, V. Sivaranjana Reddy and S. Mahapatra, Phys. Chem. Chem. Phys. 2011.

[142] S. Ghanta, V. Sivaranjana Reddy and S. Mahapatra, Phys. Chem. Chem. Phys. 2011.

[143] L. J. Allamandola, A. G. G. M. Tielens, J. R. Barker, *Astrophys. J. Suppl. Ser.* **71**, 733 (1989).

[144] F. Salama, G. A. Galazutdinov, J. Krelowski, L. J. Allamandola, F. A. Musaev, *Astrophys. J.* **526**,265 (1999).

[145] T. P. Snow, V. Le Page, Y. Keheyan, V. M. Bierbaum, *Nature* **391**, 259 (1998).

[146] V. Le Page, Y. Keheyan, T. P. Snow, V. M. Bierbaum, *J. Am. Chem. Soc.* **121**, 9435 (1999).

[147] D. G. Streets, T. A. Williams, J. Electron Spectrosc. Relat Phenom. **3**, 71 (1974).

[148] N. S. Hush, A. S. Cheung, P. R. Hilton, J. Electron Spectrosc. Relat Phenom. **7**, 385 (1975).

[149] F. Brogli, E. Heilbronner, Theor. Chim. Acta **26** 289 (1972).

[150] G. Galazutdinov *et al.* , *Mon. Not. R. Astron. Soc.* 2011, **412**, 1259.

[151] S. N. Ketkar, M. Kelly, M. Fink, R. C. Ivey, *J. Mol. Struct.* 1981, **77**, 127.

[152] S. Zilberg, Y. Haas, S. Shaik, *J. Phys. Chem.* 1995, **99**, 16561.

[153] E. Gindensperger *et al* Chem. Phys. **338**, 207 (2007).

[154] J. Cami, J. Bernard-Salas, E. Peeters, S. E. Malek, *Science* **329**, 1180 (2010).

[155] T. Kobayasi, T. Kubota and K. Ezumi, J. Am. Chem. Soc. **105**, 2172 (1983).

[156] E. Haselbach, E. Heilbronner and G. Schro der, Helv. Chim. Acta. **54**, 153 (1971).

[157] S. Yamamoto *et al.* J. Chem. Phys. **86**, 529 (1982).

[158] F. A. Van-Catledge and C. E. McBride, J. Phys. Chem. **80**, 2987 (1976).

[159] R. Gleiter *et al.* , Helv. Chem. Acta. **55**, 255 (1972).

[160] A. D. Baker, D. W. Turner, Phil. Trans. Roy. Soc. Lond. A. **268** 131 (1970).

[161] A. W. Potts, D M P Holland, A B Trofimov, J Schirmer, L. Karlsson, K. Siegbahn, J. Phys. B: At. Mol. Opt. Phys. **36** 3129 (2003).

[162] M. Riese . J. Grotemeyer, Anal. Bioanal. Chem. **386**, 59 (2006).

[163] Kuan *et al.* Mon. Not. R.Astron.Soc. **345**, 650 (2003)

[164] Peeters *et al.* Astron. Astrophys. **433**, 583 (2005).

[165] M. Nuevo *et al.* Astrobiology. **9**, 683 (2009).

[166] A. Bolovinos *et al.* J. Mol. Spec. **103**, 240 (1984).

[167] J. E. Parkin and K. K. Innes, J. Mol. Spec. **15**, 407 (1965).

[168] Robin. M.Hochstrasser and Charles. J. Marzzacco, J. Mol. Spec. **42**, 75 (1972).

[169] L. Fernholt, C. Romming, Acta. Chem. Scand. A **32** 271 (1978).

[170] S. Cradock, P. B. Liescheski, D. W. H. Rankin, H. E. Roberson, J. Am. Chem. Soc. **110** 2758 (1988).

[171] N. Mikami, Y. Sugahara, M. Ito, J. Phys. Chem. **90** 2080 (1986).

[172] MOLPRO, version 2006.1, a package of *ab initio* program, H.-J. Werner, P. J. Knowles, R. Lindh, F. R. Manby, M. Schutz, and others, see http://www.molpro.net.

List of Publications

1. Tapta Kanchan Roy, **Susanta Ghanta**, Tanmoy Mondal, Banda Saritha, S. Mahapatra, and M. Durga Prasad, *"" Conformational preferrences of mono substituted cyclhydronitrogens : A Theoretical study" "*, J. Mol. Sturct. (THEOCHEM.) **822**, 145-150 (2007).

2. **S. Ghanta** and S. Mahapatra, *"Vibronic dynamics in the low-lying coupled electronic states of methyl cyanide radical cation""*, Chem. Phys. **347**, 97-109 (2008).

3. T. Mondal, B. Saritha, **S. Ghanta**, T. K. Roy, S. Mahapatra and M. Durgaprasad, *"On some strategies to design new high energy density molecules""*, J. Mol. Sturct.(THEOCHEM.) **897**,42-47 (2008).

4. V. Sivaranjana Reddy, **S. Ghanta** and S. Mahapatra, *"First principles quantum dynamical investigation provides evidence for the role of polycyclic aromatic hydrocarbon radical cations in interstellar space "*, Phys. Rev. Lett. **104**, 111102(1-4) (2010).

5. **S. Ghanta**, V. Sivaranjana Reddy and S. Mahapatra, *"Electronically excited naphthalene and anthracene radical cations as archetypical models for interstellar observations: I. Static aspects "*, Phys. Chem. Chem. Phys. (accepted for publication).

6. **S. Ghanta**, V. Sivaranjana Reddy and S. Mahapatra, *"Electronically excited naphthalene and anthracene radical cations as archetypical models for interstellar observations: II. Dynamic aspects"*, Phys. Chem. Chem. Phys. (accepted for publication).

7. **S. Ghanta** and S. Mahapatra, *"Quantum dynamics through conical intersections: The Jahn-Teller and pseudo-Jahn-Teller effects in barrelene radical cation. "*, (to be communicated)

8. **S. Ghanta** and S. Mahapatra, *"Theoretical investigations of the photostability of pyrimidine and its radical cation "*, (to be communicated)

Presentations in Conferences

1. Participant in "Theoretical Chemistry Symposium (TCS 2006)",
   December 11-13, 2006, Bharathidasan University, Thiruchirappalli.

2. Poster presented in "Chemfest 2007",
   March 9-10, 2007, School of Chemistry, University of Hyderabad, Hyderabad.

3. Poster presented in "Spectroscopy and Dynamics of Molecules and Clusters (SDMC 2008)",
   February 22-24, 2008, Indian Institute of Technology Madras, Chennai.

4. Poster presented in "Chemfest 2008",
   March 1-2, 2008, School of Chemistry, University of Hyderabad, Hyderabad.

5. Poster presented in "Spectroscopy and Dynamics of Molecules and Clusters (SDMC 2009)",
   February 20-22, 2009, Indian Association for the Cultivation of Science, Kolkata.

6. Oral presentation in "Chemfest 2010",
   March 7-8, 2009, School of Chemistry, University of Hyderabad, Hyderabad.

7. Poster presented in "Chemfest 2010",
   March 7-8, 2009, School of Chemistry, University of Hyderabad, Hyderabad.

8. Poster presented in "XXth International Symposium on the Jahn-Teller effect ", August 16-20, 2010, University of Fribourg, Fribourg, Switzerland.

9. Poster presented in "Spectroscopy and Dynamics of Molecules and Clusters (SDMC 2011)",
   February 19-21, 2011, Ramnagar, Uttarakhand, India.